UC Irvine
UC Irvine Electronic Theses and Dissertations

Title
Micro-glassblowing Paradigm for Realization of Rate Integrating Gyroscopes

Permalink
https://escholarship.org/uc/item/46k9380z

Author
Senkal, Doruk

Publication Date
2015

Peer reviewed|Thesis/dissertation

eScholarship.org Powered by the California Digital Library
University of California

UNIVERSITY OF CALIFORNIA,
IRVINE

Micro-glassblowing Paradigm for Realization of Rate Integrating Gyroscopes

DISSERTATION

submitted in partial satisfaction of the requirements
for the degree of

DOCTOR OF PHILOSOPHY

in Mechanical and Aerospace Engineering

by

Doruk Senkal

Dissertation Committee:
Professor Andrei M. Shkel, Chair
Professor Faryar Jabbari
Professor Robert T. M'Closkey

2015

© 2015 Doruk Senkal

DEDICATION

This dissertation is dedicated to my dear parents Rubab and Nail Senkal.

TABLE OF CONTENTS

Page

LIST OF FIGURES **vi**

LIST OF TABLES **xi**

LIST OF SYMBOLS **xii**

ACKNOWLEDGMENTS **xiii**

CURRICULUM VITAE **xiv**

ABSTRACT OF THE DISSERTATION **xvii**

1 Introduction **1**
1.1 Motivation . . . 1
1.2 Background . . . 3
1.2.1 Rate Integrating Coriolis Vibratory Gyroscopes . . . 3
1.2.2 Allan Variance . . . 13
1.2.3 Thermoelastic Dissipation . . . 14
1.3 Literature Review . . . 15
1.3.1 Macro-scale Hemispherical Resonator Gyroscopes . . . 15
1.3.2 Micro Rate Integrating Gyroscope Architectures . . . 16
1.4 Research Objective . . . 27
1.5 Dissertation Outline . . . 29

2 Micro-glassblowing of High-Q Materials **31**
2.1 Design Parameters . . . 31
2.1.1 Geometric Design . . . 32
2.1.2 Stem Design . . . 34
2.1.3 Thermoelastic Dissipation . . . 35
2.2 Fabrication Process & Custom-Designed Fabrication Equipment . . . 36
2.2.1 Fabrication Process . . . 36
2.2.2 Custom-designed Furnace . . . 37
2.2.3 Laser Ablation Setup . . . 40
2.3 Analysis of Structures . . . 41
2.3.1 Surface Roughness . . . 41

2.3.2 Material Composition . . . 42
2.4 Conclusions . . . 47

3 Characterization of Micro-glassblown Wineglass Resonators 48
3.1 Introduction . . . 49
3.2 Fabrication of Wineglass Structures . . . 50
3.3 Assembled electrodes . . . 54
3.4 Piezo-pinger setup . . . 59
3.5 Comparison of excitation methods . . . 62
3.6 Conclusions . . . 63

4 Micro-glassblowing for Frequency Symmetry 64
4.1 Introduction . . . 64
4.2 Design for Frequency Symmetry . . . 66
4.2.1 Frequency Symmetry Scaling Laws . . . 66
4.2.2 Stability of Micro-glassblown Structures . . . 70
4.2.3 Factors Affecting Frequency Symmetry . . . 72
4.3 Fabrication . . . 74
4.4 Testing & Characterization . . . 76
4.5 Conclusions . . . 81

5 Micro-glassblowing for High Quality Factor 83
5.1 Introduction . . . 83
5.2 Design . . . 85
5.2.1 Out-of-plane Electrode Architecture . . . 85
5.2.2 Optimization of Q-factor . . . 87
5.3 Modeling . . . 89
5.3.1 Analytical Solution . . . 90
5.3.2 Finite Element Analysis . . . 93
5.4 Fabrication . . . 96
5.5 Experimental Results . . . 102
5.6 Conclusions . . . 103

6 Parametrically Driven Toroidal Ring Gyroscope 105
6.1 Introduction . . . 105
6.2 Design . . . 107
6.2.1 Fabrication . . . 107
6.2.2 Electrode Architecture . . . 108
6.2.3 Parametric Drive . . . 110
6.3 Control System . . . 112
6.4 Experimental Results . . . 115
6.4.1 Device Characterization and Rate Gyroscope Operation . . . 115
6.4.2 Pattern Angle Data . . . 118
6.4.3 Rate Integrating Gyroscope Operation . . . 118
6.5 Conclusions . . . 121

7 Dual Foucault Pendulum Gyroscope **123**
7.1 Introduction 123
7.2 Design 125
7.3 Experimental Results 128
7.3.1 Fabrication 128
7.3.2 Front-end Electronics 129
7.3.3 Experimental Setup 130
7.3.4 Rate Gyroscope Operation 131
7.3.5 Whole Angle Operation 133
7.4 Discussion 136
7.5 Conclusions 137

8 Conclusions **138**
8.1 Contributions of the Dissertation 139
8.2 Future Research Directions 142
8.2.1 CMOS/Micro-wineglass Integration 142
8.2.2 Parametrically Driven Micro-wineglass Gyroscopes 142
8.2.3 Virtual Carouseling for System Identification 142
8.2.4 Multi-stacked Micro-glassblowing 143
8.2.5 Micro-glassblown Optical Sensors and Systems 143
8.2.6 Micro-glassblown Micro-fluidic Devices 144

Bibliography **145**

Appendices **156**

A Cleanroom Recipes **157**
A.1 AZ4620 Lithography - 5000 rpm with 10 W power 157
A.2 Poly-Si Removal for Plasma Bonding 163
A.3 Plasma-assisted Fusion Bonding of Glass and Silicon 167
A.4 Blue-tape Application for Wet Etching of Glass 173
A.5 Fused Silica Wet Etch 175

B Effect of Thickness Variation on Wineglass Frequency Split **178**

C Gyro Front-end PCB **181**

D Gyro Controller Users Manual **188**
D.1 Setup 188
D.2 Data Stream 190
D.3 Command Line Interface 192

E Gyro Controller FPGA and Micro-controller Code **199**

F List of Vendors **224**

LIST OF FIGURES

Page

1.1 Foucault Pendulum is a proof mass suspended from a long string that is free to oscillate in any orientation along the x-y plane. Once started, oscillation pattern precesses under the effect of Coriolis forces, caused by Earth's rotation. 4
1.2 Misalignment in principal axis of elasticity (a) and damping (b) of the gyroscope with respect to the forcer/pick-off axis. For an actual gyroscope, the principal axes of elasticity and damping are not necessarily aligned ($\theta_\omega \neq \theta_\tau$). 6
1.3 Elliptical orbit of a CVG and the canonical variables. 7
1.4 Mode shapes and minimal electrode configuration required for n = 2 (a) and n = 3 (b) wineglass modes. (+) and (−) signs denote, in-phase and anti-phase motion. 12
1.5 Sample Allan variance analysis of gyroscope output, showing error in gyroscope output (deg/hr or deg/s)with respect to integration time (s). 14
1.6 Micro rate integrating gyroscope (MRIG) architectures. 18

2.1 ULE TSG / fused silica micro-glassblowing process, consists of: (a) Deep fused silica etching of device footprint into the substrate, (b) plasma assisted bonding of TSG / fused silica device layer, (c) micro-glassblowing at temperatures up to 1700 °C, (d) optional release step. Fabricated TSG and fused silica structures are shown in (e). 33
2.2 Wineglass structures with (a) 1.2 mm outer diameter and 600 µm stem diameter (hollow), (b) 4200 µm outer diameter and 500 µm stem diameter (solid) and (c) 4200 µm outer diameter and 150 µm stem diameter (solid). 34
2.3 Custom-designed furnace with process capability of 1800 °C glassblowing with a rapid cooling rate of 500 °C/min. 38
2.4 Optical photograph of glassblown fused silica inverted-wineglass structure. Outer diameter is 4200 µm. Glassblown at 1650 °C. 38
2.5 Optical photograph of fused silica spherical shell structures, glassblown at 1700 °C. Outer diameter of shells is 800 µm. 39
2.6 Optical photograph of inverted-wineglass, released along the perimeter using laser ablation and coated with iridium. 41
2.7 AFM surface profiles of TSG, (a) before and (b) after glassblowing. Glassblowing creates extremely smooth (0.2 ppm relative roughness) TSG structures. 43
2.8 Slow cooling of TSG (> 8 hr.) causes recrystallization. 44
2.9 Glassblowing with rapid cooling of TSG (< 1 min.) prevents recrystallization. 45

2.10 EDS spectral analysis of TSG and fused silica reveals that composition of the material does not change after glassblowing. 46

3.1 Schematic description of adaptable test-bed for characterization of micro-wineglass prototypes. 49
3.2 Micro-glassblown wineglass structures are fabricated by (a) etching cavities on the substrate layer, (b) etching of the glass layer to define the perimeter, (c) micro-glassblowing above the softening point of the glass layer and (d) etching away the substrate underneath the wineglass structure. 52
3.3 Released wineglass structure with central stem. 53
3.4 Electrodes are fabricated separately on an SOI stack, bonded to the resonator wafer and extended. 54
3.5 SEM image of an adjustable electrode with 400 µm maximum displacement and 10 µm positioning resolution. 55
3.6 Electrode structures assembled onto a micro-glassblown wineglass resonator with < 20 µm gaps. 56
3.7 Ratchet mechanism acting on the electrode structure, the electrode is extended gradually in 1 through 3. 57
3.8 Electrostatic frequency sweep using adjustable electrode assembly, showing Q = 40k at 14.8 kHz. 57
3.9 A glassblown spherical resonator with assembled electrodes. Diameter is 1.2 mm and thickness is 5 µm. 58
3.10 Piezo-pinger setup for time domain characterization, piezo stack is actuated to probe the wineglass resonator. 60
3.11 Piezo-pinger setup inside vacuum chamber. Optical port on the vacuum chamber allows laser Doppler vibrometer characterization. 61
3.12 A mechanical switch with 1 kΩ discharge resistor was used for controlling the piezo-stack. 61
3.13 Time decay response obtained by retracting the probe tip, beat signal between two degenerate modes shows $\Delta f = 28$ Hz. 62

4.1 Polar plots showing the first 4 harmonics of thickness imperfections. Only the 4th thickness harmonic affects the frequency symmetry (Δf) of n = 2 wineglass modes. (a) 1st harmonic, (b) 2nd harmonic, (c) 3rd harmonic, (d) 4th harmonic, (e) n = 2 wineglass modes. 66
4.2 Plot showing wineglass thickness vs thickness imperfections in the 4th harmonic and resulting frequency split. Going from precision machined wineglass resonators to micro-machined devices require 1 to 3 orders of magnitude improvement in fabrication tolerances due to the reduction in thickness. . . . 68
4.3 The effect of thickness variation of the 4th harmonic on frequency split (Δf) vs wineglass resonator radius. 69
4.4 Surface tension induced pressure differential depends on geometric parameters such as cavity radius (r_0) and height (l). $l = r_0$ marks the critically stable region for micro-glassblowing of inverted wineglass structures. 71

4.5 Process flow for fabrication of micro-glassblown wineglass resonators with integrated electrodes. (a) Device layer is bonded to pre-etched substrate, (b) device layer is etched, defining the perimeter of the wineglass and the electrodes, (c) wafer stack is glassblown, (d) silicon underneath the perimeter is etched using XeF_2, (e) a thin metal layer is blanket coated. 73
4.6 SEM image of a stand-alone micro-wineglass structure after release. Diameter 4.4 mm, thickness 50 µm. 75
4.7 Metallized micro-wineglass structure with integrated electrodes. Diameter 4.4 mm, thickness 50 µm. 75
4.8 Packaged and wirebonded micro-wineglass resonator. Diameter 4.4 mm, thickness 50 µm 76
4.9 Laser Doppler Vibrometer was used to scan along the perimeter of the wineglass to map the mode shapes associated with X forcer and Y forcer electrodes. 77
4.10 Measured velocity amplitude distribution (mm/s) identifying (a) n = 2 and (b) n = 3 wineglass modes. 78
4.11 Experimental frequency sweeps of n = 2 and n = 3 wineglass modes, showing $\Delta f = 0.16$ Hz and $\Delta f = 0.20$ Hz, respectively. 79
4.12 Frequency split vs DC bias, showing that the frequency split is within 1 Hz independent of DC bias (DC bias was varied between 20–100 V with 20 V increments). 79
4.13 Frequency sweeps of n = 2 mode of 4 additional wineglass resonators, showing Δf values in the range of 1.76 Hz to 21.08 Hz. 80

5.1 Out-of-plane electrode architecture consists of a micro-glassblown fused silica (FS) wineglass resonator and planar Cr/Au electrodes defined on fused silica, enabling batch-fabrication. 85
5.2 Out-of-plane transduction scheme utilizes out-of-plane component of wineglass modes to drive and sense in-plane motion. 86
5.3 Electrode configuration: 4 electrodes are designated as forcers (FX and FY) and 4 are designated as pick-off (PX and PY). Both the forcer and pick-off channels have differential pairs (i.e. FX+ and FX-). 87
5.4 Out-of-plane to in-plane displacement ratio for mushroom resonators: Due to the 3-D nature of the resonator, the ratio is close to 1:1. Star marks the design presented in this chapter. 88
5.5 Small central post diameters create solid stem structures (left), large diameters create hemi-toroidal structures (right). 90
5.6 Geometric parameters of an inverted-wineglass structure: Minor radius r, major radius R, inner perimeter r_1, outer perimeter r_2, etch depth h_e and wineglass height h_w. 90
5.7 Analytical solution of etch depth (h_e), wineglass diameter ($2r_2$) vs final inverted wineglass height. Stem outer diameter ($2r_1$) is 400 µm, glassblowing temperature is 875 °C. 91
5.8 Boundary conditions for finite element analysis: (a) before glassblowing, (b) after glassblowing. 93

5.9 Transient FEA of micro-glassblowing process showing the formation of self-aligned stem structures. 94
5.10 Finite elemet predictions and cross-sectional SEM shots of fabricated micro-wineglass structures. 95
5.11 Micro-glassblowing process can create arrays of inverted-wineglass structures on the wafer surface. Outer diameter of shells is $\sim$ 4 mm, over 100 Borosilicate Glass (BSG) shells were fabricated on a 100 mm wafer. 97
5.12 1 million Q-factor fused silica wineglass structure with integrated electrodes (left), close-up of capacitive gaps (right). 98
5.13 Wafer-level fabrication process for fused silica micro-wineglass structures: (a) plasma bonding of device layer to substrate with pre-etched cavities, (b) micro-glassblowing at 1700 °C, (c) removal of the substrate via back-lapping, (d) bonding the wineglass wafer to electrode wafer, (e) removal of the sacrificial layer to form capacitive gaps. 99
5.14 Uniform 10 µm capacitive gaps have been demonstrated on 7 mm shell structures, resulting in over 9 pF total active capacitance on the device. 100
5.15 Frequency sweep revealed a Q-factor of 1.14 million and as fabricated frequency split (Δf) of 14 Hz at 105 kHz center frequency. The chamber pressure was 19 µTorr during the frequency sweep. 101
5.16 Ring-down experiment at 19 µTorr shows $\tau = 3.18$ s, giving 1.05 million Q-factor at 105 kHz, confirming the frequency sweep. 102
5.17 Q-factor vs pressure level experiment. Q-factors above 1 million were obtained below 20 µTorr. 104

6.1 Toroidal Ring Gyroscope (a) consists of an outer anchor that encircles the device, as opposed to axi-symmetric devices with cenral support structures (b).106
6.2 A 100k Q-factor, epitaxial silicon encapsulated Toroidal Ring Gyroscope was used in the experiments. Device consists of an outer ring anchor, distributed suspension system and an inner electrode assembly. 107
6.3 Due to the distributed suspension system vibrational energy is trapped within the gyroscope. 109
6.4 Central electrode assembly consists of 12 discrete electrodes, divided into 4 drive and 8 pick off electrodes, and one star shaped parametric electrode. . . 110
6.5 Rate integrating gyro controller with parametric drive, implemented on a Artix 7 FPGA board running at 1 MHz. 113
6.6 Freq. sweep showing the n = 3 wineglass modes with Q-factor above 100k at central frequency of 69.8 kHz. 115
6.7 Electrostatic tuning with 3.26 V and 0.5 V resulted in $\Delta f < 100$ mHz ($\Delta f <$ 2 ppm at 69.75 kHz). 115
6.8 Scale factor of Toroidal Ring Gyroscope in force-to-rebalance mode. 117
6.9 Allan deviation of gyroscope force-to-rebalance output, showing bias stability of 0.65 ° h. 117
6.10 Tuning of the gyro based on residuals of pattern angle data from PLL, parametric AGC, and quadrature null loops. 119

6.11 Experimental demonstration of rate integrating operation under parametric drive. 120
6.12 Comparison of residual errors of conventional drive and parametric drive for different rate inputs. 121

7.1 Wineglass modes of axi-symmetric architectures, such as ring/disk systems and wineglasses gyroscopes, are inherently dynamically balanced, resulting in zero net force and torque during oscillation. 124
7.2 Dual Foucault Pendulum (DFP) gyroscope consists of two mechanically coupled Foucault Pendulums. 125
7.3 Vibration immunity and anchor loss mitigation are provided by anti-phase operation of two dynamically equivalent Foucault Pendulums. 126
7.4 FEA showing x-y symmetric anti-phase operation. Device is anchored at four points in between the proof masses. Colors correspond to total displacement. 127
7.5 Image of fabricated gyroscope with a closeups of the shuttle assemblies and the anchors. 129
7.6 High-vacuum test-bed with non-evaporable getter pump provides µTorr level vacuum for rate characterization. 130
7.7 Ring down experiment showing energy decay time constant (τ) of 30 s or Q of 301k at 3.2 kHz. 131
7.8 Rate characterization with 45 °/s step input showed a FRB scale factor of 4.66 mV/(°/s), goodness of fit: $R^2 = 0.999$. 132
7.9 Alan variance of zero rate output, showing ARW and in-run bias instability for FRB and open-loop operation. 133
7.10 Rate integrating gyro control implemented on a Artix 7 FPGA running at 500 kHz, provides closed loop control of PLL, AGC, quadrature null, and FRB. 134
7.11 Polar plots showing the pattern angle dependence of four main closed loops. 2Θ and 4Θ dependence indicate frequency mismatch and forcer misalignment. 135
7.12 Spooling of the rate integrating gyro output over 2 hours of continuous rotation. Linear fit shows angular gain factor of ~0.8 and RMSE of 22 ppm. . . . 135

LIST OF TABLES

Page

2.1 Anchor loss analysis show a large change in Q_{anchor} for different stem diameters. 35
2.2 Thermoelastic dissipation analysis of micro-wineglass structures shows that 3 to 6 orders of magnitude increase in Q_{TED} is achievable by using low expansion materials. 36
2.3 Sample design parameters for micro-glassblown mushroom structure. 39
2.4 Sample design parameters for micro-glassblown hemi-sphere. 40

3.1 Comparison of excitation methods. 62

4.1 Summary of fabrication defects and reduction approach. 72
4.2 Table summarizing frequency splits and center frequency of 5 different micro-wineglass structures. 81

5.1 Comparison of wineglass dimensions obtained from analytical solutions, FEA and experiments. 96
5.2 Summary of device parameters for a 7 mm fused silica wineglass resonator. . 103

6.1 Summary of geometric parameters. 109
6.2 As-fabricated frequency symmetry of 4 devices. 116

7.1 Summary of design parameters. 128

LIST OF SYMBOLS

Mechanical Parameters of the Resonator

Symbol	Description
Center freq. (f)	Mean frequency of the two primary modes of the resonator
τ	Mean energy decay time constant of the resonator
Q-factor	Ratio of stored energy to energy loss per vibration cycle ($\mathrm{Q} = \tau\pi f$)
Δf	Frequency split between primary modes in Hz ($\Delta f = f_x - f_y$)
$\Delta\omega$	Frequency split between primary modes in rad/s ($\Delta\omega = \omega_x - \omega_y$)
$\Delta\tau^{-1}$	Measure of anisodamping within the gyroscope ($\Delta\tau^{-1} = \lvert\tau_x^{-1} - \tau_y^{-1}\rvert$)
θ_ω	Angle defining the orientation of actual vs intended axes of elasticity
θ_τ	Angle defining the orientation of actual vs intended axes of damping
$(\mathrm{x}, \mathrm{y}, \mathrm{z})$	Coordinate frame oriented along intended axes of symmetry x and y
$\mathrm{n} = 2$ mode	A 4-node degenerate mode pair of a wineglass or ring/disk system
$\mathrm{n} = 3$ mode	A 6-node degenerate mode pair of a wineglass or ring/disk system
Precession pattern	Vibration pattern formed by superposition of x and y vibratory modes, which is capable of changing its orientation (precesses) when subjected to Coriolis forces or an external forcing function
Pattern angle (θ)	Orientation of the precession pattern in degrees, which is a measure of angular rotation in a Rate Integrating Gyroscope

Control System Abbreviations

Symbol	Description
Quadrature	Unwanted component of oscillation that interferes with estimation of the pattern angle, manifests as a result of structural imperfections
AGC	Amplitude Gain Control, closed loop control of drive amplitude
PLL	Phase Locked Loop, closed loop control system that generates an AC signal with a pre-determined phase offset from the resonator
FTR	Force-to-rebalance, closed loop control system that actively drives the pattern angle to a setpoint
Quadrature null	Closed loop control system that actively suppresses the effects of structural imperfections within the gyroscope

ACKNOWLEDGMENTS

First of all, I would like to express my deepest gratitude to my advisor Professor Andrei M. Shkel for this wonderful research opportunity. I can't thank him enough for his continuous support and guidance through my Ph.D. studies. I also would like to thank my dissertation committee, Professor Faryar Jabbari and Professor Robert M'Closkey, for taking the time out of their busy schedules to review this work and provide insightful comments. I am also deeply grateful to Dr. Alexander Trusov for providing invaluable guidance through the early years of my Ph.D.

Next, I would like to thank all my friends and colleagues at UCI MicroSystems Laboratory for their help and support through my Ph.D. studies. In particular, I would like to thank my colleagues Dr. Mohammed J. Ahamed, Mohammad Asadian Ardakani, Sina Askari, Alexandra Efimovskaya, and Dr. Christopher Raum for their invaluable help in various aspects of the project, as well as Dr. Sergei Zotov, Dr. Igor Prikhodko, Dr. Brenton R. Simon, and Dr. Montgomery Rivers for numerous technical discussions and insightful suggestions.

I also would like to thank Professor Thomas W. Kenny and his group at Stanford University, especially Eldwin Ng, Vu Hong, Yushi Yang, and Chae Hyuck Ahn, for the wonderful collaboration opportunity on epitaxially-encapsulated gyroscopes. In addition, I would like to thank UCI Integrated Nanosystems Research Facility staff Jake Hes, Dr. Mo Kebaili, Vu Phan, and Dr. Lifeng Zheng for their help and valuable suggestions on fabrication aspects of the project.

I also would like to acknowledge the funding, generously provided by Space and Naval Warfare Systems Command (SPAWAR) and Defense Advanced Research Projects Agency (DARPA), without which this work would not have been possible. Specifically, this work was supported by DARPA/SPAWAR under Grant N66001-10-1-4074 & DARPA grant W31P4Q-11-1-0006 under the Micro-PNT Program.

Finally, I would like to thank my family, as well as my longtime mentor and advisor Professor Hakan Gurocak, for their guidance and continued support.

CURRICULUM VITAE

Doruk Senkal

Doctor of Philosophy in Mechanical and Aerospace Eng. **June 2015**
University of California, Irvine *Irvine, CA, USA*

Master of Science in Mechanical Engineering **December 2009**
Washington State University, Vancouver *Vancouver, WA, USA*

Bachelor of Science in Mechanical Engineering **June 2007**
Middle East Technical University *Ankara, Turkey*

REFEREED CONFERENCE PUBLICATIONS

D. Senkal, A. Efimovskaya, and A. M. Shkel. Dual Foucault Pendulum Gyroscope. In *Solid-State Sensors, Actuators and Microsystems Workshop (TRANSDUCERS)*, Anchorage, Alaska, USA, 2015

A. Efimovskaya, D. Senkal, and A. M. Shkel. Miniature Origami-like Folded MEMS TIMU. In *Solid-State Sensors, Actuators and Microsystems Workshop (TRANSDUCERS)*, Anchorage, Alaska, USA, 2015

D. Senkal, A. Efimovskaya, and A. M. Shkel. Minimal Realization of Dynamically Balanced Lumped Mass WA Gyroscope: Dual Foucault Pendulum. In *IEEE International Symposium on Inertial Sensors and Systems (ISISS)*, pages 131–134, Hapuna Beach, HI, USA, 2015

A. Efimovskaya, D. Senkal, and A. M. Shkel. Origami-like Folded MEMS for Realization of TIMU: Fabrication Technology and Initial Demonstration. In *IEEE International Symposium on Inertial Sensors and Systems (ISISS)*, pages 58–61, Hapuna Beach, HI, USA, 2015

D. Senkal, E. J. Ng, V. Hong, Y. Yang, C. H. Ahn, T. W. Kenny, and A. M. Shkel. Parametric Drive of a Toroidal MEMS Rate Integrating Gyroscope Demonstrating 20 ppm Scale Factor Stability. In *IEEE International Conference on Micro Electro Mechanical Systems (MEMS)*, pages 29–32, Estoril, Portugal, 2015

D. Senkal, M. J. Ahamed, M. H. A. Ardakani, S. Askari, and A. M. Shkel. Out-of-Plane Electrode Architecture for Fused Silica Micro-Glassblown 3-D Wineglass Resonators. In *IEEE Sensors Conference*, pages 994 – 997, Valencia, Spain, 2014

D. Senkal, M. J. Ahamed, S. Askari, and A. M. Shkel. MEMS Micro-Glassblowing Paradigm for Wafer-Level Fabrication of Fused Silica Wineglass Gyroscopes. In *Eurosensors Conference*, pages 1489–1492, Brescia, Italy, 2014

D. Senkal, M. J. Ahamed, S. Askari, and A. M. Shkel. 1 Million Q-Factor Demonstrated on Micro-glassblown Fused Silica Wineglass Resonators with Out-of-Plane Electrostatic Transduction. In *Solid-State Sensors, Actuators and Microsystems Workshop (Hilton Head)*, pages 68–71, Hilton Head Island, South Carolina, USA, 2014

D. Senkal, S. Askari, M. J. Ahamed, E. J. Ng, V. Hong, Y. Yang, C. H. Ahn, T. W. Kenny, and A. M. Shkel. 100k Q-Factor Toroidal Ring Gyroscope Implemented in Wafer-Level Epitaxial Silicon Encapsulation Process. In *IEEE International Conference on Micro Electro Mechanical Systems (MEMS)*, pages 9–12, Taipei, Taiwan, 2014

M. J. Ahamed, D. Senkal, and A. M. Shkel. Effect of Annealing on Mechanical Quality Factor of Fused Quartz Hemispherical Resonator. In *IEEE International Symposium on Inertial Sensors and Systems (ISISS)*, pages 59–62, Laguna Beach, California, USA, 2014

M. J. Ahamed, D. Senkal, and A. M. Shkel. Improvement of Side-Wall Roughness in Deep Glass Dry Etched MEMS Vibratory Sensors. In *IEEE International Symposium on Inertial Sensors and Systems (ISISS)*, pages 127–128, Laguna Beach, California, USA, 2014

D. Senkal, M. J. Ahamed, and A. M. Shkel. Design and Modeling of Micro-Glassblown Inverted-Wineglass Structures. In *IEEE Symposium on Inertial Sensors and Systems (ISISS)*, pages 13–16, Laguna Beach, California, USA, 2014

M. J. Ahamed, D. Senkal, A. A. Trusov, and A. M. Shkel. Deep NLD Plasma Etching of Fused Silica and Borosilicate Glass. In *IEEE Sensors Conference*, pages 1767–1770, Baltimore, Maryland, USA, 2013

D. Senkal, M. J. Ahamed, A. A. Trusov, and A. M. Shkel. Demonstration of Sub-1 Hz Structural Symmetry in Micro-Glassblown Wineglass Resonators with Integrated Electrodes. In *Solid-State Sensors, Actuators and Microsystems Conference (TRANSDUCERS)*, pages 1380–1383, Barcelona, Spain, 2013

D. Senkal, M. J. Ahamed, a. a. Trusov, and a. M. Shkel. Adaptable Test-Bed for Characterization of Micro-Wineglass Resonators. In *IEEE International Conference on Micro Electro Mechanical Systems (MEMS)*, pages 469–472, Taipei, Taiwan, 2013

D. Senkal, C. R. Raum, A. A. Trusov, and A. M. Shkel. Titania Silicate/Fused Quartz Flassblowing for 3-D Fabrication of Low Internal Loss Wineglass Micro-Structures. In *Solid-State Sensors, Actuators, and Microsystems Workshop (Hilton Head)*, pages 267–270, Hilton Head Island, South Carolina, USA, 2012

D. Senkal, I. P. Prikhodko, A. A. Trusov, and A. M. Shkel. Micromachined 3-D Glass-Blown Wineglass Structures for Vibratory MEMS Applications. In *Technologies for Future Micro-Nano Manufacturing Workshop*, pages 166–169, Napa Valley, California, USA, 2011

REFEREED JOURNAL PUBLICATIONS

D. Senkal, M. J. Ahamed, M. H. A. Ardakani, S. Askari, and A. M. Shkel. Demonstration of 1 Million Q-Factor on Microglassblown Wineglass Resonators With Out-of-Plane Electrostatic Transduction. *IEEE/ASME Journal of Microelectromechanical Systems*, 24(1):29–37, 2015

D. Senkal, M. J. Ahamed, A. A. Trusov, and A. M. Shkel. Electrostatic and Mechanical Characterization of 3-D Micro-Wineglass Resonators. *Sensors and Actuators A: Physical*, 215:150–154, 2014

D. Senkal, M. J. Ahamed, A. A. Trusov, and A. M. Shkel. Achieving Sub-Hz Frequency Symmetry in Micro-Glassblown Wineglass Resonators. *IEEE/ASME Journal of Microelectromechanical Systems*, 23(1):30–38, 2014

D. Senkal, M. J. Ahamed, A. A. Trusov, and A. M. Shkel. High Temperature Micro-glassblowing Process Demonstrated on Fused Quartz and ULE TSG. *Sensors and Actuators A: Physical*, 201:525–531, 2012

ABSTRACT OF THE DISSERTATION

Micro-glassblowing Paradigm for Realization of Rate Integrating Gyroscopes

By

Doruk Senkal

Doctor of Philosophy in Mechanical and Aerospace Engineering

University of California, Irvine, 2015

Professor Andrei M. Shkel, Chair

This Ph.D. dissertation reports novel fabrication processes and architectures for implementation of Rate Integrating Gyroscopes at micro-scale. Majority of the focus is directed towards development of a surface tension and pressure driven micro-glassblowing paradigm, which is envisioned to serve as an enabling mechanism for wafer-scale fabrication of 3-D micro-wineglass gyroscopes. New 2-D silicon Micro Rate Integrating Gyroscope (MRIG) architectures are also explored to bridge the gap between conventional micro-machining techniques and micro-glassblowing processes, and to serve as a test platform for various MRIG control strategies. Closed loop Whole Angle operation of these 2-D silicon MRIG architectures is presented to identify some of the control challenges associated with MRIG control, such as energy pumping and suppression of errors caused by structural imperfections.

The main contribution of the thesis is the development of a high temperature ($> 1700\,^{\circ}$C) micro-glassblowing process for fabrication of highly symmetric and low internal dissipation 3-D fused silica wineglass resonators. Owing to the "self-healing" properties of surface tension and pressure driven micro-glassblowing paradigm, and the low internal loss fused silica material, quality factors above 1 million and frequency splits (Δf) less than 1 Hz have been demonstrated. In addition to a multi-purpose test-bed for micro-wineglass characterization, electrodes with sub 10 µm capacitive gaps are reported for electrostatic transduction.

In order to streamline the realization of MRIG control strategies, two new Si-MEMS MRIG architectures were also developed as a part of this thesis: Toroidal Ring Gyroscope (TRG) and Dual Foucault Pendulum (DFP) Gyroscope. Toroidal Ring Gyroscope consists of an outer anchor, concentric ring suspension system, and inner electrode assembly. Q-factors above 100,000 were obtained with this architecture at a compact size of 1760 µm, resulting in rate gyroscope operation with angle random walk (ARW) of $0.047\,°/\sqrt{\mathrm{h}}$ and an in-run bias stability of 0.65 ° h. First demonstration of a parametrically driven MRIG is also reported as a part of this work, showing better than < 20 ppm scale factor stability at 360 °/s rate input.

Dual Foucault Pendulum (DFP) architecture is a conventionally machined lumped mass Micro Rate Integrating Gyroscope implemented using in-house silicon-on-insulator technology. Due to high-Q degenerate mode operation and large modal mass, angle random walk (ARW) as low as $0.003\,°/\sqrt{\mathrm{h}}$ and in-run bias stability of 0.27 °/h were demonstrated in open loop operation without ovenization or temperature compensation. It is believed that this two mass DFP architecture is the minimal realization of a dynamically balanced, lumped mass MRIG.

Finally, a multi-purpose FPGA/DSP based control system was developed to demonstrate interchangeable rate and rate integrating mechanization of micro-scale gyroscope architectures developed in this thesis. Continuous Rate Integrating Gyroscope operation is demonstrated, by electronically compensating structural imperfections via control loops, such as Phase Locked Loop (PLL), Amplitude Gain Control (AGC), quadrature null loop, and closed-loop parametric drive.

Chapter 1

Introduction

Motivation of the research is presented in this chapter, including an overview and problem statement. This is followed by a literature review of Micro Rate Integrating Gyroscopes (MRIGs). Then, objectives of the research are presented. The chapter is concluded with an outline of the dissertation.

1.1 Motivation

Coriolis Vibratory Gyroscopes (CVGs) can be divided into two broad categories based on the gyroscope's mechanical element [1]: degenerate mode z-axis gyroscopes, which have x-y symmetry (Δf of $0\,\text{Hz}$), and non-degenerate mode gyroscopes, which are designed intentionally to be asymmetric in x and y modes ($\Delta f \neq 0\,\text{Hz}$). Degenerate mode z-axis gyroscopes offer a number of unique advantages compared to non-degenerate vibratory rate gyroscopes, including higher rate sensitivity, ability to implement Whole Angle mechanization with mechanically unlimited dynamic range, exceptional scale factor stability, and a potential for self-calibration.

Despite potential advantages of degenerate mode operation, due to technological limitations, most high performance MEMS CVGs have been designed to operate as non-degenerate mode devices, whereas degenerate mode operation was reserved for precision machined macro-scale CVGs, such as the Hemispherical Resonator Gyroscope (HRG) [2]. This is mainly due to the high structural symmetry, or equivalently high frequency and damping symmetry (Δf and $\Delta\tau^{-1}$) required for high performance degenerate mode operation. For macro-scale rate integrating gyroscopes this frequency symmetry is obtained through a combination of precision machining processes (10^{-6} relative tolerance) and post-fabrication trimming of the resonators [2]. Whereas conventional micro-machining processes are generally associated with precision machining ($10^{-2} - 10^{-4}$ relative tolerance) and low aspect ratios (height-to-footprint ratio), making large-scale fabrication of these devices challenging. Factors, such as etch non-uniformity, alignment errors or high surface roughness and granularity of deposited thin films have so far prevented fabrication of high precision degenerate mode gyroscopes using MEMS techniques.

In addition to high precision fabrication processes, maximization of the quality Q-factor is key to enhancing performance of vibratory MEMS devices in demanding signal processing, timing, and inertial applications [3]. For example, timing devices rely heavily on high Q-factors for low close-to-carrier phase noise and low energy consumption [4]. Whereas devices such as high performance rate integrating gyroscopes (RIGs) and mode-matched rate gyroscopes rely heavily on long energy decay times and high Q-factors [5]. Current MEMS fabrication techniques limit the maximum achievable Q-factor by restricting the material choice to a few materials. Available materials, such as single-crystal silicon, have relatively high coefficient of thermal expansion (CTE of ~3 ppm/°C [6]) and consequently high thermoelastic dissipation (TED) [7]. Materials with low CTE, such as fused silica (0.5 ppm/°C) and ultra low expansion titania silicate glass (ULE TSG, 0.03 ppm/°C) can provide a dramatic increase in fundamental Q_{TED} limit. However, when compared to silicon, titania silicate glass and fused silica dry etching suffers from an order of magnitude higher surface roughness, lower

mask selectivity ($\sim 1:1$ for photoresist), and lower aspect ratio, $< 5:1$ [8, 9].

The macro-scale Hemispherical Resonator Gyroscope (HRG) with Q-factors over 25 million [2] motivates the investigation of 3-D fused silica micro-wineglass structures for use as vibratory elements in MEMS applications, due to potential advantages of the wineglass architecture in terms of structural symmetry, minimization of energy losses, and immunity to external vibrations. To take full advantage of the 3-D wineglass architecture, however, fabrication techniques with high symmetry, low surface roughness, as well as materials with high isotropy and low TED are required.

1.2 Background

This section gives a brief overview of Rate Integrating Gyroscopes and common terms used throughout the thesis.

1.2.1 Rate Integrating Coriolis Vibratory Gyroscopes

Foucault Pendulum, first demonstrated by French physicist Lèon Foucault back in 1851, is a device that consists of a proof mass suspended from a long string. The proof mass is free to oscillate in any orientation along the x-y plane. When the device is caused to oscillate at a fixed orientation, the orientation of the oscillation can be observed to slowly precess under the affect of Coriolis forces caused by Earth's rotation. For this reason, the device can be used to experimentally demonstrate Earth's rotation and is quite possibly the first Rate Integrating Gyroscope that was conceived.

If the motion of the Foucault pendulum along the z-axis is sufficiently small, the dynamics can be approximated by a point mass system in a non-inertial frame with equations of motion

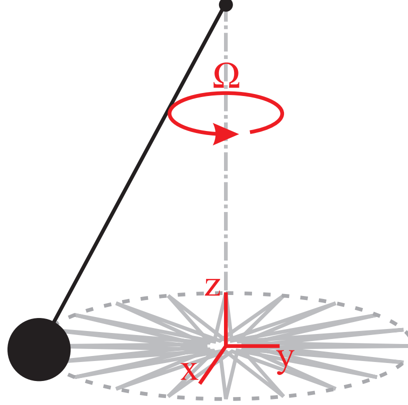

Figure 1.1: Foucault Pendulum is a proof mass suspended from a long string that is free to oscillate in any orientation along the x-y plane. Once started, oscillation pattern precesses under the effect of Coriolis forces, caused by Earth's rotation.

defined by two coupled spring-mass-dashpot systems. This forms a mathematical basis for all Coriolis Vibratory Gyroscopes [10]:

$$
\begin{aligned}
\ddot{x} + \frac{2}{\tau_x}\dot{x} + (\omega_x^2 - \eta'\Omega_z^2)x - \eta\dot{\Omega}_z y &= \frac{F_x}{m_{eq}} + 2\eta\dot{y}\Omega_z \ , \\
\ddot{y} + \frac{2}{\tau_y}\dot{y} + (\omega_y^2 - \eta'\Omega_z^2)y + \eta\dot{\Omega}_z y &= \frac{F_y}{m_{eq}} - 2\eta\dot{x}\Omega_z \ ,
\end{aligned}
\tag{1.1}
$$

where τ_x and τ_y are the highest and the lowest energy decay time constants along x and y axes, respectively. Energy decay time constant is defined as the time that takes for vibration amplitude of the resonator to decay down to $1/e \approx 36.8\%$ of initial amplitude.

The parameters ω_x and ω_y are the highest and lowest resonance frequencies, in rad/s, along x and y axis. Throughout the thesis f_x and f_y are also used for the resonance frequencies, in this case the units would be in Hz or kHz ($f = 2\pi\omega$).

Finally, m_{eq} is the equivalent mass of the gyroscope, which is the mass that is sensitive to Coriolis forces. F_x and F_y are the forcing functions along x and y axes, respectively. Ω_z is the angular velocity along z axis and η is the angular gain factor of the gyroscope. For an ideal gyroscope $\eta = 1$, but typically $\eta < 1$, and this is due to the additional mass in the system

that does not contribute to Coriolis forces. It must be also noted that due to slow angular rotation rates compared to gyroscope resonance frequency ($\omega \gg \Omega$) and small amplitude of oscillation, the contribution of higher order Coriolis terms Ω^2 and $\dot{\Omega}$ in the equations of motion are generally negligible.

1.2.1.1 Fabrication Imperfections

Due to fabrication imperfections, x and y energy decay time constants and resonance frequencies differ from each other. The so-called, aniso-damping (damping split) and aniso-elasticity (frequency split) can be represented as:

$$\Delta\omega = \omega_x - \omega_y \text{ or } \Delta f = f_x - f_y \ , \tag{1.2}$$

$$\Delta\tau^{-1} = \tau_x^{-1} - \tau_y^{-1} \ , \tag{1.3}$$

where the center frequency and nominal energy decay constant are:

$$\omega = \frac{\omega_x + \omega_y}{2} \text{ or } f = \frac{f_x + f_y}{2} \ , \tag{1.4}$$

$$\tau = \frac{\tau_x + \tau_y}{2} \ , \tag{1.5}$$

The axes where the highest and lowest resonance frequencies and energy decay time constant occur are called the principal axes of elasticity and damping, respectively. So far, it was assumed that the principal axes of elasticity and damping are aligned with the x-y coordinate axes, Eq. 1.1. This is never the case for an actual gyroscope. Due to fabrication imperfections, as well as electrode misalignments, the principal axes of elasticity and damping are generally misaligned to the forcer/pick-off axis. Effect of such a misalignment is shown in Fig. 1.2 for principal axis of elasticity and damping.

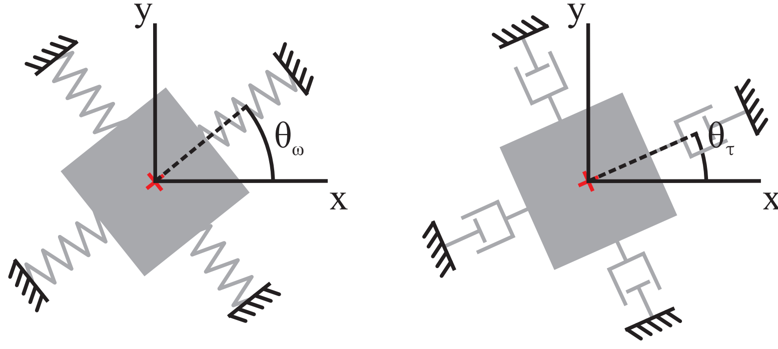

Figure 1.2: Misalignment in principal axis of elasticity (a) and damping (b) of the gyroscope with respect to the forcer/pick-off axis. For an actual gyroscope, the principal axes of elasticity and damping are not necessarily aligned ($\theta_\omega \neq \theta_\tau$).

This effect can be represented using an orthogonal transformation by introducing the rotation angles θ_τ and θ_ω [10]. Here, θ_τ represents the orientation of the τ_x axis and θ_ω represents the orientation of the ω_y axis. For an actual gyroscope, the principal axes of elasticity and damping are not necessarily aligned ($\theta_\omega \neq \theta_\tau$).

After the introduction of aniso-elasticity, aniso-damping terms and their orientation with respect to forcer/pick-off axis, the equations of motion become [10]:

$$\begin{aligned}
\ddot{x} + \frac{2}{\tau}\dot{x} + \Delta\tau^{-1}(\dot{x}\cos(2\theta_\tau) + \dot{y}\sin(2\theta_\tau)) + (\omega_x^2 - \eta'\Omega_z^2)x - \eta\dot{\Omega}_z y \\
-\omega\Delta\omega(x\cos(2\theta_\omega) + y\sin(2\theta_\omega)) = \frac{F_x}{m_{eq}} + 2\eta\dot{y}\Omega_z\ , \\
\ddot{y} + \frac{2}{\tau}\dot{y} + \Delta\tau^{-1}(\dot{x}\sin(2\theta_\tau) - \dot{y}\cos(2\theta_\tau)) + (\omega_y^2 - \eta'\Omega_z^2)y + \eta\dot{\Omega}_z x \\
-\omega\Delta\omega(x\sin(2\theta_\omega) - y\cos(2\theta_\omega)) = \frac{F_y}{m_{eq}} - 2\eta\dot{x}\Omega_z\ ,
\end{aligned} \tag{1.6}$$

It is important to note that after the introduction of the misalignment errors in principal axis of elasticity and damping, the two vibratory modes of the gyroscope are not only coupled by the Coriolis forces, but also through the aniso-elasticity and aniso-damping terms $\Delta\omega$ and $\Delta\tau^{-1}$, respectively.

1.2.1.2 Canonical Variables

For non-zero initial velocity and in the absence of rate input, damping, and aniso-elasticity, the equivalent point-mass system described in Eq. 1.6 would trace a constant elliptical orbit, as shown in Fig. 1.3 [11].

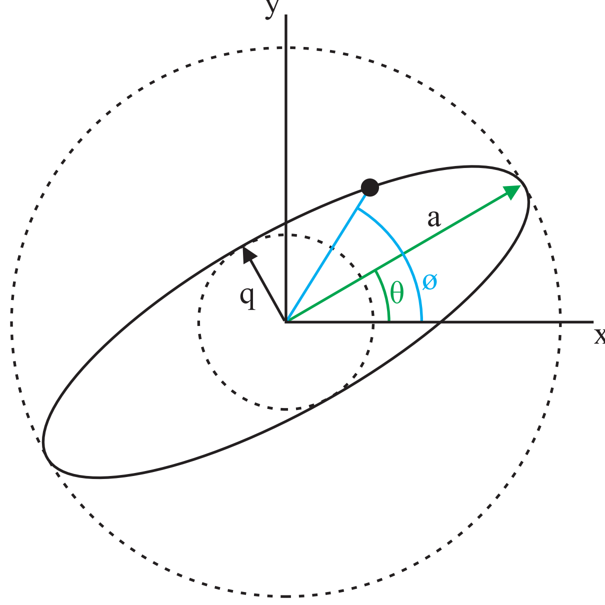

Figure 1.3: Elliptical orbit of a CVG and the canonical variables.

In Fig. 1.3, “a” and “q” are major and minor radii of the eliptical orbit, θ is the orientation of the major radius (also known as pattern angle), and ϕ is the phase of the oscillation.

For an ideal Rate Integrating Gyroscope, where there is no damping or aniso-elasticity, the major radius of the elliptical trajectory “a” is expected to remain constant and minor radius “q” is expected to be constant and zero, while the orientation of major radius (pattern angle) precesses in time under the effect of Coriolis forces, according to:

$$\theta = -\eta \int \Omega_z dt = -\eta \theta_{actual} \, , \tag{1.7}$$

where η is the angular gain factor and Ω_z is the angular velocity of the gyroscope. As can be

seen in Eq. 1.7, the orientation of the precession pattern θ is directly related to the integral of the angular velocity of the gyroscope through angular gain factor η. Due to this close relationship, the orientation of precession pattern (θ) becomes a measure of actual rotation of the gyroscope (θ_{actual}). Hence, this mode of mechanization is called Rate Integrating or Whole Angle Gyroscope operation.

1.2.1.3 Effect of Structural Imperfections

So far, the canonical variables were described for an ideal gyroscope, where the damping and aniso-elasticity is zero. However, due to imperfections within the system, such as a non-zero dissipation term as well as aniso-elasticity and aniso-damping, these variables "a", "q", and ϕ vary slowly in time. In addition to this, the pattern angle θ is no longer only a function of Coriolis input (Ω), but is affected by aniso-elaticiy and aniso-damping.

Despite this slow variation, the terms "a", "q", ϕ, and θ can be used to describe the state of the CVG, particularly if the aniso-damping and aniso-elasticity terms are sufficiently small with respect to ω, such that $\Delta\omega \ll \omega$ and $\Delta\tau^{-1} \ll \omega$. In this case, the state of the gyroscope can be defined by using the four canonical variables: pattern angle θ, the phase angle ϕ, as well as the energy term [10]:

$$\mathrm{E} = \mathrm{a}^2 + \mathrm{q}^2, \tag{1.8}$$

and the quadrature term:

$$\mathrm{Q} = 2\mathrm{aq}\,. \tag{1.9}$$

The so-called quadrature error (Q), is the unwanted component of the oscillation, which

manifests as a result of aniso-elasticity within the mechanical element. The quadrature error (Q) can inadvertently interfere with estimation of the pattern angle, due to imperfections in pick-off and control electronics. Moreover, if the quadrature term is allowed to grow to a point, such that the elliptical orbit of the RIG degenerates into a circle (a = q), it becomes impossible to estimate the pattern angle θ, Fig. 1.3.

As described in the previous section, for an ideal gyroscope, the time evolution of these canonical variables would be [10]:

$$\begin{aligned}
&\dot{\mathrm{E}} = 0,\ \mathrm{E} \neq 0\,, \\
&\dot{\mathrm{Q}} = 0\,, \mathrm{Q} = 0\,, \\
&\dot{\theta} = -\eta\Omega\,.
\end{aligned} \tag{1.10}$$

However, when the structural imperfections are introduced, the time evolution of the canonical variables become [10]:

$$\begin{aligned}
\dot{\mathrm{E}} =& -\frac{2}{\tau}\mathrm{E} - \Delta\tau^{-1}\cos 2(\theta-\theta_\tau)\sqrt{\mathrm{E}^2-\mathrm{Q}^2} - \frac{a}{\omega}f_{as}\cos\delta\phi + \frac{q}{\omega}\left(f_{qc}\cos\delta\phi + f_{qs}\sin\delta\phi\right)\,, \\
\dot{\mathrm{Q}} =& -\frac{2}{\tau}\mathrm{Q} - \Delta\omega\sin 2(\theta-\theta_\omega)\sqrt{\mathrm{E}^2-\mathrm{Q}^2} + \frac{a}{\omega}\left(f_{qc}\cos\delta\phi + f_{qs}\sin\delta\phi\right) - \frac{q}{\omega}f_{as}\cos(\delta\phi)\,, \\
\dot{\theta} =& -\eta\Omega + \frac{1}{2}\Delta\tau^{-1}\sin 2(\theta-\theta_\tau)\frac{E}{\sqrt{\mathrm{E}^2-\mathrm{Q}^2}} + \frac{1}{2}\Delta\omega\cos 2(\theta-\theta_\omega)\frac{Q}{\sqrt{\mathrm{E}^2-\mathrm{Q}^2}} \\
&- \frac{a}{2\omega\sqrt{E^2-Q^2}}(f_{qs}\cos\delta\phi - f_{qc}\sin\delta\phi) + \frac{q}{2\omega\sqrt{E^2-Q^2}}f_{as}\sin\delta\phi\,,
\end{aligned} \tag{1.11}$$

where f_{as}, f_{ac}, f_{qs} and f_{qc} are external forcing functions that can be potentially used to control the shape and orientation of the precession pattern [10] of the gyroscope and null the effects of structural imperfections, such as aniso-damping and aniso-elasticity. Here the subscripts “a” and “q” denote forces acting on major and minor radius of the ellipsoid, respectively. Whereas the subscripts “c” and “s”, denote forcing functions that are in-phase

and in quadrature to the oscillation of the mechanical element, respectively. The forcing functions, which are necessary to achieve continuous RIG operation are discussed in detail in Chapter 6. However, it is important to note here that the forcing functions f_{as}, f_{ac}, f_{qs} and f_{qc} used to control the gyroscope, act on multiple canonical variables simultaneously, Eq. 1.11. This makes it extremely important that the cross-talk between the four control loops as well as errors in pattern angle estimation (θ) is minimized in order to eliminate unwanted perturbations on the precession pattern.

As can be seen in Eq. 1.11, in order to achieve the ideal behavior described in Eq. 1.10, where amplitude is constant, quadrature error is zero and pattern angle is only a function of Coriolis forces, we would need to achieve:

$$\tau = \infty \,, \tag{1.12}$$

$$\Delta\omega = 0 \,, \tag{1.13}$$

$$\Delta\tau^{-1} = 0 \,. \tag{1.14}$$

This brings us to the following important criteria regarding the mechanical element of a Rate Integrating Gyroscope:

1. In order to minimize the unwanted drift in the angle of precession pattern (θ), the structural imperfections $\Delta\omega$ and $\Delta\tau^{-1}$ need to be minimized.

2. To keep the quadrature error small, the aniso-elasticity ($\Delta\omega$) needs to be minimized.

3. Finally, the energy decay time constant τ need to be maximized, so that the energy pumping necessary to sustain oscillation amplitude (E) can be minimized.

1.2.1.4 Continuous Rate Integrating Gyroscope Operation

As shown in Eq. 1.11, it is desirable to minimize the mechanical imperfections within the mechanical element of the gyroscope, so that their effect on precession pattern is minimal. However, it is also understood that for any real mechanical element, no matter how well it is built, there will be a certain degree of structural asymmetry and damping. This non-zero damping within the structure would result in the amplitude of oscillation (E) of the gyroscope to decay over time and the unwanted quadrature error (Q) to grow due to aniso-elasticity. For this reason, if continuous Rate Integrating Gyroscope operation is desired, the residual structural asymmetry and damping need to be compensated through a closed loop control system. Such a closed loop control system would need to fulfill the following roles:

1. Orientation of the precession pattern θ needs to be estimated, so that the magnitude of the rotation input can be measured, which is the gyroscope output.
2. Energy needs to be continuously added along the orientation of the precession pattern (θ), so that the amplitude of oscillation (E) remains constant.
3. Quadrature error (Q) needs to be nulled so that:
   - The vibration pattern never degenerates into the critical condition $a = q$,
   - The quadrature error does not interfere with estimation of the precession pattern.

This functionality is typically achieved through the following control loops [12]:

1. A Phase Locked Loop (PLL), so that the gyroscope output can be demodulated and the pattern angle can be estimated along with other canonical variables E and Q,
2. An Amplitude Gain Control (AGC) loop to keep the amplitude of oscillation (E) stable,

3. A Quadrature Null loop to actively drive the quadrature error (Q) to zero.

In addition, if rate gyroscope operation is desired, an optional force-to-rebalance (FTR) loop can be utilized to control the orientation of the precession pattern and achieve rate gyroscope mechanization. These three control loops (and the fourth, optional force-to-rebalance loop) are used on all commercial, high performance degenerate mode Coriolis Vibratory Gyroscopes. Implementation of a control system based on these guiding principles will be discussed in detail in Chapter 6.

1.2.1.5 Wineglass Modes

Lumped mass gyroscopes, such as the Foucault Pendulum, has distinct modes that consist of translation of the proof mass along x and y axis. Axi-symmetric gyroscopes, such as ring/disk and wineglass gyroscopes, on the other hand utilize the so-called "wineglass" modes for gyroscope operation. These modes consist of sinusoidal deformations along the radius of the structure and are characterized by a mode number "n" depending on the period of the sinusoid.

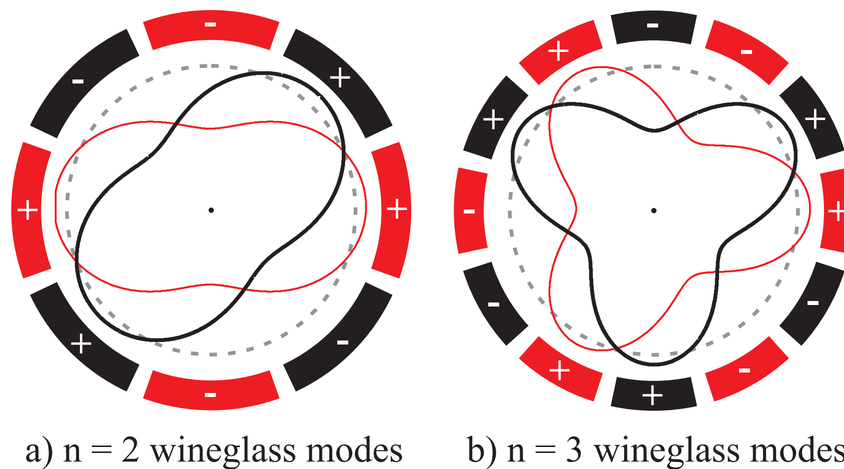

Figure 1.4: Mode shapes and minimal electrode configuration required for n = 2 (a) and n = 3 (b) wineglass modes. (+) and (−) signs denote, in-phase and anti-phase motion.

For axi-symmetric gyroscope applications, such as ring/disk and wineglass gyroscopes, the most commonly used resonance modes are the first two wineglass modes or the so-called n = 2 (4-node) and n = 3 (6-node) wineglass modes, Fig. 1.4. This is due to the fact that lower order wineglass modes have higher angular gain factors and lower resonance frequencies. Each wineglass mode has two degenerate modes that are spaced 45° and 30° apart for n = 2 and n = 3 modes, respectively. For very low fundamental frequency splits, the degenerate mode pair becomes indistinguishable, becoming a standing wave pattern. Coriolis input into the resonator causes this standing wave pattern to rotate at an angle proportional to angle of rotation (θ), analogous to the Foucualt pendulum.

1.2.2 Allan Variance

Allan variance analysis is frequently used to analyze various noise processes present in the gyroscope output [13]. To perform Allan variance analysis, first the amplitude of oscillation within the gyroscope is stabilized via the closed loop control system. This is followed by data acquisition of gyroscope output at zero rate (ZRO) over a long period of time and then, binning the data into groups with different integration times. This is followed by estimating the uncertainty between bins of same integration times and plotting the uncertainty $\sigma(\tau)$ with respect to integration time (τ), Fig. 1.5.

The technique can reveal information about various noise processes within the gyroscope. The most common noise processes are listed below:

- **Quantization noise** is mainly caused by quantization noise within the Analog-to-Digital Converters (ADCs) of the gyroscope, shows up on Allan variance curve with a slope of τ^{-1}.
- **Angle Random Walk (ARW)** is typically caused by white thermo-mechanical and

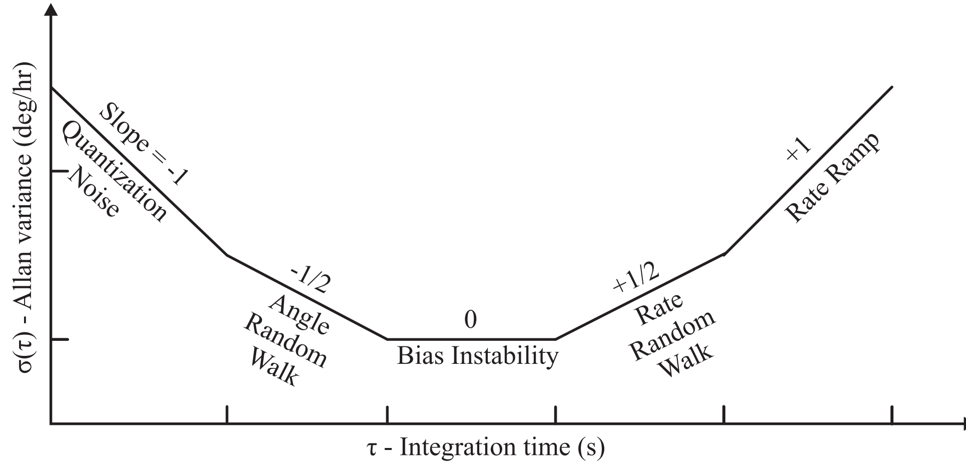

Figure 1.5: Sample Allan variance analysis of gyroscope output, showing error in gyroscope output (deg/hr or deg/s)with respect to integration time (s).

thermo-electrical noise within the gyroscope, shows up with a slope of $\tau^{-1/2}$. Usually reported with the units $°/\sqrt{\text{h}}$ for high performance gyroscopes.

- **Bias instability** is the lowest point of the Allan variance curve, shows up with a slope of zero. It can also be seen as the minimum detectable rate input within the gyroscope and is reported with units °/h.

- **Rate Random Walk (RRW)** is the random drift term within the gyroscope, shows up with a slope of $\tau^{+1/2}$.

- **Rate ramp**, also-called the thermal ramp is caused by temperature changes in the environment, shows up with a slope of τ^{+1}

1.2.3 Thermoelastic Dissipation

Thermoelastic Dissipation (TED) is a source of internal loss, present in all materials, caused by the interaction of temperature fluctuations and oscillations within a vibratory structure [3, 7]. Structures that are vibrating, exhibit stress/strain gradients as a result of vibrations. These stress/strain gradients create localized temperature gradients within the structure,

which inevitably result in heat transfer within the structure and the associated energy loss.

The degree of coupling between the temperature gradients and stress/strain gradients is controlled by the material's Coefficient of Thermal Expansion (CTE), which is an intrinsic property of the material [14, 15]. Even though the Thermoelastic Dissipation within a vibratory structure depends on a wide variety of factors, such as resonator geometry, vibration frequency, temperature of the environment, resonators fabricated out of low CTE materials typically exhibit significantly lower TED, due to reduced coupling between thermal and mechanical domains.

1.3 Literature Review

This section reports state-of-the-art on mode-matched (degenerate mode) gyroscopes and resonators. Due to degenerate mode operation, fundamentally all devices presented in this section are capable of Rate Integrating Gyroscope (RIG) operation, even though the actual RIG mechanization has not been demonstrated on all of them.

1.3.1 Macro-scale Hemispherical Resonator Gyroscopes

In this section macro-scale fused silica Hemispherical Resonator Gyroscopes (HRG) are reviewed. Current state of the art HRGs are fabricated through macro-scale precision machining techniques with very small relative tolerances. When fabricated out of materials such as low internal loss of fused silica, combined with high structural symmetry can lead to very high Q-factors, in excess of 25 million [2].

- The highest performance macro-scale solid state gyroscope is the Hemi Spherical Resonator Gyro (HRG) [2] that has been under development since 1975 by various or-

ganizations such as Draper Labs, Delco, Litton, and the current developer Northrop Grumman. The gyroscope went through many design iterations over the years [16–18], however the extremely high performace of the HRG has always been associated with the precision machined fused silica "wineglass resonator", that constitutes the heart of the gyroscope. Due to the extremely high Q-factors over 25 million provided by the fused silica resonator, HRG demonstrates exceptional bias stability (0.000 080 °/h) and noise performance (ARW 0.000 010 °/$\sqrt{\text{h}}$). However, the gyroscope is primarily used for aerospace applications due to extremely high cost and relatively large size $>$ 30 mm. Despite the current development efforts by Northrop Grumman Corporation to further reduce the size of the gyroscope [19, 20], cost and size remains a prohibiting factor for large-scale integration.

- Another HRG architecture has been developed and commercialized by French SAGEM [21, 22]. The gyroscope employs a precision machined fused silica resonator at its core, but with a mushroom/bell type resonator with an internal stem structure, Fig. 1.6. The possibility of integrating planar electrode structures was also proposed as part of this design, which might help lower the fabrication cost associated with outer electrode fabrication [23–26].

1.3.2 Micro Rate Integrating Gyroscope Architectures

This section gives an overview of micro-scale rate integrating gyroscope architectures. Although the actual rate integrating operation have not been demonstrated in all of the gyroscopes presented in this section, fundamentally they are all capable of rate integrating operation as they are all of the degenerate mode type.

RIG architectures in this section are divided into three main categories: (1) lumped mass systems, (2) ring/disk systems and (3) micro-wineglasses. Ring/disk systems are further

divided into three categories: (1) rings, (2) concentric ring systems and (3) disks. Whereas, micro-wineglasses are divided into two categories according to fabrication technology: surface micro-machined and bulk micro-machined wineglass gyroscope architectures. The complete hierarchy of MRIG architectures presented in this section is shown in Fig. 1.6.

1.3.2.1 Lumped Mass Systems

Lumped mass systems closely resemble conventionally micro-machined gyroscopes, they are composed of one or more proof masses, shuttle assemblies, and arrays of parallel plates or comb fingers. In multi-mass systems weak springs and lever mechanisms can also be included in order to synchronize different proof masses. The designs are typically x-y symmetric, even though axi-symmetric variants do exist.

- A lumped mass micro-machined angle-measuring gyroscope was proposed by [27]. Gyroscope consists of drive and sense electrodes and a proof mass coupled to an isotropic suspension system, such that the proof mass can move in any direction. A central anchor architecture as well as an outer anchor architecture with a distributed suspension system were discussed. Gyroscope was later fabrictated using surface-micromachining and a method for suppressing structural errors was proposed in [28, 29]. Open loop free angle precession of the mechanical element was also demonstrated up to 1 s duration.
- A Quadruple Mass Gyroscope (QMG) was reported in [30]. Gyroscope consists of four tines coupled to each other using lever mechanisms to achieve phase synchronization. Q-factors as high as 1.2 million were reported in [31]. Alan Variance analysis using temperature compensation showed angle random walk of $0.07\,°/\sqrt{\text{h}}$ and in-run bias stability of $0.22\,°/\text{h}$ [31]. Closed loop rate integrating operation was also demonstrated in [32].
- A large-displacement lumped mass gyroscope was reported in [33]. Due to the shaped-

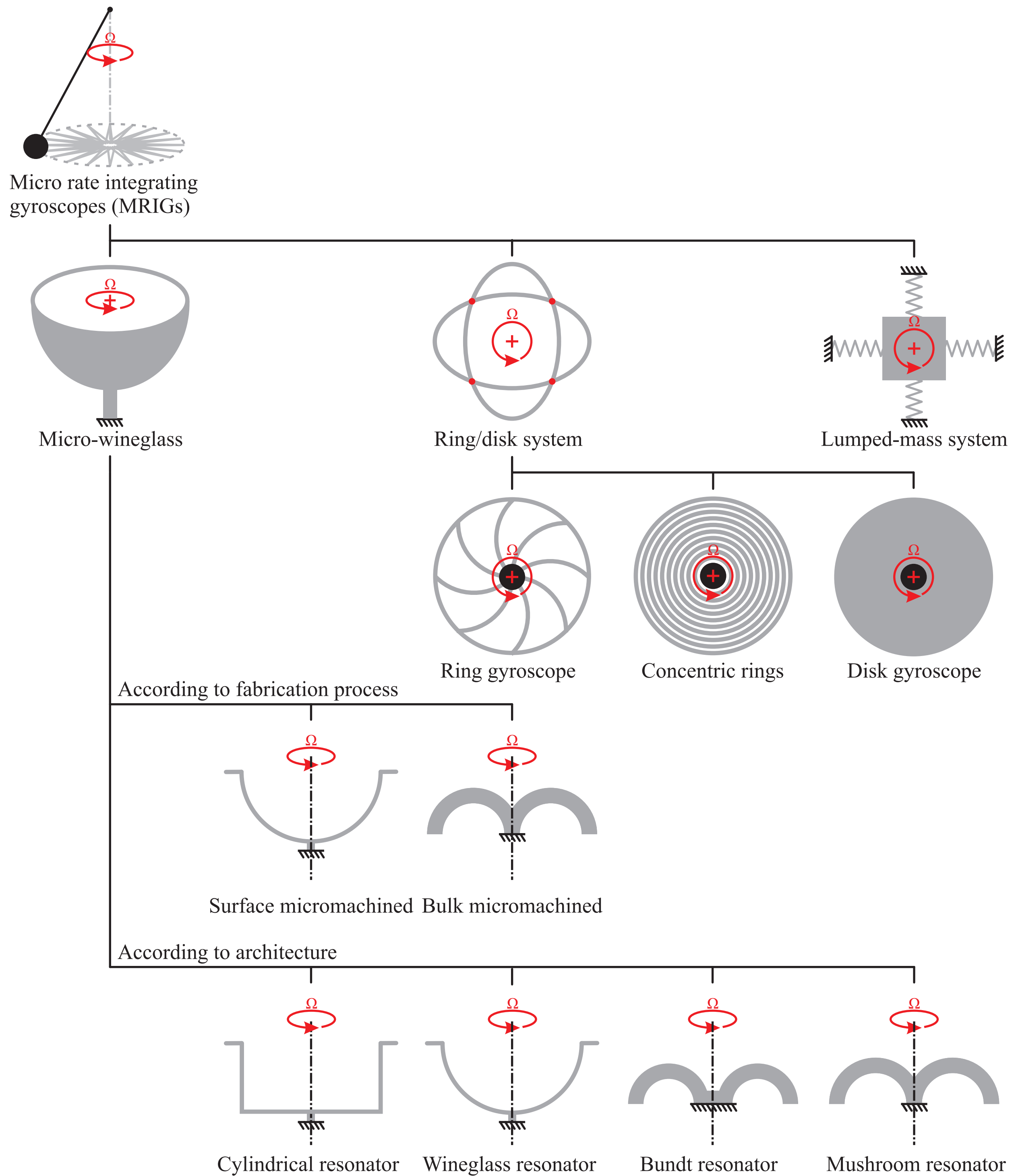

Figure 1.6: Micro rate integrating gyroscope (MRIG) architectures.

comb finger design displacements as high as 12.9 µm was reported. Q-factors were on the order of 25k [33] for a 9.5 kHz gyroscope. Alan Variance analysis for rate gyroscope operation showed an Angle Random Walk (ARW) of $0.78\,°/\sqrt{\mathrm{h}}$ and in-run bias stability of 6.1 °/h. Stress effects on gyroscope performance were investigated in [34, 35].

1.3.2.2 Ring/Disk Systems

Axi-symmetric silicon MEMS gyroscopes typically take the form of extruded 2-D geometries such as rings, concentric ring systems, and disks. The most common fabrication method is deep reactive etching (DRIE) of crystalline silicon, although poly-silicon and even fused silica variants do exist.

1.3.2.2.1 Ring Gyroscopes

- One of the earliest examples of MEMS ring gyros was reported by British Aerospace [36]. The gyroscope consists of a single ring held in place by outer suspension elements, Fig. 1.6. Like most other gyroscopes in this category, the $n = 2$ wineglass modes of the ring structure are used for gyroscope operation. One of the main advantages of the architecture is that the electrodes are placed both inside and outside of the ring structure, effectively doubling the total capacitance of the gyroscope. These electrodes can be used for forcing, pick-off as well as DC frequency tuning [37]. Even though originally it was marketed as a rate gyroscope, rate integrating operation has also been demonstrated on the same type of architecture [38, 39].
- Another MEMS ring gyroscope was reported by [40–42]. In contrast to the outer suspension elements seen in [36], this design utilized an inner suspension system and a central anchor structure to hold the ring in place. The gyroscope was fabricated using a high aspect-ratio combined poly and single-crystal silicon process (HARPSS)

[43, 44]. HARPSS process combines surface and bulk micro-machining techniques to create high aspect ratio vibratory structures with very small capacitive gaps (as low as 50 nm). The vibratory structure is created by depositing a sacrificial SiO2 layer on the side-walls of DRIE etched trenches, filling them with LPCVD polysilicon and finally etching away the sacrificial SiO2 layer. A Q-factor of 1200 and an as-fabricated frequency split (Δf) of 63 Hz at 28 kHz was reported on a ring structure with 1.1 mm diameter. Rate gyroscope operation was demonstrated with a minimum detectable signal of 0.04 °/s at 10 Hz bandwidth, limited by the noise in the interface electronics. The device is fundamentally capable of Whole Angle mechanization.

1.3.2.2.2 Concentric Ring Systems

- A Disk Resonator Gyroscope (DRG) was reported in [45–47]. Gyroscope consists of multiple concentric ring structures, connected to each other using spokes and a central anchor system. Concentric rings increase the modal mass of the gyroscope, whereas the central anchor decouples the vibratory system from the anchor. A Q-factor of 80,000 was measured at 14 kHz center frequency for a 8 mm Disk Resonator Gyroscope (DRG). Alan Variance analysis of the rate gyroscope operation showed an ARW of $0.0023\,°/\sqrt{\mathrm{h}}$ and an uncompensated in-run bias stability of $0.025 - 0.012\,°/\mathrm{h}$ was reported. With temperature compensation, the in-run bias stability was further reduced to below 0.01 °/h. The gyroscope is also potentially capable of Whole Angle mechanization. A noise analysis of DRG and closed-loop vibratory rate gyroscopes in general was reported in [48, 49].

- A model based approach for permanent frequency tuning of Disk Reonator Gyro was reported in [50]. Gold balls were used to iteratively tune the frequency splits of n = 2 and n = 3 wineglass modes of the gyroscope. A Disk Resonator Gyroscope was successfully tuned, starting from a frequency split of 14.1 Hz on the n = 2 mode, down

to 0.07 Hz. A similar mass perturbation technique was also used to decouple the resonator from linear acceleration [51]. More recently, a wafer level frequency tuning process based on ablation of a Parylene protective layer was reported [52].

- Significantly smaller polysilicon and single crystal silicon DRG prototypes at 600 µm were later fabricated in epitaxial polysilicon encapsulation (epi-seal) process. The epi-seal process utilizes an ultra-clean high temperature encapsulation step to seal the device under high vacuum [53]. Single crystal silicon variants were geometrically compensated to achieve lower as-fabricated frequency splits (Δf). Polysilicon DRG showed Q-factor around 60,000 and an as-fabricated frequency split (Δf) of 135 Hz [54] at ~250 kHz center frequency, whereas single crystal silicon DRG showed Q-factor around 100,000 [55] and as-fabricated frequency split (Δf) of 96 Hz at a center frequency of ~250 kHz. Alan variance analysis of the rate gyro operation showed ARW as low as $0.12\,°/\sqrt{\mathrm{h}}$ and in-run bias stability as low as 1.5 °/h [56]. Rate Integrating Gyroscope operation was also demonstrated in [57].

- A single-crystal-silicon Cylindrical Rate Integrating Gyroscope (CING) was reported in [58, 59]. The gyroscope was fabricated on a glass substrate and consists of concentric silicon cylinders (rings) that are connected to each other through a silicon back-plate. Electrostatic characterization of a 2.5 mm radius CING showed Q-factors on the order of 20,000 and an as-fabricated frequency split (Δf) of ~10 Hz at 18 kHz center frequency. A CING with 12 mm diameter was later reported with Q-factors up to ~100000. On this 12 mm prototype, an ARW of $0.09\,°/\sqrt{\mathrm{h}}$ and in-run bias stability of 129 °/h was demonstrated. Rate integrating operation has also been demonstrated in [60–62]. The main advantage of this architecture is an order of magnitude increase in modal mass over a single ring structure, however it was later found that the gyroscope has an angular gain of 0.011 due to the fact that majority of the kinetic energy is stored in the out of plane mode [63].

1.3.2.2.3 Disk Gyroscopes

- Bulk Acoustic Wave (BAW) silicon disk gyroscopes were reported in [64–67]. The gyroscope consists of a silicon disk with release holes held in place by a central anchor. As opposed to most flexural type gyroscopes the BAW disk gyroscopes operate in the MHz range. Lower amplitude of motion due to the higher stiffness of the vibratory modes is compensated by the use of HARPSS process to create extremely small capacitive gaps of 180 nm. Q-factors as high as 243,000 were reported on higher order wineglass modes of a 800 µm BAW disk gyroscope at a center frequency of 5.9 MHz. Rate gyro operation of a 1200 µm BAW disk gyroscope showed an ARW of $0.28\,°/\sqrt{\mathrm{h}}$ and in-run bias stability of 17 °/h. Due to the axi-symmetric resonator element, the Whole Angle mechanization is also fundamentally possible on this gyroscope.

1.3.2.3 Micro-Wineglass Gyroscope Architectures

In this section recent efforts in fabricating 3-D micro-wineglass gyroscopes are discussed. This type of gyroscope architecture is closely related to the topic of this thesis. The section is divided into two main approaches: (1) micro-wineglass gyroscopes fabricated through deposition of thin films onto pre-defined molds and (2) micro-wineglass gyroscopes fabricated through plastic deformation of bulk materials.

1.3.2.3.1 Surface Micro-machined Micro-Wineglassses

Surface-micromachined micro-wineglass gyroscopes are almost exclusively fabricated by depositing a thin film onto a pre-defined mold with a sacrificial layer to create the resonator element. Due to the nature of thin film deposition processes, they typically exhibit a small size ($< 1 - 2$ mm diameter) and thin structures (< 5 µm thickness).

- Isotropic wet etching of silicon molds using HF-HNO3 and silicon nitride molds have been investigated at Cornell University [68], with the goal of depositing a thin film material (i.e., silicon nitride) into the mold at a later step to create hemispherical shell structures. Authors experimented with different HF and HNO3 ratios as well as different silicon orientations, $< 100 >$ and $< 111 >$ wafers. The mold isotropy was analyzed using optical profilometry. The level of anisotropy was measured using optical profilometry, due to the crystalline nature of silicon the hemispherical molds were deformed towards a square shape for $< 100 >$ silicon and towards a hexagonal shape for $< 111 >$ silicon. Lowest measured anisotropy of 1.4% was obtained for $< 111 >$ silicon wafers using higher HF:HNO3 ratios. The process was later used to fabricate opto-mechanical light transducers [69].

- Hemispherical shell structures were fabricated at Georgia Institute of Technology by isotropically etching silicon cavities, thermally growing SiO2 inside and later removing the silicon mold using XeF2 etching [70]. As opposed to wet etching performed in [68], the molds in this work were created using a dry etching process (SF6 plasma etching). A radial deviation of 3.37 µm along the perimeter at a diameter of 1105 µm was reported [70]. Hemispherical shell structures were subsequently coated with TiN using atomic layer deposition (ALD) for electrical conductivity. Electrostatic testing revealed a resonant mode with a Q-factor of ~6000 at 113 kHz. Similar structures were also fabricated out of polysilicon with integrated electrostatic transducers by using the SiO_2 layer inside the mold cavity as a sacrificial layer and depositing polysilicon on top to create the device layer [71]. A Q-factor of ~8,000 was observed at 421 kHz for these structures. Fabrication effect of thickness anisotropy on oxide micro-hemispherical shell resonators was analyzed using Finite Element Analysis (FEA) in [72]. Experimental results showed a frequency split (Δf) of ~94 Hz, the thickness anisotropy was associated to different oxide growth rates at different crystalline planes of the silicon wafer. A detailed overview of design and analysis of these structures is presented in [73].

- Poly-crystalline diamond hemispherical shell structures were fabricated at University of California, Davis by depositing poly-diamond thin films into hemispherical molds on a silicon wafer [74]. Primary advantages of poly-crystaline diamond films are potentially high Q-factor [75] and potential for boron doping, creating inherently conductive shell structures, bypassing the need for an additional metal layer. Instead of wet/dry etching as in [68, 70], the hemispherical molds were created by μ-EDM (electro-discharge machining), followed by HNA (HF, nitric acid, acetic acid) wet etching to smooth the mold surface. A piezo-electric shaker was used to excite the diamond hemispherical shell structures. Frequency sweeps using this method revealed a Q-factor of ~3,000 at 35 kHz. A frequency split (Δf) of ~1 kHz was observed between two degenerate n = 2 wineglass modes (5% relative split). The frequency split was associated with the roughness at the rim of the shell structures. Later, frequency splits (Δf) as low as 5 Hz were reported [76]. Rate gyroscope operation was demonstrated in [77]. More recently, a DRIE etched cylindrical mold was used in [78] to create poly-diamond cylindrical resonators demonstrating Q-factors in excess of 300,000 and frequency splits as low as 3 Hz.

- Another poly-diamond hemispherical resonator gyroscope was reported at Charles Stark Draper Laboratory [79]. In this research, wet etching of Corning 1715 glass was used to achieve highly isotropic cavities compatible with temperatures required for poly-diamond deposition, while retaining a closer coefficient of expansion match (CTE) to the poly-diamod structure. Using this techique, average cavity diameters of 1288 µm were etched, with perfect roundness within the resolution of the measurement (±0.5 µm). Q-factors as high as 20,000 were reported on n = 2 wineglass modes.

- Another SiO2 hemispherical shell fabrication process was reported by University of Utah in [80], this process also relies on isotropically etched hemispherical molds on a silicon wafer. Thermally grown SiO2 was used as an etch stop layer along with a poly-

silicon sacrificial layer underneath the oxide shells. Piezo-actuation and electrostatic drive using a probe tip were used for testing with laser Doppler vibrometry pick-off. Later electrostatic transduction and Q-factors above 10,000 at 22 kHz center frequency were reported [81]. In addition, thin film sputtered ULE (Ultra Low Expansion Glass) shells were reported using a process called 'Poached-Egg Micro-molding' [82]. As opposed to using hemispherical molds on a silicon wafers, the authors utilized precision ball lenses as a mold. The ball lenses were coated with a poly-silicon sacrificial layer followed by sputtering of ULE glass as the device layer. The coated ball lenses were placed onto silicon posts and the ULE above the equator line of the lens was etched using Ar plasma etching. Subsequently the ball lens was removed by etching the ULE above the equator of the ball lens and XeF2 of the poly-silicon device layer, leaving a sputtered ULE shell structure in the shape of the ball lens. Piezo shakers were used along with optical fiber pick-off for characterization. Q-factor of ~20,000 was observed at 17.3 kHz. Later, Silicon-on-Insulator (SOI) electrode structures were reported for electrostatic transduction [83].

- All-dielectric (SiO2) cylindrical gyroscopes were reported by HRL Laboratories [84, 85]. The main difference from cylindrical resonators in [83] is the SiO2 resonator material. Transduction was achieved by using electric field gradients generated by interdigitated electrodes, eliminating the need for deposition of a conductive metal layer, which might potentially degrade the resonator performance. Q-factors as high as 12,000 were reported at 47.6 kHz center frequency using this technique.

- Poly-crystalline diamond half-toroidal resonators were reported by Honeywell International in [86]. Resonators were fabricated by depositing poly-diamond onto micro-glassblown hemi-toroidal molds along with a poly-silicon sacrificial layer. Frequency splits (Δf) as low as 2.4 Hz was reported on resonators with 2 mm diameter.

- Extremely small (200 µm diameter) cenosphere-derived hemispherical shells were re-

ported by University of Michigan in [87]. The shells are fabricated by ion-milling borosilicate glass cenospheres. For a sphere of 214 µm shell, quality factor of 130 was measured at 332.5 kHz.

1.3.2.3.2 Bulk Micro-Machined Micro-Wineglassses

Next, we look at MEMS wineglass fabrication processes that rely on plastic deformation of bulk materials. A process based on ultrasonic machining (and EDM) is also reviewed in this section.

- Bulk metallic glass (BMG) spherical shells were fabricated at Yale University using blow molding [88, 89]. Platinum based ($Pt_{57.5}Cu_{14.7}Ni_{5.3}P_{22.5}$) bulk metallic glass with a processing temperatures of 275 °C were used for the shell structures. Inert gases were used during most of the processing steps, due to low oxidation stability. Primary advantages of BMGs are low processing temperatures compared to most glasses, as well as inherent conductivity of the material, eliminating the need for metallization [90]. Frequency splits as low as 5 Hz at 13.8 kHz and Q-factors as high as 7,800 at 9.4 kHz were demonstrated using this process.
- Fused silica blow torch molding was used to create bird-bath (hemi-toroidal) and hemi-spherical shell structures at University of Michigan [91]. To create the fused silica shells, thin layers of fused silica pieces were individually pressed onto graphite fixtures and deformed one at a time using the heat from a blow torch. Shells structures were later lapped from the backs-side to release the devices around their perimeter. Finally, the shells were sputter coated with thin layer of Ti/Au for conductivity. Ring-down testing under vacuum showed Q-factors as high as ~1.2 million at 8.7 kHz center frequency. Relative frequency split ($\Delta f_{n=2}/f_{n=2}$) ranged between 0.24 % and 4.49 % with a mean value at around 1-1.5 % (100-150 Hz) [91]. Better alignment between the blow-torch

and the mold as well as better temperature uniformity were proposed as a means to reduce the frequency split. At a later study, fused silica rods were embedded into the fused silica shell to create stem structures, showing Q-factors as high as 2.55 million [92] at 22.6 kHz center frequency on uncoated resonators. Shells were later assembled into Silicon-on-Insulator (SOI) electrode structures to demonstrate rate gyroscope operation [93, 94], showing angle random walk of $0.106\,^{\circ}/\sqrt{\mathrm{h}}$ and bias stability of $1\,^{\circ}/\mathrm{h}$. In addition, a micro-machining process that utilizes ultrasonic machining (USM), electro-discharge machining (EDM), and lapping was proposed (3D-SOULE) to create micro-wineglass structures [95]. EDM was mainly used to shape the stainless steel tooling, which was then used to USM fused silica spheres. Fused silica spherical-concave and mushroom type structures were created using this process. Laser Doppler Vibrometry was used to characterize the micro-wineglass structures, showing a Q-factor of 345 at 1.38 MHz in air.

1.4 Research Objective

To sum up, motivated by the proven performance of macro-scale Hemispherical Resonator Gyroscopes (HRG) [2], there has been a growing interest in 3-D MEMS wineglass resonator architectures for use in timing and inertial sensing applications. However, MEMS wineglass resonators with sufficient stiffness (Δf) and damping ($\Delta\tau$) symmetry, surface smoothness and low thermoelastic dissipation (TED) have not yet been demonstrated in the literature. To take full advantage of the 3-D wineglass architecture, fabrication techniques with low surface roughness and high symmetry as well as materials with high isotropy and low TED are desired.

In this thesis, we explore the micro-glassblowing paradigm as an enabling mechanism for wafer-level fabrication of atomically smooth, low internal loss Titania Silicate Glass (TSG)

and fused silica 3-D wineglass gyroscopes. Micro-glassblowing process relies on surface tension and pressure driven deformation of the device layer to define the 3-D shell structure as opposed to conventional deposition, molding, or etching techniques. Surface tension forces act on the 3-D shell structure at an atomic level to minimize surface roughness and structural imperfections. This may lead to levels of smoothness and structural symmetry that is not available through conventional fabrication techniques. In addition, micro-glassblowing of low thermal expansion materials such as fused silica and Titania Silicate Glass (TSG) can enable MEMS resonant devices with intrinsically low internal losses (Q_{TED}).

Pyrex glassblowing at 850 °C on a silicon substrate was previously demonstrated by University of California, Irvine for fabrication of smooth, symmetric 3-D structures [96–99]. However, fused silica/TSG glassblowing requires temperatures upwards of 1600 °C due to its higher softening point, which prevents the use of fabrication processes that rely on a silicon substrate. This thesis explores the hypothesis that high temperature glassblowing (up to 1800 °C), may serve as an enabling mechanism for wafer-scale fabrication of TSG and fused silica 3-D wineglass structures.

New 2-D silicon MRIG architectures are also explored to serve as a test platform for various MRIG control strategies, in addition to bridging the gap between conventional micromachining techniques and the micro-glassblowing process. Specifically, two new Si-MEMS MRIG architectures are explored: Toroidal Ring Gyroscope (TRG) and Dual Foucault Pendulum (DFP) Gyroscope. For example, higher order wineglass modes ($n = 3$) are being explored on the Toroidal Ring Gyroscope, with the goal of reducing frequency asymmetry (Δf) induced by anisotropic modulus of elasticity of silicon. In addition, parametric energy pumping is investigated, to reduce errors associated with amplitude control of MRIGs. Lastly, a new dynamically balanced, lumped mass gyroscope architecture, Dual Foucault Pendulum is explored, with the goal of demonstrating closed-loop Rate Integrating Gyroscope operation in a conventionally micro-machined, "nested" two mass structure.

Finally, various control strategies are explored to electronically compensate for large structural imperfections associated with micro-machining processes. Challenges such as quadrature suppression, energy pumping along the orientation of the precession pattern, and identification/control of the precession pattern need to be addressed in order to realize continuous Whole Angle (WA) operation at micro-scale. To this end, techniques such as parametric pumping, force-to-rebalance, and virtual carouseling are employed in this thesis.

1.5 Dissertation Outline

In Chapter 2, a MEMS fabrication process is presented for building atomically smooth, symmetric 3-D wineglass and spherical shell structures, using low internal loss materials, namely fused silica and Ultra Low Expansion Titania Silicate Glass (ULE TSG). Feasibility of the process has been demonstrated by fabrication of fused silica and TSG micro-glassblown structures. Inverted-wineglass shells with self-aligned stem structures and extremely low surface roughness (0.23 nm Surface Average) were demonstrated using this process.

In Chapter 3, we present methods for characterization of 3-D micro-wineglass resonators. Two interchangeable modes of excitation are demonstrated: (1) Mechanical pinging using a piezo actuated probe assembly, (2) electrostatic excitation using assembled electrode structures. Two interchangeable modes of detection are also presented: optical pick-up using Laser Doppler Vibrometry and capacitive detection. Electrostatic excitation was used to obtain the frequency response of micro-glassblown resonators, whereas piezo-pinging was used to obtain the time domain response of the resonators.

In Chapter 4, we demonstrate, for the first time, sub-1 Hz frequency symmetry in micro-glassblown wineglass resonators with integrated electrode structures. A new fabrication process based on deep glass dry etching was developed to fabricate micro-wineglasses with

self-aligned stem structures and integrated electrodes. The wineglass modes were identified by electrostatic excitation and mapping the velocity of motion along the perimeter using laser Doppler interferometry.

In Chapter 5, we report Q-factor over 1 million, on both n = 2 wineglass modes, and high frequency symmetry ($\Delta f/f$) of 132 ppm on wafer-level micro-glassblown 3-D fused silica wineglass resonators at a compact size of 7 mm diameter and center frequency of 105 kHz. In addition, we demonstrate for the first time, out-of-plane capacitive transduction on MEMS wineglass resonators. High Q-factor is enabled by a high aspect ratio, self-aligned glassblown stem structure, careful surface treatment of the perimeter area, and low internal loss fused silica material. Electrostatic transduction is enabled by detecting the spatial deformation of the 3-D wineglass structure using a new out-of-plane electrode architecture.

In Chapter 6, a new type of concentric ring gyroscope architecture, Toroidal Ring Gyroscope (TRG), is presented. The goal of this architecture is to achieve high-Q factor through a distributed suspension system and high frequency symmetry through the higher order $n = 3$ wineglass mode. The architecture consists of an outer anchor, concentric ring suspension system and inner electrode assembly. First demonstration of a parametrically driven MRIG is also reported as part of this work.

In Chapter 7, a new type of conventionally micro-machined, degenerate mode lumped mass gyroscope architecture is presented to serve as a test-bed for various MRIG control schemes. The Dual Foucault Pendulum (DFP) gyroscope consists of two dynamically equivalent, mechanically coupled proof masses, oscillating in anti-phase motion. This dual axis tuning fork behavior creates a dynamically balanced resonator with x-y symmetry in frequency and damping, suitable for Whole Angle mechanization.

Finally, thesis is concluded in Chapter 8 with a summary of results and future research directions.

Chapter 2

Micro-glassblowing of High-Q Materials

This chapter investigates the intriguing possibility of micro-glassblowing as a means to fabricate low internal loss fused silica and Ultra Low Expansion Titania Silicate Glass (ULE TSG) 3-D shell micro-structures. In Section 2.1, the design parameters for micro-glassblown structures is presented. This is followed by details of the fabrication process and the custom-designed fabrication equipment in Section 2.2. The chapter concludes with analysis of the micro-glassblown structures in Section 2.3, and discussion of the results in Section 2.4.

2.1 Design Parameters

This section focuses on analysis of geometric design parameters and the effect of material choice on fundamental Q-factor limits. In order to establish the relationships between material choice, device dimensions and Q-factor, parametric Finite Element Analysis (FEA) was conducted using Comsol Multiphysics Package.

2.1.1 Geometric Design

Micro-glassblowing process utilizes an etched cavity on a substrate wafer and a glass layer that is bonded on top of this cavity, creating a volume of trapped gas for subsequent glassblowing of self-inflating spherical shells. When the bonded wafer stack is heated above the softening point of the structural glass layer, two effects are activated at the same time: (1) the glass layer becomes viscous, and (2) the air pressure inside the pre-etched cavity increases above the atmospheric level. This results in plastic deformation of the glass layer, driven by gas pressure and surface tension forces (glassblowing). The expansion of air (and hence the formation of the shell) stops when the pressure inside and outside of the glass shell reaches an equilibrium, creating a self-limiting process. During this deformation, the surface tension acting on the now viscous glass layer works towards minimizing the surface area of the structure as a result a highly symmetric spherical shell with low surface roughness forms. The process allows simultaneous fabrication of an array of identical (or different, if desired) shell structures on the same substrate.

Shape and size of the final glassblown structure can be designed by changing starting conditions such as thickness of the device layer, cavity shape and dimensions as well as environment temperature and pressure during glassblowing [96]. For example, changing the cavity diameter directly affects the diameter of the final glassblown shell, whereas changing the cavity depth (or volume) affects the height of the glassblown structure. It is also possible to fabricate entirely different geometries by changing the initial conditions, for example a circular cavity creates a spherical shell, when glassblown, Fig. 2.1 (right). Inverted-wineglass structures can also be fabricated by defining a central post inside the etched cavity, Fig. 2.1 (left). When the device layer is bonded to this central post, it acts as an anchor point, which allows the glassblown shell to fold around it, creating a self-aligned stem structure as in Fig. 2.1(e).

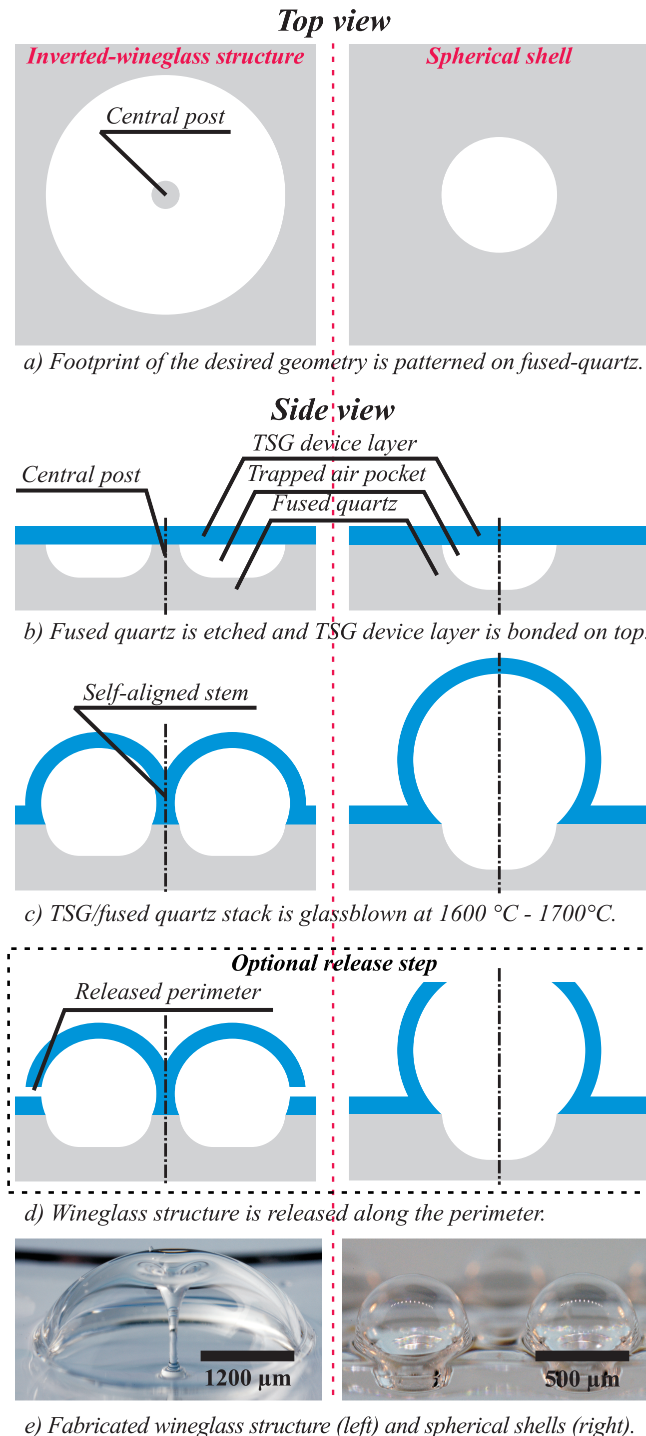

Figure 2.1: ULE TSG / fused silica micro-glassblowing process, consists of: (a) Deep fused silica etching of device footprint into the substrate, (b) plasma assisted bonding of TSG / fused silica device layer, (c) micro-glassblowing at temperatures up to 1700 °C, (d) optional release step. Fabricated TSG and fused silica structures are shown in (e). Photo of shell structures by Dr. A. A. Trusov [100].

2.1.2 Stem Design

Anchor loss is the dissipation of kinetic energy within the vibrating structure into the substrate and the environment by means of acoustic waves, which ultimately limits the overall Q-factor of the resonator. The focus of the analysis was to investigate the impact of stem diameter on Q_{anchor} and use the results of the FEA as design guidelines. Two types of geometries were analyzed: (1) Wineglass structures with hollow stem [101] shown in Fig. 2.2(a), and (2) inverted wineglass structures as in Fig. 2.2(b) and 2.2(c). The structure in Fig. 2.2(a) was fabricated by first glassblowing a spherical structure through a stencil layer and then cutting the top half of the spherical shell using laser ablation to create a wineglass structure. Whereas the structures in Fig. 2.2(b) and (c) were fabricated by etching a toroidal cavity as described in Fig. 2.1.

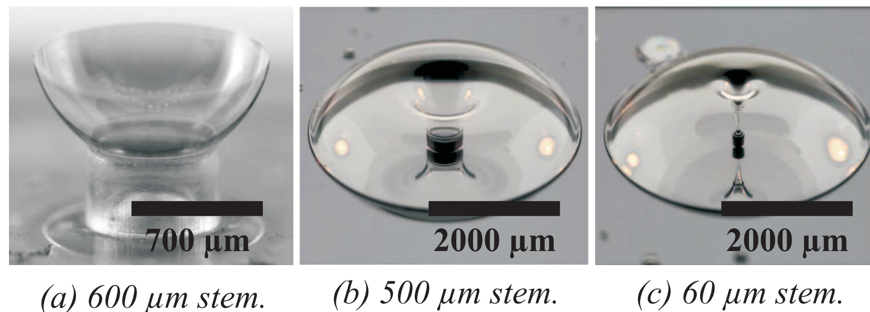

(a) 600 µm stem. *(b) 500 µm stem.* *(c) 60 µm stem.*

Figure 2.2: Wineglass structures with (a) 1.2 mm outer diameter and 600 µm stem diameter (hollow), (b) 4200 µm outer diameter and 500 µm stem diameter (solid) and (c) 4200 µm outer diameter and 150 µm stem diameter (solid). Photos by Dr. A. A. Trusov [100].

The structure in Fig. 2.2(a) had a shell diameter of 1142 µm, anchor diameter of 600 µm and average thickness of 4 µm, which gives roughly 1:2 attachment to shell diameter ratio. In contrast, the inverted-wineglass structures with the integrated stem, Fig. 2.2(b) and (c), had a shell diameter of 4200 µm, an average thickness of 80 µm with 500 µm and 150 µm stem diameters respectively, giving a 1:8 and 1:28 stem to shell diameter ratios.

To simulate the acoustic loss in an infinite medium, a perfectly matched layer (PML) within

Comsol Multiphysics Package was used for modeling the substrate domain. PML works by absorbing acoustic waves over a large frequency range at any non-zero angle of incidence. The simulation was run for perfectly symmetric structures, neglecting the contribution of mass imbalance to the anchor loss. For this reason, the values obtained from FEA represent the fundamental anchor loss limit (theoretical maximum) of the structures, Table 2.1.

Stem diameter (µm)	600	500	60
Wineglass diameter (µm)	1200	4200	4200
$\mathbf{Q_{anchor}}$	1×10^3	2×10^6	5×10^{10}

Table 2.1: Anchor loss analysis show a large change in Q_{anchor} for different stem diameters.

The wineglass structure with 1:2 anchor to shell diameter ratio, Fig. 2.2(a), had a fundamental Q_{anchor} limit of 3000, which is in close agreement with the experimentally obtained quality factor of 1256 [101]. Analysis of the wineglass structure with outer diameter ratio of 1:8 in 2.2(b) showed moderate anchor loss (fundamental $Q_{anchor} > 2 \times 10^6$). In contrast, the analysis of the wineglass structure with the integrated stem (1:14 ratio), Fig. 2.2(b), showed potential for significantly lower anchor loss (fundamental $Q_{anchor} > 5 \times 10^{10}$).

2.1.3 Thermoelastic Dissipation

The goal of the analysis was to understand the effect of CTE on Q_{TED}. Four different materials: silicon, pyrex, fused silica, and TSG were investigated using Comsol Multiphysics Package. Energy loss caused by TED was analyzed using a coupled thermo-mechanical model, where compressive and tensile stresses within the vibrating structure affected the temperature distribution and vice versa. Damping term was calculated as the total irreversible heat flow due to the change in the temperature distribution. The model was solved for the n = 2 wineglass modes, and Q_{TED} values were extracted from the ratio of the real and imaginary parts of the eigenfrequencies. It was found that the material choice has a significant impact on the Q_{TED} for the analyzed geometry, Table 2.2.

Material	Silicon	Pyrex	FQ	TSG
$\mathbf{Q_{TED}}$	6×10^4	7×10^6	2×10^7	7×10^{10}

Table 2.2: Thermoelastic dissipation analysis of micro-wineglass structures shows that 3 to 6 orders of magnitude increase in Q_{TED} is achievable by using low expansion materials.

TSG, with the lowest CTE among the materials investigated, had the highest fundamental Q_{TED} value at 7×10^{10}, which was followed by fused silica at $Q_{TED} > 2 \times 10^7$.

2.2 Fabrication Process & Custom-Designed Fabrication Equipment

2.2.1 Fabrication Process

Fabrication process for TSG wineglass structures consists of four main steps, namely: (1) Etching of the fused silica (or fused silica) substrate, (2) bonding of fused silica or TSG device layer to fused silica, (3) glassblowing, and subsequently (4) releasing the wineglass structure by etching around the perimeter, Fig. 2.1. The process starts by LPCVD deposition of a 2 µm poly-silicon hard mask onto the fused silica substrate. The cavity openings are defined on the PolySi hard-mask using RIE, followed by wet etching of ~150 µm deep toroidal cavities or 300 µm deep cylindrical cavities into the substrate wafer using concentrated HF (49%). In order to establish the etch rate of HF on fused silica and TSG, 75 minutes long test runs were performed at room temperature. Etch depth was measured every 15 minutes by stopping the etch and measuring with a DEKTAK 3 profilometer. Linear regression fits showed an etch rate of 1.07 µm/min for fused silica and 2.86 µm/min for TSG, with a linearity of $R^2 = 0.996$ and $R^2 = 0.997$, respectively. Complete process flow for wet etching of fused silica can be found in Appendices A.4 and A.5.

Once the etch was complete, PolySi layer was stripped and the wafers were thoroughly cleaned using RCA clean. Details of the PolySi removal step can be found in Appendix A.2.

The next step of the fabrication process is bonding of the TSG device layer onto the etched fused silica wafer. Due to the subsequent high temperature glassblowing process the bond needs to survive up to 1700 °C, which prevents the use of intermediate materials. For this reason, a plasma activated fusion bonding process was developed, Fig. 2.1(b). The bond is performed by plasma activating the TSG and fused silica wafers and then bringing them into optical contact [102].

Plasma assisted fusion bonding works by creating hydrogen bonds between the device and the substrate wafers, it requires highly polished, flat, clean surfaces (< 10 nm Sa roughness). The process for bonding fused silica or TSG wafer pairs can be divided into four main steps:

1. Cleaning of the wafer pair using solvent and RCA clean,
2. Plasma activation using oxygen plasma,
3. DI water rinse followed by N2 dry and optical contacting of the activated surfaces,
4. Curing the wafer stack at 400 °C for 6 hours.

Once cured, the bond creates a seamless hermetic seal around the etched cavities without using any intermediate material. A step-by-step process flow for plasma assisted fusion bonding can be found in Appendix A.3.

2.2.2 Custom-designed Furnace

The TSG/fused silica wafer stack is then glassblown at 1600–1700 °C in a custom-designed high temperature furnace with a rapid cooling rate of 500 °C/min, Fig. 2.3. The furnace

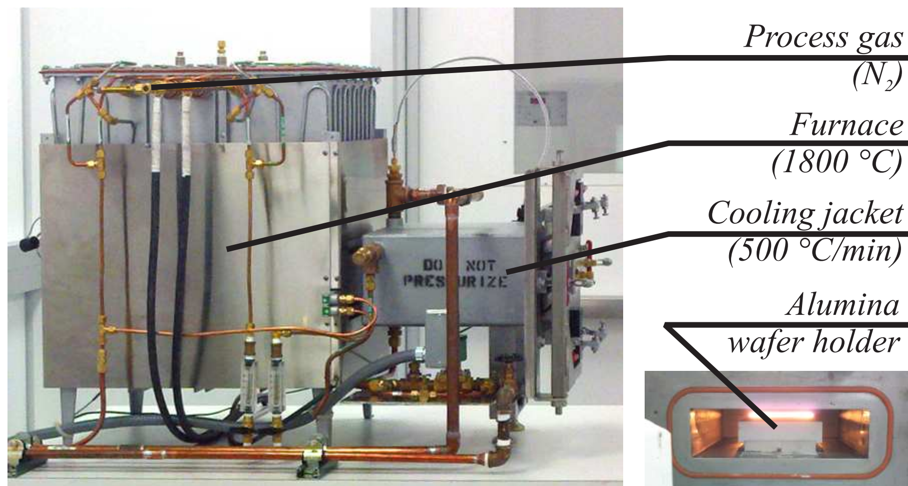

Figure 2.3: Custom-designed furnace with process capability of 1800 °C glassblowing with a rapid cooling rate of 500 °C/min.

consists of two main chambers that are connected to each other through a third vestibule chamber. The first chamber is used for heating and can go up to 1800 °C, the second chamber is enveloped by a water cooled jacket, that maintains < 200 °C temperature. The samples are transferred between the heating and cooling chambers by using a sliding alumina wafer holder. A typical glassblowing run involves keeping the wafer stack at glassblowing temperature for one minute and then extracting the wafer stack into the water cooled jacket for solidification.

Figure 2.4: Optical photograph of glassblown fused silica inverted-wineglass structure. Outer diameter is 4200 µm. Glassblown at 1650 °C.

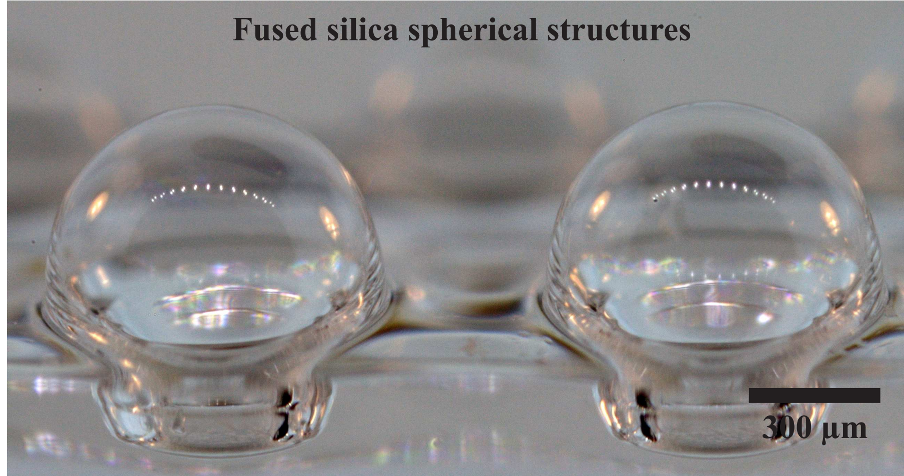

Figure 2.5: Optical photograph of fused silica spherical shell structures, glassblown at 1700 °C. Outer diameter of shells is 800 µm. Photo by Dr. A. A. Trusov [100]

During glassblowing, as previously described two phenomena occur simultaneously: device layer becomes viscous due to the elevated temperature and the air inside the etched cavity expands, creating the 3-D glassblown structure. Because the device layer is bonded both around the circular cavity and the cylindrical post in the middle, the glassblown structure creates a self-aligned stem, Fig. 2.4. Whereas if no central post is defined, the glassblown structure forms a spherical shell as in Fig. 2.5. Typical design parameters for a mushroom and hemi-spherical shell structures can be found in Table 2.3 and Table 2.4, respectively.

Table 2.3: Sample design parameters for micro-glassblown mushroom structure.

Parameter	Unit	Value
Device diameter	(µm)	3800
Central post diameter	(µm)	400
Device layer thickness	(µm)	300
Etch depth	(µm)	250
Final height	(µm)	900
Glassblowing temperature	(°C)	1700
Glassblowing time	(min)	3
Cooling rate	(°C/min)	500

Table 2.4: Sample design parameters for micro-glassblown hemi-sphere.

Device diameter	(µm)	900
Device layer thickness	(µm)	200
Etch depth	(µm)	350
Final height	(µm)	900
Final equator diameter	(µm)	1200
Glassblowing temperature	(°C)	1700
Glassblowing time	(min)	3
Cooling rate	(°C/min)	500

2.2.3 Laser Ablation Setup

The final step of the fabrication process is to release the wineglass around its perimeter, which can be accomplished by laser ablation or dry etching of the device layer. The wineglass structure in Fig. 2.6 was released with laser ablation, using a 2-axis laser micromachining system, Resonetics RapidX 250. 3-axis laser ablation capability was added by implementing a custom built rotary stage assembly from National Aperture, Inc. The wineglass structure was mounted onto the rotary stage and its axis of symmetry was aligned with the rotation axis using an x-y stage. Laser ablation was performed by focusing the laser beam onto the perimeter of the wineglass at a perpendicular angle and rotating the wineglass structure at constant angular velocity. For the laser source, an ArF excimer laser (193 nm wavelength, Coherent COMPexPRO 110) was used with 20 ns pulse duration, 50 Hz repetition rate and a laser spot size of 40 µm.

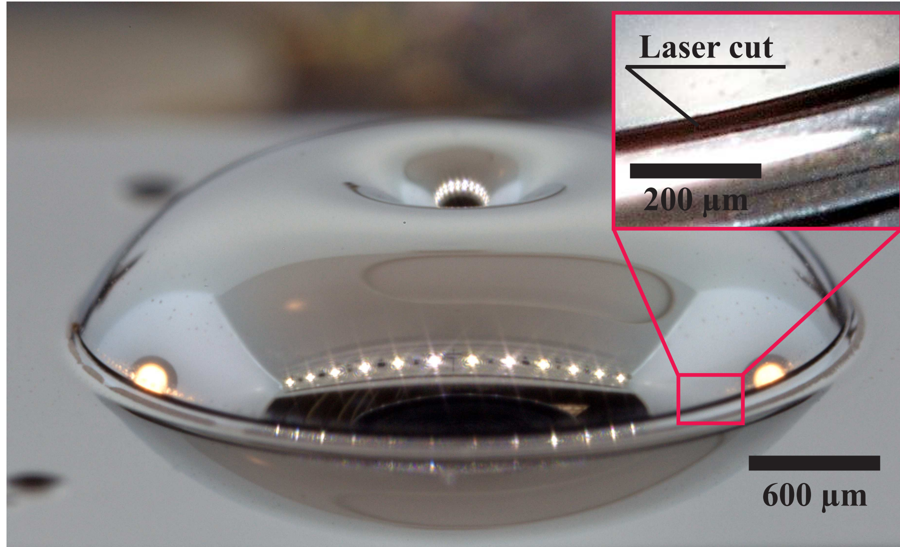

Figure 2.6: Optical photograph of inverted-wineglass, released along the perimeter using laser ablation and coated with iridium. Photo by Dr. A. A. Trusov [100]

2.3 Analysis of Structures

In this section the surface roughness and the material composition of TSG device layer before and after glassblowing and the symmetry of the fabricated glassblown structure is analyzed.

2.3.1 Surface Roughness

In order to minimize the surface losses in resonant and optical applications highly smooth surfaces are required. Surface roughness measurements of TSG glassblown samples were performed using an atomic force microscope (AFM) from Pacific Nanotechnology (Nano-R). With a sensor noise level of < 0.13 nm in the z-direction, Nano-R can resolve sub-nanometer features. Samples were cleaned using standard solvent clean (acetone, IPA, methanol) before each scan. No additional treatment was performed on the samples. The AFM was run in tapping mode, using a < 0.13 nm radius probe tip (Agilent U3120A).

Surface roughness of the samples before and after glassblowing were analyzed, with the

hypothesis that glassblowing can improve the surface roughness. Highly polished TSG wafers were used for the device layer, which was verified by AFM scans, showing a surface roughness of 0.40 nm Sa, Fig. 2.7(b). Characterization of the glassblown samples showed a two-fold improvement in surface roughness, down to 0.23 nm Sa, Fig 2.7(a). We also observed that the angstrom level scratches in Fig Fig 2.7(b), associated with the lapping operation, disappeared after glassblowing, Fig 2.7(a), confirming the hypothesis.

Two-fold improvement in surface roughness is attributed to viscous flow of the glass layer and the associated surface tension forces. As the glassblowing is performed above the glass softening temperature, TSG device layer becomes viscous and the surface tension forces become active, working towards minimizing the surface area of the glass structure. This creates an effect analogous to ”stretching out” the wrinkles on the surface, lowering the surface roughness.

2.3.2 Material Composition

For resonant and optical applications, it is critical that TSG retains its original material composition and properties after glassblowing, which are structural integrity, material uniformity and optical transparency. We found that glassblowing temperature and the rate of cooling are the most important parameters that affect the quality of the TSG layer after glassblowing.

The structure in Fig. 2.8 was glassblown using a conventional high temperature furnace at 1600 °C, which does not allow removal of the samples at elevated temperatures. For this reason, the structure was left to cool-down to room temperature over an 8 hour period. Recrystallization as well as micro-cracks were observed on the surface. In order to establish the nature of the recrystallization electron dispersive spectroscopy (EDS) was employed. Philips XL-30 FEG SEM with a Thermo Scientific UltraDry silicon drift X-ray detector was

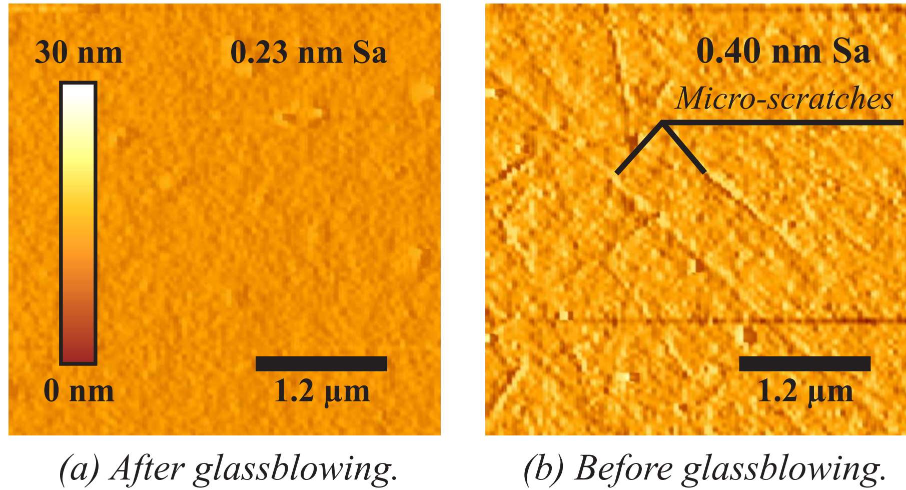

(a) After glassblowing. *(b) Before glassblowing.*

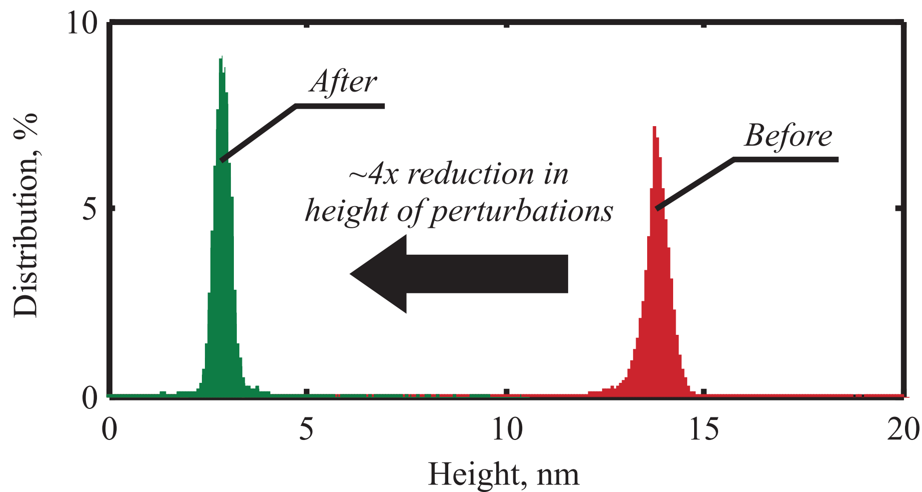

(c) AFM histograms of before and after glassblowing.

Figure 2.7: AFM surface profiles of TSG, (a) before and (b) after glassblowing. Glassblowing creates extremely smooth (0.2 ppm relative roughness) TSG structures.

used for EDS characterization. An acceleration voltage of 10 kV was used at 10 mm working distance, and samples were coated with 5 nm of sputtered iridium to prevent charging. EDS analysis of the crystals in Fig. 2.8 revealed higher concentrations of titanium, implying that TiO^2 is exsolving from the SiO$^{/}$TiO^{m}atrix. In contrast, the structure in Fig. 2.9 was glassblown using rapid cooling by bringing the temperature of the sample from 1600–1700 °C to $\sim$ 200 °C within a minute. No micro-cracks or recrystallization were observed, as can be validated by the optical transparency. EDS spectral plots showed homogeneous SiO^2 and TiO^2 distribution in Fig. 2.9 as opposed to heterogeneous distribution in Fig. 2.8. The

absence of recrystallization makes rapid cooling an essential step in micro-glassblowing of fused silica and TSG.

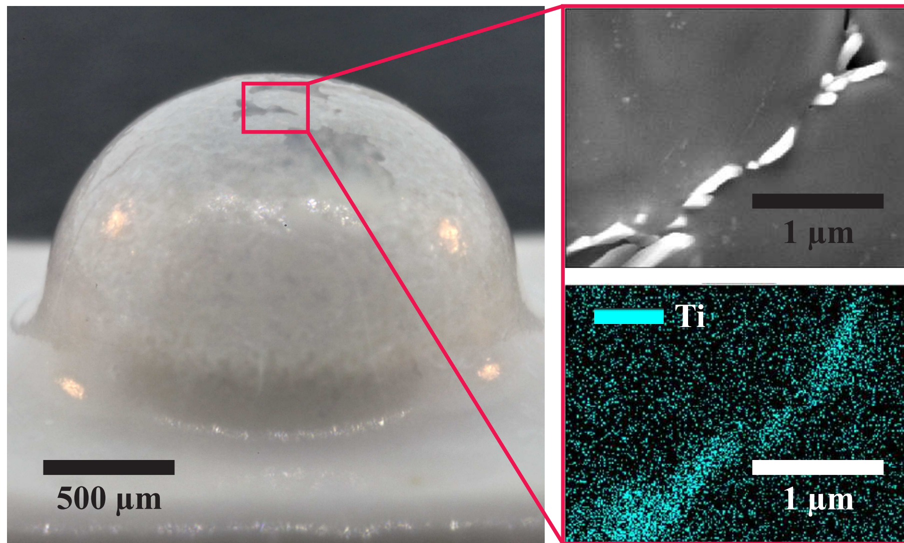

Figure 2.8: Slow cooling of TSG (> 8 hr.) causes recrystallization. Optical photograph by Dr. A. A. Trusov [100].

EDS was used to obtain the spectral signatures of TSG before and after glassblowing. No change in the composition of TSG was observed after glassblowing, Fig. 2.10. EDS spectrum also revealed 7 to 8 weight percent of $TiO2$ in TSG, which is in agreement with the nominal TiO^2 concentration of Corning ULE TSG.

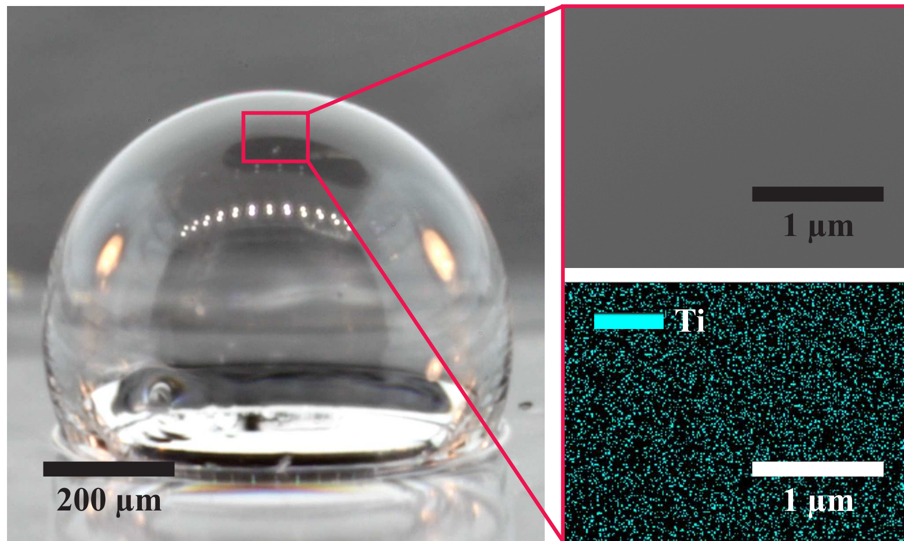

Figure 2.9: Glassblowing with rapid cooling of TSG (< 1 min.) prevents recrystallization. Optical photograph by Dr. A. A. Trusov [100].

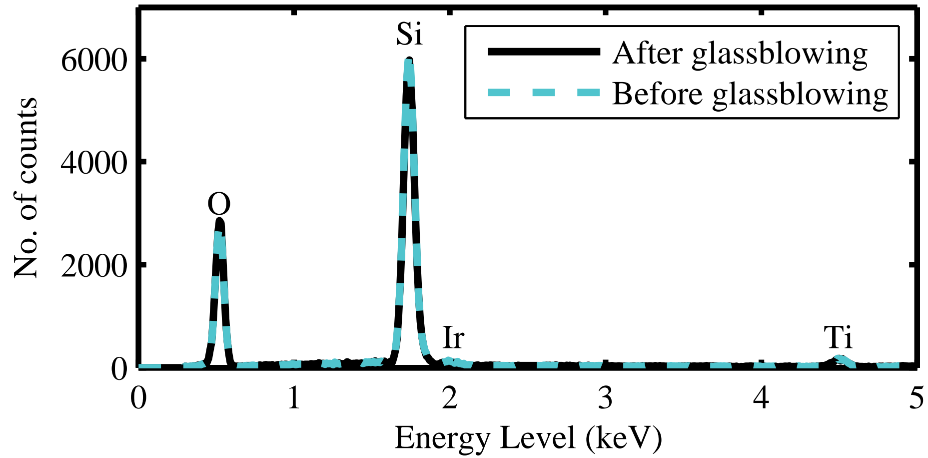

(a) EDS spectral analysis of ULE TSG.

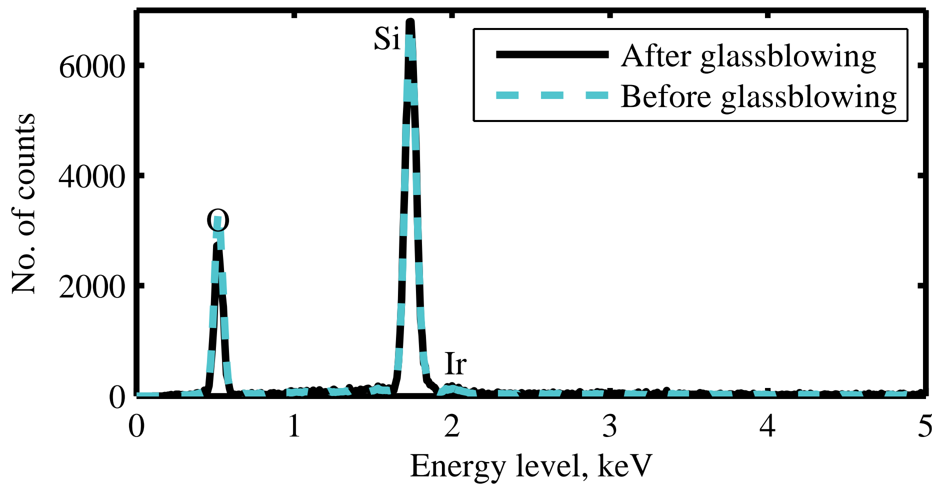

(b) EDS spectral analysis of fused silica.

Figure 2.10: EDS spectral analysis of TSG and fused silica reveals that composition of the material does not change after glassblowing.

2.4 Conclusions

A new high temperature micro-glassblowing process for batch fabrication of 3-D low internal loss fused silica and ULE TSG wineglass structures was developed and experimentally demonstrated. The process was enabled by the development of an in-house high temperature glassblowing capability of 1800 °C with a cooling rate of > 500 °C/min and plasma assisted fusion bonding of TSG to fused silica. EDS spectral analysis of TSG before and after glassblowing revealed that the material retained its properties after glassblowing with no re-crystallization or change in glass composition. AFM surface scans of the glassblown structures showed surface roughness of 0.23 nm Sa, which is 2× smaller than the roughness of the optically smooth device wafer. A novel inverted-wineglass architecture was also implemented, providing self-aligned stem structures. The method may enable new classes of TSG/fused silica MEMS devices with atomically smooth surfaces, intrinsically low internal losses ($Q_{TED} > 5 \times 10^{10}$) and highly symmetric structures (radial error $<$ 500ppm).

Wafer-scale nature of the micro-glassblowing process allows integration with existing MEMS technologies. Examples include deposition of conductive thin films before or after glassblowing [98] and bonding of wafers with separately fabricated optical waveguides or silicon-on-insulator (SOI) electrode structures onto the glassblown fused silica/TSG wafers. Main areas of future work include experimental characterization of various stem designs, investigation of optical properties and integration of MEMS electrode structures for electrostatic transduction.

Chapter 3

Characterization of Micro-glassblown Wineglass Resonators

In Chapter 1 a literature review of various micro-wineglass architectures was presented, in Chapter 2 micro-glassblowing of fused silica for fabrication of micro-wineglass structures was reported. Despite these recent advances in micro-wineglass resonator fabrication, the technology development is in its infancy and characterization of the early stage prototypes presents a challenge. This chapter introduces interchangeable excitation and detection methods for characterization of micro-wineglass devices of any shape or size, eliminating the need for in-situ electrode fabrication during the development cycle of the resonator architecture. Additionally, mechanical excitation capability eliminates the need for conductive coating of dielectric resonators, electrical feed-through or DC biasing, all of which can obscure the actual resonator performance.

3.1 Introduction

Two interchangeable modes of excitation are presented: mechanical pinging and electrostatic excitation, Fig. 3.1 [103, 104]. Mechanical pinging is provided by a piezo-actuated probe assembly, whereas electrostatic excitation is provided by assembled electrode structures with $< 20\,\mu m$ capacitive gaps. Two modes of detection are also available: Optical pick-up and capacitive detection, Fig. 3.1. Optical pick-up is provided by laser Doppler vibrometry (LDV) and capacitive detection is provided by assembled electrode structures. 3D micro-glassblown wineglass resonators were used to demonstrate the capabilities of the test-bed in extracting resonator parameters such as Q-factor or frequency split between degenerate wineglass modes.

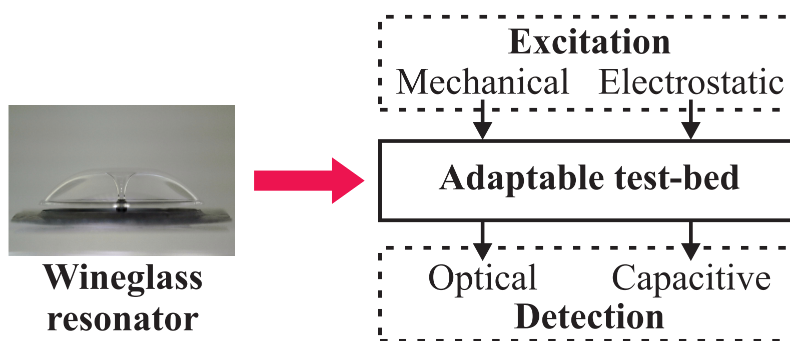

Figure 3.1: Schematic description of adaptable test-bed for characterization of micro-wineglass prototypes.

In the following sections, we will first present the micro-wineglass resonator fabrication process, Section 3.2. This will be followed by the design and operation of the assembled electrode structures in Section 3.3, and the piezo-pinger setup in Section 3.4. The chapter concludes with a comparative analysis of the two testing methods in Section 3.5 and a discussion of the results in Section 3.6

3.2 Fabrication of Wineglass Structures

Micro-wineglass resonators were fabricated using a micro-glassblowing process, Fig. 3.2. This process utilizes an etched cavity on a substrate wafer and a glass layer that is bonded on top of this cavity, creating a volume of trapped gas for subsequent glassblowing of self-inflating shells. When the bonded wafer stack is heated above the softening point of the structural glass layer, two effects are activated at the same time: (1) the glass layer becomes viscous, and (2) the air pressure inside the pre-etched cavity raises above the atmospheric level. This results in plastic deformation of the glass layer, driven by gas pressure and surface tension forces (glass-blowing). The expansion of air (and hence the formation of the shell) stops when the pressure inside and outside of the glass shell reaches an equilibrium. During this deformation, the surface tension acting on the (now viscous) glass layer works toward minimizing the surface area of the structure, as a result a highly symmetric shell with low surface roughness forms, Fig. 3.3.

In order to fabricate the micro-wineglass resonators, first cylindrical cavities with a central post are etched to a depth of 250 µm on a silicon substrate wafer using DRIE, Fig. 3.2. This is followed but bonding of the glass layer with a thickness of 100 µm onto the silicon substrate. The glass layer bonds to the substrate along the perimeter of the cylindrical cavity and at the central post. Then the outer perimeter of the wineglass resonator and the central via hole Fig. 3.2(b) is defined using glass dry etching. The glass etching is performed using a magnetic neutral loop discharge plasma oxide etcher (ULVAC NLD 570 Oxide Etcher) [105]. A low-stress electroplated Cr/Ni hard-mask was used to etch the 100 µm deep trenches. This is followed by micro-glassblowing of the wafer stack at 875 °C inside a RTA system, where the glass layer becomes viscous and the air inside the cavity expands, creating the 3-D shell structure seen in Fig. 3.2(c). A self-aligned central stem structure is also formed at this step due to the deformation of the glass layer around the central anchor point. The

perimeter of the wineglass structure does not deform as there is no etched cavity under these structures, enabling lithographic definition of the perimeter of the wineglass. The next step is XeF2 etching of the substrate underneath the glass layer in order to release the wineglass resonator along its perimeter, Fig. 3.2(d). XeF2 is chosen because of the extremely high selectivity to glass (as high as 1:1000 selectivity). Once the etch is complete a free standing micro-wineglass structure with a self-alinged stem structure is obtained, Fig. 3.3. Final step of the fabrication process is blanket metallization by sputtering or atomic layer deposition (ALD), Fig. 3.2(e). A monolayer of Iridium was chosen for the metal layer seen in Fig. 3.2, because of high conductivity, corrosion resistance and the ability to apply without utilizing an adhesion layer. The metal layer coats the top surface of the resonator shell, the side walls of the capacitive gaps as well as inside of the central via hole. Electrical feed-through to the resonator is obtained through the central via structure, which connects the resonator onto the substrate.

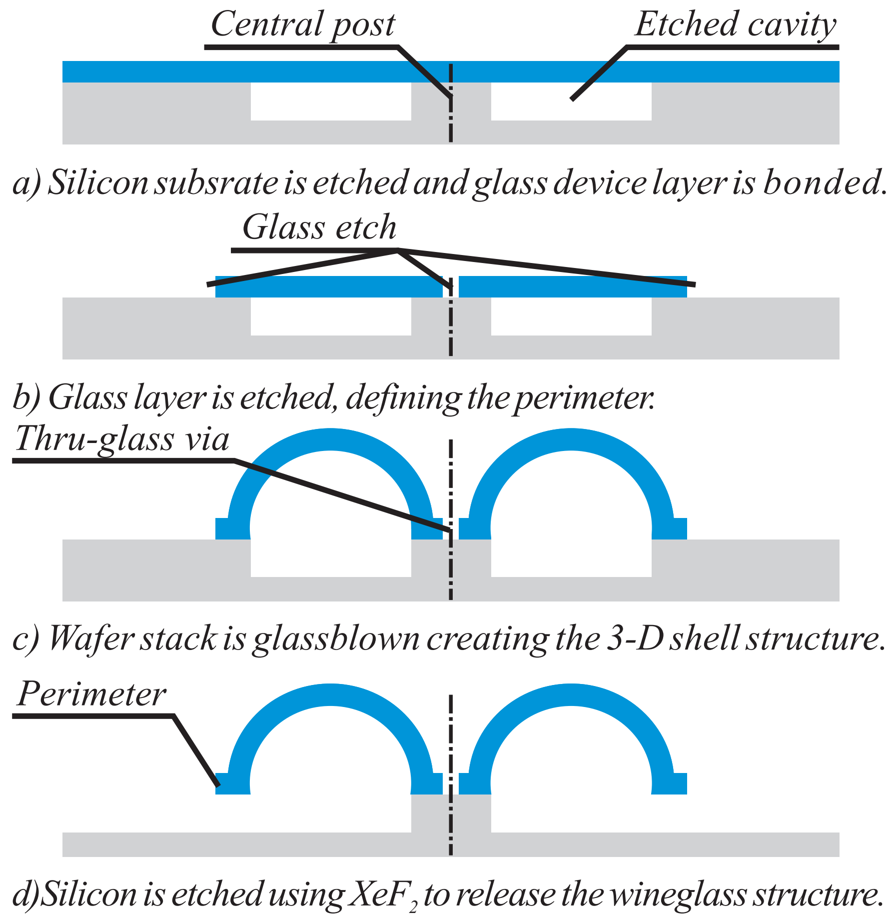

Figure 3.2: Micro-glassblown wineglass structures are fabricated by (a) etching cavities on the substrate layer, (b) etching of the glass layer to define the perimeter, (c) micro-glassblowing above the softening point of the glass layer and (d) etching away the substrate underneath the wineglass structure.

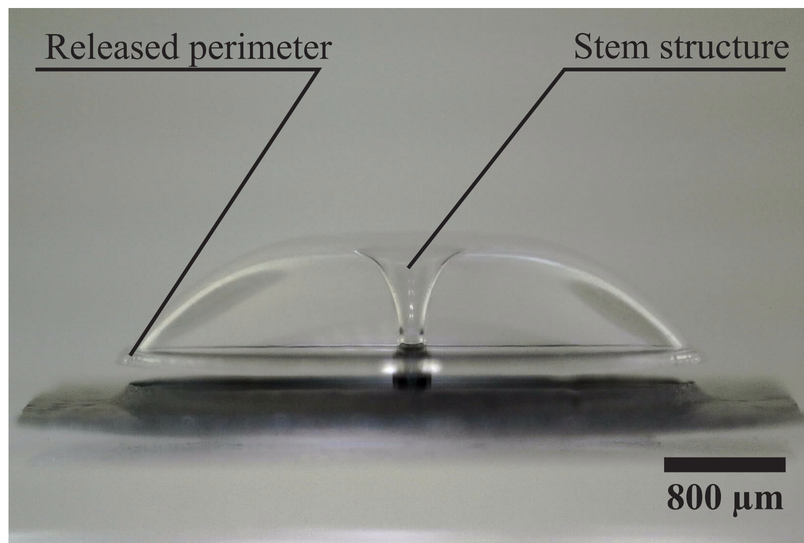

Figure 3.3: Released wineglass structure with 4.2 mm diameter, 50 µm thickness and 300 µm central stem.

3.3 Assembled electrodes

Electrostatic excitation and detection is provided by assembled electrode structures, which are fabricated separately from the micro-glassblown resonator on a SOI wafer, Fig. 3.4. The SOI stack consists of 500 µm silicon substrate layer, 5 µm buried oxide layer and 100 µm silicon device layer. Each electrode assembly consists of 8 independent electrodes that are spaced 45 °C apart around a central thru-hole. Large spring structures on each electrode allow an adjustment distance up to 400 µm for each individual electrode (total of 800 µm along the resonator diameter), which permits a single electrode design to be used for different wineglass architectures and diameters, Fig. 3.5. Electrode assemblies with 7 different central-hole diameters were fabricated on the same SOI wafer, which covers all wineglass diameters from 1 mm to 4.5 mm.

The fabrication of SOI electrodes start by lithographically patterning the back-side thru-hole and etching using DRIE to a depth of 500 µm. This is followed by patterning and etching the device layer to create the electrode structures. For the electrode structures, the DRIE is performed to a depth of 100 µm, using a 1.6 µm oxide hard-mask for better feature resolution, then O2 ashing, followed by RCA-1 cleaning is used to get rid of excess photoresist and etch residues. The final step of the fabrication process is HF wet etching of buried oxide layer to release the electrode structures.

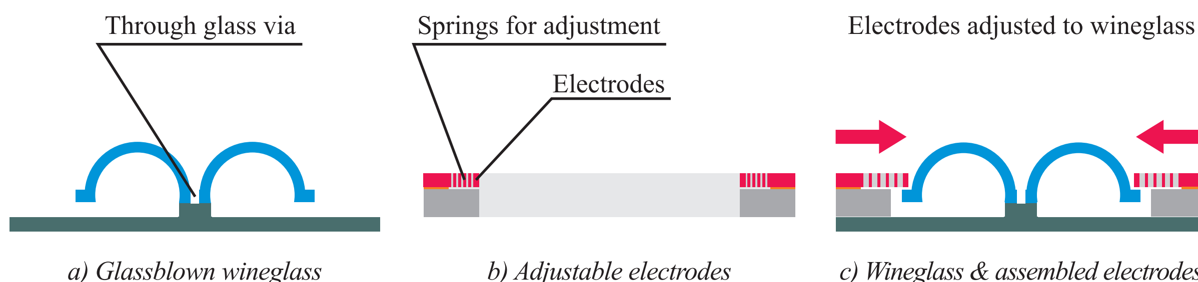

Figure 3.4: Electrodes are fabricated separately on an SOI stack, bonded to the resonator wafer and extended.

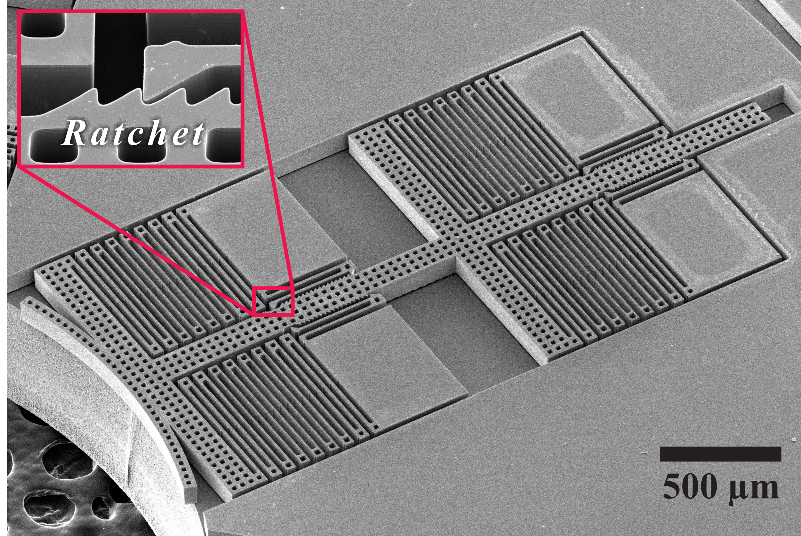

Figure 3.5: SEM image of an adjustable electrode with 400 µm maximum displacement and 10 µm positioning resolution. SEM image by Dr. M. J. Ahamed [104].

3.3.0.1 Operation

Once the fabrication is complete the electrode structures are singulated and bonded onto the micro-wineglass die, Fig. 3.4. Then, each electrode is pushed to close proximity of the wineglass by using a micro-manipulator. When the correct location is achieved four ratchet mechanisms (2 front, 2 back) keep the electrodes in place, Fig. 3.7. The ratchet mechanisms act on 2 rack gears placed on the electrode. The pitch distance on the rack gears are 20 µm. By offsetting the front and rear ratchet mechanisms by 10 µm relative to the teeth pitch of the rack gear, a positioning resolution of 10 µm was obtained (minimum capacitive gap).

For experimental characterization, assembled electrode structures were bonded onto micro-glassblown wineglass structures, Fig. 3.3. A wineglass with 4.2 mm diameter, 50 µm thickness, and 300 µm central stem was tested using an assembled electrode structure with 4.5 mm thru-hole. The entire assembly was placed into a ceramic DIP package with gold back-plate and wirebonded at the anchors of each electrode, Fig. 3.6. The bias voltage to the resonator is applied through the gold back-plate, which connects to the resonator die, through it to

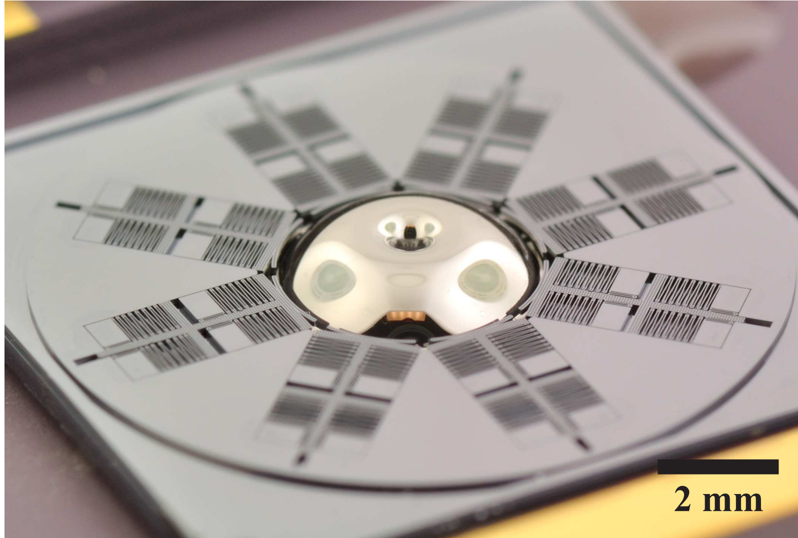

Figure 3.6: Electrode structures assembled onto a micro-glassblown wineglass resonator with $< 20\,\mu\text{m}$ gaps.

the via at the center of the stem and to the resonator metal layer.

Frequency sweeps were obtained using an Agilent 4395A network analyzer. Two opposite electrodes were used with the goal of forced excitation of the n = 2 wineglass mode. A DC voltage of 10 V and AC voltage of 5 V were used. A Q-factor of 40.000 was observed at 14.8 kHz, giving a time decay constant of ~0.9 s, Fig. 3.8.

Adjustable nature of the assembled electrode structures allow, characterization of 3-D resonator structures with varying size and diameter. Fig. 3.9 shows assembled electrodes structures around a 1.2 mm micro-glassblown spherical resonator with resonant frequencies in the MHz range.

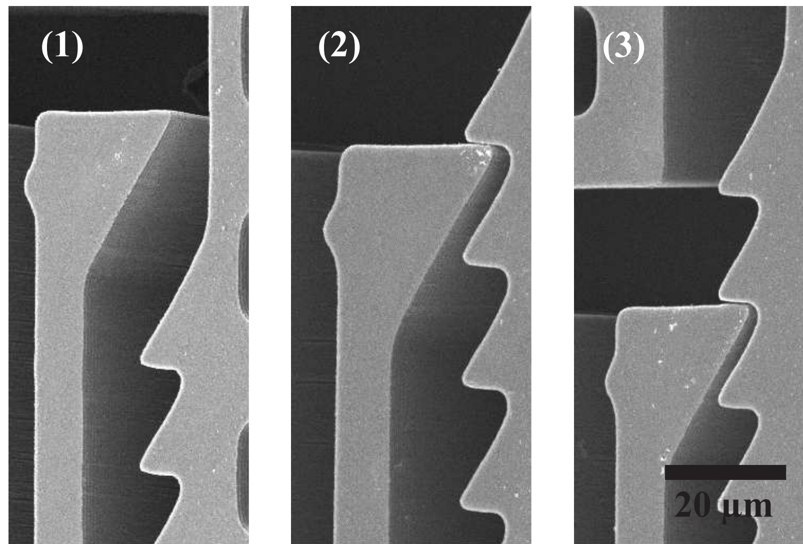

Figure 3.7: Ratchet mechanism acting on the electrode structure, the electrode is extended gradually in 1 through 3. SEM image by Dr. M. J. Ahamed [104].

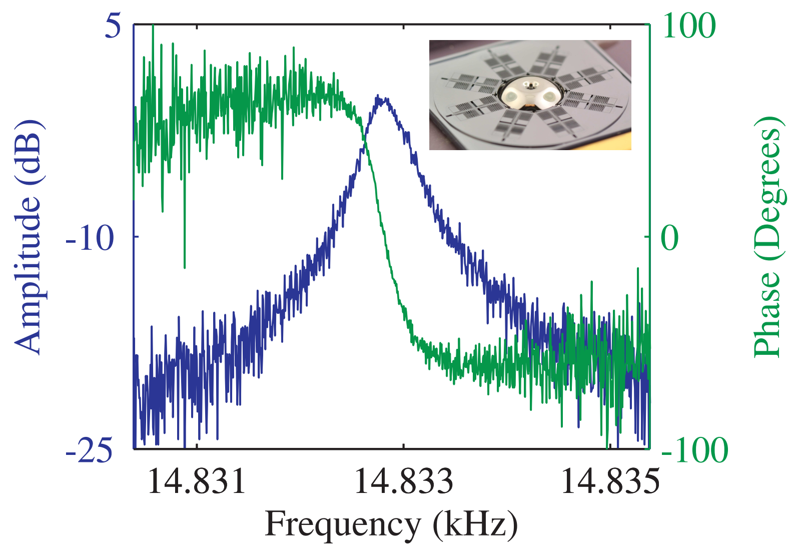

Figure 3.8: Electrostatic frequency sweep using adjustable electrode assembly, showing Q = 40k at 14.8 kHz.

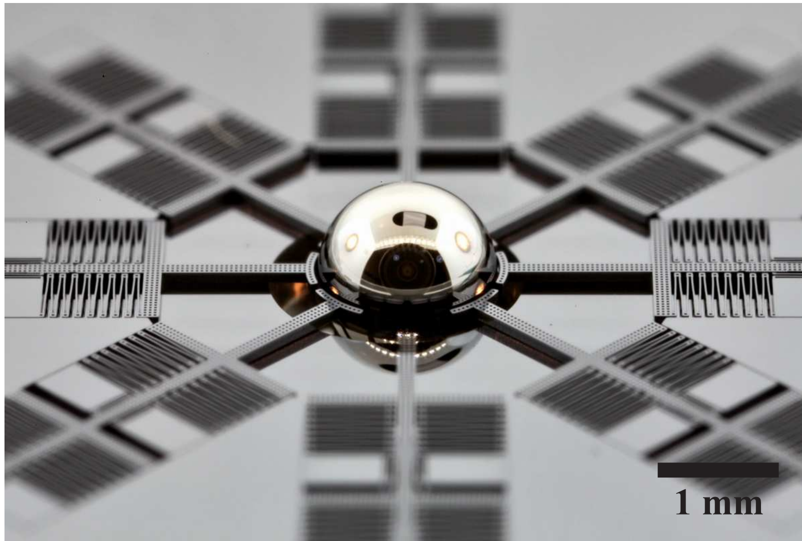

Figure 3.9: A glassblown spherical resonator with assembled electrodes. Diameter is 1.2 mm and thickness is 5 µm. Photo by Dr. A. A. Trusov [104].

3.4 Piezo-pinger setup

Capacitive transduction requires an electrical connection to the resonator body, which can be achieved either by using a conductive resonator material or coating the resonator with a conductive layer. If the resonator is made out of a dielectric material, such as SiO2, conductive coating with an appropriate feed-through might not be available during early stages of the resonator fabrication. Otherwise, it might be undesirable to use capacitive transduction for testing, since factors such as electrostatic coupling effect or metallization losses can obscure the actual mechanical characteristics of the wineglass resonator. For these reasons a mechanical excitation method that can operate under vacuum and directionally excite the wineglass modes is highly desirable as an alternative to electrostatic transduction.

A piezo-pinger setup was constructed using off-the-shelf components and rapid prototyped fixtures. The piezo-pinger assembly consists of 3 main components: A linear micro-stage with a positioning accuracy of 1 µm, a high displacement (32 µm) piezo-stack, and a tungsten probe tip (100 µm tip radius), Fig. 3.10. The setup is built with vacuum compatible components and fits into a bounding box of 80 mm × 30 mm × 20 mm.

3.4.0.2 Operation

Wineglass resonator is placed on the linear stage and kept in place using a non-permenant bonding method, such as indium or double sided kapton tape. Linear stage is adjusted under a microscope until the probe tip is within 5–10 µm proximity of the wineglass. Then, the piezo-pinger is placed into the vacuum chamber and connected to a high-voltage power supply, Fig. 3.12. A mechanical switch with 1 kΩ discharge resistor was used for controlling the piezo-stack, Fig. 3.11. A Polytec laser Doppler vibrometer pointed onto the outer edge of the wineglass resonator through the optical port of the vacuum chamber is used for detection,

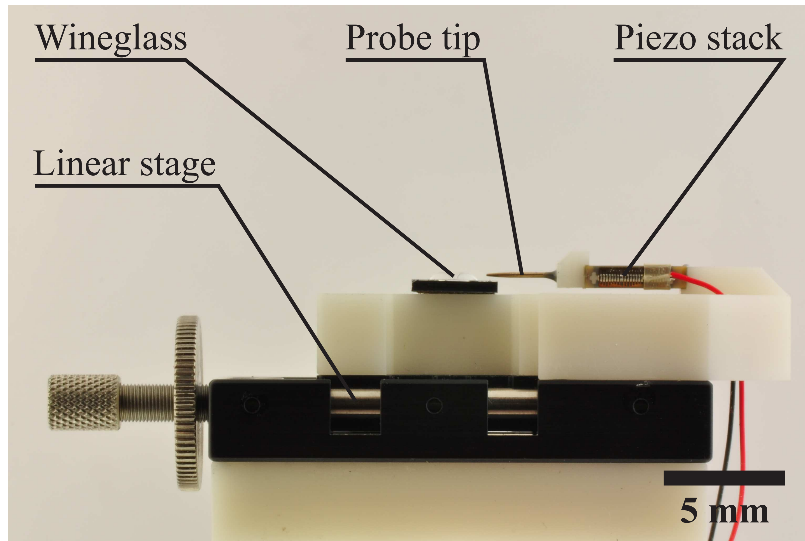

Figure 3.10: Piezo-pinger setup for time domain characterization, piezo stack is actuated to probe the wineglass resonator.

Fig. 3.11.

Experiment starts by increasing the voltage on the piezo-stack until the probe tip barely makes contact with the edge of the wineglass (up to 100 V DC), which applies a point load onto the wineglass resonator. At the beginning of the experiment the probe tip is retracted by shorting the piezo-stack over the 1 kΩ discharge resistor, 3.12. A short period (1–5 ms) of transient behavior is observed, where the shell undergoes a large deformation due to the interaction with the piezo pinger. After this transient, which saturates the laser Doppler vibrometer (LDV), free vibration of the shell structure starts (t = 0). Time domain response is captured using the laser Doppler vibrometer at a sampling rate of 1256 kHz. The data can later be analyzed either in the time domain or in frequency domain using a Fast Fourier Transform (FFT) algorithm.

Time domain response, in Fig. 3.13, was obtained on a wineglass resonator using the described piezo-pinger setup and laser Doppler vibrometer detection. Fig. 3.13 shows a 28 Hz beat signal created by the frequency split between two degenerate wineglass modes. Post-processing using a FFT algorithm confirms the frequency split of 28 Hz at resonant frequen-

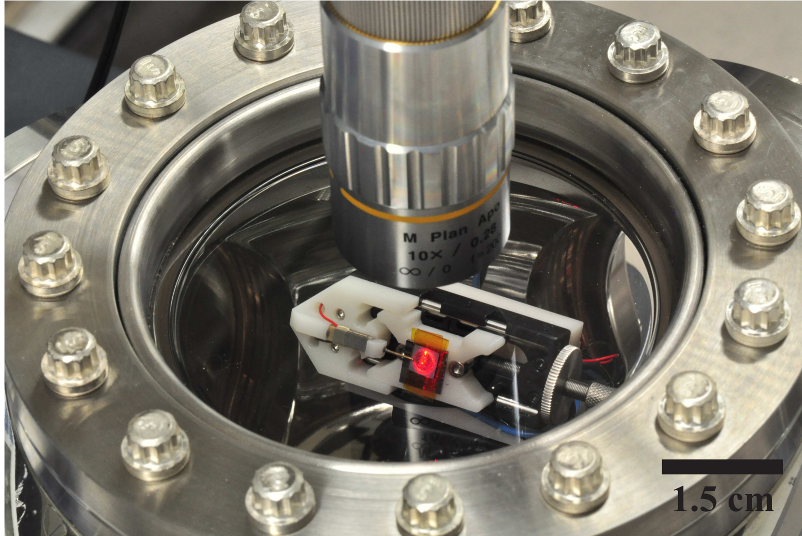

Figure 3.11: Piezo-pinger setup inside vacuum chamber. Optical port on the vacuum chamber allows laser Doppler vibrometer characterization.

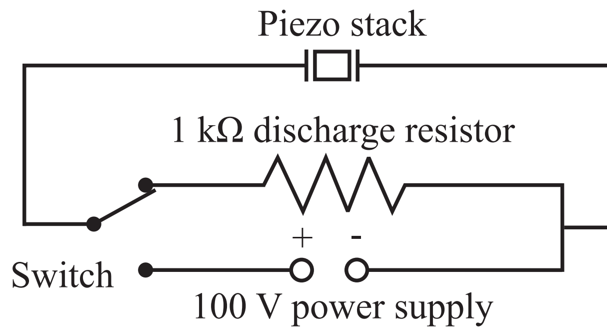

Figure 3.12: A mechanical switch with $1\,\mathrm{k}\Omega$ discharge resistor was used for controlling the piezo-stack.

cies $f_1 = 22\,036\,\mathrm{Hz}$ and $f_2 = 22\,064\,\mathrm{Hz}$. Large frequency split is associated primarily with dry etch defects at around the perimeter of the wineglass, followed by the influence of g-forces and thermal non-uniformities within the micro-glassblowing furnace. These effects have been addressed recently [105] to achieve sub-Hz frequency symmetry in micro-glassblown wineglass resonators [106].

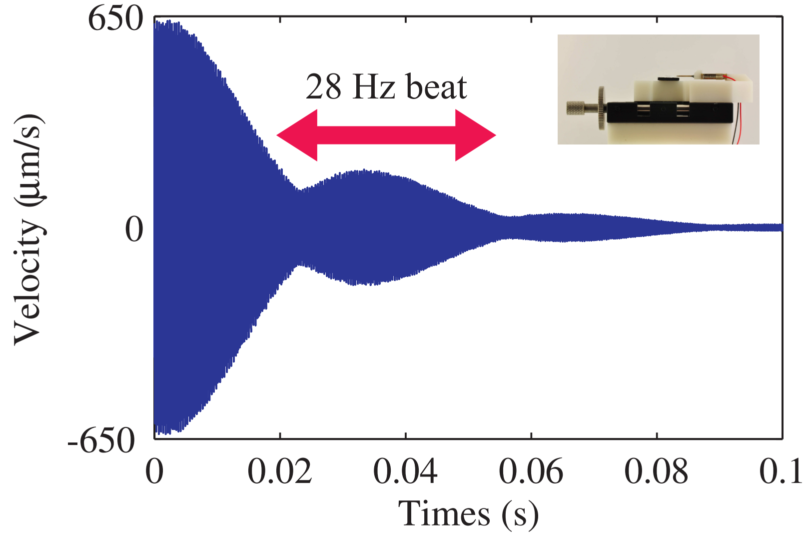

Figure 3.13: Time decay response obtained by retracting the probe tip, beat signal between two degenerate modes shows $\Delta f = 28$ Hz.

3.5 Comparison of excitation methods

A comparative summary of the two excitation methods is presented in Table 3.1. Assembled electrode structures are more suited for detailed characterization of wineglasses due to the capability of mode selection and continuous excitation at the cost of potentially unwanted need for metallization and permanent attachment to the shell. Whereas, piezo-pinger setup is ideal for rapid characterization of wineglasses as it does not require permanent attachment or metallization.

	Assembled electrodes	**Piezo-pinger**
Attachment	Permanent	Non-permanent
Coating	Metalized	None required
Detection	Electrostatic	Laser vibrometer
Mode selection	Yes	No

Table 3.1: Comparison of excitation methods.

Another advantage of the piezo-pinger setup is the fact that metallization of the shells is not required for characterization. This way unwanted metallization losses can be eliminated,

which could potentially obscure the actual resonator behaviour. Even though no significant Q-factor change has been observed on borosilicate glass shells, metallization losses are expected to play a role in higher Q-factor fused silica and ULE TSG shells.

3.6 Conclusions

In order to characterize micro-wineglass resonators at the early stages of the development cycle, an adaptable test-bed was developed. Two interchangeable modes of excitation are demonstrated: (1) Mechanical pinging using a piezo actuated probe assembly, (2) electrostatic excitation using assembled electrode structures.

Electrostatic excitation has advantages in terms of mode selectivity as unwanted modes can be suppressed by using a combination of balanced electrodes. However, it can potentially obscure the actual resonator behavior due to metallization losses or the electrostatic coupling effect. Both of these effects can be avoided by using a purely mechanical excitation method, such as piezo-pinging. Another benefit of the piezo-pinger setup is the non-permanent attachment of the resonator, which allows quick testing of multiple wineglass resonators.

By decoupling the resonator development from electrode fabrication, a greater flexibility in design and fabrication is obtained. In addition, the methods presented in this chapter is universally applicable to any micro-wineglass resonator, regardless of shape, size or fabrication process involved.

Chapter 4

Micro-glassblowing for Frequency Symmetry

In this chapter, we explore the hypothesis that surface tension and pressure driven micro-glassblowing paradigm may serve as an enabling mechanism for wafer-scale fabrication of extremely symmetric ($\Delta f < 1\,\mathrm{Hz}$) 3-D wineglass structures. A new fabrication process based on deep glass dry etching was developed to fabricate micro-wineglasses with self-aligned stem structures and integrated electrodes. The wineglass modes were identified by electrostatic excitation and mapping the velocity of motion along the perimeter using laser Doppler interferometry.

4.1 Introduction

In Chapter 1, it was shown that Rate Integrating Gyroscope performance relies heavily on the stiffness asymmetry (Δf) and damping asymmetry ($\Delta\tau$) between the two degenerate modes [5]. For example, according to Eq. 1.11 an increase in frequency asymmetry (Δf or

$\Delta\omega$), not only would result in an increase in quadrature error but would also increase the drift of the pattern angle (θ) over time, preventing accurate measurement of angular rotation. For this reason reduction of frequency asymmetry (Δf) is of paramount importance for high performance Rate Integrating Gyroscope operation.

Micro-glassblowing process relies on viscous deformation of the device layer under the influence of surface tension and pressure forces to define the 3-D shell structure as opposed to conventional deposition, molding or etching techniques. During the brief duration while the device layer is still viscous, surface tension forces act on the 3-D shell structure at an atomic level to minimize surface roughness and structural imperfections [107, 108]. Our hypothesis is that this may lead to levels of smoothness and structural symmetry that is not available through conventional fabrication techniques.

Characterization methods to identify wineglass modes were presented in Chapter 3 by using assembled electrode structures and mechanical stimuli. Mechanical characterization of these initial prototypes using the piezo-pinger setup with optical pick-off showed a frequency split of ~28 Hz on n = 2 degenerate wineglass modes. This chapter focuses on improvements in fabrication process to incorporate in-situ electrode structures [106, 109], as well as further improvement in as-fabricated frequency split.

In the following sections, we will first present application of frequency symmetry scaling laws to MEMS wineglass resonators. This will be followed by effect of surface tension forces on micro-glassblown resonators in Section 4.2.1 and factors affecting frequency symmetry in Section 4.2.3. In Section 4.3 we will present improvements in fabrication process to incorporate in-situ electrode structures to the micro-glassblown resonators as well as further improvement in as-fabricated frequency split. In Section 4.4 we will present the frequency symmetry characterization results from 5 wineglass resonators. The chapter concludes with a discussion of the results and Δf comparison between multiple micro-glassblown wineglass resonators in Section 4.5.

4.2 Design for Frequency Symmetry

4.2.1 Frequency Symmetry Scaling Laws

Compared to macro-scale HRGs [2], MEMS wineglass resonators have orders of magnitude smaller dimensions, both in shell thickness and diameter. This act of miniaturization requires fabrication processes with very demanding absolute tolerances in order to obtain the required frequency symmetry. In this section, HRG scaling laws are applied to MEMS sized wineglass resonators to demonstrate the effect of miniaturization.

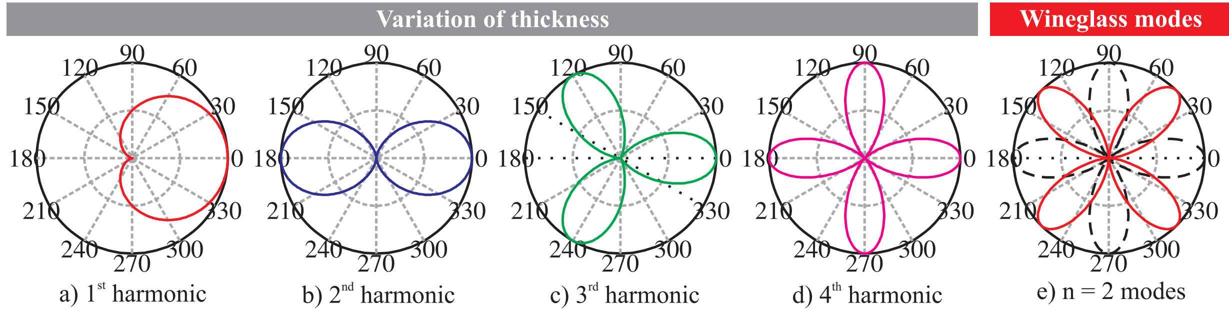

Figure 4.1: Polar plots showing the first 4 harmonics of thickness imperfections. Only the 4th thickness harmonic affects the frequency symmetry (Δf) of n = 2 wineglass modes. (a) 1st harmonic, (b) 2nd harmonic, (c) 3rd harmonic, (d) 4th harmonic, (e) n = 2 wineglass modes.

The geometric imperfections of wineglass resonators can be specified using Fourier series representation of the thickness around the central axis of symmetry, Fig. 4.1 [110]:

$$h(\varphi) = h_0 + \sum_{i=1}^{\infty} h_i \cos i(\phi - \phi_i) \,, \tag{4.1}$$

where $h(\varphi)$ is the thickness of the wineglass resonator along its perimeter and Eq. 4.1 is the Fourier series representation of $h(\varphi)$ with respect to azimuth angle ϕ such that: h_0 is the average thickness and h_i is the i th thickness harmonic. This thickness variation will create a corresponding mass variation around the central axis of symmetry of the wineglass

resonator according to [110]:

$$M(\varphi) = M_0 + \sum_{i=1}^{\infty} M_i \cos i(\phi - \phi_i) \ , \tag{4.2}$$

where M_0 is the average mass per unit angle and M_i is the i th harmonic of the thickness variation.

For gyroscope applications the most commonly used resonance modes are the first two wineglass modes or the so called n = 2 and n = 3 wineglass modes, Fig. 1.4. This is due to the fact that lower order wineglass modes have higher angular gain factors and lower resonance frequencies. Each wineglass mode has two degenerate modes that are spaced 45° and 30° apart for n = 2 and n = 3 modes respectively. For very low fundamental frequency splits, the degenerate mode pair becomes indistinguishable. Any coriolis input into the resonator causes the mode shape to rotate at an angle proportional to angle of rotation. Rate integrating gyroscopes operate by directly measuring this angle.

It has been shown in [111, 112] that a fundamental frequency split in these degenerate modes will be observed only if there is a thickness variation on $i = 4$ or $i = 6$ harmonics, respectively (only if i = 2 n). This fact makes the wineglass resonators robust to frequency asymmetries. For example, any imperfection in the 1st, 2nd or 3rd thickness harmonics will have no effect on the frequency symmetry of the n = 2 wineglass mode (see Appendix B).

When the 4th thickness harmonic is not zero, the contribution to the fundamental frequency splitting of n = 2 wineglass mode becomes linearly proportional to the 4th harmonic of the shell mass and consequently the shell thickness [111, 112]:

$$\Delta f \cong f \frac{M_4}{M_0} \cong f \frac{h_4}{h_0} \ , \tag{4.3}$$

The equation 4.3 sets the basis for the scaling laws for frequency imperfections. Because of the thickness term in the denominator, the resonator will become more susceptible to frequency asymmetries as the thickness of the resonator decreases. This effect is shown in Fig. 4.2 for a 10 kHz resonator. The thickness axis is divided in 3 regimes from right to left: macro-scale devices such as the Hemispherical Resonator Gyroscopes [2], bulk micromachined devices which have a thickness range of 10 µm to 250 µm and surface micromachined wineglass resonators which have a thickness range of 100 nm to 10 µm. As can be seen in Fig. 4.2 going from macro-scale devices to MEMS wineglass resonators requires 1 to 3 orders of magnitude improvement in absolute tolerances to obtain the same frequency symmetry (Δf).

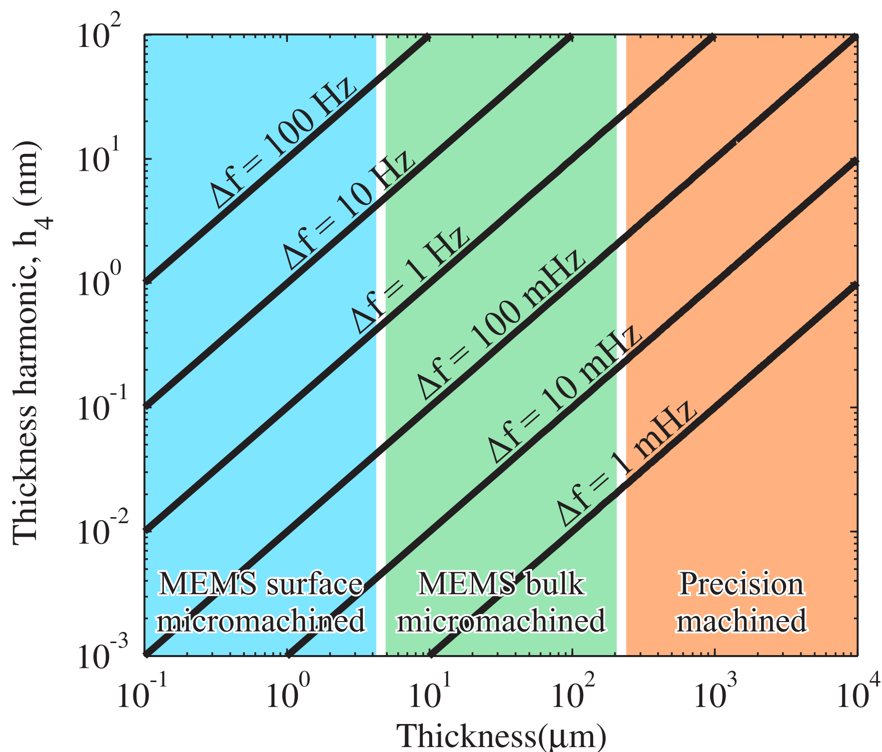

Figure 4.2: Plot showing wineglass thickness vs thickness imperfections in the 4th harmonic and resulting frequency split. Going from precision machined wineglass resonators to micromachined devices require 1 to 3 orders of magnitude improvement in fabrication tolerances due to the reduction in thickness.

A similar relationship can be derived for the radius of the wineglass resonator using the

Rayleigh-Ritz solution for resonance frequency [113]:

$$f = \sqrt{\frac{n^2(n^2-1)^2h^2E}{3(1+\mu)\rho\pi^2r^4}\frac{\int_0^{\pi/2}\sin\phi\tan\frac{\phi}{2}d\phi}{\int_0^{\pi/2}\{(n+\cos\phi)^2+2\sin^2\phi\}\sin\phi d\phi}}\,. \tag{4.4}$$

When the above Rayleigh-Ritz solution is inserted into equation 4.3. Thickness term in the equation can be eliminated to be replaced with the radius of the wineglass:

$$\Delta f \propto \frac{h_4}{r^2}\,. \tag{4.5}$$

The resultant equation shows an even stronger dependence of Δf on radius as the denominator term is squared. For every 10× reduction in radius the frequency symmetry deteriorates by 100× 4.3.

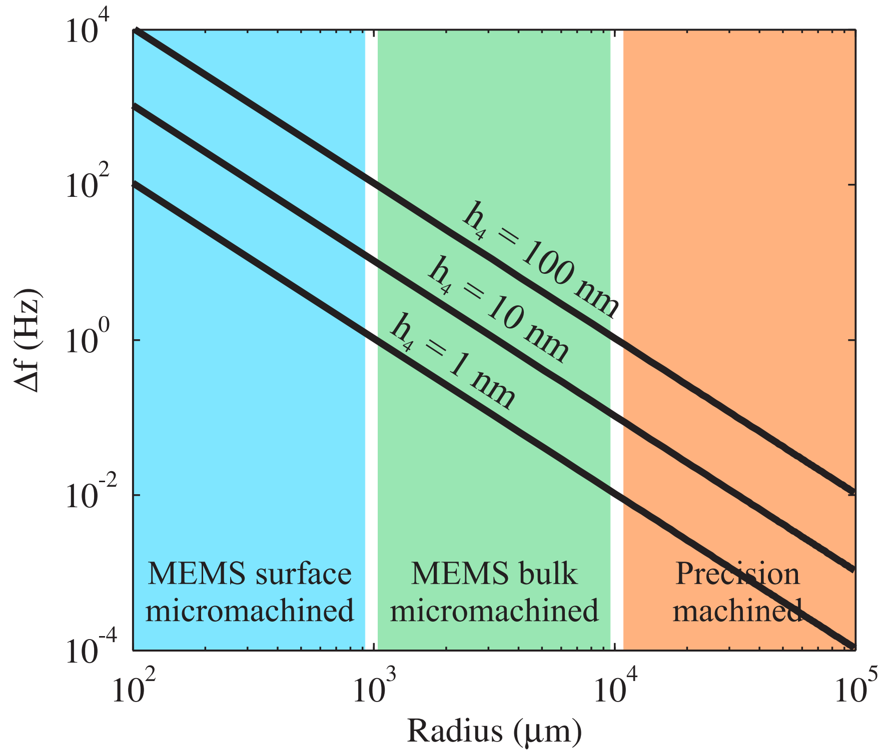

Figure 4.3: The effect of thickness variation of the 4th harmonic on frequency split (Δf) vs wineglass resonator radius.

4.2.2 Stability of Micro-glassblown Structures

During micro-glassblowing, surface tension forces become active for a brief duration. These forces work towards minimizing the surface energy of the resonator and as a result mitigate the effects of imperfections, such as surface roughness or structural asymmetry. However, if care is not taken, surface tension forces can work towards unbalancing the resonator by creating a pressure instability within the micro-glassblown inverted-wineglass structure.

To analyze this effect we start with the Young-Laplace equation for surface tension:

$$\Delta P = 2\,\gamma\,(\frac{1}{R_1} + \frac{1}{R_2})\,, \tag{4.6}$$

where ΔP is the pressure, γ is the surface tension coefficient, R_1 and R_2 are the principal radii of curvature of an arbitrary surface. The coefficient 2 on the right hand side comes from the fact that the micro-glassblown structures have two interface surfaces (inner and outer surfaces), as opposed to a single interface surface such as a droplet of water.

The curvature of an inverted-wineglass structure can be approximated as a hemi-toroid where the principal radius of curvature becomes the major and the minor radius of the hemi-toroid ($R_1 = R$ and $R_2 = r$ respectively). And the minor radius of the hemi-toroid will depend on the height (l) of the structure according to the following geometric expression:

$$r = \frac{l^2 + r_0^2}{2l}\,, \tag{4.7}$$

where r_0 is the half-width of the trench opening.

Equation 4.6 and 4.7 can be combined to solve for surface tension induced pressure difference with respect to l. Figure 4.4 shows results of this calculation for inverted-wineglass structures

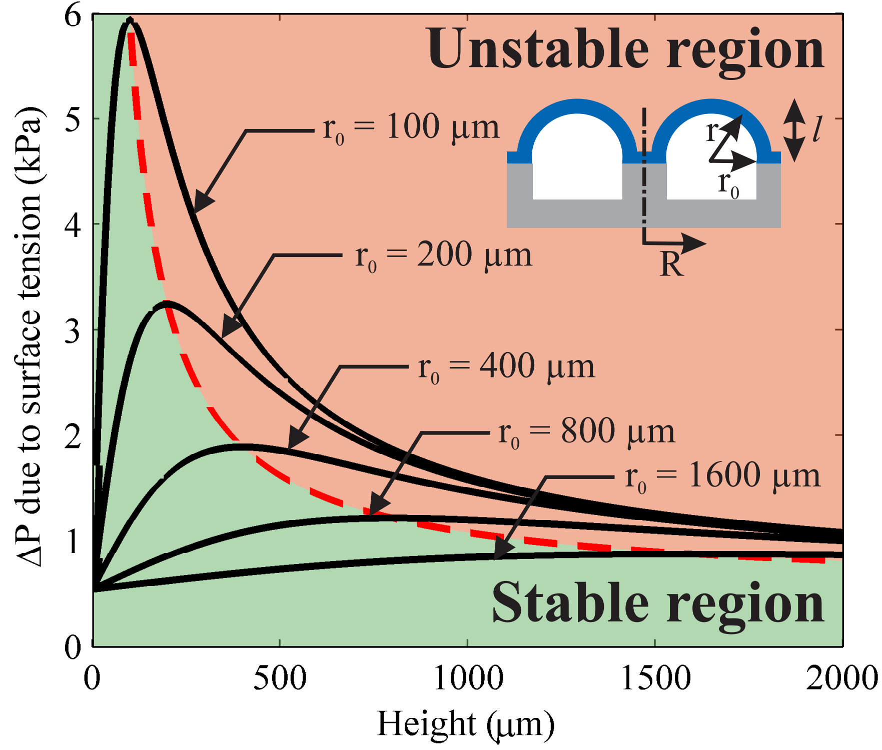

Figure 4.4: Surface tension induced pressure differential depends on geometric parameters such as cavity radius (r_0) and height (l). $l = r_0$ marks the critically stable region for micro-glassblowing of inverted wineglass structures.

with $R = 1$ mm and $r_0 = 100$ µm to 1600 µm.

It can be seen that ΔP has a local maxima for all designs, which occur at $r_0 = l$. Interpretation of this result is that the surface tension forces will progressively increase and work towards keeping the structure symmetric if the structure is designed to have $l < r_0$. However, if the shell is glass-blown beyond $l > r_0$, the surface tension forces will progressively decrease. As a result any perturbation on the geometric shape will be amplified by the further reduction in surface tension induced pressure ΔP, creating instability within the micro-glassblown structure.

To summarize, in order to achieve high structural symmetry and avoid surface tension induced instability during micro-glassblowing, inverted-wineglass structures should be designed to have $l < r_0$.

4.2.3 Factors Affecting Frequency Symmetry

Table 4.1: Summary of fabrication defects and reduction approach.

Cause	Defect	Reduction Approach
Dry etch defects	Micro-masking & mouse bites	Improved dry-etch mask
Perturbations at High T.	Structural deformation	Uniform temp. / gas flow
Mask Misalignment	$< 2\mu$m misalignment	Stepper
Wafer flatness	$< 0.1°$ across wafer	Ultra-flat wafers
Wafer bow	$< 0.1°$ across wafer	CTE matched materials

Fabrication process was optimized with two design goals in mind: (1) batch-scale compatible fabrication process, (2) elimination of process steps that can contribute to frequency asymmetry. For compatibility with batch-scale fabrication, only standard MEMS processes were used in fabrication of the micro-wineglass resonators: the process consists of two lithography steps, three dry etch steps, one electroplating and one sputtering step. The glassblowing is performed in a standard rapid thermal annealing system, which can provide uniform heating and cooling for up to 6" diameter wafers (Heatpulse 610 RTA).

It has been found that edge defects and thermal/mechanical perturbations during glassblowing are the primary factors affecting the frequency symmetry of micro-glassblown resonators, Table 4.1. These effects were eliminated by using an improved dry-etch mask [105] and optimizing the glassblowing conditions to have uniform temperature and gas flow. In order to minimize the frequency asymmetry further, additional precautions were taken. Pick-and-place or wafer alignment steps that can create misalignment and potentially contribute to frequency asymmetry were eliminated. Contribution of mask misalignment errors were also minimized by incorporating only two lithography steps and using a self-aligned stem structure. Both of the lithography steps were performed before the micro-glassblowing step, while the device layer is still two dimensional, Fig. 4.5(b). This eliminates the need for more challenging patterning techniques such as 3-D lithography, shadow masks or laser ablation of the 3-D structure. Finally, anisotropic dry etching was used to define both the substrate cavity

and the outer perimeter of the structure, eliminating etch asymmetries that may occur due to crystalline orientation of silicon [68].

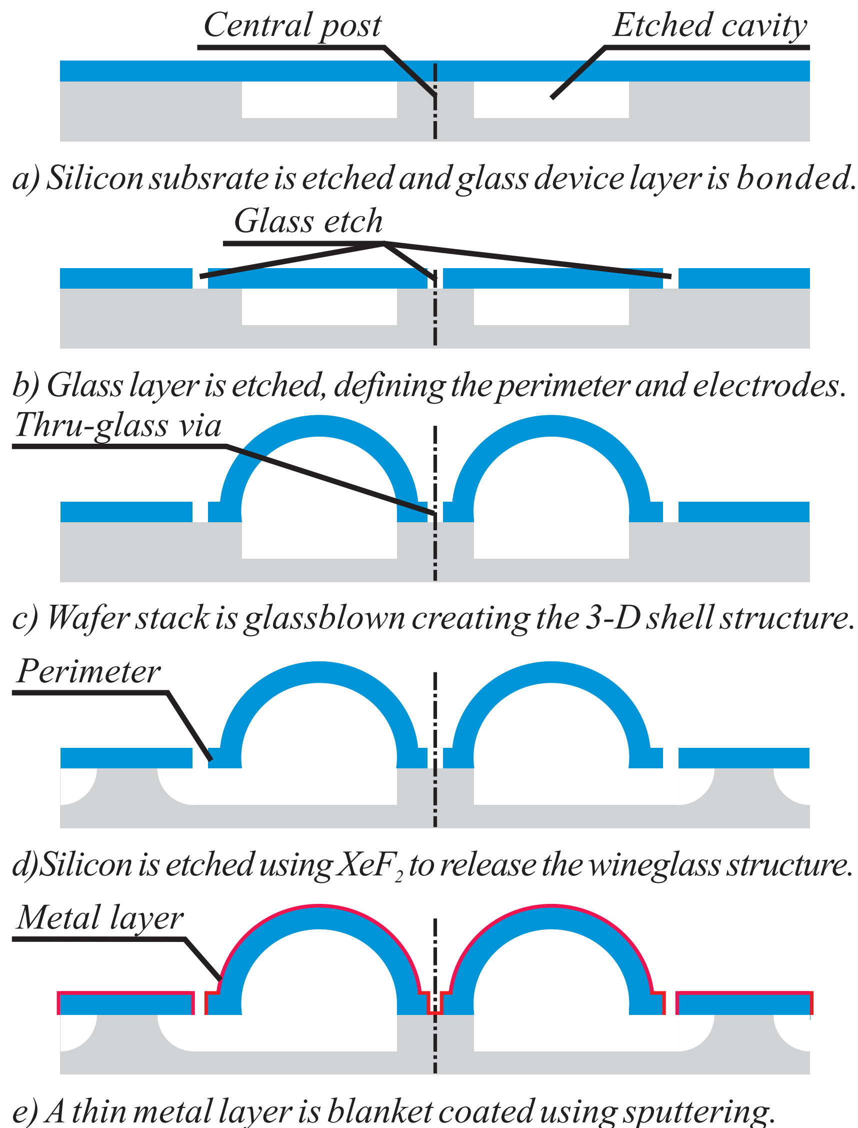

Figure 4.5: Process flow for fabrication of micro-glassblown wineglass resonators with integrated electrodes. (a) Device layer is bonded to pre-etched substrate, (b) device layer is etched, defining the perimeter of the wineglass and the electrodes, (c) wafer stack is glassblown, (d) silicon underneath the perimeter is etched using XeF_2, (e) a thin metal layer is blanket coated.

4.3 Fabrication

In order to fabricate the micro-wineglass resonators, first cylindrical cavities with a central post were etched to 250 µm depth on a 100 mm silicon substrate wafer using DRIE, Fig. 4.5(a). Then, a thin glass layer (100 µm) was anodically bonded onto the silicon substrate. Anodic bonding was performed using a DC voltage of 600 V and a load of 100 N at 400 °C. The glass layer was bonded to the substrate along the perimeter of the cylindrical cavity and at the central post, hermetically sealing atmospheric pressure air within the cavities. This was followed by deep glass dry etching to define the outer perimeter of the wineglass resonator and central via hole, Fig. 4.5(b). Capacitive gaps and individual electrodes as well as the central via hole were defined at this step. The glass etching was performed using a magnetic neutral loop discharge plasma oxide etcher (ULVAC NLD 570 Oxide Etcher) [105]. A $\sim 5\ \mu$m thick low-stress electroplated Cr/Ni hard-mask was used to etch the 100 µm deep trenches. This was followed by micro-glassblowing of the wafer stack at 875 °C inside a RTA system, where the glass layer becomes viscous and the air inside the cavity expands, creating the 3-D shell structure, Fig. 4.5(c). Once the 3-D micro-glassblown structure forms, the wafer was rapidly cooled to room temperature for solidification. During the micro-glassblowing step, the perimeter of the wineglass structure and the planar electrodes do not deform as there is no etched cavity under these structures, enabling lithographic definition of the capacitive gaps. The next step was XeF_2 etching of the substrate underneath the glass layer in order to release the wineglass resonator along its perimeter, Fig. 4.5(d). XeF2 was chosen because of the extremely high glass to silicon selectivity (as high as 1:1000 selectivity). Once the etch was complete a free standing micro-wineglass structure with a self-aligned stem structure was obtained, Fig 4.6.

Final step of the fabrication process is blanket metallization by sputtering, Fig. 4.7. A 30 nm sputtered Iridium layer was chosen for the metal layer, because of high conductivity,

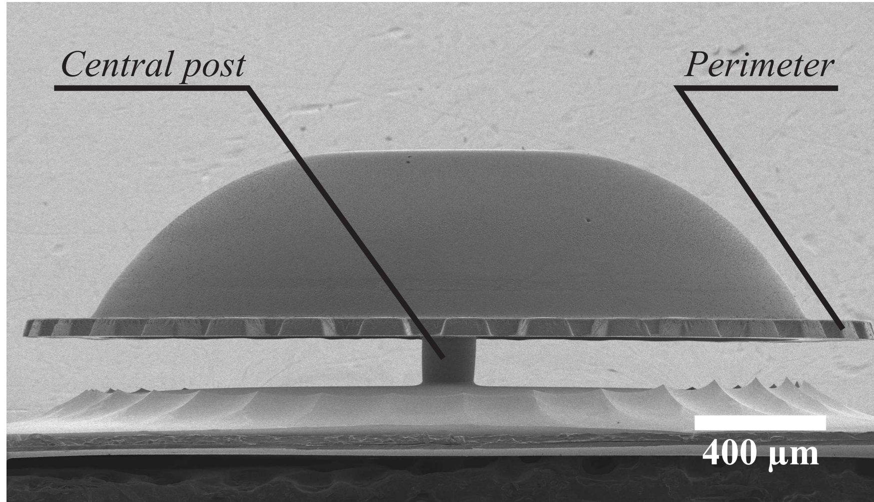

Figure 4.6: SEM image of a stand-alone micro-wineglass structure after release. Diameter 4.4 mm, thickness 50 µm. SEM image courtesy of Dr. M. J. Ahamed [114].

corrosion resistance and the ability to apply without utilizing an adhesion layer (such as Cr or Ti). The metal layer coats the top surface of the resonator shell, the side walls of the capacitive gaps as well as inside of the central via hole. However, directionality of the sputtering process prevents the metal layer from coating the undercut created by the XeF2 etch, electrically isolating the electrodes and the resonator, Fig. 4.5(e). Electrical feed-through to the resonator was obtained through the central via structure, which connects the resonator to the substrate, Fig. 4.8.

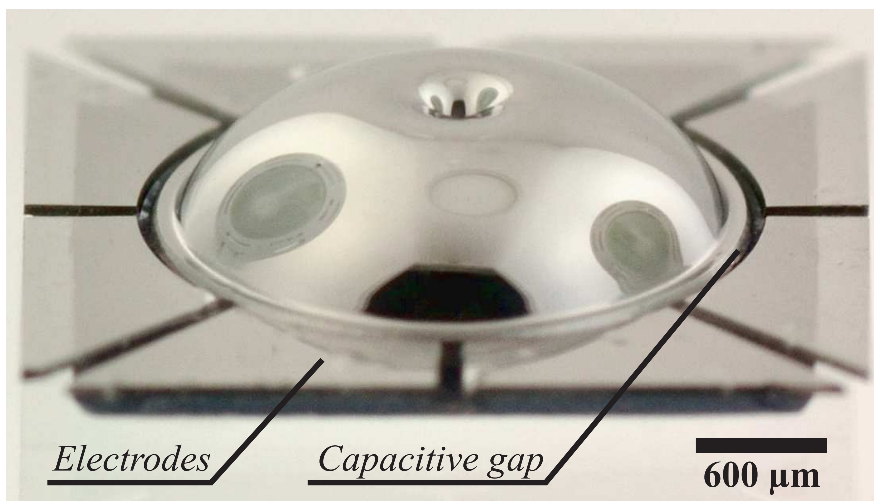

Figure 4.7: Metallized micro-wineglass structure with integrated electrodes. Diameter 4.4 mm, thickness 50 µm.

4.4 Testing & Characterization

In order to experimentally identify the mode shapes associated with different resonant frequencies, the wineglass resonator was excited electrostatically using the integrated electrode structures, Fig. 4.8. The amplitude of motion at different points along the outer perimeter was mapped using Laser Doppler Vibrometry (LDV), creating a representation of the mode-shapes associated with different resonant frequencies, Fig. 4.9. This was accomplished by moving the laser spot along the perimeter while driving the resonator with two different sets of electrode configurations for each degenerate wineglass mode, Fig. 4.10.

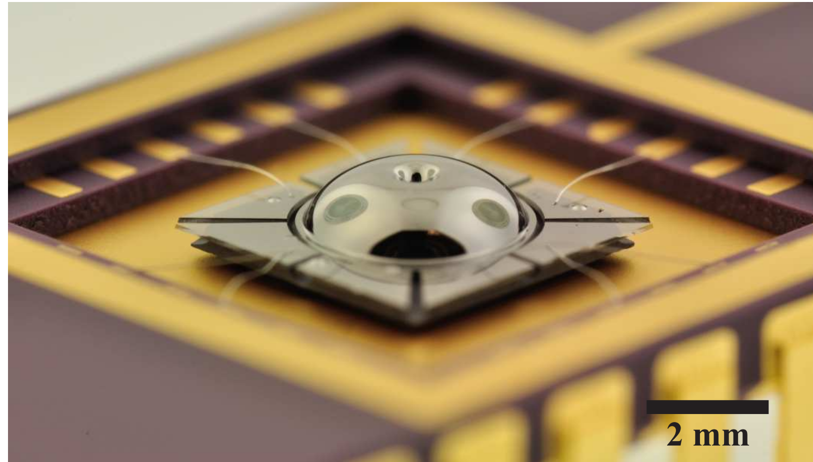

Figure 4.8: Packaged and wirebonded micro-wineglass resonator. Diameter 4.4 mm, thickness 50 µm

For n = 2 wineglass mode, 4 electrodes were used for each degenerate mode with 45° angle between the two electrode sets. Two of the electrodes were driven in anti-phase, this electrode configuration excites the n = 2 wineglass mode selectively, while suppressing all other modes. For n = 3 mode, a single electrode was used for each degenerate wineglass mode. Excitation using a single electrode was necessary, as a balanced excitation using 2 or 4 electrodes inherently suppresses the n = 3 mode. A DC bias voltage of 100 V and an AC drive voltage of 5 V was used in all experiments. Large drive voltages used in this experiment were due to large capacitive gaps of the current prototypes (> 30 µm).

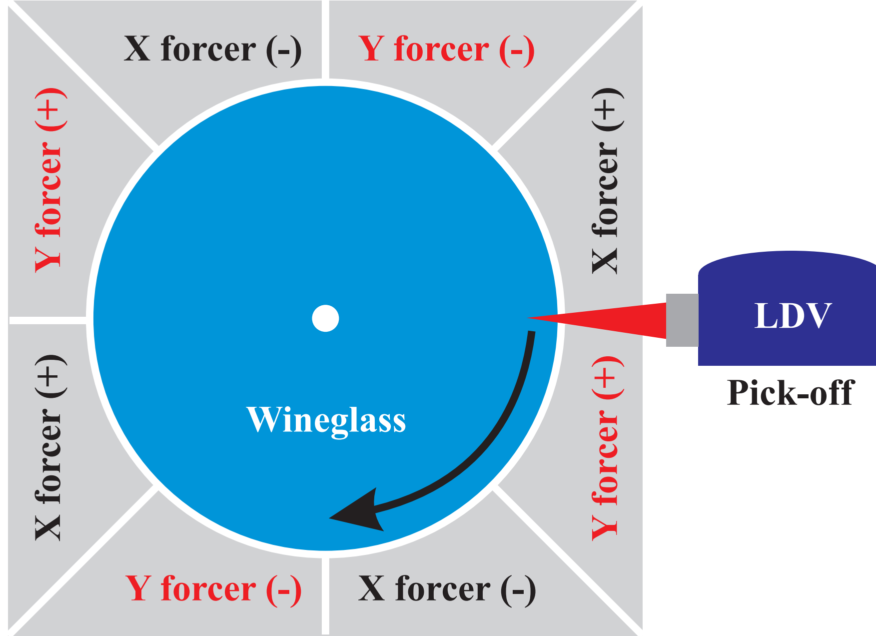

Figure 4.9: Laser Doppler Vibrometer was used to scan along the perimeter of the wineglass to map the mode shapes associated with X forcer and Y forcer electrodes.

For device #1, Table. 4.2 center frequencies of degenerate wineglass modes were identified at 27 389 Hz and 64 583 Hz for n = 2 and n = 3 wineglass modes, respectively, Fig. 4.11. Frequency splits between the two degenerate modes were measured by fitting a second order system response onto the frequency sweep data of each degenerate wineglass mode. For the device #1 highlighted in these measurements, frequency split (Δf) of 0.15 Hz and 0.2 Hz were observed for n = 2 and n = 3 wineglass modes with 95% confidence levels at 0.23 Hz for n = 2 and 0.3 Hz for n = 3, Fig. 4.11. In order to estimate the contribution of electrostatic spring softening effect, DC bias voltage was varied between 20 V - 100 V, frequency split stayed below 1 Hz for both modes, attributing the low frequency split to high structural symmetry and not to capacitive tuning, Fig. 4.12.

In order to verify the repeatability of the results, four other wineglass resonators were characterized using the same method described above. Three of the five wineglass resonators had frequency split less than 5 Hz, one less than 10 Hz for the n = 2 wineglass mode, with one outlier at Δf = ~21 Hz, Fig. 4.13.

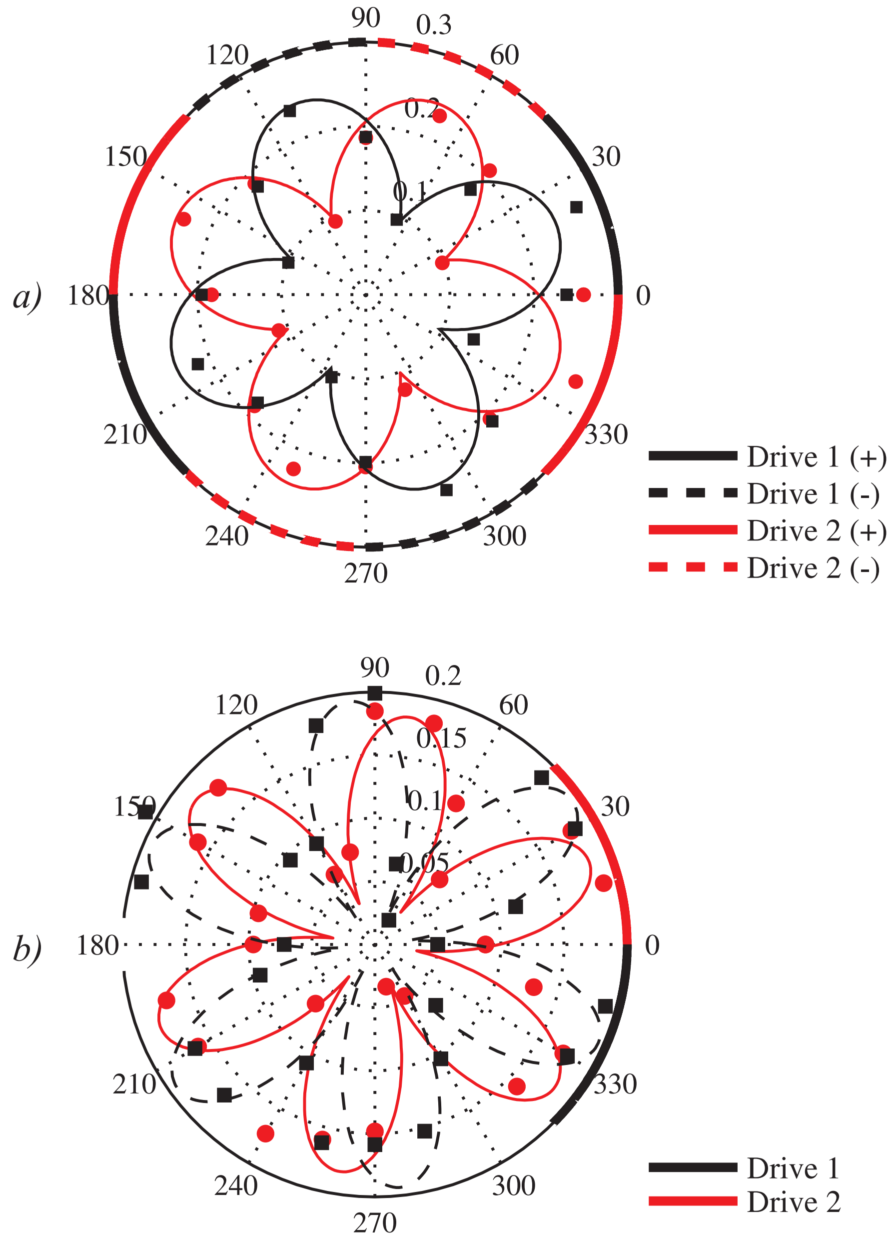

Figure 4.10: Measured velocity amplitude distribution (mm/s) identifying (a) n = 2 and (b) n = 3 wineglass modes.

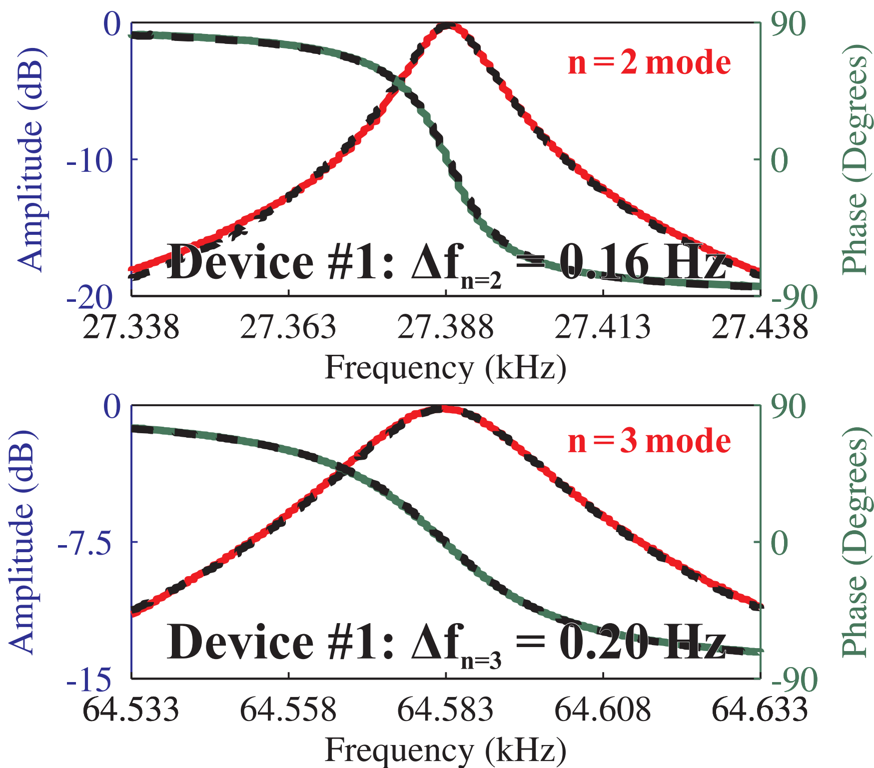

Figure 4.11: Experimental frequency sweeps of n = 2 and n = 3 wineglass modes, showing $\Delta f = 0.16\,\mathrm{Hz}$ and $\Delta f = 0.20\,\mathrm{Hz}$, respectively.

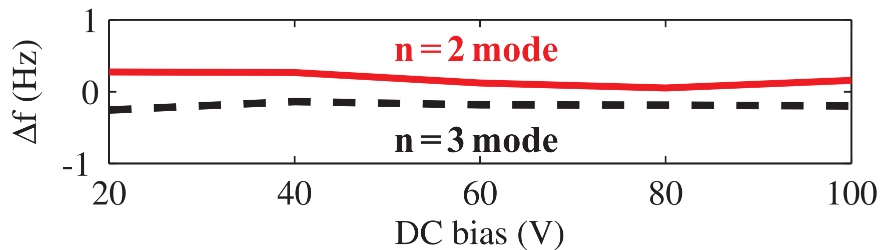

Figure 4.12: Frequency split vs DC bias, showing that the frequency split is within 1 Hz independent of DC bias (DC bias was varied between 20–100 V with 20 V increments).

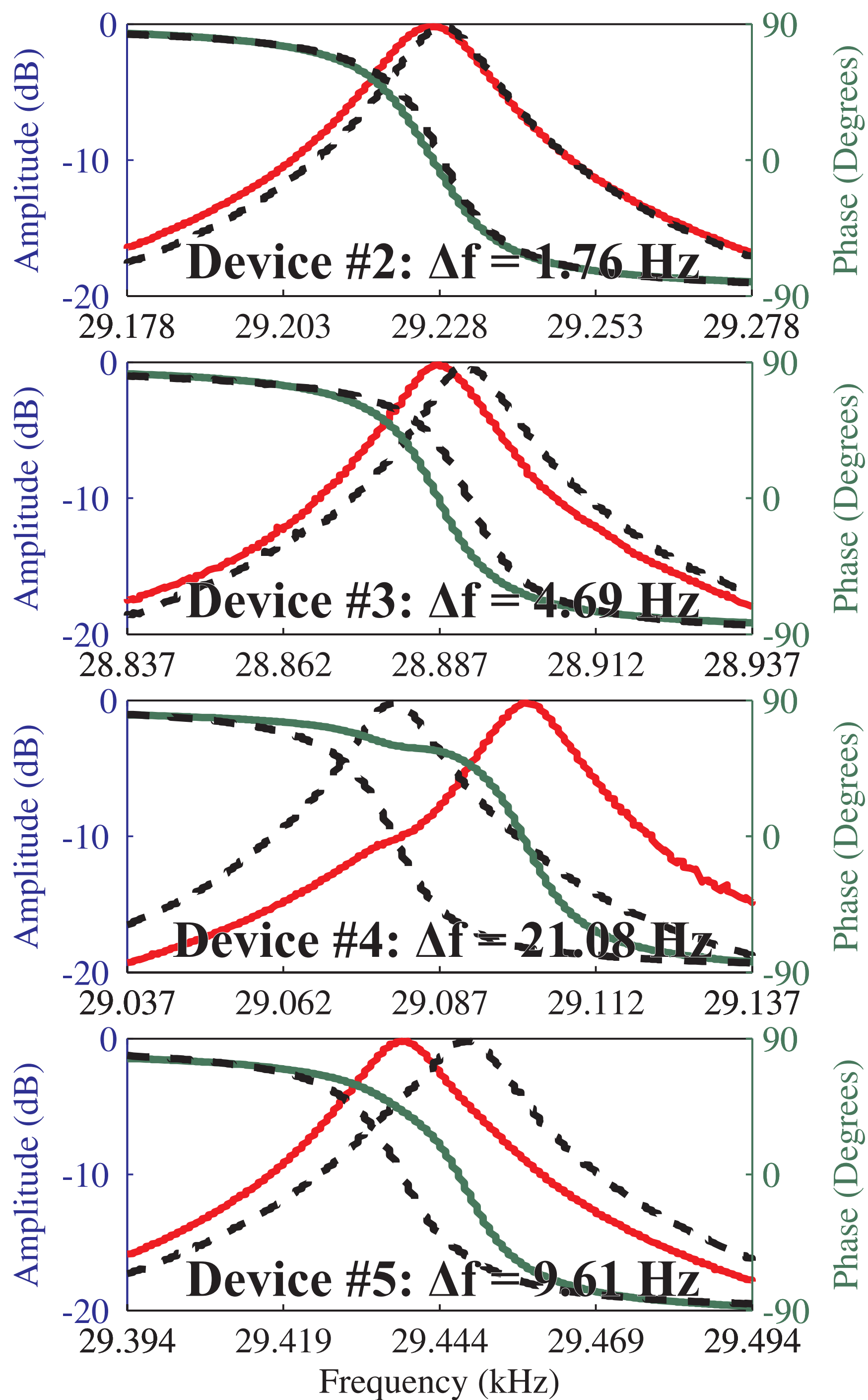

Figure 4.13: Frequency sweeps of n = 2 mode of 4 additional wineglass resonators, showing Δf values in the range of 1.76 Hz to 21.08 Hz.

4.5 Conclusions

Micro-glassblown resonators with integrated electrode structures were fabricated. Electrostatic excitation of micro-glassblown resonators using integrated electrode structures were experimentally demonstrated for the first time. Integrated electrode structures within the glass device layer eliminate the need for additional assembly steps and misalignment errors between the resonator and the electrodes. In addition, by using the same material for the resonator and the electrodes, thermal stress effects due to thermal expansion mismatch are reduced.

Identification of the mode shapes using Laser Doppler Vibrometry revealed frequency splits as low as $\sim < 1$ Hz at ~27 kHz center frequency on device #1, giving a relative frequency split of $\Delta f_{\mathrm{n=2}}/f_{\mathrm{n=2}} < 10$ ppm (or 0.001%). Three of the five wineglass resonators had frequency split less than 5 Hz, one less than 10 Hz for the n = 2 wineglass mode, with one outlier at $\Delta f =$ ~21 Hz, Table 4.2.

Table 4.2: Table summarizing frequency splits and center frequency of 5 different micro-wineglass structures.

Device #	Center Freq. (Hz)	Δf (Hz)	σ (Hz)	$\Delta f/f$ (ppm)
1	27388.65	0.16	0.04	5.67
2	28889.18	4.69	0.05	162.18
3	29227.60	1.76	0.05	60.30
4	29090.38	21.08	0.06	724.65
5	29442.98	9.61	0.07	326.40

The focus of this study was on frequency symmetry of micro-glassblown resonators, for this reason borosilicate glass was used as the resonator material. As expected, low Q-factors (several thousands) were observed due to the high internal dissipation of borosilicate glass. Also, large capacitive gaps were used for electrostatic transduction, due to challenges associated with deep glass dry etching, which required use of high DC bias voltages for

excitation. Future research directions include high-Q materials such as ULE TSG / fused silica for the resonator material as well as smaller capacitive gaps in order to achieve high performance rate-integrating gyroscope operation. ULE TSG / fused silica glassblowing process previously demonstrated by the authors [100, 115] and a high temperature substrate such as tungsten may help achieve the Q-factors required for rate-integrating gyroscope operation. Improved dry etching performance of 7:1 aspect ratio also demonstrated by the authors [105], coupled with a thinner device layer is expected to provide smaller capacitive gaps and improved electrostatic transduction.

These results demonstrate the feasibility of surface tension driven micro-glassblowing process as a means to fabricate extremely symmetric and smooth 3-D wineglass resonators. High structural symmetry ($\Delta f < 1\,\mathrm{Hz}$ and atomically smooth surfaces (0.23 nm Sa) of the resonators may enable new classes of high performance 3-D MEMS devices, such as rate-integrating MEMS gyroscopes and mode-matched angular rate gyroscopes.

Chapter 5

Micro-glassblowing for High Quality Factor

In this chapter, we explore fused silica micro-glassblowing paradigm for fabrication of high Q-factor micro-wineglass gyroscopes through anchor loss mitigation provided by a high aspect ratio, self-aligned glassblown stem structure, careful surface treatment of the perimeter area, and low internal loss fused silica material. In addition, we propose an out-of-plane electrode architecture, to address challenges related to electrode integration with 3-D micro-glassblowing paradigm, due to the high aspect ratio, aspherical resonator element, and high temperature fabrication process (1700 °C).

5.1 Introduction

In Chapter 1, it was shown that maximization of Q-factor is key to enhancing performance of Rate Integrating Gyroscopes. Higher Q-factors not only improve the sensor's noise performance (Angle Random Walk) [48, 49, 116], but also lowers the magnitude of drive signals

(f_{as} and f_{qs} in, Eq. 1.11) required for Amplitude Gain Control, by increasing the energy decay time constant (τ). This reduction in drive signals, result in lower power consumption and more importantly reduces unwanted perturbation of the precession pattern (θ) via the drive signals f_{as} and f_{qs}.

Aside from challenges associated with obtaining a high-Q resonator with low frequency split (Δf), defining electrodes on these 3-D MEMS structures with sufficiently small gaps and uniformity provides an additional challenge for gyroscope operation. For thin film devices this is accomplished by defining electrode structures within the pre-etched cavity by placing a sacrificial layer in between the electrode and the device [71, 76]. For glassblown devices a wide variety architectures have been demonstrated, including deep glass dry etching of the capacitive gaps [114] ($> 30\,\mu m$), utilization of thermal mismatch between the shell and the mold to create the capacitive gaps [88] (~15 µm), and various assembly techniques [103, 117] (~15 µm). Despite these advances, factors such as alignment errors between the shell and the electrodes, cross-talk between electrodes, relatively large gaps created by assembly based techniques and lack of scalability remain a challenge.

In the following sections, we will first present design of out-of-plane architecture and discuss parameters affecting Q-factor in Section 5.2. This will be followed by analytical and finite element models for predicting the final geometry of the micro-glassblown structure in Section 5.3 [118]. In Section 5.4, we will present the fabrication process for fused silica wineglass resonators with out-of-plane electrodes [119–122]. In Section 5.5, we will present frequency and time domain characterization of wineglass resonators. The chapter concludes with a discussion of the results in Section 5.6.

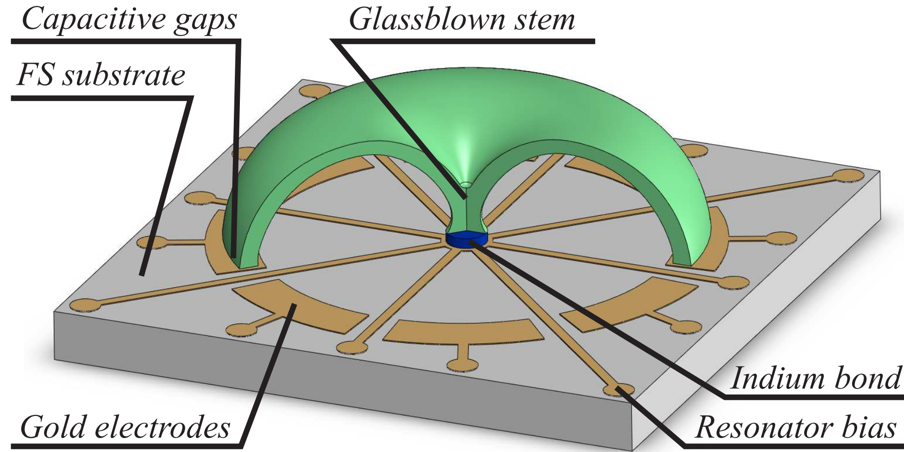

Figure 5.1: Out-of-plane electrode architecture consists of a micro-glassblown fused silica (FS) wineglass resonator and planar Cr/Au electrodes defined on fused silica, enabling batch-fabrication.

5.2 Design

5.2.1 Out-of-plane Electrode Architecture

Wineglass Coriolis Vibratory Gyroscopes (CVGs) typically utilize 8 or more electrodes to drive and sense the primary wineglass modes. One of the main challenges of fabricating micro-wineglass resonators is the definition of electrode structures in a manner compatible with batch-fabrication, Fig. 5.11. 3-D side-walls of the wineglass geometry makes it challenging to fabricate radial electrodes with small capacitive gaps and to keep the gap uniform across the height of the structure. Even though post-fabrication assembly techniques have been successfully demonstrated [103, 117], these approaches create a bottle-neck in batch-fabrication of the devices at wafer level.

In this chapter, we explore an alternative transduction paradigm based on out-of-plane electrode architecture. The architecture consists of a micro-glassblown fused silica wineglass resonator and planar Cr/Au electrodes defined on a fused silica substrate, Fig. 5.1. Out-

of-plane capacitive gaps are formed between the Cr/Au metal traces and the perimeter of the wineglass resonator. Electrostatic transduction is made possible by the 3-D mode shape of the wineglass resonator. In-plane deformation of wineglass modes is accompanied by an out-of-plane deformation, Fig. 5.2. This permits the use of out-of-plane transduction to drive and sense the in-plane oscillations, which are sensitive to coriolis forces along the z-axis of the structure [26].

In our implementation, a total of 8 electrodes are used, which is the minimal configuration to drive and sense the n = 2 wineglass modes. 4 electrodes are designated as forcer (FX and FY) and 4 are designated as pick-off (PX and PY). Both the forcer and pick-off channels have differential pairs (i.e. FX+ and FX-). The resonator is biased using any of the 8 traces that extend from the central anchor point. These traces also help suppress parasitic coupling between adjacent electrodes by sinking stray currents, Fig. 5.3.

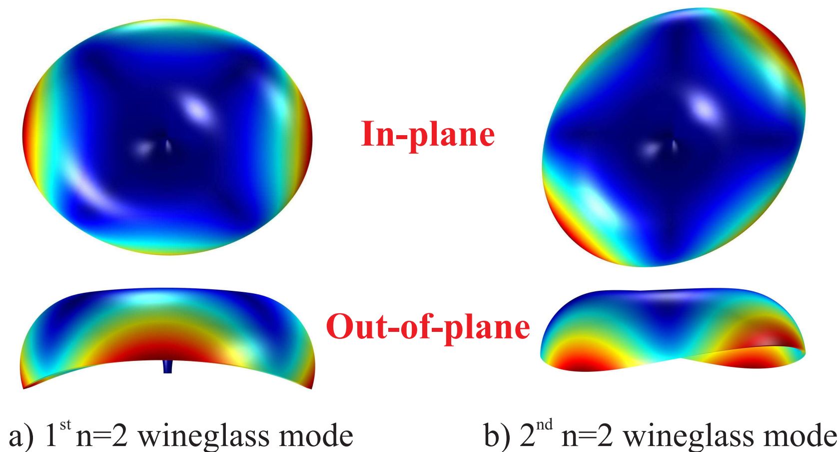

Figure 5.2: Out-of-plane transduction scheme utilizes out-of-plane component of wineglass modes to drive and sense in-plane motion.

As the thickness of the shell limits the maximum surface area for the out-of-plane electrodes, typically a smaller surface area is utilized for capacitive gaps compared to radial electrodes. However, this is offset by the fact that planar nature of the electrode structure, which makes it easier to obtain smaller capacitive gaps and helps to compensate for the loss of surface area. In addition, sacrificial layers and wafer-to-wafer bonding techniques can be used to

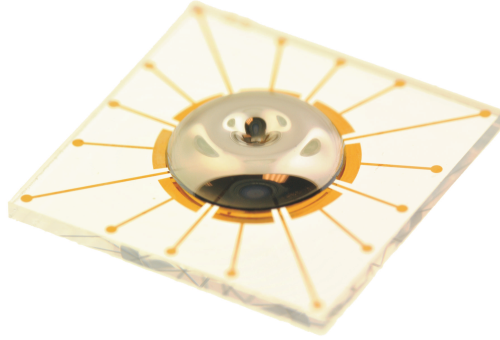

a) Fused silica wineglass with out of plane electrodes. Shell diameter is 3.8 mm.

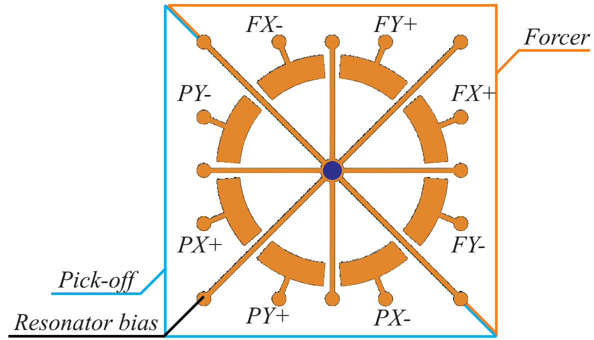

b) Schematic of the out-of-plane electrodes, showing resonator bias, pick-off and forcer electrodes.

Figure 5.3: Electrode configuration: 4 electrodes are designated as forcers (FX and FY) and 4 are designated as pick-off (PX and PY). Both the forcer and pick-off channels have differential pairs (i.e. FX+ and FX-).

define the capacitive gaps, which makes the process very robust to alignment errors, as the gap uniformity is defined by the thickness of the sacrificial layer and not by the wafer to resonator alignment accuracy. Finally, the metal traces for the electrodes can be defined on the same material used for the resonator (i.e. fused silica), providing uniform coefficient of thermal expansion between the electrode die and the resonator.

Another important parameter to consider is the ratio of out-of-plane motion to in-plane motion, which indicates the transduction efficiency of the out-of-plane electrodes. Finite element modeling using Comsol Multiphysics package revealed that, for mushroom type geometries the ratio of out-of-plane motion to in-plane motion is close to 1:1, leading to very efficient out-of-plane transduction, Fig. 5.4.

5.2.2 Optimization of Q-factor

Total Q-factor of the vibratory structure can be calculated from contribution of individual dissipation mechanisms in a manner analogous to solving a parallel resistor network, Eq. 5.1. For this reason the total Q-factor is dominated by the dissipation mechanism with the lowest

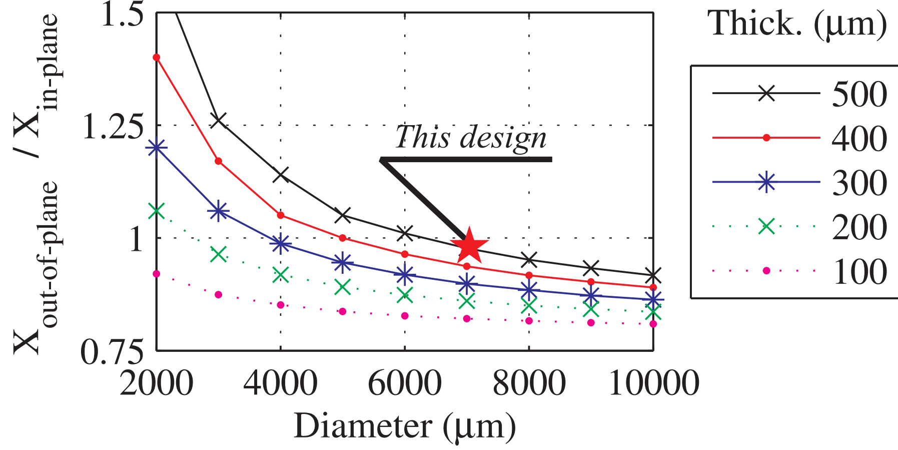

Figure 5.4: Out-of-plane to in-plane displacement ratio for mushroom resonators: Due to the 3-D nature of the resonator, the ratio is close to 1:1. Star marks the design presented in this chapter.

Q-factor (weakest link).

$$Q_{\text{total}}^{-1} = Q_{\text{visc}}^{-1} + Q_{\text{anchor}}^{-1} + Q_{\text{mat}}^{-1} + Q_{\text{surf}}^{-1} + Q_{\text{etc}}^{-1}\,. \tag{5.1}$$

In order to optimize the Q-factor all loss mechanisms affecting the system need to be individually addressed:

- Viscous damping, Q_{visc}, is the most dominant affect with Q-factor of several thousands at atmospheric conditions. However, it can easily be eliminated by operating the device in moderate to high vacuum.
- Anchor losses, Q_{anchor}, are caused by acoustic losses into the substrate and are minimized by decoupling the resonator and the substrate through a self-aligned, solid stem structure, Fig. 5.11.
- Material losses, Q_{mat}, can be divided into several individual loss mechanisms. Thermoelastic dissipation is caused by an interaction between the thermal fluctuations and mechanical oscillations and is minimized by using materials with low coefficient of ther-

mal expansion (CTE), such as fused silica (0.5 ppm/°C). Additional material losses are caused by microscopic effects, such as presence of foreign materials within the matrix of the resonator material and lattice defects at grain boundaries [110]. These effects are minimized by using a high purity, isotropic fused silica material.

- Surface losses, Q_{surf}, are mainly caused by high surface roughness and metallization losses [110]. These effects are minimized through atomically smooth surfaces of micro-glassblown structures [100] and keeping the thickness of the metal layer very small with respect to the resonator shell thickness (50 nm of sputtered Iridium).
- Additional loss mechanisms, Q_{etc}, such as Akheiser dissipation have typically very high Q-factors at kHz range and are not taken into account [123].

5.3 Modeling

In this section, first analytical expressions to predict the final micro-glassblown geometry will be developed. This will be followed by finite element methods to predict thickness of the shell structure and stem diameter.

In micro-glassblowing, the final device geometry heavily depends on the photolithographic pattern on the wafer surface as well as the etch depth of the cavity. For example, solid self-aligned stem structures were obtained for a central post diameter of 400 µm, whereas hollow hemi-toroidal structures were obtained for a central post diameter of 600 µm, Fig. 5.5. For this reason an accurate method to estimate the final geometry from initial dimensions is required.

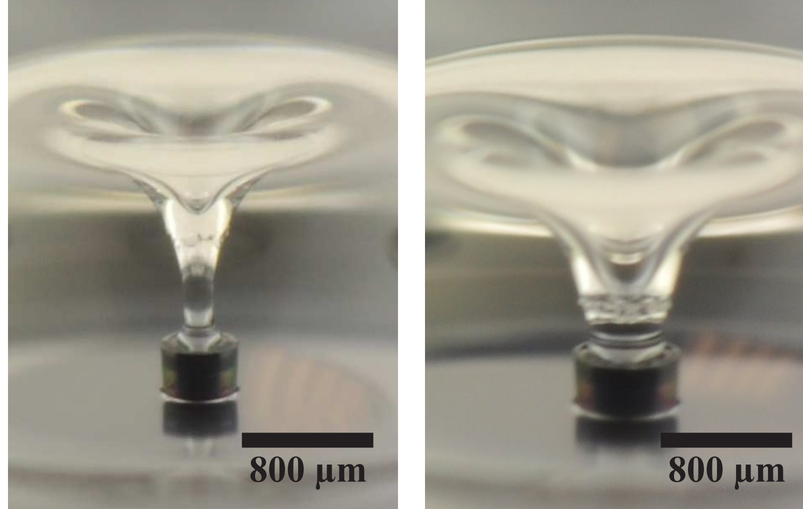

Figure 5.5: Small central post diameters create solid stem structures (left), large diameters create hemi-toroidal structures (right).

5.3.1 Analytical Solution

In this section analytical expressions for predicting the dimensions of the final inverted-wineglass structure are derived [118]. These expressions can be used to calculate height and minor radius of the structure (h and r) based on the initial cavity dimensions. These expressions assume ideal hemi-toroidal shell structures with zero thickness, as such it is not possible to predict the thickness of the wineglass shell or the diameter of the stem structure.

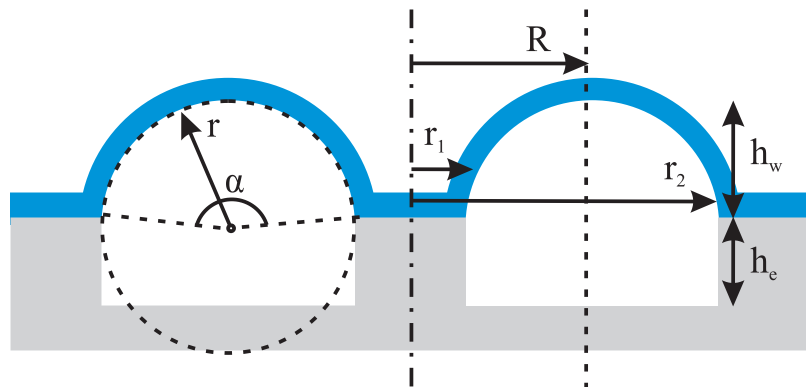

Figure 5.6: Geometric parameters of an inverted-wineglass structure: Minor radius r, major radius R, inner perimeter r_1, outer perimeter r_2, etch depth h_e and wineglass height h_w.

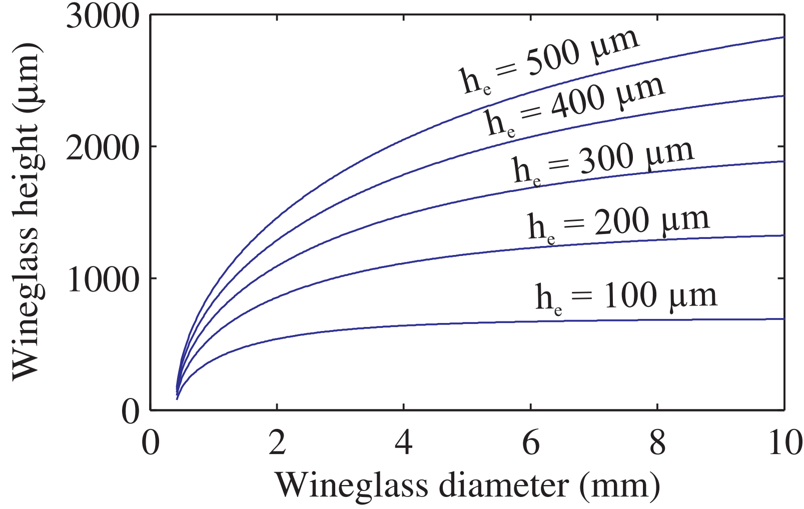

Figure 5.7: Analytical solution of etch depth (h_e), wineglass diameter ($2r_2$) vs final inverted wineglass height. Stem outer diameter ($2r_1$) is 400 µm, glassblowing temperature is 875 °C.

Calculation starts by finding the volume of the etched cavity:

$$V_{cavity} = \pi(r_2^2 - r_1^2)h_e \, , \tag{5.2}$$

where r_2 is the outer perimeter of the cavity, r_1 is the perimeter of the central post, and h_e is the etch depth, Fig. 5.6. Upon heating, air inside the cavity will expand to fill the volume of the wineglass shell. This volume can be calculated using the ideal gas law:

$$V_{wineglass} = (\frac{T_{final}}{T_{initial}} - 1)V_{cavity} \, , \tag{5.3}$$

where $T_{initial}$ and T_{final} are initial and final glass-blowing temperatures in degree Kelvin. It is assumed that the air inside the cavity is at atmospheric pressure, which is also the pressure of the glassblowing chamber. The volume of the wineglass can also be calculated

from geometric parameters using:

$$V_{wineglass} = \pi R r^2(\alpha - \sin(\alpha)) \ , \tag{5.4}$$

where r is the minor radius, R is the major radius of the partial toroid and α is the fullness parameter in radians (central angle of the arc formed by the minor radius), Fig. 5.6. Minor and major radii can be removed from the above expression using:

$$r = \frac{r_2 - r_1}{2\sin(\alpha/2)}, \ R = \frac{r_1 + r_2}{2} \ . \tag{5.5}$$

Substituting (5.2) into (5.3) and (5.5) into (5.4), leaves α to be the only unknown variable, which can be solved numerically. Once α is known, all other parameters of the glassblown shell structure can be extracted using geometric relationships in Fig. 5.6. For example a relationship between minor radius (r), fullness parameter (α) and wineglass height (h_e) can be given as:

$$h_w = r(1 - \cos(\alpha/2)) \ . \tag{5.6}$$

Solutions of these expressions for a large variety of micro-wineglass structures are presented in Fig. 5.7. The expressions presented in this section are not sufficient to calculate the shell thickness or the stem diameter, finite element methods to calculate these parameters will be presented in the next section.

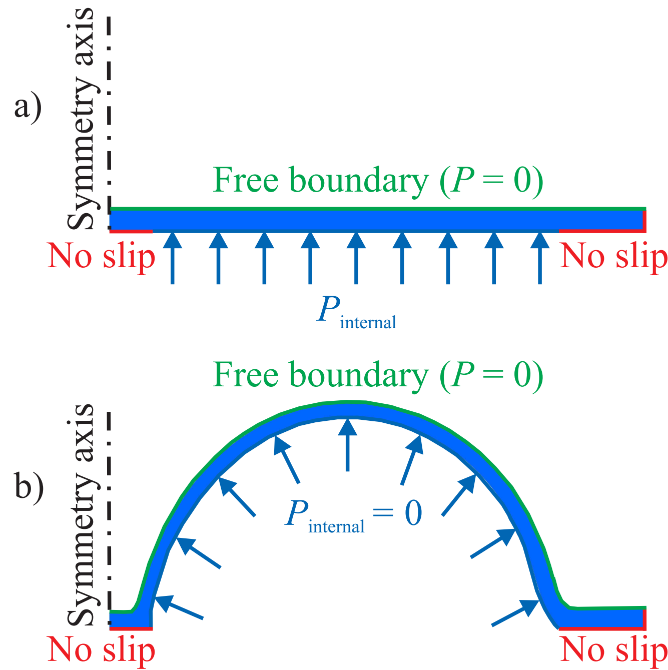

Figure 5.8: Boundary conditions for finite element analysis: (a) before glassblowing, (b) after glassblowing.

5.3.2 Finite Element Analysis

Analytical expressions presented in (5.2) through (5.5) are not sufficient to predict the shell thickness and the stem diameter. For this reason, Finite Element Method (FEM) models for micro-glassblowing process were developed to predict the effect of subtle changes in initial dimensions on the final geometry [118].

Due to the large deformation of the shell structure, Arbitrary Lagrangian-Eulerian (ALE) technique [124, 125] was used. ALE allows the mesh to deform, as to track the deformation of the structure in the time domain and reapply the boundary conditions at every time step. Comsol Multiphysics Package was used for the analysis, the following assumptions were used for boundary conditions:

- At the glassblowing temperature ($> 850\,°C$ for borosilicate glass and $> 1600\,°C$ for fused silica), the deformation of the glass can be modeled using viscous fluid flow with

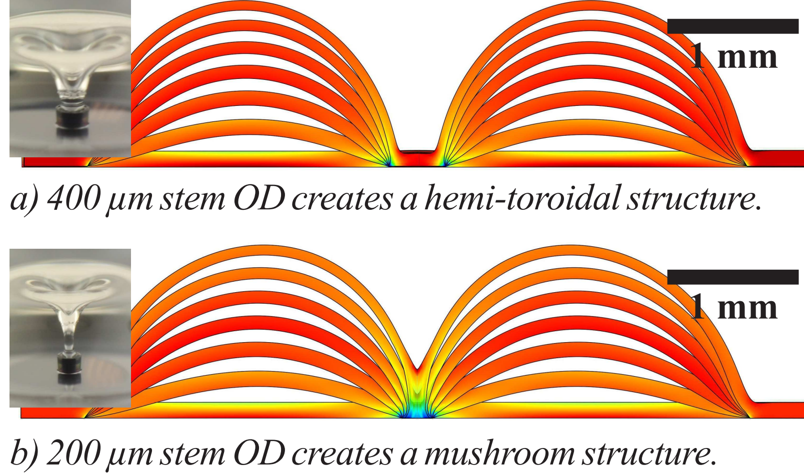

Figure 5.9: Transient FEA of micro-glassblowing process showing the formation of self-aligned stem structures.

a viscosity of 1×10^3 to $1 \times 10^6\,\mathrm{Pa \cdot s}$ [126].

- The driving force is a slowly varying (quasi-static) uniform pressure field within the shell cavity, Fig. 5.8.
- Initial pressure inside the cavity is equal to atmospheric pressure.
- Outer surface of the shell is exposed to atmospheric pressure ($P_{gauge} = 0$).
- The surfaces that are bonded to the substrate are not moving (no-slip condition).
- The shells are axi-symmetric as such a 2-D axi-symmetric model with < 1000 elements is sufficient for solution.

Using the above assumptions, the gauge pressure inside the cavity can be written as:

$$P_{internal} = \frac{T_{final} P_{initial} V_{cavity}}{T_{initial}(V_{cavity} + V_{wineglass})} - P_{initial}\,, \tag{5.7}$$

where T is the temperature in degree Kelvin and $P_{internal}$ is applied uniformly to the inner surface of the micro-wineglass structure during glassblowing, Fig. 5.8.

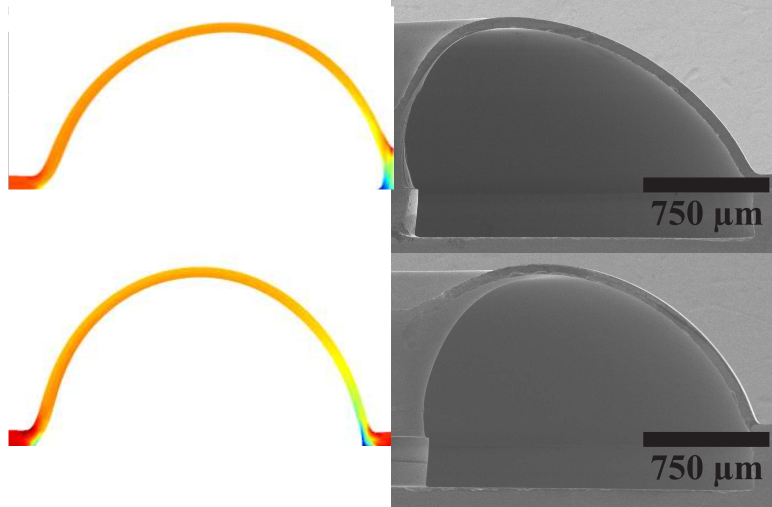

Figure 5.10: Finite elemet predictions and cross-sectional SEM shots of fabricated micro-wineglass structures. SEM images by Dr. M. J. Ahamed [122].

Since the volume of the wineglass will continuously change during the transient solution, (5.4) can not be used to calculate $V_{wineglass}$. Instead, a surface integral for the inner surface of the wineglass is used:

$$V_{wineglass} = \oint 2\pi r'^2 dnr \ , \tag{5.8}$$

where r' is the distance of any point in the shell structure from the symmetry axis and dnr is the projection of the infinitesimal surface area onto the symmetry axis. (5.8) allows continuous calculation of the shell volume and consequently the cavity pressure as the structure deforms. This allows the model to reach equilibrium when the final volume is reached ($P_{internal} = 0$).

Fig. 5.9 shows time domain solution of the micro-glassblowing process and the formation of the self-aligned stem structure. Decreasing the central post diameter from 400 µm to 200 µm is sufficient to change the shell structure from a hemi-toroidal geometry to an inverted-wineglass with a solid stem structure. Fig. 5.10 shows a side-by-side comparison of the finite element models and the actual fabricated geometries. The results from the models are

compared to cross-sectional SEM shots in Table 5.1, showing ~20% accuracy for device #1 and better than 10% accuracy for device #2 in prediction of final geometry for device. This small variation is attributed to variation in furnace temperature from assumed values.

Table 5.1: Comparison of wineglass dimensions obtained from analytical solutions, FEA and experiments.

			Device # 1	Device # 2
Initial thickness		(µm)	80	300
Outer diameter		(mm)	4.2	4.2
Etch depth		(µm)	240	200
Glassblowing temperature		(°C)	875	1700
Analytical	Final Height	(µm)	971	1182
	Thickness	(µm)	N/A	N/A
FEA	Final Height	(µm)	1025	1260
	Thickness	(µm)	52	205
Experimental	Final Height	(µm)	832	1288
	Thickness	(µm)	44	229

5.4 Fabrication

Fabrication process utilizes two wafers: a wineglass shell wafer and an electrode wafer. Fabrication process starts with LPCVD poly-silicon deposition on 1 mm thick fused silica wafers of up to 2 µm thickness. The poly-silicon mask is later patterned lithographically and is used to etch cavities into fused silica wafers down to ~300 µm in depth. Once the etch is complete, the poly-silicon mask is removed using a 45% KOH bath. The next step of the fabrication process is plasma assisted fusion bonding of a 500 µm thick fused silica device layer (Corning 7980) [100], Fig 5.13(a). The plasma assisted fusion bonding process for bonding fused silica wafer pairs can be summarized as follows:

1. Cleaning of the wafer pair using solvent and RCA clean,

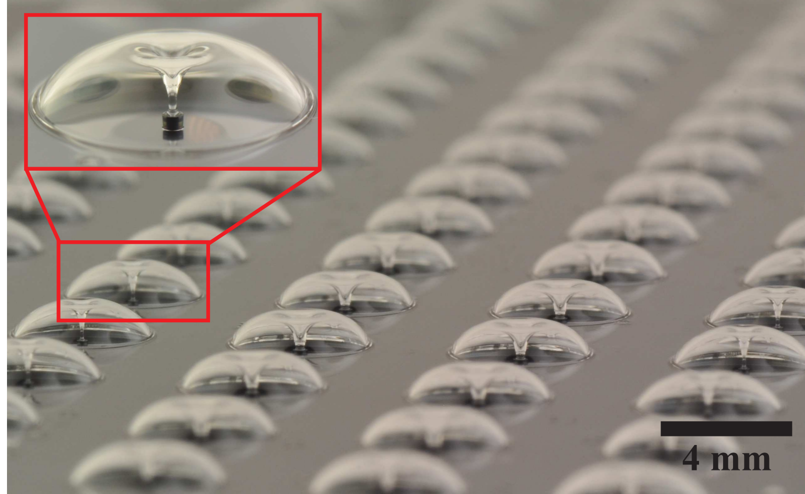

Figure 5.11: Micro-glassblowing process can create arrays of inverted-wineglass structures on the wafer surface. Outer diameter of shells is $\sim$ 4 mm, over 100 Borosilicate Glass (BSG) shells were fabricated on a 100 mm wafer.

2. Plasma activation using oxygen plasma (50 W power for 2 minutes, 24 sccm O2 flow),
3. DI water rinse followed by N2 dry,
4. Contacting of the activated surfaces,
5. Room temperature anneal for $>$ 48 hours,
6. Curing the wafer stack at 400 °C for 6 hours.

The bond creates a seamless hermetic seal around the etched cavities without using any intermediate material. The glassblowing is performed at 1700 °C for 2 minutes and rapidly cooled to room temperature, Fig 5.13(b). During glassblowing the device layer at the central post merges to create a solid, self-aligned stem structure, critical for high-Q operation. Shells are released by back-lapping the wafer stack to release using an Allied Multiprep 12" lapping system, Fig 5.13(c). A series of diamond lapping films with descending grit size of 30 µm $\Rightarrow$ 6 µm $\Rightarrow$ 3 µm $\Rightarrow$ 1 µm $\Rightarrow$ 0.5 µm $\Rightarrow$ 0.1 µm are used for lapping, followed by final polish using 50 nm colloidal suspension and polishing cloth. Interior surface of the wineglasses is metallized with 50 nm thick sputtered Iridium. Only the interior surface is metallized to

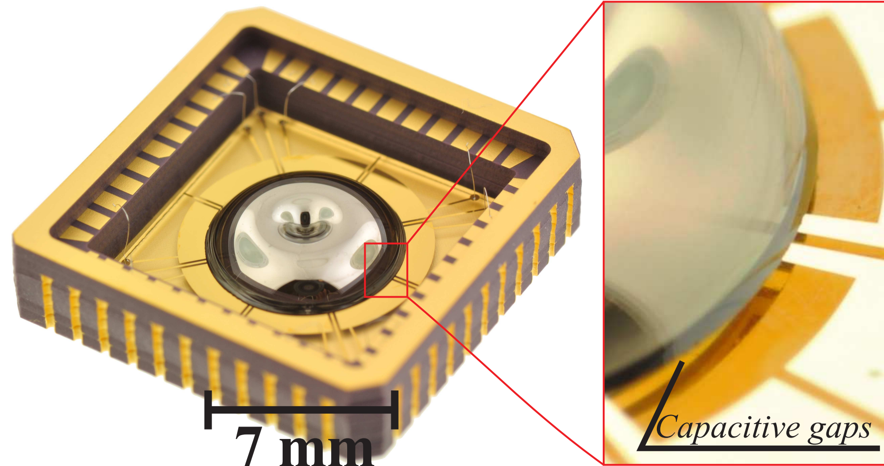

Figure 5.12: 1 million Q-factor fused silica wineglass structure with integrated electrodes (left), close-up of capacitive gaps (right).

minimize the influence of the metal film on the shell resonator. Metallization is performed on a two axis planetary stage for film uniformity, in which the wafer is continuously rotated along z-axis and oscillated ±15 °C along x-axis.

Fused silica out-of-plane electrode structures are fabricated on a separate wafer by blanket coating with Cr/Au (100 nm / 500 nm), spinning a thin layer of photo-resist sacrificial layer and patterning the Cr/Au features using etch-back. In this process, the photoresist is used both to pattern the electrodes and as a sacrificial layer to create the capacitive gaps. Subsequently, lapped and metalized wineglass wafer is bonded to the out-of-plane electrode wafer at the stem of each wineglass using low out-gassing epoxy, Ablebond JM7000 or Indium, Fig 5.13(d). Once the bonding is complete, the sacrificial layer is removed to release the inverted wineglass structures around their perimeter, Fig 5.13(e), creating capacitive gaps between the metalized inverted wineglass structures and the Cr/Au electrodes, Fig 5.14.

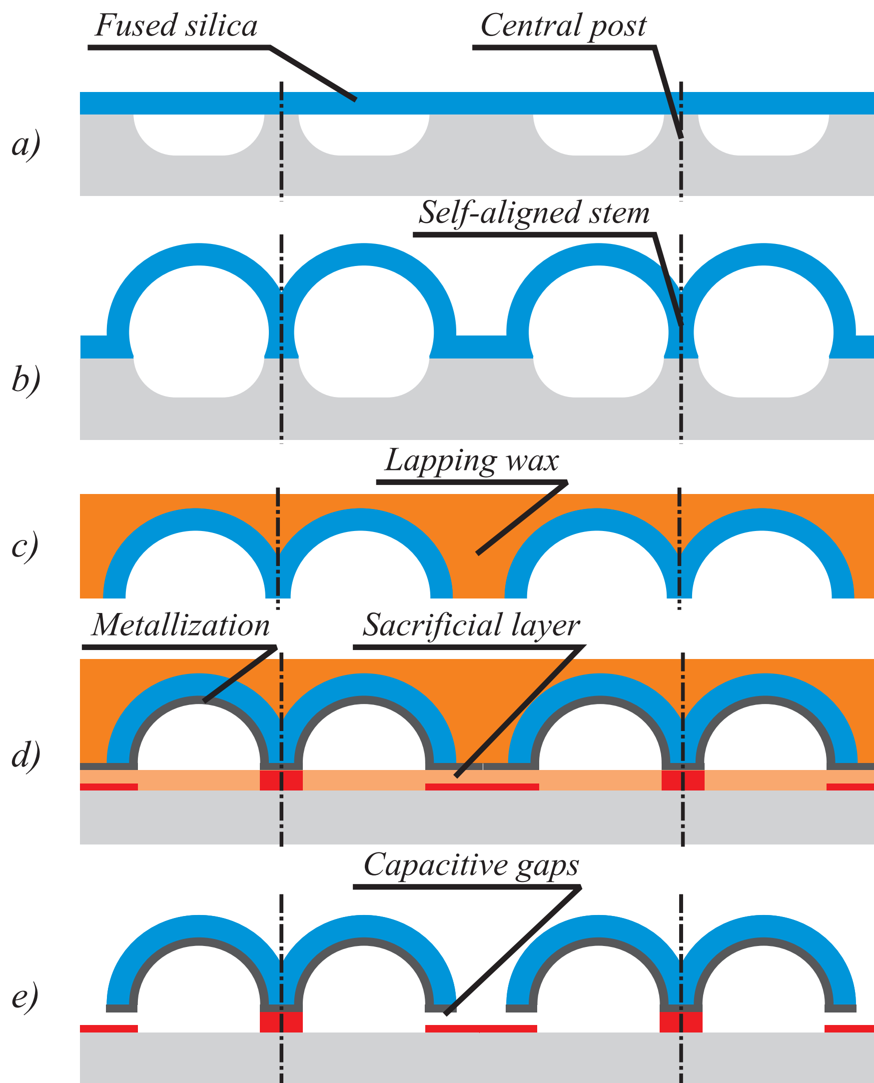

Figure 5.13: Wafer-level fabrication process for fused silica micro-wineglass structures: (a) plasma bonding of device layer to substrate with pre-etched cavities, (b) micro-glassblowing at 1700 °C, (c) removal of the substrate via back-lapping, (d) bonding the wineglass wafer to electrode wafer, (e) removal of the sacrificial layer to form capacitive gaps.

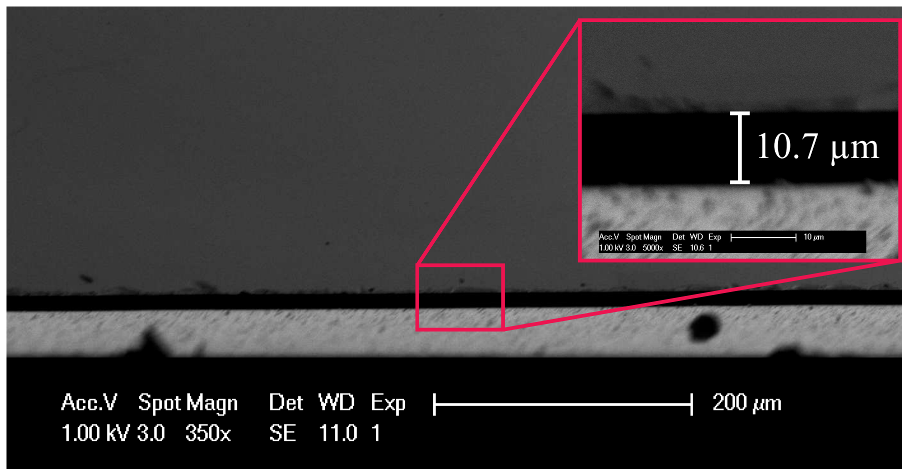

Figure 5.14: Uniform 10 µm capacitive gaps have been demonstrated on 7 mm shell structures, resulting in over 9 pF total active capacitance on the device.

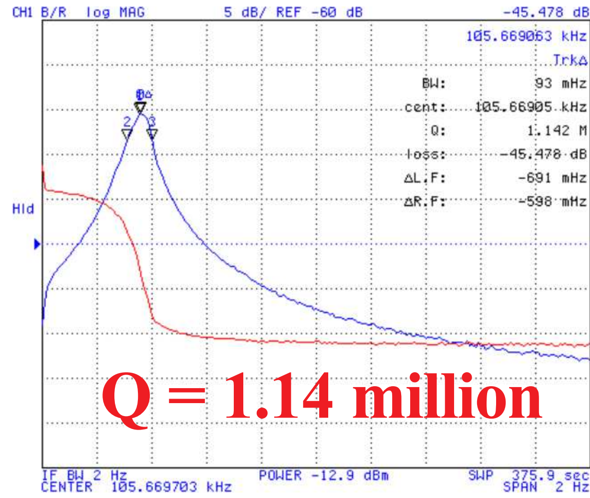

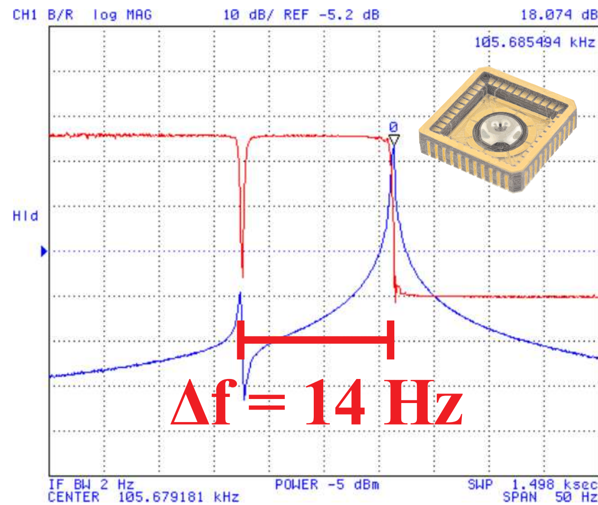

Figure 5.15: Frequency sweep revealed a Q-factor of 1.14 million and as fabricated frequency split (Δf) of 14 Hz at 105 kHz center frequency. The chamber pressure was 19 µTorr during the frequency sweep.

5.5 Experimental Results

Frequency sweep using out-of-plane electrodes with ~30 µm capacitive gaps revealed Q-factor of 1.14 million and frequency split of 14 Hz at a center frequency of 105 kHz ($\Delta f/f$ = 132 ppm), Fig. 5.15. Frequency sweep using the same set of forcer and pick-off electrodes showed an amplitude difference of ~30 dB between the two modes, indicative of misalignment between the electrodes and the principle axis of elasticity and/or quadrature coupling between the two modes. A separate ring down experiment was performed where the device was excited with a narrow bandwidth swept sine-wave impulse and resonator output during free vibration was recorded. Ring down experiment demonstrated a time constant of 3.18 seconds and Q-factor of 1.05 million, confirming the frequency sweeps, Fig. 5.16. In order to observe the effect of viscous damping on the overall Q-factor, the frequency sweep was repeated at different pressure levels. Q-factor of 1 million was obtained below < 20 µTorr, Fig. 5.17. No further improvement in Q-factor was observed at 15 µTorr. Subsequently, capacitive gaps as low as 10 µm have been demonstrated on other 7 mm shells, resulting in over 9 pF of total active capacitance within the device (Total dC/dX of 970 nF/m), Fig 5.14.

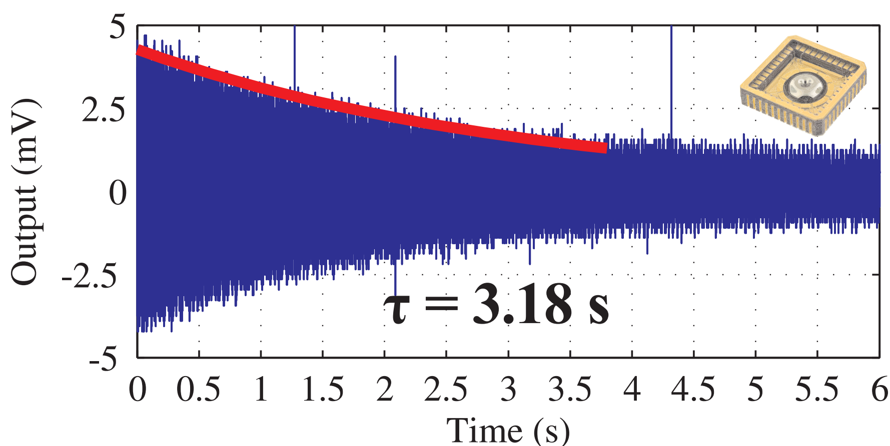

Figure 5.16: Ring-down experiment at 19 µTorr shows $\tau = 3.18$ s, giving 1.05 million Q-factor at 105 kHz, confirming the frequency sweep.

5.6 Conclusions

Micro-glassblown fused silica wineglass resonators with out-of-plane electrode structures have been fabricated. Q-factor over 1 million, on both degenerate wineglass modes, and high frequency symmetry ($\Delta f/f$) of 132 ppm have been experimentally demonstrated at a compact size of 7 mm diameter, Table 5.2. In addition, out-of-plane capacitive transduction on MEMS wineglass resonators with 10 µm capacitive gaps have been demonstrated for the first time.

Table 5.2: Summary of device parameters for a 7 mm fused silica wineglass resonator.

Shell diameter	7 mm
Shell thickness	~500 µm
Effective mass	8 µg
Quality factor	$>$ 1million
Center frequency	105 kHz
Frequency split (Δf)	14 Hz

Even though a fairly low frequency split of 14 Hz (132 ppm) was measured, this number is larger than previously reported 0.16 Hz (5.67 ppm) on dry etched borosilicate glass wineglass structures [114]. The increase in frequency split is attributed to the introduction of back-lapping process, which can induce asymmetry in the structure due to edge roughness. High performance degenerate mode gyroscope operation requires an even higher degree of symmetry in order to leverage the high Q-factors seen on 3-D fused silica wineglass resonators. Further improvement in the back-lapping process and addition of post-lapping surface treatment steps might help improve the structural symmetry further.

Low internal dissipation of fused silica combined with high structural symmetry of MEMS micro-glassblowing paradigm may enable batch-fabrication of high performance fused silica wineglass gyroscopes on a wafer surface at a significantly lower cost than their precision-machined macro-scale counterparts.

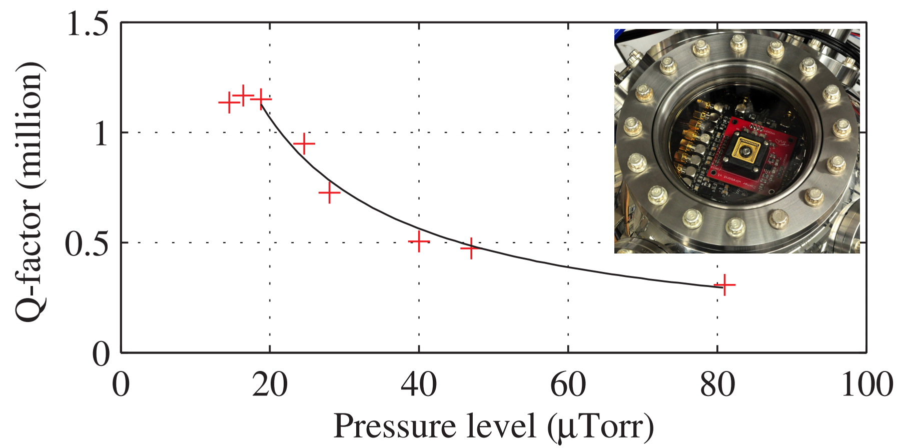

Figure 5.17: Q-factor vs pressure level experiment. Q-factors above 1 million were obtained below 20 µTorr.

Chapter 6

Parametrically Driven Toroidal Ring Gyroscope

In this chapter, a new 2-D silicon Toroidal Ring Gyroscope (TRG) architecture is presented to serve as a test-bed for various MRIG control strategies. A closed-loop control system for electronic compensation of structural imperfections, such as aniso-elasticity and damping, is also introduced, along with first demonstration of a parametrically driven Micro Rate Integrating Gyroscope.

6.1 Introduction

In contrast to axi-symmetric designs with central support structures, such as [36, 40, 46, 127], we explore an alternative support structure for anchor loss minimization. The vibrational energy in the introduced design is concentrated towards the innermost ring, and the device is anchored at the outer perimeter, Fig. 6.1. The distributed support structure prevents vibrational motion propagating to the outer anchor, which helps trap the vibrational energy

within the gyroscope [128].

In addition, we explore parametric drive of Toroidal Ring Gyroscope during rate integrating operation for reduction of drifts induced by drive electronics. In contrast to the conventional amplitude control architecture, the central star electrode of the gyroscope, connected to a single drive channel was utilized for amplitude control of both modes. Due to the parametric pumping effect, energy added to each (x and y) mode is proportional to the existing amplitude of the respective mode. As a result, errors associated with finding the orientation of the standing wave and x-y drive gain drift are bypassed. Compared to conventional x-y drive architecture, as high as 14x improvement in scale factor stability was observed with parametric pumping, resulting in better than 20 ppm scale factor stability without any compensation or temperature stabilization [129].

In Section 6.2, we will present design of Toroidal Ring Gyroscope. The implementation of the closed-loop control system for Whole Angle mechanization and parametric drive is presented in Section 6.3. This will be followed by experimental characterization of the mechanical element, rate and Rate Integrating Gyroscope operation in Section 6.4. The chapter concludes with a discussion of the results in Section 6.5.

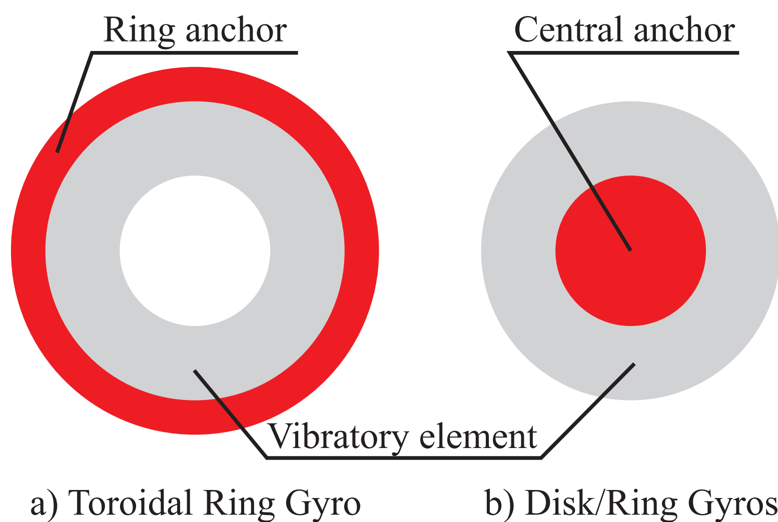

Figure 6.1: Toroidal Ring Gyroscope (a) consists of an outer anchor that encircles the device, as opposed to axi-symmetric devices with cenral support structures (b).

6.2 Design

Toroidal ring gyroscope consists of an outer anchor that encircles the device, a distributed ring support structure and an inner electrode assembly, Fig. 6.2. As opposed to axi-symmetric devices with central support structures [36, 40, 46, 127], vibration energy is concentrated at the innermost ring, Fig. 6.3. The distributed support structure decouples the vibrational motion from the substrate, Fig. 6.3. This decoupling mitigates anchor losses into the substrate and prevents die/package stresses from propagating into the vibratory structure.

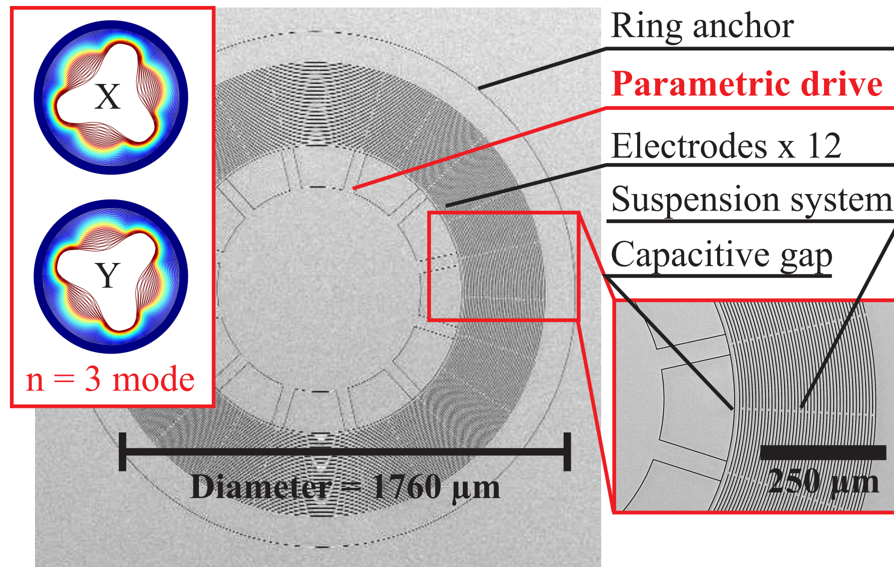

Figure 6.2: A 100k Q-factor, epitaxial silicon encapsulated Toroidal Ring Gyroscope was used in the experiments. Device consists of an outer ring anchor, distributed suspension system and an inner electrode assembly. SEM image by Micro Structures & Sensors Lab at Stanford (Prof. Kenny 's Group) [129].

6.2.1 Fabrication

The Toroidal Ring Gyroscope (TRG) was fabricated using a wafer-level epitaxial silicon encapsulation process (EpiSeal) [130]. EpiSeal process utilizes epitaxially grown silicon to

seal the device layer at extremely high temperatures, which results in an ultra-clean wafer-level seal. This results in high vacuum levels (as low as 1 Pa) without the need for getter materials for absorption of sealing by-products. The epi-seal encapsulation process was proposed by researchers at the Robert Bosch Research and Technology Center in Palo Alto and then demonstrated in a close collaboration with Stanford University. This collaboration is continuing to develop improvements and extensions to this process for many applications, while the baseline process has been brought into commercial production by SiTime Inc.

The device was fabricated on single-crystal ⟨100⟩ silicon wafers. For this reason device was designed to operate in n = 3 wineglass modes instead of the more commonly used lower order n = 2 wineglass modes, Fig. 6.3. This eliminates frequency split induced by anisotropic modulus of elasticity of crystalline silicon and makes the frequency splits (Δf) insensitive to misalignment errors in crystalline orientation of the silicon wafer. The draw-back of operation in n = 3 modes are slightly lower angular gain factor, higher resonance frequency and smaller amplitude of motion.

The device was fabricated on a 2 mm × 2 mm die, the mechanical element has an outer diameter of 1760 µm and was fabricated on a device layer thickness of 40 µm, Table 6.1. The suspension system consists of 44 concentric rings. The rings are connected to each other using 12 spokes between the rings, the spokes are interleaved with an offset of 15° between two consecutive rings. The suspension rings have a thickness of 5 µm. The innermost ring is designed to have a slightly higher ring thickness of 8.5 µm, this mitigates the effect of spokes on the overall mode shape and helps retain a truer wineglass shape at the electrode interface.

6.2.2 Electrode Architecture

Electrode assembly is located at the center of the gyroscope and consists of twelve discrete electrodes and one central star electrode, Fig. 6.4. Discrete electrodes are distributed in

Table 6.1: Summary of geometric parameters.

Device diameter	(µm)	1760
Device layer thickness	(µm)	40
Capacitive gaps	(µm)	1.5
Ring thickness	(µm)	5
Innermost ring thickness	(µm)	8.5
Number of rings		44

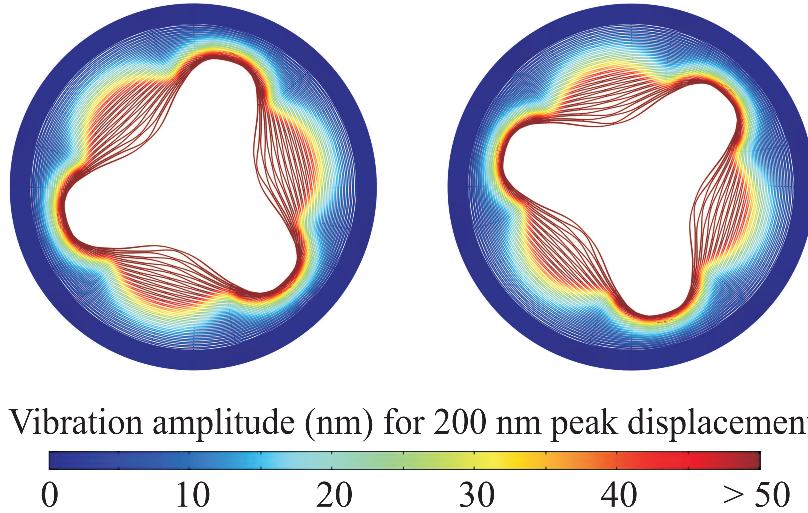

Figure 6.3: Due to the distributed suspension system vibrational energy is trapped within the gyroscope.

groups of six onto the two degenerate wineglass modes. Out of six electrodes, two electrodes were used as a forcer and four as a pick-off for each mode, giving a total of four forcer and eight pick-off electrodes across the gyro.

In this work, the central star-shaped electrode is used for parametric pumping. Due to the twelve-pointed circular nature of this electrode, parametric pumping has equal contribution to the both degenerate n = 3 wineglass modes.

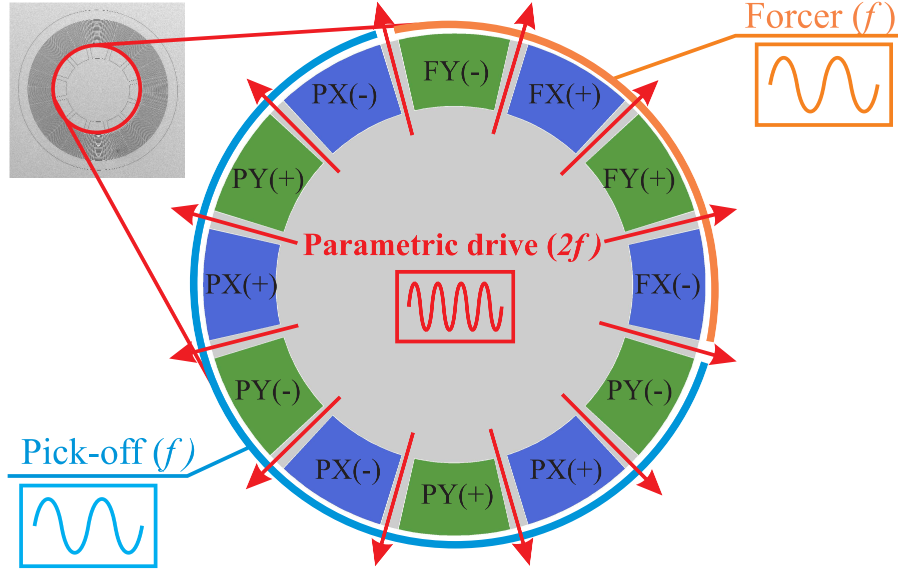

Figure 6.4: Central electrode assembly consists of 12 discrete electrodes, divided into 4 drive and 8 pick off electrodes, and one star shaped parametric electrode.

6.2.3 Parametric Drive

All axi-symmetric MEMS gyroscope architectures are capable of whole angle mechanization. Typically, these architectures utilize two sets of drive electrodes for the two resonant modes of the gyroscope. As a result, amplitude control in whole angle mechanization would require finding the orientation of the standing wave and pumping energy along this direction using two sets of drive electrodes (vector drive). However, this method is susceptible to drift due to gain unbalance in drive electronics, errors in calculating the angle of the standing wave, as well as, the time delay between estimation of the standing wave and the actual amplitude command.

In this section, we explore parametric drive for amplitude control of MEMS rate integrating gyroscopes, which has previously been reserved for high performance macro-scale Vibratory Gyros [2]. In contrast to conventional amplitude control, a single drive channel connected to the central star electrode of the gyroscope was utilized for amplitude control of both modes (scalar drive). Even though a single drive channel is used, due to the parametric pumping

effect, energy added to each (x and y) mode is proportional to the existing amplitude of the respective mode. This permits amplitude control of the standing wave at any arbitrary angle with minimal amount of perturbation. The scalar nature of the amplitude controller helps bypass errors associated with finding the orientation of the standing wave, time delay in the calculation, and x-y drive gain drift.

For the, parametric drive, a secondary numerically controlled oscillator (NCO) is used to generate a sine wave at twice the PLL frequency. This signal is applied to the central star-shaped electrode to parametrically pump energy in x-y plane at twice the resonance frequency, Fig 6.5. Due to the parametric pumping effect, energy added to each (x and y) mode is proportional to the existing amplitude of the respective mode [12]:

$$\ddot{x} + \frac{\omega_x}{\mathrm{Q}_x}\dot{x} + \left(\omega_x^2 + \frac{F_p}{m_{eq}}\sin(2\omega t + \phi_p)\right)x = \frac{F_x}{m_{eq}} sin(\omega t + \phi_f) + 2\eta\dot{y}\Omega_z \, , \tag{6.1}$$

$$\ddot{y} + \frac{\omega_y}{\mathrm{Q}_y}\dot{y} + \left(\omega_y^2 + \frac{F_p}{m_{eq}}\sin(2\omega t + \phi_p)\right)y = \frac{F_y}{m_{eq}} sin(\omega t + \phi_f) - 2\eta\dot{x}\Omega_z \, , \tag{6.2}$$

where ω_x, ω_y are the resonance frequencies and $\mathrm{Q_x}$, $\mathrm{Q_y}$ are the Q-factors of the two degenerate modes, m_{eq} is the equivalent mass of the vibratory system, η is the angular gain factor, ω is the drive frequency and ϕ_p, ϕ_f are the phase of the parametric and vector drives respectively.

This creates a preferential direction of pumping along the orientation of the standing wave without the need for any coordinate transformation around θ:

$$\theta = \arctan\left(\frac{y}{x}\right) \, . \tag{6.3}$$

An additional benefit of parametric drive of MEMS gyroscopes is the minimization of the electrical feed-through between the actuation and pick-off channels [131]. For a conventional MEMS gyroscope, actuation and pick-off signals occur at the same frequency. Any

feed-through from the actuation signal will corrupt the pick-off channel, lowering overall performance of the system. Parametric drive mitigates this problem by separating the frequency of drive and pick-off channels. Since parametric drive frequency is a multiple of systems drive frequency, the electrostatic feed-through into the sense channel can be filtered out.

6.3 Control System

A hybrid FPGA/micro-controller control system was developed for whole-angle gyro control. The control system is responsible for driving the gyroscope to constant amplitude, suppressing the quadrature error, tracking/controlling the orientation of the precession pattern.

The key component of this approach is a phase locked loop (PLL) that tracks the gyro motion at any arbitrary pattern angle as opposed to locking onto one of the primary gyro axis, Fig. 6.5. Once the PLL lock is established, the FPGA demodulates in-phase and in-quadrature signals from x and y channels. From these demodulated signals the slow moving variables: amplitude (E), quadrature error (Q), and pattern angle (θ) can be extracted using the equations [10]:

$$\mathrm{E} = \mathrm{c_x^2 + s_x^2 + c_y^2 + s_y^2}\ , \tag{6.4}$$

$$\mathrm{Q} = 2(\mathrm{c_x s_y - c_y s_x})\ , \tag{6.5}$$

$$\mathrm{R} = \mathrm{c_x^2 + s_x^2 - c_y^2 - s_y^2}\ , \tag{6.6}$$

$$\mathrm{S} = 2(\mathrm{c_x c_y + s_x s_y})\ , \tag{6.7}$$

$$\mathrm{L} = \mathrm{c_x^2 - s_x^2 + c_y^2 - s_y^2 + 2i(c_x s_x + c_y s_y)}\ , \tag{6.8}$$

where E is a measure of energy within the system and is used for amplitude stabilization. Q is the measure of quadrature error, independent of drive orientation.

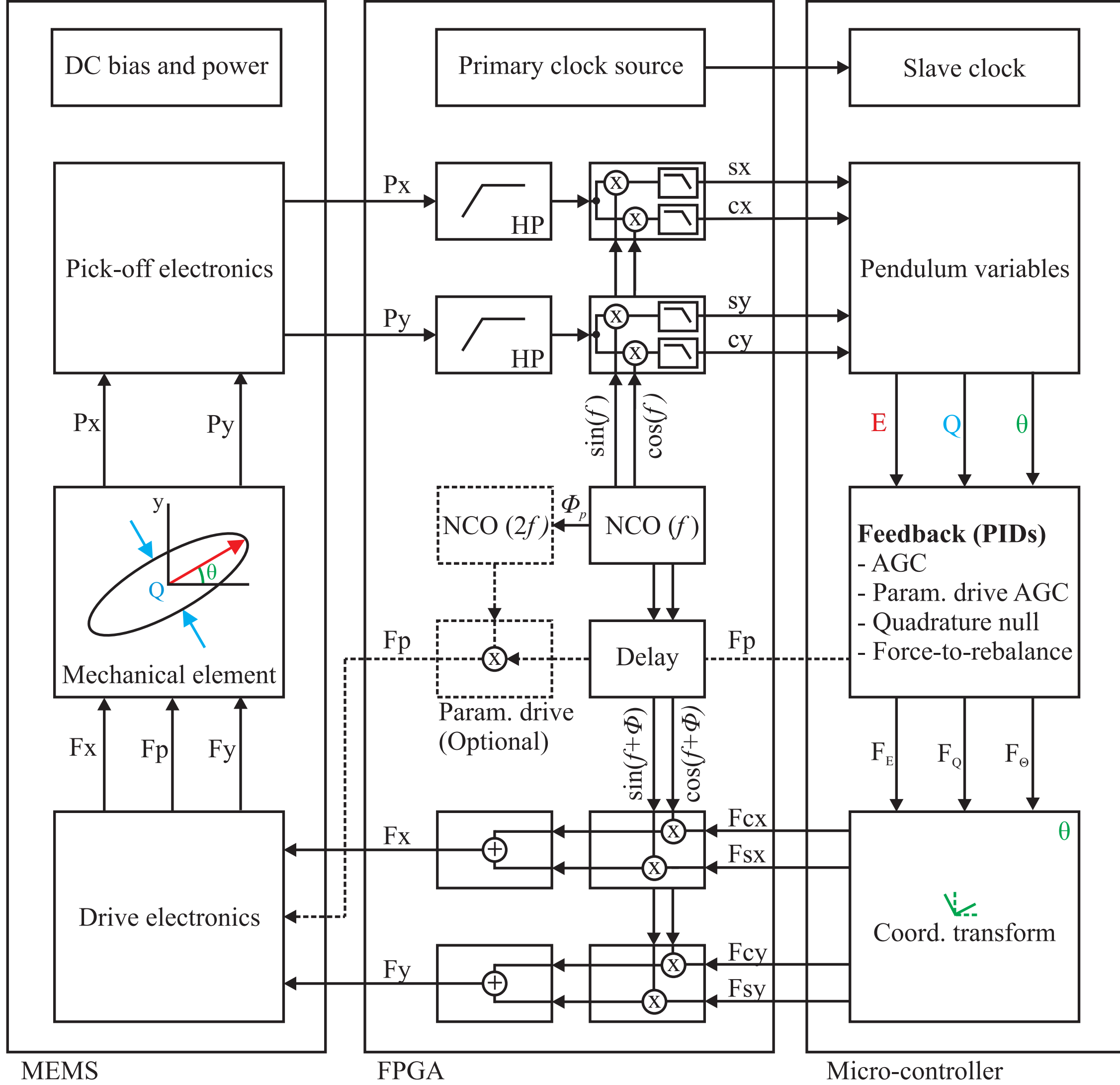

Figure 6.5: Rate integrating gyro controller with parametric drive, implemented on a Artix 7 FPGA board running at 1 MHz.

Imaginary component of L is a measure of phase error and used to establish a phase lock to the vibratory motion of the gyroscope. R and S are the projections of pattern angle on x and y axis and can be used to find the orientation of the precession pattern using:

$$\theta = \frac{1}{2}\arctan(\frac{\mathrm{S}}{\mathrm{R}})\,. \tag{6.9}$$

A PID controller acts on each of these variables. These are Amplitude Gain Control (AGC)

acting on E, quadrature null acting on Q and force-to-rebalance (FRB) that controls pattern angle (θ). For the whole angle mechanization, FRB is disabled so that the standing wave is free to precess. Once the correct command voltages $\mathrm{F_E}, \mathrm{F_Q}$ and F_θ are established, a coordinate transform around θ is performed to align these signals to the standing wave pattern:

$$\mathrm{F_{cx}} = \mathrm{F_E} \cdot \cos(\theta) - F_\theta \cdot \sin(\theta) \; , \tag{6.10}$$

$$\mathrm{F_{cy}} = \mathrm{F_E} \cdot \sin(\theta) + F_\theta \cdot \cos(\theta) \; , \tag{6.11}$$

$$\mathrm{F_{sx}} = -\mathrm{F_Q} \cdot \sin(\theta) \; , \tag{6.12}$$

$$\mathrm{F_{sy}} = \mathrm{F_Q} \cdot \cos(\theta) \; , \tag{6.13}$$

This is followed by modulation of the command voltages at the PLL frequency. A set amount of phase delay is also added during modulation so that the total phase of the feed-back system is a multiple of 360°. The FPGA and micro-controller code used for the controller is presented in Appendix E. A users manual is also included in Appendix D, along with a part list.

Open loop parametric drive is typically unstable for nominal drive amplitudes [131, 132], which causes the gyro amplitude to increase exponentially for a fixed parametric drive signal. For this reason a secondary AGC controls the parametric drive voltage as to keep the gyro amplitude stable. This closed loop operation permits parametric drive of the gyro at a wide range of drive amplitudes, outside the stability boundary of open loop parametric drive.

Typical gyro startup procedure begins with driving the gyro to a preset amplitude using conventional (at resonance) drive. Once the PLL and AGC stabilize, drive signal is disabled and immediately parametric drive AGC is enabled. This switch occurs within one clock cycle of the FPGA and eliminates over-shoots in drive amplitude, which would otherwise occur while starting up the high-Q resonator.

6.4 Experimental Results

6.4.1 Device Characterization and Rate Gyroscope Operation

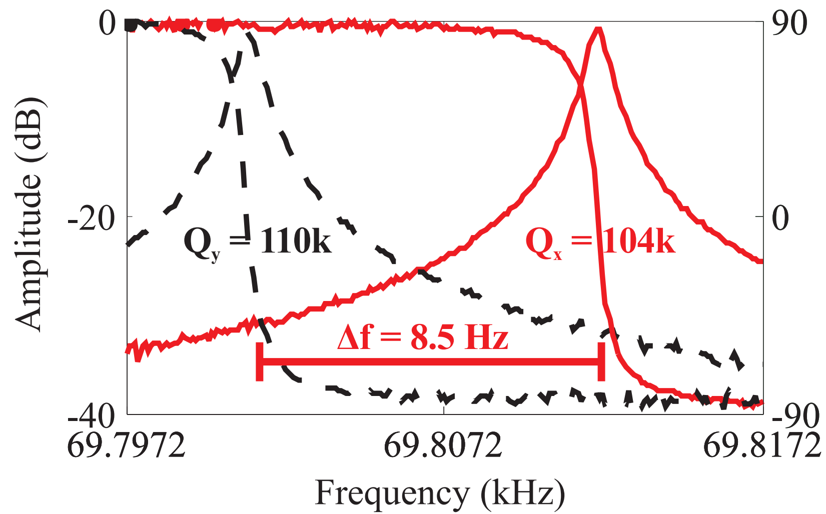

Figure 6.6: Freq. sweep showing the n = 3 wineglass modes with Q-factor above 100k at central frequency of 69.8 kHz.

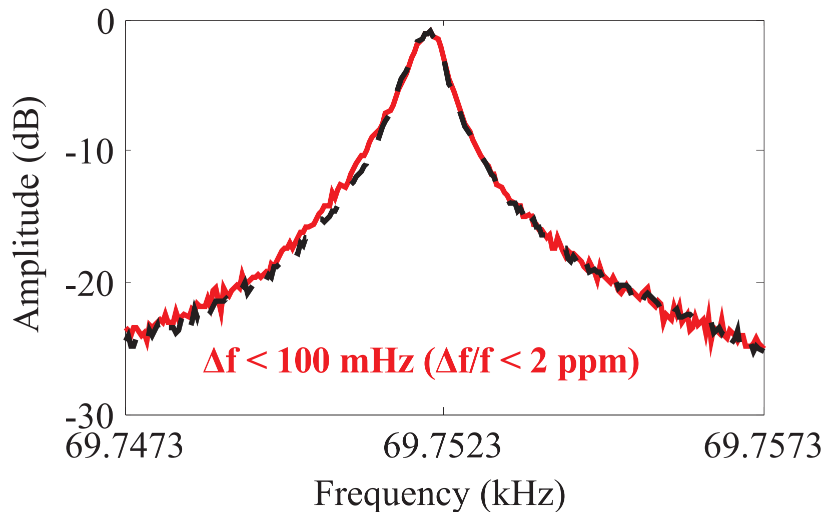

Figure 6.7: Electrostatic tuning with 3.26 V and 0.5 V resulted in $\Delta f < 100$ mHz ($\Delta f <$ 2 ppm at 69.75 kHz).

Devices were wirebonded to ceramic Leadless Chip Carriers (LCCs) and istrumented with discrete electronics. Electromechanical Amplitude Modulation (EAM) at 1 MHz was used to

mitigate the effects of parasitic feed through on the pick-off electronics. DC bias voltage of 1 V on both modes and AC voltage of 20 mV was used for initial characterization. Frequency response characterization of the fabricated gyroscopes revealed a Q-factor of $> 100,000$ on both n = 3 modes at ~70 kHz center frequency, Fig. 6.6.

As-fabricated frequency split (Δf) of 4 devices were characterized. Lowest frequency split observed was 8.5 Hz Hz, Fig. 6.6, ($\Delta f/f = 122$ ppm) with a mean frequency split of 21 Hz (($\Delta f/f = 300$ ppm) across 4 devices, Table6.2. Low frequency split is attributed to robustness of the high order (n = 3) wineglass mode to fabrication imperfections and the ultra-clean EpiSeal process.

After initial characterization the frequency split was further reduced using electrostatic tuning of DC bias on forcer and quadrature null electrodes. DC bias voltages of 3.26 V and 0.5 V was sufficient to reduce the frequency split to < 100 mHz ($\Delta f/f < 2$ ppm) on Device #1, Fig. 6.7.

Table 6.2: As-fabricated frequency symmetry of 4 devices.

Device #	**Δf(Hz)**	**f(kHz)**	**$\Delta f/f$(ppm)**
# 1	8.5	69.75	122
# 2	11	69.69	158
# 3	25	71.29	350
# 4	40	69.4	576

For force-to-rebalance operation an ADAU1442 DSP board from Analog Devices was used to implement the control algorithms. A 24 bit audio codec (AD1938) operating at 192 kHz sampling rate was used for forcer and pick-off signals. An Arduino Due micro-controller board was interfaced with the DSP board over I2S protocol, which was used to down-sample the gyro output and transmit over RS232 protocol for data acquisition.

To evaluate rate gyro performance the pattern angle was locked to X axis by enabling the FRB loop. A force-to-rebalance scale factor of 0.046 mV/(°/s) was observed with a linearity

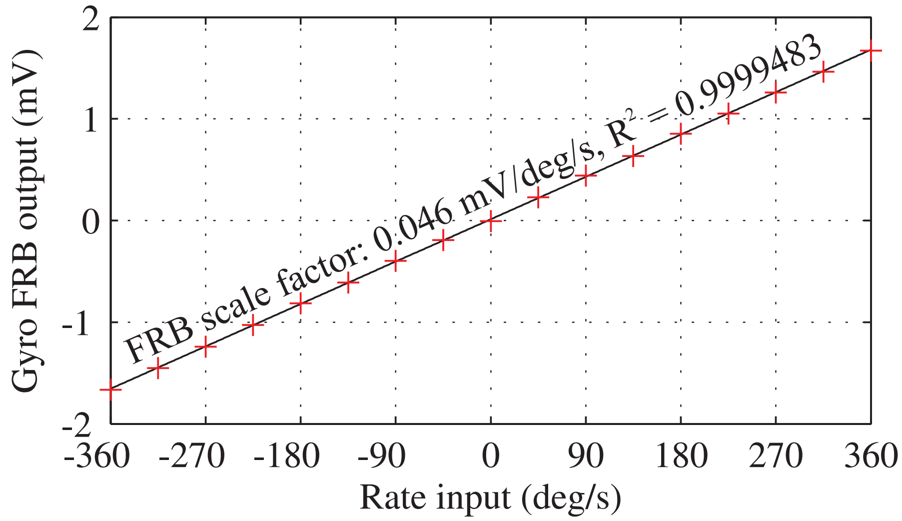

Figure 6.8: Scale factor of Toroidal Ring Gyroscope in force-to-rebalance mode.

of R^2 = 0.9999483 within 360 °/s range, Fig. 6.8. Alan variance analysis of FRB output revealed ARW of 0.047 °/$\sqrt{\text{h}}$ and an in-run bias stability of 0.65 °/h at 32 s integration time, Fig. 6.9.

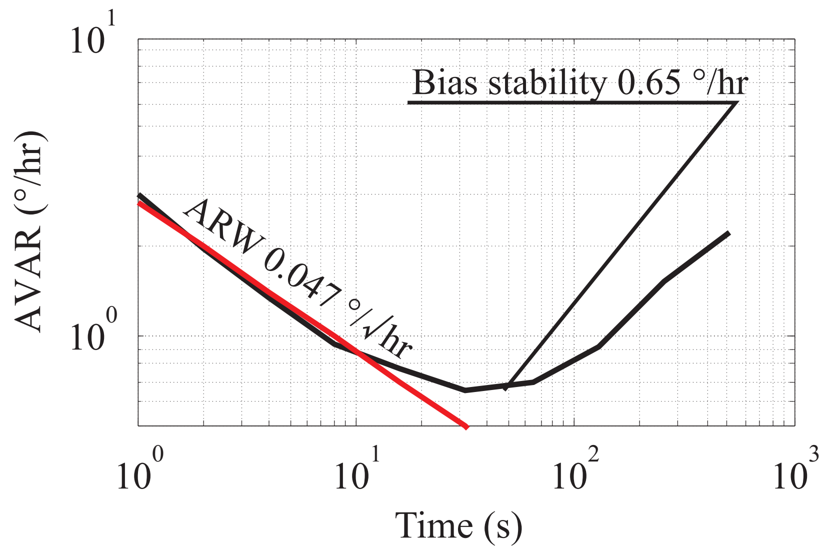

Figure 6.9: Allan deviation of gyroscope force-to-rebalance output, showing bias stability of 0.65 ° h.

6.4.2 Pattern Angle Data

Pattern angle data for the gyroscope was obtained by changing the orientation of the standing wave (θ) using the force-to-rebalance loop and recording the gyro state with respect to pattern angle (θ). By changing the pattern angle from 0° to 360° in a continuous fashion and recording the output of PLL, AGC, quadrature null and force-to-rebalance command signals polar plots seen in Fig. 6.10 can be created. As a result, each polar plot shows the output of a particular control loop at the prescribed drive orientation.

Variation of command signals across pattern angle is a measure of imperfections within the gyroscope. And as can be seen in Fig. 6.10, these variations are sinusoidal in nature. For this reason Fourier series expansion of pattern angle data from PLL, quadrature, and AGC loops was used for calibrating the gyro. For example, second harmonic of the PLL output provides run-time identification of the frequency split (Δf), which was used to tune the frequency split down to 50 mHz (700 ppb). Parametric AGC command signal displayed a 2 mV (~4%) variation on second harmonic, which was attributed to pick-off gain unbalance between x and y modes. Adjusting the pick-off gains in the FPGA, we were able to reduced this unbalance down to < 0.5 mV. The combined effect of tuning the frequency split and the pick-off gain unbalance resulted in an overall 2.5$\times$ reduction in the required quadrature null command signal, Fig. 6.10.

6.4.3 Rate Integrating Gyroscope Operation

In order to test the rate integrating operation, the gyro was driven using parametric drive and a constant rotation rate was applied for 1 hour, switching the direction at 30 minutes mark. Fig. 6.11 shows the unwrapped gyro response for four different speeds. This experiment was later repeated using conventional (vector) drive. A linear fit to the data revealed a

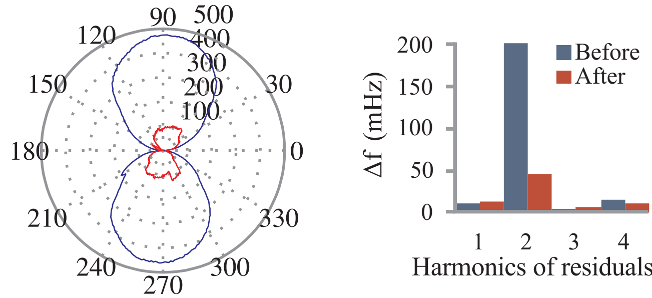

a) PLL frequency (Δf) with respect to pattern angle (mHz).

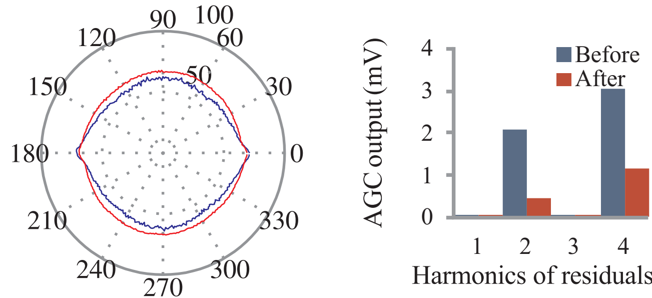

b) Parametric drive amplitude gain control (AGC) output (mV).

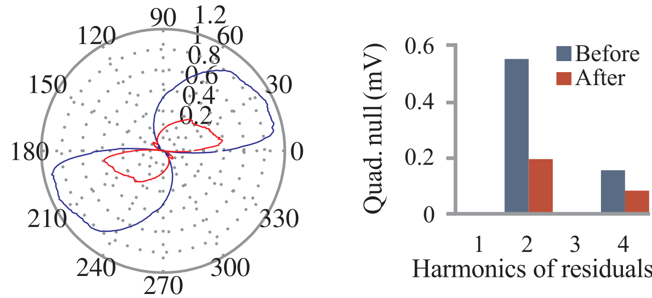

c) Quadrature null control output (mV).

Figure 6.10: Tuning of the gyro based on residuals of pattern angle data from PLL, parametric AGC, and quadrature null loops.

combined electrical/mechanical angular gain factor of ~0.6. Comparison of residuals from both experiments is shown in, Fig. 6.12. For all rate inputs the parametric drive resulted in better scale factor stability compared to conventional drive architecture. As predicted, the highest difference between conventional drive and parametric drive occurred at higher rotation rates. Time lag in calculation of the drive vector becomes more important at higher rotation rates as this lag can cause the drive vector to couple into the gyro output. As a result, any change in the drive vector amplitude either due to drive gain drifts or a Q-factor change in the resonator element can affect scale factor stability.

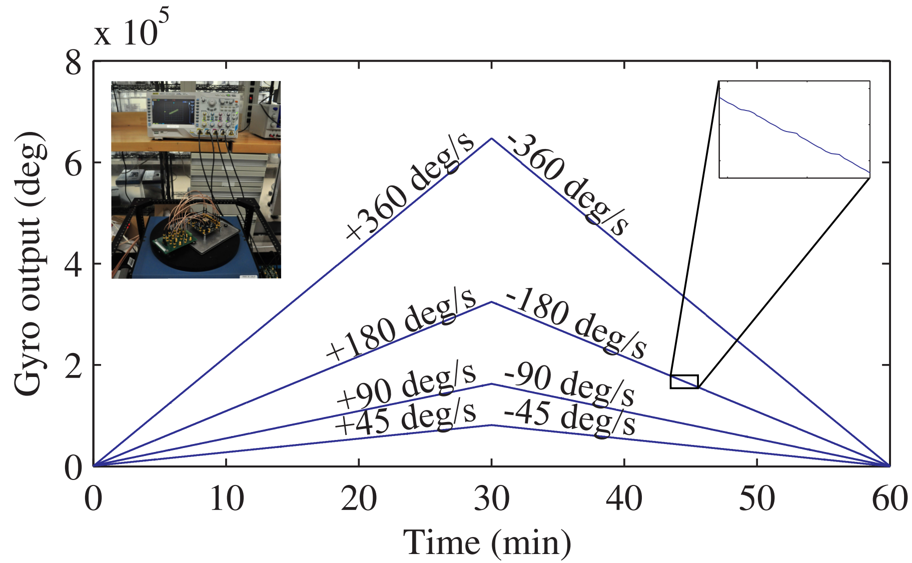

Figure 6.11: Experimental demonstration of rate integrating operation under parametric drive.

For 360 °/s rate input over a 30 min period standard deviation of accumulated error for conventional drive was 176° versus 13° for parametric drive. This resulted in 14× improvement for parametric drive and < 20 ppm scale factor stability overall, without any compensation or temperature stabilization.

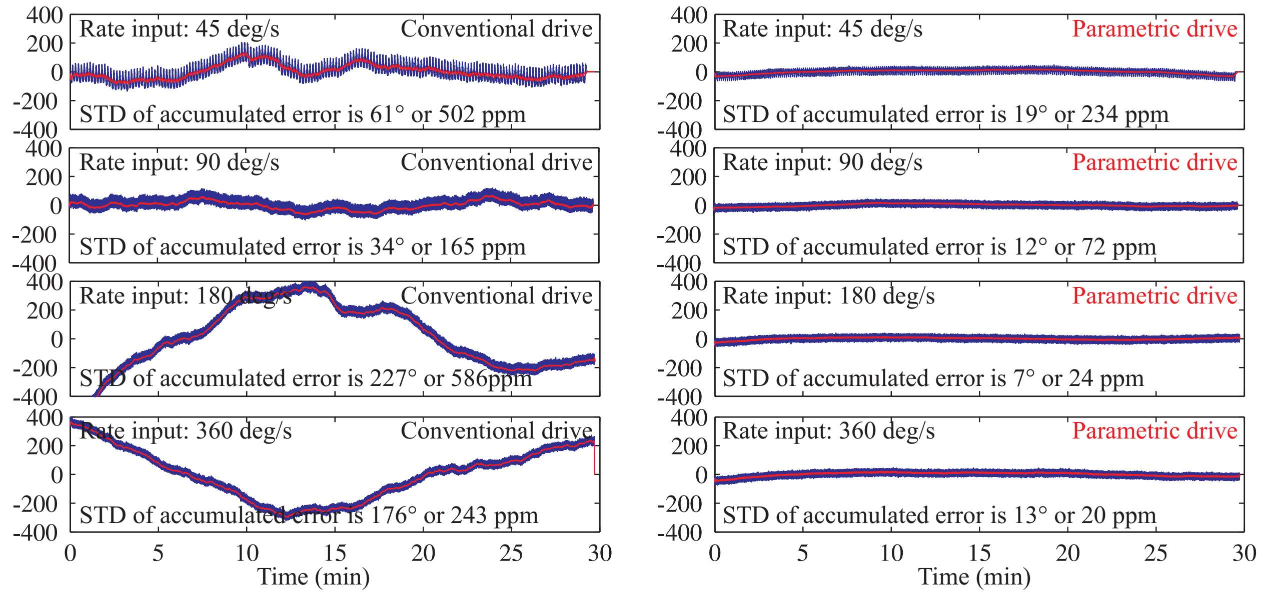

Figure 6.12: Comparison of residual errors of conventional drive and parametric drive for different rate inputs.

6.5 Conclusions

Parametric drive of a MEMS rate integrating gyroscope was presented for the first time. Parametric pumping was used to bypass the errors associated with finding the orientation of the standing wave, time delay in the calculation and drift in gain of x-y drive electronics. This resulted in as high as 14× improvement in scale factor stability compared to conventional x-y drive and better than 20 ppm scale factor stability without any compensation or temperature stabilization. In addition, parametric drive reduces drive to pick-off electrical feed-through by creating a frequency separation between drive and pick-off channels.

A Toroidal Ring Gyroscope with Q-factor above 100,000 at central frequency of ~70 kHz was designed and implemented in wafer-level epitaxial silicon encapsulation process. The gyroscope consists of a robust ring anchor and a distributed suspension system. In contrast to axi-symmetric designs with central support structures, the vibrational energy in the introduced design is concentrated towards the innermost ring, and the device is anchored at the

outer perimeter. The distributed support structure prevents vibrational motion propagating to the outer anchor, which helps trap the vibrational energy within the gyroscope. Combined with the ultra-clean EpiSeal process Q-factors above 100,000 were obtained at ~70 kHz and a compact size of 1760 µm without using getter materials.

Frequency splits (Δf) as low as 8.5 Hz ($\Delta f/f$ = 122 ppm) and a mean frequency split of 21 Hz ($\Delta f/f$ = 300 ppm) were observed across 4 devices. Low frequency split is attributed to the ultra-clean EpiSeal process and robustness of the high order (n = 3) wineglass mode to fabrication imperfections, at the cost of potential decrease in angular gain factor and vibration amplitude.

Whole angle and pattern angle control loops were implemented on a custom FPGA system. Characterization of the gyro performance using force rebalance mechanization revealed ARW of 0.047 °/$\sqrt{\text{h}}$ and an in-run bias stability of 0.65 ° h. Due to the high Q-factor, degenerate mode operation on n = 3 modes and robust support structure, the device can potentially be instrumented for high-g environments that require high angular rate sensitivity.

Techniques presented in this chapter can be used to improve performance of other axi-symmetric gyro architectures, such as ring, disk, and wineglass gyros.

Chapter 7

Dual Foucault Pendulum Gyroscope

In this chapter, we report a conventionally micro-machined, lumped mass Micro Rate Integrating Gyroscope architecture, Dual Foucault Pendulum (DFP) Gyroscope, to serve as a test-bed for various MRIG control schemes. The gyroscope consists of two dynamically equivalent, mechanically coupled proof masses, oscillating in anti-phase motion. This dual axis tuning fork behavior creates a dynamically balanced resonator with x-y symmetry in frequency and damping, suitable for Whole Angle mechanization.

7.1 Introduction

Axi-symmetric gyroscope architectures that utilize the so-called "wineglass" modes, such as ring/disk systems and wineglass gyroscopes, are inherently force and torque balanced. The wineglass modes exhibit a behavior akin to a tuning fork, where the motion at one part of the gyroscope is balanced by an equal and opposite motion, Fig. 7.1 [133, 134]. This balanced motion provides anchor loss mitigation and certain degree of vibration isolation.

Conventional micro-machined gyroscopes, on the other hand, typically consist of proof

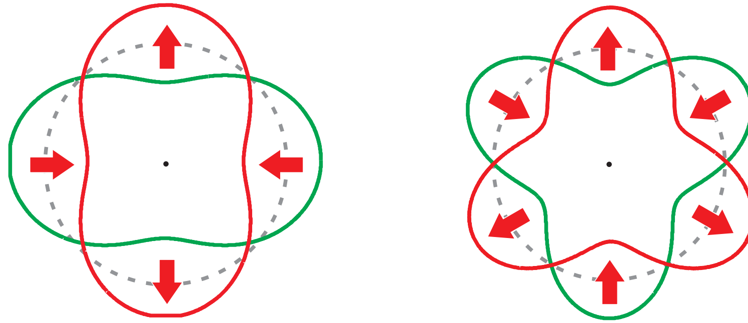

Figure 7.1: Wineglass modes of axi-symmetric architectures, such as ring/disk systems and wineglasses gyroscopes, are inherently dynamically balanced, resulting in zero net force and torque during oscillation.

masses, folded beam suspensions, and comb fingers, that are not inherently force and torque balanced. To achieve force and torque balance, tuning fork architectures such as [135] can be utilized. However, conventional tuning fork architectures are not x-y symmetric and the force and torque balance occurs only on one axis. On the other hand, x-y symmetric single-mass systems such as [33] or multi-mass systems such as the Quadruple Mass Gyroscope (QMG) [136] do exist. Single-mass systems are not inherently balanced, whereas multi-mass systems require complicated mechanical systemst achieve force/torque balance and phase synchronization.

In this chapter, we are exploring a new gyro architecture that combines simplicity and dynamic balance of tuning fork gyros [135] (two mass anti-phase motion) with high rate sensitivity of degenerate mode gyroscopes (x-y symmetry). Core of the gyroscope architecture is two mechanically coupled and dynamically equivalent proof masses, oscillating in anti-phase motion, Fig. 7.2(b). Each proof mass is free to swing in any direction on the x-y plane, analogous to a Foucault Pendulum, Fig. 7.2(a). However, unlike a conventional tuning fork gyroscope, center of masses of the two proof masses are aligned. This creates force and moment balance for both x and y modes, providing immunity to vibration and shock as well

as anchor loss mitigation. We believe this two-mass architecture is the minimum lumped mass gyroscope configuration that can provide a dynamically balanced system in both x and y directions.

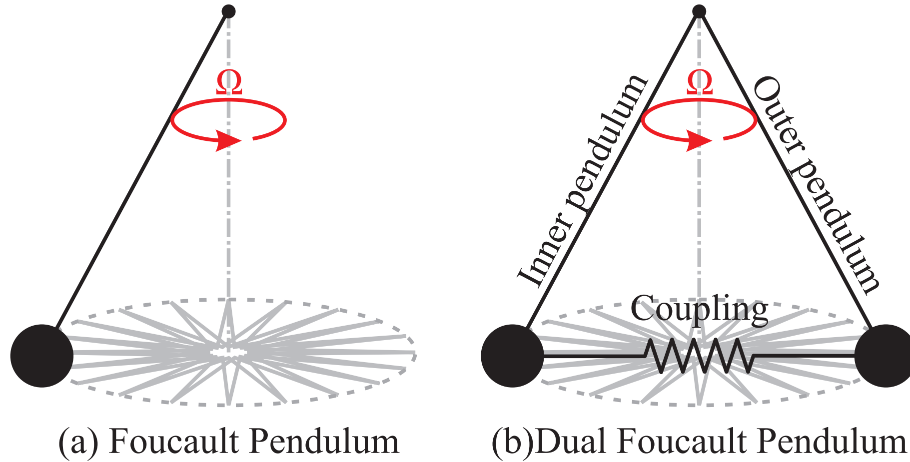

Figure 7.2: Dual Foucault Pendulum (DFP) gyroscope consists of two mechanically coupled Foucault Pendulums.

In the following sections, we will first present design of Dual Foucault Pendulum Gyroscope in Section 7.2. In Section 7.3, we will present the fabrication of the mechanical element and details of the experiment setup. This will be followed by demonstration of rate and Rate Integrating Gyroscope operation. The chapter concludes with a discussion of the results in Section 7.4 and conclusions in Section 7.5.

7.2 Design

Core of the Dual Foucault Pendulum (DFP) Gyroscope is two mechanically coupled and dynamically equivalent proof masses, oscillating in anti-phase motion. Dynamic balance is obtained by aligning the center of masses of each proof mass. This allows the center of mass of the system to remain stationary during oscillation, causing the net force and torques generated by the combined system to be zero at all times, Fig. 7.3. Unlike a conventional tuning fork gyroscope, the force and torque balance is obtained on both x and y modes of

the gyroscope.

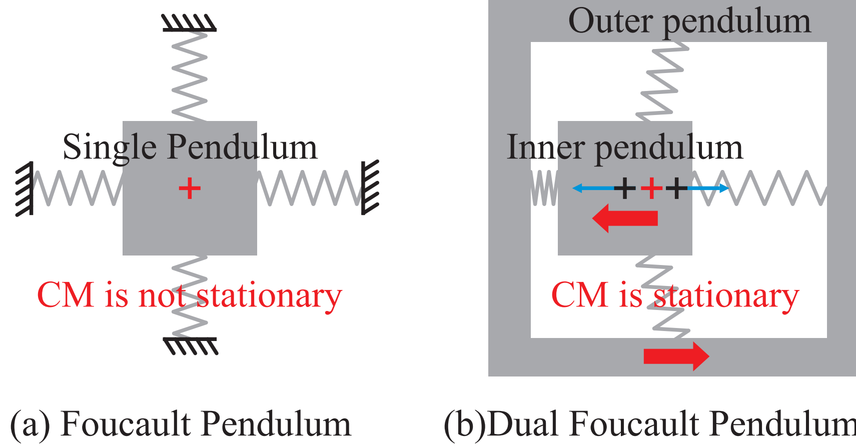

Figure 7.3: Vibration immunity and anchor loss mitigation are provided by anti-phase operation of two dynamically equivalent Foucault Pendulums.

In our implementation, dynamic equivalence of the two proof masses is achieved by using identical (mirrored) suspension elements and shuttle assemblies, while designing the two proof masses to have equal masses. This results in same resonance frequencies for individual proof masses, which is further reinforced by mechanical coupling of the two proof masses. This mechanical coupling is achieved via "weak springs" between shuttle assemblies of inner and outer proof masses, which synchronizes the phases of the proof masses, Fig. 7.4.

There are four shuttle pairs within the gyroscope. Each shuttle pair is connected to both inner and outer proof masses and can only move in one direction. This helps mitigate cross-axis coupling between the x and y modes by restricting electrode movement in one direction. During gyroscope operation, for each x and y mode, two shuttle pairs remain parked, whereas the other two shuttles oscillate in anti-phase motion together with their respective proof masses.

Electrostatic transduction is provided by arrays of parallel plates located on the shuttle assemblies. In order to achieve large displacements necessary for low noise operation, 8 µm capacitive gaps are used on the parallel plates. Large free space between the two proof masses allows placement of 12 layers of parallel plate electrodes per shuttle pair, resulting

in over 12.5 pF total capacitance ($dC/dx = 1.5\,\mu\text{F/m}$).

Device is suspended from 4 anchors placed in between the two proof masses. Each anchor is shared by one x and one y shuttle pair. To help protect the mechanical element from unwanted packaging stresses, attachment of the gyroscope die to the package is done in between the 4 anchors, via a central attachment point.

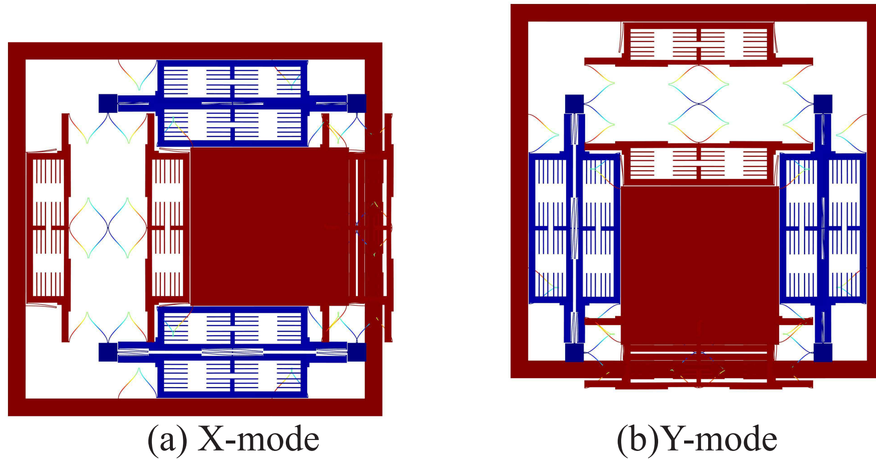

Figure 7.4: FEA showing x-y symmetric anti-phase operation. Device is anchored at four points in between the proof masses. Colors correspond to total displacement.

Table 7.1: Summary of design parameters.

Device width & height	(µm)	6800
Device layer thickness	(µm)	100
Buried oxide (BOX) thickness	(µm)	5
Buried oxide (BOX) thickness	(µm)	5
Release hole width & height	(µm)	20
Inner tine width & height	(µm)	2880
Outer tine frame width & height	(µm)	320
Folded beam width	(µm)	10
Folded beam length	(µm)	550
Number of folded beams	#	48
Nominal center frequency	kHz	3
Parallel plate overlap length	#	1600
Number of parallel plates per axis	#	24
Capacitive gaps	(µm)	8
Stop gaps	(µm)	5
Total nominal capacitance	(pF)	12.5

7.3 Experimental Results

7.3.1 Fabrication

Device was fabricated on a standard SOI process, with a footprint of 6700 µm $\times$ 6700 µm, Fig 7.5. A device layer of 100 µm and a buried oxide layer of 5 µm were used. AZ 4620 photoresist and conventional contact lithography was used to define the sensor features. DRIE etching of the device layer was done in a STS DRIE system, which was followed by a HF release step using an Idonus Vapor Phase Etcher. After dicing, individual dies were attached to 44 pin ceramic LCC packages and wirebonded for characterization.

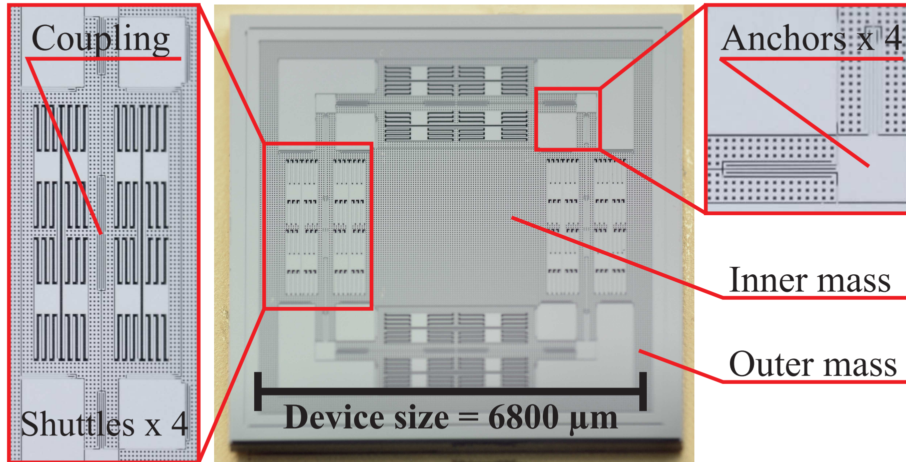

Figure 7.5: Image of fabricated gyroscope with a closeups of the shuttle assemblies and the anchors.

7.3.2 Front-end Electronics

A low-outgassing ceramic PCB was used for front-end electronics. First stage amplification of the gyroscope output was done using dual trans-impedance amplifiers (Analog Devices AD8066) with $1\,\mathrm{M}\Omega$ gain resistors and $2.2\,\mathrm{pF}$ capacitors. Output of the transimpedance amplifiers were cascaded into an instrumentation amplifier (Analog Devices AD8429).

The same instrumentation amplifiers (Analog Devices AD8429) were also used for forcer electronics. Unity gain was used on the forcer electronics due to extremely low voltage levels required to drive the gyroscope (less than $1\,\mathrm{mV}$). DC biasing was done only on the forcer electrodes and the resonator.

Finally, low dropout voltage regulators (Texas Instruments TPS7A3001 and TPS7A4901) were used for supplying power to the active components on the PCB. These helped to reduce system noise by rejecting a large portion of the power supply noise.

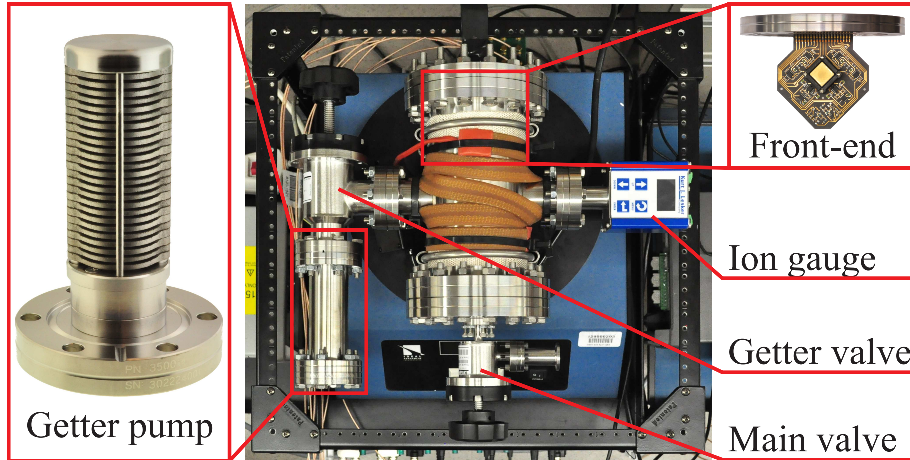

Figure 7.6: High-vacuum test-bed with non-evaporable getter pump provides µTorr level vacuum for rate characterization.

7.3.3 Experimental Setup

A high-vacuum test-bed was used for gyro characterization, Fig. 7.6. The test-bed consists of four main components:

- Low-outgassing ceramic PCB front-end electronics,
- Macro-scale non-evaporable getter pump,
- Stainless steel vacuum chamber assembly,
- Rate table with slip rings.

For rate table characterization, the device is mounted onto the front-end PCB and inserted into the vacuum chamber assembly. Electrical feed-through from the vacuum chamber is provided by a 37 pin D-SUB connector, which is then routed through the slip rings. Angle valve is used to seal the getter pump, during insertion of the device into the vacuum chamber. Another angle valve is used to seal the entire vacuum chamber, so that the external turbo pump can be disconnected for continuous 360° rotation of the rate table.

After the system is pumped down using an external turbo pump, the non-evaporable getter pump is activated using the internal resistive heater and the chamber is sealed off. Due to the large absorption capacity of the getter pump and the low-outgassing ceramic front-end electronics, the system can sustain high vacuum without the need for active pumping. This eliminates unwanted vibrations caused by rotary pump systems and permits continuous 360° rotation of the rate table at sustained vacuum levels of $< 10\,\mu$Torr.

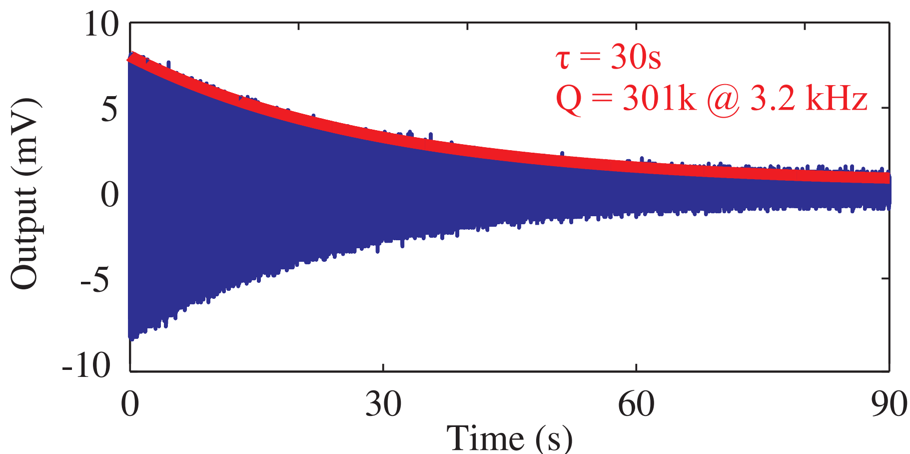

Figure 7.7: Ring down experiment showing energy decay time constant (τ) of 30 s or Q of 301k at 3.2 kHz.

7.3.4 Rate Gyroscope Operation

Ring-down characterization was used to measure the Q-factor of the mechanical element at a vacuum level of An exponential curve fit to the ring-down data, showed an energy decay time constant (τ) of 30 s at 3.2 kHz, which corresponds to Q-factor over 300,000, Fig. 7.7.

An as-fabricated frequency split (Δf) of 18 Hz was observed, which was later electrostatically tuned to < 100 mHz by biasing the forcer electrodes. This was achieved by applying a DC bias of 10 V DC at the resonator, while applying 9 V DC to the x forcer electrodes and -6.75 V DC to the y forcer electrodes. Lower DC bias voltages can be used if pick-off electrodes in addition to the forcer electrodes are used for electrostatic tuning.

After electrostatic tuning, Phase Locked Loop (PLL), Amplitude Gain Control (AGC) and Quadrature Null loops were implemented on a Zurich HF2LI lock-in amplifier [12]. PLL was locked to the drive mode and AGC was used to stabilize the drive amplitude. In the experiments, an AC quadrature null loop was utilized, where the sense mode forcer electrodes were used to drive the quadrature output of the sense mode to zero. Device was tested with both open-loop and force-to-rebalance configurations.

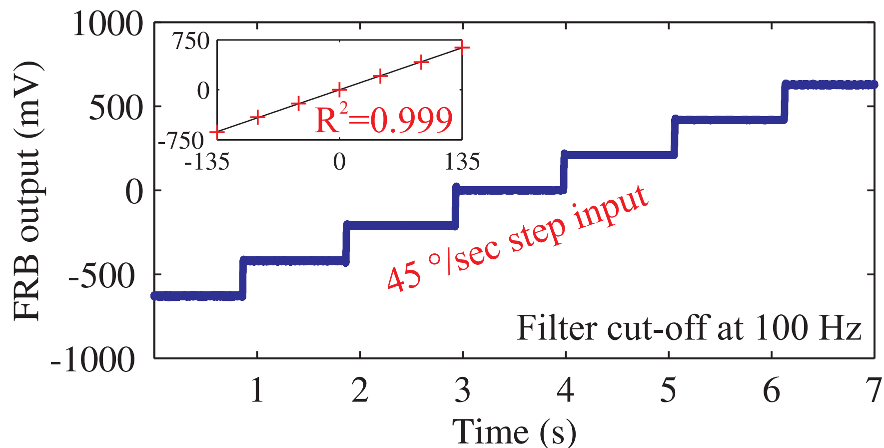

Figure 7.8: Rate characterization with 45 °/s step input showed a FRB scale factor of 4.66 mV/(°/s), goodness of fit: $R^2 = 0.999$.

Scale factor characterization was done using continuous rotation of the rate table and incrementally changing the angular velocity. A linear fit to the gyro output was used to extract the scale factor. An open-loop scale factor of 26.4 mV/(°/s) and force-to-rebalance scale factor of 4.66 mV/(°/s) were measured with a goodness of fit: $R^2 = 0.999$, Fig. 7.8. After the scale factor was obtained, Alan variance analysis of the gyroscope zero rate output was performed for both open-loop and force-to-rebalance operation, Fig. 7.9. No temperature stabilization or compensation was used during the experiment. For open-loop operation, angle random walk (ARW) of $0.003\,°/\sqrt{\text{h}}$ an an in-run bias stability of 0.27 °/h were measured. Whereas for FRB configuration an ARW of $0.06\,°/\sqrt{\text{h}}$ and bias stability of 1.5 °/h were measured. Higher ARW in FRB operation was associated with feedback noise from the digital to analog converters (DACs).

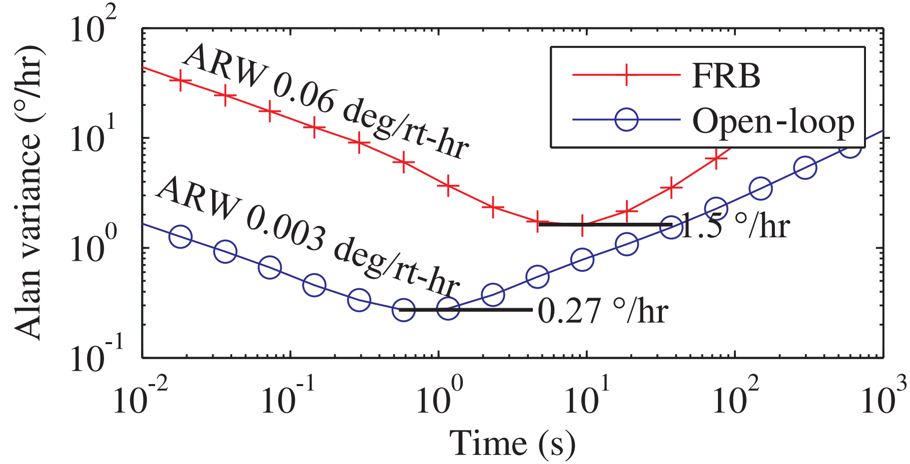

Figure 7.9: Alan variance of zero rate output, showing ARW and in-run bias instability for FRB and open-loop operation.

7.3.5 Whole Angle Operation

Control system was described in Chapter 6, a simplified control system schematic is included in this section for convenience, Fig. 7.10.

After electrostatic tuning, closed loop control of the gyroscope was implemented on Artix 7 FPGA board, Fig. 7.10. Virtual carouseling experiments were performed to identify the pattern angle dependence of Phase Locked Loop (PLL), Amplitude Gain Control (AGC), AC quadrature null, and force-to-rebalance loops (FRB), Fig. 7.10 [12]. Frequency mismatch of $\Delta f < 0.1\,\text{Hz}$ was observed on x and y geometric axes, whereas a stiffening up to 0.5 Hz was observed at 45° pattern angle. A nominal drive voltage of 1 mV was used for amplitude control. Maximum variation in quadrature null command signal was $< 25\,\text{mV}$, whereas the variation on force-to-rebalance command signal was $< 5\,\text{mV}$. Uncompensated quadrature null and force-to-rebalance loops showed 2θ and 4θ dependence on pattern angle, Fig. 7.11.

In order to permit precession of the vibration pattern the force-to-rebalance loop was disabled. Rate integrating gyroscope operation was demonstrated by applying a continuous rate input of 180 °s over 2 h duration on a rate table, Fig. 7.12. A linear fit to the experimental

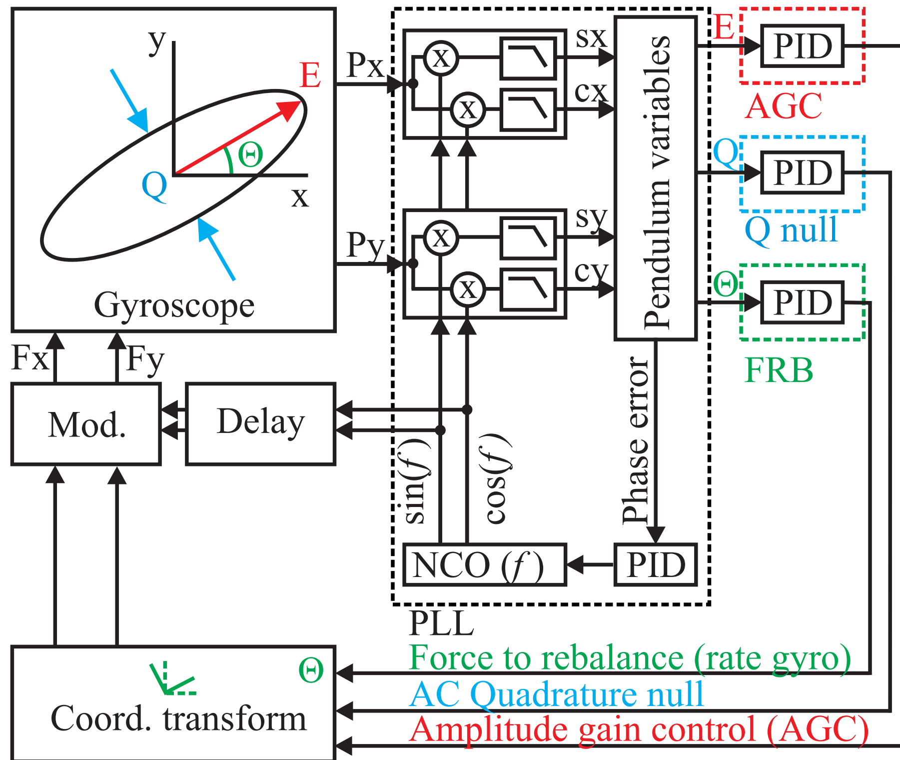

Figure 7.10: Rate integrating gyro control implemented on a Artix 7 FPGA running at 500 kHz, provides closed loop control of PLL, AGC, quadrature null, and FRB.

data revealed an angular gain factor of ~0.8. Local perturbations of $> 5°$ were observed in the uncompensated gyro output due to pattern angle dependent bias (angular error and pattern drift). Despite these perturbations, RMS error of a linear fit to the 10 Hz data was found to be 29° over 2 h duration (1 296 000° of rotation), showing a scale factor variation of 22 ppm RMS.

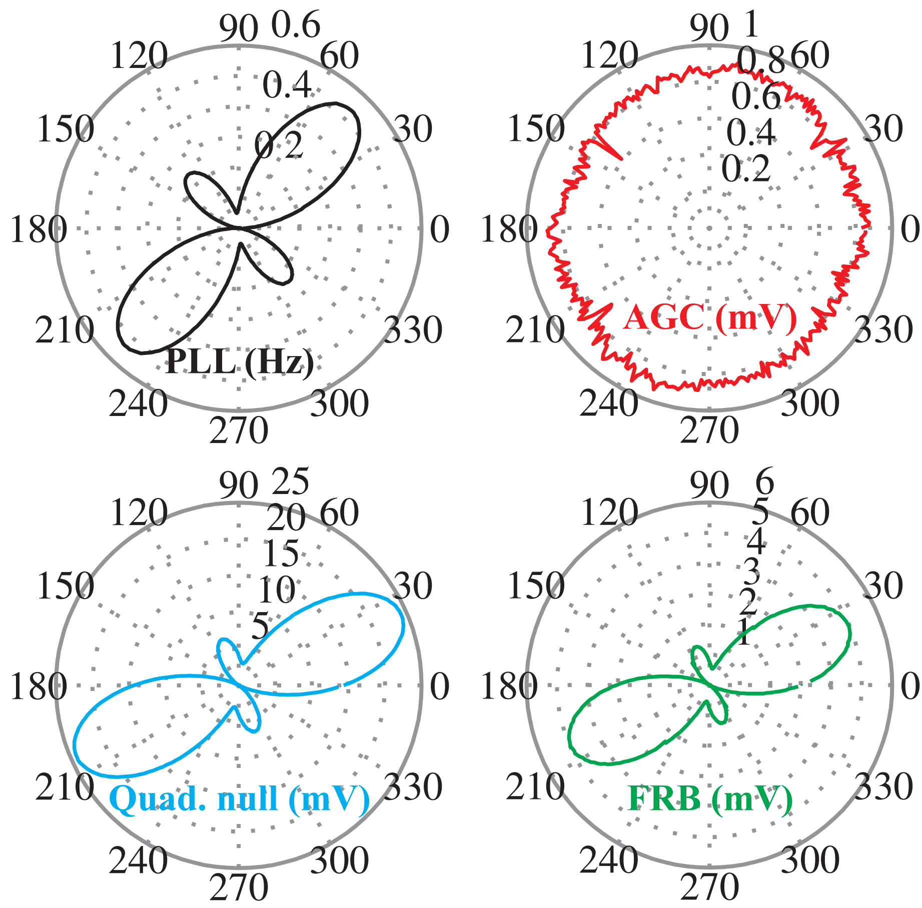

Figure 7.11: Polar plots showing the pattern angle dependence of four main closed loops. 2Θ and 4Θ dependence indicate frequency mismatch and forcer misalignment.

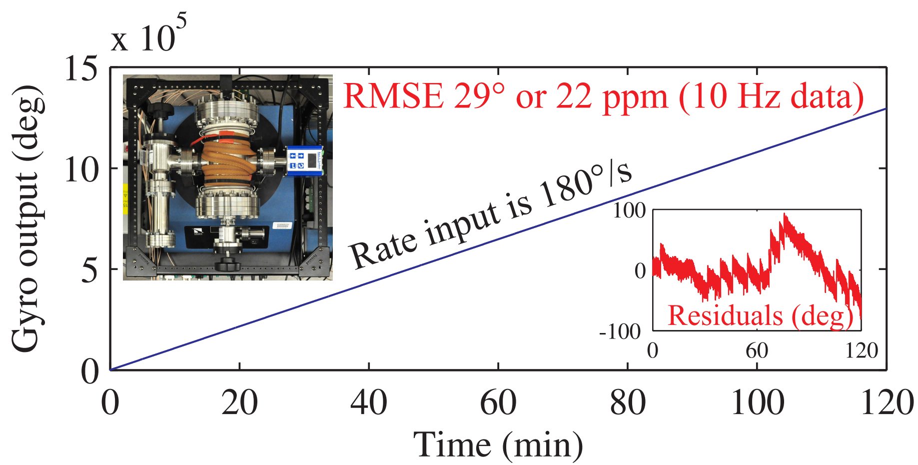

Figure 7.12: Spooling of the rate integrating gyro output over 2 hours of continuous rotation. Linear fit shows angular gain factor of ~0.8 and RMSE of 22 ppm.

7.4 Discussion

Due to the high-Q degenerate mode operation, large modal mass, and large nominal capacitance angle random walk (ARW) as low as $0.003\,°/\sqrt{\text{h}}$ an an in-run bias stability of $0.27\,°/\text{h}$ was demonstrated in open loop operation without ovenization or temperature compensation. Whereas for FRB configuration an ARW of $0.06\,°/\sqrt{\text{h}}$ and bias stability of $1.5\,°/\text{h}$ were measured. Higher ARW in FRB operation was associated with feedback noise from the digital to analog converters (DACs), which can be lowered with better control electronics.

Continuous rate integrating operation was demonstrated using a FPGA based controller, Fig. 7.10. Virtual carouseling was performed to characterize the imperfections within the mechanical element, Fig. 7.11. Largest frequency asymmetry was observed at 45° pattern angle with a 2θ harmonic, Fig. 7.11. This frequency asymmetry is attributed to residual cross-axis coupling between x and y modes. A smaller frequency asymmetry with a 4θ harmonic was also observed at 45° pattern angle, which is attributed to structural non-linearities of folded-beam suspensions at large displacement

Change in Amplitude Gain Control (AGC) command signal with respect to pattern angle was minimal, Fig. 7.11. Although a large noise was observed. This is due to the extremely small voltages required to drive the gyroscope, which starts approaching the digital-to-analog converter (DAC) noise floor.

Both quadrature null and force-to-rebalance loops showed large 2θ harmonic imperfections, which was attributed to the mechanical cross-axis coupling between x and y modes, and the resultant frequency asymmetry.

Continuous rate integrating operation over 2 hours was demonstrated using the closed loop control system, Fig. 7.12. Despite cyclic perturbations due to aniso-elasticity and aniso-damping, an angular gain factor of ~0.8 was measured with a very high degree of linearity

(22 ppm). This high degree of linearity is attributed to the ability of whole angle operation to tap into the angular gain parameter (η), which is an inherently robust geometric parameter of the gyroscope. With further improvements in structural symmetry, this may lead to gyroscopes with very good scale factor stability.

7.5 Conclusions

A new type of MEMS degenerate mode gyroscope is presented. Dual Foucault Pendulum (DFP) Gyroscope aims to combine dynamic balance of tuning fork gyroscopes with high rate sensitivity and rate integrating capability of high quality factor degenerate mode gyroscopes, in a minimal (two-mass) configuration. Ring-down characterization of the mechanical element at a vacuum level of 5 µTorr showed an energy decay time constant (τ) of 30 s at 3.2 kHz, which corresponds to Q-factor over 300,000 on both modes. Initial characterization of open-loop gyro performance at zero rate showed angle random walk (ARW) of $0.003\,°/\sqrt{\mathrm{h}}$ and an in-run bias stability of 0.27 °/h. Whereas FRB operation showed higher noise with an ARW of $0.06\,°/\sqrt{\mathrm{h}}$ and bias stability of 1.5 °/h, which was associated with feedback noise from the digital to analog converters (DACs).

Rate integrating operation of the gyroscope is experimentally demonstrated via FPGA-based closed loop control. An angular gain factor of ~0.8 and scale factor variation of 22 ppm RMS was measured over 2 h hours of rate integrating operation.

We believe, Dual Foucault Pendulum (DFP) is the minimal realization of a dynamically balanced lumped mass gyroscope. Combination of a simple gyro architecture and high-Q degenerate mode operation may potentially lead to low-cost, high performance MEMS gyroscopes.

Chapter 8

Conclusions

This Ph.D. dissertation reports novel fabrication processes and architectures in an effort to address challenges associated with Micro Rate Integrating Gyroscope (MRIG) operation, such as structural imperfections and energy dissipation. Majority of the focus is directed towards surface tension and pressure driven micro-glassblowing paradigm, which may serve as an enabling mechanism for wafer-scale fabrication of extremely symmetric and low internal loss 3-D micro-wineglass gyroscopes. New 2-D silicon MRIG architectures are also explored to bridge the gap between conventional micro-machining techniques and micro-glassblowing process, and to serve as a test platform for various MRIG control strategies. Closed loop Whole Angle operation of these 2-D silicon MRIG architectures is presented to identify some of the control challenges associated with MRIG control, such as energy pumping and suppression of errors caused by structural imperfections. Specific contributions of the dissertation are summarized below.

8.1 Contributions of the Dissertation

1. A new high temperature micro-glassblowing process for batch fabrication of 3-D low internal loss fused silica and ULE TSG wineglass structures was developed. The process was enabled by the development of an in-house high temperature glassblowing capability of 1800 °C with a cooling rate of $> 500\,^{\circ}\mathrm{C/min}$ and plasma assisted fusion bonding of TSG to fused silica. EDS spectral analysis of TSG before and after glassblowing revealed that the material retained its properties after glassblowing with no recrystallization or change in glass composition. AFM surface scans of the glassblown structures showed surface roughness of 0.23 nm Sa, which is 2× smaller than the roughness of the optically smooth device wafer.

2. For the first time, sub-1 Hz frequency symmetry in micro-glassblown wineglass resonators with integrated electrode structures was demonstrated. A new fabrication process based on deep glass dry etching was developed to fabricate micro-wineglasses with self-aligned stem structures and integrated electrodes. The wineglass modes were identified by electrostatic excitation and mapping the velocity of motion along the perimeter using laser Doppler interferometry. A frequency split (Δf) of 0.15 Hz and 0.2 Hz was demonstrated for n = 2 and n = 2 wineglass modes, respectively. To verify the repeatability of the results a total of 5 devices were tested, 3 out of 5 devices showed $\Delta f < 5$ Hz. Frequency split stayed below 1 Hz for DC bias voltages up to 100 V, confirming that the low frequency split is attributed to high structural symmetry and not to capacitive tuning.

3. Q-factors over 1 million, on wafer-level micro-glassblown 3-D fused silica wineglass resonators at a compact size of 7 mm diameter and center frequency of 105 kHz was reported. In addition, out-of-plane capacitive transduction on MEMS wineglass resonators. High Q-factor was achieved by implementation of a high aspect ratio, self-

aligned glassblown stem structure, careful surface treatment of the perimeter area, and low internal loss fused silica material. Out-of-plane electrode architecture enables the use of sacrificial layers to define the capacitive gaps, as a result 10 µm capacitive gaps have been demonstrated on a 7 mm shell. This resulted in over 9 pF of active capacitance within the device.

4. A test-bed for rapid characterization of micro-wineglass structures was reported. Two interchangeable modes of excitation are presented: Mechanical pinging and electrostatic excitation. Mechanical pinging is provided by a piezo actuated probe assembly, whereas electrostatic excitation is provided by assembled electrode structures with $<$ 20 µm capacitive gaps. Two modes of detection are also available: Optical pick-up and capacitive detection. Optical pick-up is provided by laser Doppler vibrometry (LDV) and capacitive detection is provided by assembled electrode structures. 3D micro-glassblown wineglass resonators were used to demonstrate the capabilities of the test-bed in extracting resonator parameters such as Q-factor or frequency split between degenerate wineglass modes. By decoupling the resonator development from electrode fabrication, a greater flexibility in design and fabrication is obtained.

5. A toroidal ring gyroscope with Q-factor above 100,000 at a central frequency of ~70 kHz was designed and implemented in wafer-level epitaxial silicon encapsulation process. The gyroscope consists of a robust ring anchor and a distributed suspension system. In contrast to axi-symmetric designs with central support structures, the vibrational energy in the introduced design is concentrated towards the innermost ring, and the device is anchored at the outer perimeter. The distributed support structure prevents vibrational motion propagating to the outer anchor, which helps trap the vibrational energy within the gyroscope. Higher order wineglass modes (n = 3) were also explored as a part of this design, with the goal of reducing frequency splits (Δf) induced by anisotropic modulus of elasticity of silicon. Frequency splits as low as 8.5 Hz Hz were

demonstrated at a center frequency of ~70 kHz.

6. Parametric drive of a MEMS rate integrating gyroscope was presented for the first time. Parametric pumping was used to bypass the errors associated with finding the orientation of the standing wave, time delay in the calculation and x-y drive gain drift. This resulted in as high as 14× improvement in scale factor stability compared to conventional x-y drive and better than 20 ppm scale factor stability without any compensation or temperature stabilization. In addition, parametric drive reduces drive to pick-off electrical feed-through by creating a frequency separation between drive and pick-off channels.

7. A new type of Micro Rate Integrating Gyroscope architecture, Dual Foucault Pendulum (DFP) is presented, to serve as a test platform for MRIG control algorithms. The Dual Foucault Pendulum (DFP) gyroscope consists of two dynamically equivalent, mechanically coupled proof masses, oscillating in anti-phase motion. This dual axis tuning fork behavior creates a dynamically balanced resonator with x-y symmetry in frequency and damping. Dual axis tuning fork behavior provides vibration immunity and anchor loss mitigation, resulting in a Q-factor over 300,000 on both modes at a center frequency of 3.2 kHz. Due to high-Q degenerate mode operation, open-loop performance of $0.003\,°/\sqrt{\mathrm{h}}$ ARW and 0.27 °/h in-run bias stability were experimentally demonstrated. Whereas FRB operation showed higher noise with an ARW of $0.06\,°/\sqrt{\mathrm{h}}$ and bias stability of 1.5 °/h, which was associated with feedback noise from the digital to analog converters (DACs). Rate integrating operation of the gyroscope is experimentally demonstrated via FPGA-based closed loop control. An angular gain factor of ~0.8 and scale factor variation of 22 ppm RMS was measured over 2 h hours of rate integrating operation. It is believed that the Dual Foucault Pendulum (DFP) is the minimal realization of a dynamically balanced MRIG.

8.2 Future Research Directions

8.2.1 CMOS/Micro-wineglass Integration

Micro-glassblown wineglass resonators with out-of-plane electrode structures were demonstrated as part of this thesis. Due to the simplicity of the out-of-plane electrode architecture, the process can be modified to include CMOS front-end electronics. This can be achieved by replacing the fused silica out-of-plane electrode wafer with a CMOS wafer, so that the metal electrode structures that were previously defined on the fused silica wafer, can instead be defined on the top layer of the CMOS wafer. Integration of CMOS into the fabrication process would permit placement of front-end electronics right underneath the electrode structures, which has potential advantages in terms of reduction of parasitic currents and improving signal-to-noise ratio.

8.2.2 Parametrically Driven Micro-wineglass Gyroscopes

Parametric drive can be used to improve robustness of Micro-wineglass Rate Integrating Gyroscopes. Specifically, to achieve parametric drive on fused silica micro-glassbown wineglass gyroscopes, either continuous ring electrodes can be defined on out-of-plane electrode structures or secondary micro-glassblown structures can be placed around the micro-wineglass shell.

8.2.3 Virtual Carouseling for System Identification

Another advantage of Rate Integrating Gyroscope architectures is the ability to do virtual carouseling, which has the potential of making imperfections within the gyroscope observable.

Examples include, aniso-elasticity, aniso-damping, electrode misalignments, x-y forcer and pick-off gain balance. Characterization of these parameters through vitual carouseling, may lead to a path towards continuous, run-time self-calibration.

8.2.4 Multi-stacked Micro-glassblowing

Plasma assisted fusion bonding process demonstrated in this thesis can be used to create stacks of three or more bonded fused silica wafers. Wet etching can be used, prior to bonding, to create cavities at each layer, which would permit micro-glassblowing of complex multi-bubble architectures. If metal layers are also introduced in between the wafers, this kind of technique can be used to define capacitive gaps by micro-glassblowing electrode structures on top of micro-glassblown resonators. Other examples include, hermetic cap layers on top of micro-glassblown resonators, 3-D tuning-fork architectures, and coupled micro-glassblown resonators.

8.2.5 Micro-glassblown Optical Sensors and Systems

A high temperature fused silica micro-glassblowing process developed in this dissertation is able to produce arrays of 3-D fused silica structures on top of a fused silica substrate. In the absence of any metal or additional coating, entire wafer stack is transparent. Due to high purity and optical transparency of fused silica, a wide variety of optical sensors and systems can be created using this technique. Examples include, optical resonators, opto-mechanical systems, lens and mirror arrays.

8.2.6 Micro-glassblown Micro-fluidic Devices

Monolithic glass micro-fluidic devices can be created by defining micro-channels on the substrate layer of the micro-glassblowing process. This way transparent micro-channels can be created with very good chemical resistance and low pressure drop, thanks to the near-circular profile of micro-glassblown channels. Optical interrogation techniques can also be applied with ease, thanks to the transparency of glass micro-channels. Finally, micro-glassblown micro-lenses and mirrors can be co-fabricated with the micro-channels.

Bibliography

[1] A. M. Shkel. Type I and Type II Micromachined Vibratory Gyroscopes. In *IEEE/ION Position Location and Navigation Symposium (PLANS)*, pages 586–593, San Diego, California, USA, 2006.

[2] D. M. Rozelle. The Hemispherical Resonator Gyro: From Wineglass to the Planets. In *AAS/AIAA Space Flight Mechanics Meeting*, pages 1157–1178, 2009.

[3] M. Weinberg, R. Candler, S. Chandorkar, J. Varsanik, T. Kenny, and A. Duwel. Energy Loss in MEMS Resonators and The impact n Inertial and RF Devices. In *Solid-State Sensors, Actuators and Microsystems Conference (TRANSDUCERS)*, pages 688–695, 2009.

[4] T. Niu and M. Palaniapan. A Low Phase Noise 10MHz Micromechanical Lamé-mode Bulk Oscillator Operating in Nonlinear Region. *IEEE International Frequency Control Symposium (FCS)*, pages 189–194, 2010.

[5] C. C. Painter and A. M. Shkel. Active Structural Error Suppression in MEMS Vibratory Rate Integrating Gyroscopes. *IEEE Sensors Journal*, 3(5):595–606, 2003.

[6] Y. Okada and Y. Tokumaru. Precise determination of lattice parameter and thermal expansion coefficient of silicon between 300 and 1500 K. *Journal of Applied Physics*, 56(2):314, 1984.

[7] Z. Hao and F. Ayazi. Thermoelastic Damping in Flexural-Mode Ring Gyroscopes. *International Mechanical Engineering Congress and Exposition*, pages 335–343, 2005.

[8] T. Ray, H. Zhu, and I. Elango. Characterzaton of KMPR 1025 as a masking layer for deep reactve ion etchng of fused silica. In *IEEE International Conference on Micro Electro Mechanical Systems (MEMS)*, pages 213–216, Cancun, Mexico, 2011.

[9] K. Kolari, V. Saarela, and S. Franssila. Deep plasma etching of glass for fluidic devices with different mask materials. *Journal of Micromechanics and Microengineering*, 18(6):1–6, 2008.

[10] D. D. Lynch. Vibratory Gyro Analysis by The Method of Averaging. In *Saintt Petersburg Conference on Gyroscopic Technology and Navigation*, pages 26–34, Saint Petersburg, Russia, 1995.

[11] B. Friedland and M. Hutton. Theory and Error Analysis of Vibrating-Member Gyroscope. *IEEE Transactions on Automatic Control*, 23(4):545–556, 1978.

[12] D. D. Lynch. Coriolis Vibratory Gyros. In *Symposium Gyro Technology*, Stuttgart, Germany, 1998.

[13] IEEE Standard Specification Format Guide and Test Procedure for Single-Axis Interferometric Fiber Optic Gyros - IEEE Std 952. Technical report, 1997.

[14] C. Zener. Internal Friction in Solids I. Theory of Internal Friction in Reeds. *Physical review*, 52:230–234, 1937.

[15] C. Zener. Internal Friction in Solids II. General Theory of Thermoelastic Internal Friction. *Physical Review*, 53:90–99, 1938.

[16] E. J. J. Loper and D. D. Lynch. Sonic vibrating bell gyro. *US Patent 4,157,041*, 1979.

[17] L. Kumar, M. J. Foster, and T. A. Bittner. Vibratory Rotation Sensor with AC Forcing and Sensing Electronics. *US Patent 5,850,041*, 1998.

[18] D. Lynch. Bell gyro and improved means for operating same. *US Patent 3,656,354*, 1972.

[19] A. Meyer and D. Rozelle. Milli-HRG Inertial Navigation System. In *IEEE/ION Position Location and Navigation Symposium (PLANS)*, pages 24–29, Myrtle Beach, South Carolina, USA, 2012.

[20] R. E. Stewart. Micro Hemispheric Resonator Gyro. *US Patent 8,109,145*, 2007.

[21] G. Johnson. Vibratory Sensor with Self-Calibration and Low Noise Digital Conversion. *US Patent 6,189,382*, 2001.

[22] A. Jeanroy. Gyroscopic Sensor. *US Patent 6,662,656*, 2000.

[23] A. Jeanroy. Method for Calibrating a Scale Factor in an Axisymmetrical Vibrating Gyrometer. *US Patent 8,210,023*, 2008.

[24] A. Jeanroy and P. Leger. Gyroscopic Sensor and Rotation Measurement Apparatus Constituting an Application Thereof. *US Patent 6,474,161*, 2002.

[25] A. Renault. Method for Implementing a Resonator Under Electrostatic Forces. *US Patent 7,127,946*, 2006.

[26] A. Renault and P. Vandebeuque. Hemispherical Resonator with Divided Shield Electrode. *US Patent 6,945,109*, 2005.

[27] A. M. Shkel and R. T. Howe. Micro-Machined Angle-Measuring Gyroscope. *US Patent 6,481,285*, 2002.

[28] C. C. Painter and A. M. Shkel. Active Structural Error Suppression in MEMS Vibratory Rate Integrating Gyroscopes. *IEEE Sensors Journal*, 3:595–606, 2003.

[29] C. C. Painter and A. M. Shkel. Experimental Evaluation of a Control System for an Absolute Angle Measuring Micromachined Gyroscope. In *IEEE Sensors Conference*, pages 1084–1087, Irvine, California, USA, 2005.

[30] A. A. Trusov, A. R. Schofield, and A. M. Shkel. Micromachined Tuning Fork Gyroscopes with Ultra-High Sensitivity and Shock Rejection. *US Patent 8,322,213*, 2012.

[31] I. P. Prikhodko, A. a. Trusov, and A. M. Shkel. Compensation of Drifts in High-Q MEMS Gyroscopes Using Temperature Self-sensing. *Sensors and Actuators A: Physical*, 201:517–524, 2013.

[32] A. A. Trusov, D. M. Rozelle, G. Atikyan, S. A. Zotov, B. R. Simon, A. M. Shkel, and A. D. Meyer. Non-axisymmetric Coriolis Vibratory Gyroscope with Whole Angle, Force Rebalance, and Self-Calibration. In *Solid-State Sensors, Actuators, and Microsystems Workshop (Hilton Head)*, pages 419–422, Hilton Head Island, South Carolina, USA, 2014.

[33] C. Guo, E. Tatar, and G. K. Fedder. Large-Displacement Parametric Resonance Using a Shaped Comb Drive. In *IEEE International Conference on Micro Electro Mechanical Systems (MEMS)*, pages 173–176, Taipei, Taiwan, 2013.

[34] E. Tatar, T. Mukherjee, and G. K. Fedder. Simulation of Stress Effects on Mode-Matched MEMS Gyroscope Bias and Scale Factor. In *IEEE/ION Position Location and Navigation Symposium (PLANS)*, pages 16–20, Monterey, California, USA, 2014.

[35] E. Tatar, T. Mukherjee, and G. K. Fedder. On-Chip Characterization of Stress Effects on Gyroscope Zero Rate Output and Scale Factor. In *IEEE International Conference on Micro Electro Mechanical Systems (MEMS)*, pages 813–816, Estoril, Portugal, 2015.

[36] M. P. Varnham, D. Hodgins, T. S. Norris, and H. D. Thomas. Vibrating Planar Gyro. *US Patent 5,226,321*, 1993.

[37] B. Gallacher, J. Hedley, J. Burdess, A. Harris, A. Rickard, and D. King. Electrostatic Correction of Structural Imperfections Present in a Microring Gyroscope. *IEEE/ASME Journal of Microelectromechanical Systems*, 14(2):221–234, 2005.

[38] B. Gallacher. Principles of a Micro-Rate Integrating Ring Gyroscope. *IEEE Transaction on Aerospace and Electronic Systems*, 48(1):658–672, 2012.

[39] S. R. Bowles, B. J. Gallacher, Z. X. Hu, C. Gregory, and K. Townsend. Control Scheme for a Rate Integrating MEMS Gyroscope. In *IEEE International Symposium on Inertial Sensors and Systems (ISISS)*, pages 25–28, Laguna Beach, California, USA, 2014.

[40] F. Ayazi and K. Najafi. Design and Fabrication of High-Performance Polysilicon Vibrating Ring Gyroscope. In *IEEE International Conference on Micro Electro Mechanical Systems (MEMS)*, 1998.

[41] F. Ayazi, H. Chen, F. Kocer, H. Guohong, and K. Najafi. A High Aspect-Ratio Polysilicon Vibrating Ring Gyroscope. In *Solid-State Sensors, Actuators, and Microsystems Workshop (Hilton Head)*, pages 289–292, Hilton Head Island, South Carolina, USA, 2000.

[42] F. Ayazi and K. Najafi. A HARPSS Polysilicon Vibrating Ring Gyroscope. *IEEE/ASME Journal of Microelectromechanical Systems*, 10(2):169–179, 2001.

[43] F. Ayazi and K. Najafi. High Aspect-Ratio Polysilicon Micromachining Technology. *Sensors and Actuators A: Physical*, 87(1-2):46–51, 2000.

[44] F. Ayazi and K. Najafi. High Aspect-Ratio Combined Poly and Single-Crystal Silicon (HARPSS) MEMS technology. *IEEE/ASME Journal of Microelectromechanical Systems*, 9(3):288–294, 2000.

[45] A. D. Challoner and K. V. Shcheglov. Isolated Resonator Gyroscope with a Drive and Sense Plate. *US Patent 7,093,486*, 2006.

[46] A. D. Challoner, H. H. Ge, and J. Y. Liu. Boeing Disc Resonator Gyroscope. In *IEEE/ION Position Location and Navigation Symposium (PLANS)*, pages 504–514, Savannah, Georgia, USA, 2014.

[47] R. Kubena and D. Chang. Disc Resonator Gyroscopes. *US Patent 7,581,443*, 2009.

[48] D. Kim and R. T. M'Closkey. Noise Analysis of ClosedLoop Vibratory Rate Gyros. *American Control Conference (ACC)*, pages 92–97, 2012.

[49] D. Kim and R. T. M'Closkey. Spectral Analysis of Vibratory Gyro Noise. *IEEE Sensors Journal*, 13(11):4361–4374, 2013.

[50] D. Schwartz, D. Kim, and R. M. Closkey. A Model-Based Approach to Multi-Modal Mass Tuning of a Micro-Scale Resonator. In *IEEE American Control Conference (ACC)*, 2012.

[51] D. Schwartz and R. T. MCloskey. Decoupling of a Disk Resonator From Linear Acceleration Via Mass Matrix Perturbation. *Journal of Dynamic Systems, Measurement, and Control*, 134(2):021005, 2012.

[52] D. Kim, A. Behbahani, R. T. M'Closkey, P. Stupar, and J. Denatale. Wafer-Scale Etch Process for Precision Frequency Tuning of MEMS Gyros. In *IEEE International Symposium on Inertial Sensors and Systems (ISISS)*, pages 1–2, Hapuna Beach, HI, USA, 2015.

[53] E. Ng, H. Lee, C. Ahn, R. Melamud, and T. W. Kenny. Stability Measurements of Silicon MEMS Resonant Thermometers. In *IEEE Sensors Conference*, pages 1257–1260, Limerick, Ireland, 2011.

[54] S. Nitzan, C. H. Ahn, T.-H. Su, M. Li, E. J. Ng, S. Wang, Z. M. Yang, G. O'Brien, B. E. Bose, T. W. Kenny, and D. A. Horsley. Epitaxially-Encapsulated Polysilicon Disk Resonator Gyroscope. In *IEEE International Conference on Micro Electro Mechanical Systems (MEMS)*, pages 625–628, Taipei, Taiwan, 2013.

[55] C. H. Ahn, E. J. Ng, V. A. Hong, Y. Yang, B. J. Lee, M. W. Ward, and T. W. Kenny. Geometric Compensation of (100) Single Crystal Silicon Disk Resonating Gyroscope for Mode-Matching. In *Solid-State Sensors, Actuators and Microsystems Conference (TRANSDUCERS)*, number June, pages 1723–1726, Barcelona, Spain, 2013.

[56] S. Nitzan, T. H. Su, C. Ahn, E. Ng, V. Hong, Y. Yang, T. Kenny, and D. A. Horsley. Impact of Gyroscope Operation Above The Critical Bifurcation Threshold on Scale Factor and Bias Instability. In *IEEE International Conference on Micro Electro Mechanical Systems (MEMS)*, pages 749–752, San Francisco, CA, USA, 2014.

[57] P. Taheri-Tehrani, O. Izyumin, I. Izyumin, C. H. Ahn, E. J. Ng, V. A. Hong, Y. Yang, T. W. Kenny, B. E. Boser, and D. A. Horsley. Disk Resonator Gyroscope with Whole-angle Mode Operation. In *IEEE International Symposium on Inertial Sensors and Systems (ISISS)*, pages 1–4, Hapuna Beach, HI, USA, 2015.

[58] J. Cho, J. Gregory, and K. Najafi. Single-Crystal-Silicon Vibratory Cylinderical Rate Integrating Gyroscope (CING). In *Solid-State Sensors, Actuators and Microsystems Conference (TRANSDUCERS)*, pages 2813–2816, 2011.

[59] J. Y. Cho. *High-performance Micromachined Vibratory Rate and Rate-integrating Gyroscopes*. PhD thesis, University of Michigan, 2012.

[60] J. Gregory, J. Cho, and K. Najafi. MEMS Rate and Rate-Integrating Gyroscope Control with Commercial Software Defined Radio Hardware. In *Solid-State Sensors, Actuators and Microsystems Conference (TRANSDUCERS)*, pages 2394–2397, 2011.

[61] J. Gregory, J. Cho, and K. Najafi. Novel Mismatch Compensation Methods for Rate-Integrating Gyroscopes. In *IEEE/ION Position Location and Navigation Symposium (PLANS)*, pages 252–258, Myrtle Beach, South Carolina, USA, 2012.

[62] J. Gregory, J. Cho, and K. Najafi. Characterization and control of a high-Q MEMS inertial sensor using low-cost hardware. In *IEEE/ION Position Location and Navigation Symposium (PLANS)*, pages 239–247, Myrtle Beach, South Carolina, USA, 2012.

[63] J. Cho, J. Gregory, and K. Najafi. High-Q, 3kHz Single-Crystal-Silicon Cylindrical Rate-Integrating Gyro (CING). In *IEEE International Conference on Micro Electro Mechanical Systems (MEMS)*, pages 172–175, Paris, France, 2012.

[64] H. Johari and F. Ayazi. Capacitive Bulk Acoustic Wave Silicon Disk Gyroscopes. In *IEEE International Electron Devices Meeting*, pages 1–4, San Francisco, CA, USA, 2006.

[65] H. Johari. *Micromachined Capacitive Silicon Bulk Acoustic Wave Gyroscopes*. PhD thesis, Georgia Institute of Technology, 2008.

[66] H. Johari and F. Ayazi. High-Frequency Capacitive Disk Gyroscopes in (100) and (111) Silicon. In *IEEE International Conference on Micro Electro Mechanical Systems (MEMS)*, pages 47–50, Hyogo, Japan, 2007.

[67] F. Ayazi and H. Johari. Capacitive Bulk Acoustic Wave Disk Gyroscopes. *US Patent 7,543,496*, 2009.

[68] L. C. Fegely, D. N. Hutchison, and S. A. Bhave. Isotropic Etching of 111 SCS for Wafer-Scale Manufacturing of Perfectly Hemispherical Silicon Molds. In *Solid-State Sensors, Actuators and Microsystems Conference (TRANSDUCERS)*, pages 2295–2298, Beijing, China, 2011.

[69] A. K. Bhat, L. C. Fegely, and S. A. Bhave. GOBLIT : A Giant Opto-Mechanical Bulk-Machined Light Transducer. In *Solid-State Sensors, Actuators and Microsystems Workshop (Hilton Head)*, pages 247–250, Hilton Head Island, South Carolina, USA, 2014.

[70] P. Shao, L. D. Sorenson, X. Gao, and F. Ayazi. Wineglass-on-a-Chip. In *Solid-State Sensors, Actuators, and Microsystems Workshop (Hilton Head)*, volume 7, pages 275–278, Hilton Head Island, South Carolina, USA, 2012.

[71] L. D. Sorenson, X. Gao, and F. Ayazi. 3-D Micromachined Hemispherical Shell Resonators with Integrated Capacitive Transducers. In *IEEE International Conference on Micro Electro Mechanical Systems (MEMS)*, pages 168–171, Paris, France, 2012.

[72] L. D. Sorenson, P. Shao, and F. Ayazi. Effect of Thickness Anisotropy on Degenerate Modes in Oxide Micro-Hemispherical Shell Resonators. In *IEEE International Conference on Micro Electro Mechanical Systems (MEMS)*, pages 169–172, Taipei, Taiwan, 2013.

[73] L. D. Sorenson. *Design and Analysis of Microelectromechanical Resonators with Ultra-Low Dissipation*. PhD thesis, Georgia Institute of Technology, 2013.

[74] M. L. Chan, J. Xie, P. Fonda, H. Najar, K. Yamazaki, L. Lin, and D. A. Horsley. Micromachined Polycrystalline Diamond Hemispherical Shell Resonators. In *Solid-State Sensors, Actuators, and Microsystems Workshop (Hilton Head)*, pages 355–358, Hilton Head Island, South Carolina, USA, 2012.

[75] H. Najar, A. Heidari, M.-L. Chan, H.-A. Yang, L. Lin, D. G. Cahill, and D. A. Horsley. Microcrystalline Diamond Micromechanical Resonators with Quality Factor Limited by Thermoelastic Damping. *Applied Physics Letters*, 102(7):071901, 2013.

[76] A. Heidari, M. Chan, H.-A. Yang, G. Jaramillo, P. Taheri-Tehrani, P. Fonda, H. Najar, K. Yamazaki, L. Lin, and D. A. Horsley. Micromachined Polycrystalline Diamond Hemispherical Shell Resonators. In *Solid-State Sensors, Actuators, and Microsystems Conference (TRANSDUCERS)*, pages 2415–2418, Barcelona, Spain, 2013.

[77] P. Taheri-Tehrani, T. Su, A. Heidari, G. Jaramillo, C. Yang, S. Akhbari, H. Najar, S. Nitzan, D. Saito, L. Lin, and D. A. Horsley. Micro-Scale Diamond Hemispherical Resonator Gyroscope. In *Solid-State Sensors, Actuators, and Microsystems Workshop (Hilton Head)*, pages 289–292, Hilton Head Island, South Carolina, USA, 2014.

[78] D. Saito, C. Yang, A. Heidari, H. Najar, L. Lin, and D. A. Horsley. Batch-Fabricated High Q-Factor Microcrystalline Diamond Cylindrical Resonator. In *IEEE International Conference on Micro Electro Mechanical Systems (MEMS)*, pages 801–804, Estoril, Portugal, 2015.

[79] J. J. Bernstein, M. G. Bancu, E. H. Cook, M. V. Chaparala, W. A. Teynor, and M. S. Weinberg. A MEMS Diamond Hemispherical Resonator. *Journal of Micromechanics and Microengineering*, 23(12):125007, 2013.

[80] P. Pai, F. K. Chowdhury, C. H. Mastrangelo, and M. Tabib-Azar. MEMS-Based Hemispherical Resonator Gyroscopes. In *IEEE Sensors Conference*, Taipei, Taiwan, 2012.

[81] P. Pai, F. K. Chowdhury, H. Pourzand, and M. Tabib-azar. Fabrication and Testing of Hemispherical MEMS Wineglass Resonators. In *IEEE International Conference on Micro Electro Mechanical Systems (MEMS)*, pages 677–680, Taipei, Taiwan, 2013.

[82] Y. Xie, H. C. Hsieh, P. Pai, H. Kim, M. Tabib-Azar, and C. H. Mastrangelo. Precision Curved Micro Gemispherical Resonator Shells Fabricated by Poached-Egg Micro-Molding. In *IEEE Sensors Conference*, pages 279–283, Taipei, Taiwan, 2012.

[83] M. Rahman, Y. Xie, C. Mastrangelo, and H. Kim. 3-D Hemispherical Micro Glass-shell Resonator with Integrated Electrostatic Excitation and Capacitive Detection Transducers. In *IEEE International Conference on Micro Electro Mechanical Systems (MEMS)*, pages 672–675, San Francisco, CA, USA, 2014.

[84] R. Perahia, J. J. Lake, S. S. Iyer, D. J. Kirby, H. D. Nguyen, T. J. Boden, R. J. Joyce, L. X. Huang, L. D. Sorenson, and D. T. Chang. Electric Gradient Force Drive Mechanism for Novel Micro-Scale All-Dielectric Gyroscope. In *IEEE International Conference on Micro Electro Mechanical Systems (MEMS)*, pages 721–724, San Francisco, CA, USA, 2014.

[85] R. Perahia, H. D. Nguyen, L. X. Huang, T. J. Boden, J. J. Lake, D. J. Kirby, R. J. Joyce, L. D. Sorenson, and D. T. Chang. Novel Touch-Free Drive, Sense, and Tuning Mechanism for All-Dielectric Micro-Shell Gyroscope. In *Solid-State Sensors, Actuators and Microsystems Workshop (Hilton Head)*, pages 383–386, Hilton Head Island, South Carolina, USA, 2014.

[86] B. R. Johnson, C. Boynton, E. Cabuz, S. Chang, K. Christ, S. Moore, J. Reinke, and K. Winegar. Toroidal Resonators with Small Frequency Mismatch for Rate Integrating Gyroscopes. In *IEEE International Symposium on Inertial Sensors and Systems (ISISS)*, pages 5–8, Laguna Beach, California, USA, 2014.

[87] E. Hendarto, T. Li, and Y. B. Gianchandani. Investigation of Wine Glass Mode Resonance in 200-m-Diameter Cenosphere-Derived Borosilicate Hemispherical Shells. *Journal of Micromechanics and Microengineering*, 23(5):055013, 2013.

[88] M. Kanik, P. Bordeenithikasem, J. Schroers, D. Kim, and R. M'Closkey. Microscale Three-Dimensional Hemispherical Shell Resonators Fabricated from Metallic Glass. In *IEEE International Symposium on Inertial Sensors and Systems (ISISS)*, pages 9–12, Laguna Beach, California, USA, 2014.

[89] M. Kanik, P. Bordeenithikasem, D. Kim, N. Selden, A. Desai, R. M. Closkey, and J. Schroers. Metallic Glass Hemispherical Shell Resonators. *IEEE/ASME Journal of Microelectromechanical Systems*, 24(1):19–28, 2015.

[90] B. Sarac, G. Kumar, T. Hodges, S. Ding, A. Desai, and J. Schroers. Three-Dimensional Shell Fabrication Using Blow Molding of Bulk Metallic Glass. *IEEE/ASME Journal of Microelectromechanical Systems*, 20(1):28–36, 2011.

[91] J. Y. Cho, J. Yan, J. A. Gregory, H. Eberhart, R. L. Peterson, and K. Najafi. High-Q Fused Silica Birdbath and Hemispherical 3-D Resonators Made by Blow Torch Molding. In *IEEE International Conference on Micro Electro Mechanical Systems (MEMS)*, pages 177–180, Taipei, Taiwan, 2013.

[92] J. Y. Cho and K. Najafi. A High-Q All-Fused Silica Solid-Stem Wineglass Hemispherical Resonator Formed Using Micro Blow Torching snd Welding. In *IEEE International Conference on Micro Electro Mechanical Systems (MEMS)*, pages 821–824, Estoril, Portugal, 2015.

[93] J. Y. Cho, J. K. Woo, J. Yan, J. L. Peterson, and K. Najafi. Fused-Silica Micro Birdbath Resonator Gyroscope (μ-BRG). *IEEE/ASME Journal of Microelectromechanical Systems*, 23(1):66–77, 2013.

[94] J.-K. Woo, J. Y. Cho, C. Boyd, and K. Najafi. Whole-Angle-Mode Micromachined Fused-Silica Birdbath Resonator Gyroscope (WA-BRG). In *IEEE International Conference on Micro Electro Mechanical Systems (MEMS)*, pages 20–23, San Francisco, CA, USA, 2014.

[95] K. Visvanathan, T. Li, and Y. B. Gianchandani. 3D-SOULE: A fabrication Process for Large Scale Integration and Micromachining of Spherical Structures. In *IEEE International Conference on Micro Electro Mechanical Systems (MEMS)*, pages 45–48, Cancun, Mexico, 2011.

[96] E. J. Eklund and A. M. Shkel. Glass Blowing on a Wafer Level. *IEEE/ASME Journal of Microelectromechanical Systems*, 16(2):232–239, 2007.

[97] E. J. Eklund and A. M. Shkel. Self-Inflated Micro-Glass Blowing. *US Patent 8,151,600*, 2012.

[98] I. P. Prikhodko, S. A. Zotov, A. A. Trusov, and A. M. Shkel. Microscale glass-blown three-dimensional spherical shell resonators. *IEEE/ASME Journal of Microelectromechanical Systems*, 20(3):691–701, 2011.

[99] S. A. Zotov, I. P. Prikhodko, A. A. Trusov, and A. M. Shkel. 3-D Micromachined Spherical Shell Resonators with Integrated Electromagnetic and Electrostatic Transducers. In *Solid-State Sensors, Actuators, and Microsystems Workshop (Hilton Head)*, pages 11–14, Hilton Head Island, South Carolina, USA, 2010.

[100] D. Senkal, M. J. Ahamed, A. A. Trusov, and A. M. Shkel. High Temperature Microglassblowing Process Demonstrated on Fused Quartz and ULE TSG. *Sensors and Actuators A: Physical*, 201:525–531, 2012.

[101] D. Senkal, I. P. Prikhodko, A. A. Trusov, and A. M. Shkel. Micromachined 3-D Glass-Blown Wineglass Structures for Vibratory MEMS Applications. In *Technologies for Future Micro-Nano Manufacturing Workshop*, pages 166–169, Napa Valley, California, USA, 2011.

[102] M. Eichler, B. Michel, P. Hennecke, M. Gabriel, and C. Klages. Low-Temperature Direct Bonding of Borosilicate, Fused Silica, and Functional Coatings. In *International Symposium on Semiconductor Wafer Bonding: Science, Technology, and Applications*, volume 33, pages 339–348, Las Vegas, Nevada, USA, 2010.

[103] D. Senkal, M. J. Ahamed, a. a. Trusov, and a. M. Shkel. Adaptable Test-Bed for Characterization of Micro-Wineglass Resonators. In *IEEE International Conference on Micro Electro Mechanical Systems (MEMS)*, pages 469–472, Taipei, Taiwan, 2013.

[104] D. Senkal, M. J. Ahamed, A. A. Trusov, and A. M. Shkel. Electrostatic and Mechanical Characterization of 3-D Micro-Wineglass Resonators. *Sensors and Actuators A: Physical*, 215:150–154, 2014.

[105] M. J. Ahamed, D. Senkal, A. A. Trusov, and A. M. Shkel. Deep NLD Plasma Etching of Fused Silica and Borosilicate Glass. In *IEEE Sensors Conference*, pages 1767–1770, Baltimore, Maryland, USA, 2013.

[106] D. Senkal, M. J. Ahamed, A. A. Trusov, and A. M. Shkel. Demonstration of Sub-Hz Frequency Symmetry in Micro-Glassblown Wineglass Resonators with Integrated Electrodes. In *Solid-State Sensors, Actuators and Microsystems Conference (TRANSDUCERS)*, pages 1380–1383, Barcelona Spain, 2013.

[107] M. J. Ahamed, D. Senkal, and A. M. Shkel. Effect of Annealing on Mechanical Quality Factor of Fused Quartz Hemispherical Resonator. In *IEEE International Symposium on Inertial Sensors and Systems (ISISS)*, pages 59–62, Laguna Beach, California, USA, 2014.

[108] M. J. Ahamed, D. Senkal, and A. M. Shkel. Improvement of Side-Wall Roughness in Deep Glass Dry Etched MEMS Vibratory Sensors. In *IEEE International Symposium on Inertial Sensors and Systems (ISISS)*, pages 127–128, Laguna Beach, California, USA, 2014.

[109] D. Senkal, M. J. Ahamed, A. A. Trusov, and A. M. Shkel. Demonstration of Sub-1 Hz Structural Symmetry in Micro-Glassblown Wineglass Resonators with Integrated Electrodes. In *Solid-State Sensors, Actuators and Microsystems Conference (TRANSDUCERS)*, pages 1380–1383, Barcelona, Spain, 2013.

[110] B. S. Lunin. Physical and chemical bases for the development of hemispherical resonators for solid-state gyroscopes. *Moscow Aviation Institute, Moscow*, 2005.

[111] V. F. Zhuravlev and D. M. Klimov. A Hemispherical Resonator Gyroscope. *Moscow: Nauka*, 1985.

[112] N. E. Egarmin and V. E. Yurin. *Introduction to Theory of Vibratory Gyroscopes*. 1993.

[113] S. Y. Choi, Y. H. Na, and J. H. Kim. Thermoelastic Damping of Inextensional Hemispherical Shell. *World Academy of Science, Engineering and Technology*, 56:198–203, 2009.

[114] D. Senkal, M. J. Ahamed, A. A. Trusov, and A. M. Shkel. Achieving Sub-Hz Frequency Symmetry in Micro-Glassblown Wineglass Resonators. *IEEE/ASME Journal of Microelectromechanical Systems*, 23(1):30–38, 2014.

[115] D. Senkal, C. R. Raum, A. A. Trusov, and A. M. Shkel. Titania Silicate/Fused Quartz Flassblowing for 3-D Fabrication of Low Internal Loss Wineglass Micro-Structures. In *Solid-State Sensors, Actuators, and Microsystems Workshop (Hilton Head)*, pages 267–270, Hilton Head Island, South Carolina, USA, 2012.

[116] R. Leland. Mechanical-thermal noise in MEMS gyroscopes. *IEEE Sensors Journal*, 5(3):493–500, 2005.

[117] J. Y. Cho, T. Nagourney, A. Darvishian, B. Shiari, J. Woo, and K. Najafi. Fused Silica Micro Birdbath Shell Resonators with 1.2 Million Q and 43 Second Decay Time Constant. In *Solid-State Sensors, Actuators and Microsystems Workshop (Hilton Head)*, pages 103–104, Hilton Head Island, South Carolina, USA, 2014.

[118] D. Senkal, M. J. Ahamed, and A. M. Shkel. Design and Modeling of Micro-Glassblown Inverted-Wineglass Structures. In *IEEE Symposium on Inertial Sensors and Systems (ISISS)*, pages 13–16, Laguna Beach, California, USA, 2014.

[119] D. Senkal, M. J. Ahamed, S. Askari, and A. M. Shkel. 1 Million Q-Factor Demonstrated on Micro-glassblown Fused Silica Wineglass Resonators with Out-of-Plane Electrostatic Transduction. In *Solid-State Sensors, Actuators and Microsystems Workshop (Hilton Head)*, pages 68–71, Hilton Head Island, South Carolina, USA, 2014.

[120] D. Senkal, M. J. Ahamed, S. Askari, and A. M. Shkel. MEMS Micro-Glassblowing Paradigm for Wafer-Level Fabrication of Fused Silica Wineglass Gyroscopes. In *Eurosensors Conference*, pages 1489–1492, Brescia, Italy, 2014.

[121] D. Senkal, M. J. Ahamed, M. H. A. Ardakani, S. Askari, and A. M. Shkel. Out-of-Plane Electrode Architecture for Fused Silica Micro-Glassblown 3-D Wineglass Resonators. In *IEEE Sensors Conference*, pages 994 – 997, Valencia, Spain, 2014.

[122] D. Senkal, M. J. Ahamed, M. H. A. Ardakani, S. Askari, and A. M. Shkel. Demonstration of 1 Million Q-Factor on Microglassblown Wineglass Resonators With Out-of-Plane Electrostatic Transduction. *IEEE/ASME Journal of Microelectromechanical Systems*, 24(1):29–37, 2015.

[123] S. Chandorkar, M. Agarwal, R. Melamud, R. N. Candler, K. E. Goodson, and T. W. Kenny. Limits of quality factor in bulk-mode micromechanical resonators. In *IEEE International Conference on Micro Electro Mechanical Systems (MEMS)*, pages 74–77, Tucson, AZ, USA, 2008.

[124] J. Donea, S. Giuliani, and J. Halleux. An Arbitrary Lagrangian-Eulerian Finite Element Method for Transient Dynamic Fluid-Structure Interactions. *Computer Methods in Applied Mechanics and Engineering*, 33:689–723, 1982.

[125] C. Hirt, A. Amsden, and J. Cook. An Arbitrary Lagrangian-Eulerian Computing Method for All Flow Speeds. *Journal of Computational Physics*, 253(14):227–253, 1974.

[126] J. Shelby. *Introduction to Glass Science and Technology*. 2005.

[127] Z. Hao, S. Pourkamali, and F. Ayazi. VHF Single-Crystal Silicon Elliptic Bulk-Mode Capacitive Disk Resonators-Part I: Design and Modeling. *IEEE/ASME Journal of Microelectromechanical Systems*, 13(6):1043–1053, 2004.

[128] D. Senkal, S. Askari, M. J. Ahamed, E. J. Ng, V. Hong, Y. Yang, C. H. Ahn, T. W. Kenny, and A. M. Shkel. 100k Q-Factor Toroidal Ring Gyroscope Implemented in Wafer-Level Epitaxial Silicon Encapsulation Process. In *IEEE International Conference on Micro Electro Mechanical Systems (MEMS)*, pages 9–12, Taipei, Taiwan, 2014.

[129] D. Senkal, E. J. Ng, V. Hong, Y. Yang, C. H. Ahn, T. W. Kenny, and A. M. Shkel. Parametric Drive of a Toroidal MEMS Rate Integrating Gyroscope Demonstrating 20 ppm Scale Factor Stability. In *IEEE International Conference on Micro Electro Mechanical Systems (MEMS)*, pages 29–32, Estoril, Portugal, 2015.

[130] R. N. Candler, M. a. Hopcroft, B. Kim, W.-T. Park, R. Melamud, M. Agarwal, G. Yama, A. Partridge, M. Lutz, and T. W. Kenny. Long-Term and Accelerated Life Testing of a Novel Single-Wafer Vacuum Encapsulation for MEMS Resonators. *IEEE/ASME Journal of Microelectromechanical Systems*, 15(6):1446–1456, 2006.

[131] K. M. Harish, B. J. Gallacher, J. S. Burdess, and J. A. Neasham. Experimental Investigation of Parametric and Externally Forced Motion in Resonant MEMS Sensors. *Journal of Micromechanics and Microengineering*, 19(1):015021, 2009.

[132] L. A. Oropeza-Ramos, C. B. Burgner, and K. L. Turner. Robust Micro-rate Sensor Actuated by Parametric Resonance. *Sensors and Actuators A: Physical*, 152(1):80–87, 2009.

[133] D. Senkal, A. Efimovskaya, and A. M. Shkel. Minimal Realization of Dynamically Balanced Lumped Mass WA Gyroscope: Dual Foucault Pendulum. In *IEEE International Symposium on Inertial Sensors and Systems (ISISS)*, pages 131–134, Hapuna Beach, HI, USA, 2015.

[134] D. Senkal, A. Efimovskaya, and A. M. Shkel. Dual Foucault Pendulum Gyroscope. In *Solid-State Sensors, Actuators and Microsystems Workshop (TRANSDUCERS)*, Anchorage, Alaska, USA, 2015.

[135] J. Bernstein, S. Cho, A. T. King, P. Kourepenis, P. Maciel, and M. Wienberg. A Micromachined Comb-Drive Tuning Fork Rate Gyroscope. In *IEEE International Conference on Micro Electro Mechanical Systems (MEMS)*, pages 143–148, Fort Lauderdale, Florida, USA, 1993.

[136] A. A. Trusov, G. Atikyan, D. M. Rozelle, A. D. Meyer, S. A. Zotov, B. R. Simon, and A. M. Shkel. Flat is not dead: Current and future performance of Si-MEMS Quad Mass Gyro (QMG) system. In *IEEE/ION Position Location and Navigation Symposium (PLANS)*, pages 252–258, Savannah, Georgia, USA, 2014.

[137] A. Efimovskaya, D. Senkal, and A. M. Shkel. Miniature Origami-like Folded MEMS TIMU. In *Solid-State Sensors, Actuators and Microsystems Workshop (TRANSDUCERS)*, Anchorage, Alaska, USA, 2015.

[138] A. Efimovskaya, D. Senkal, and A. M. Shkel. Origami-like Folded MEMS for Realization of TIMU: Fabrication Technology and Initial Demonstration. In *IEEE International Symposium on Inertial Sensors and Systems (ISISS)*, pages 58–61, Hapuna Beach, HI, USA, 2015.

[139] S. Choi and J. H. Kim. Natural Frequency Split Estimation for Inextensional Vibration of Imperfect Hemispherical Shell. *Journal of Sound and Vibration*, 330(9):2094–2106, 2011.

Appendix A

Cleanroom Recipes

A.1 AZ4620 Lithography - 5000 rpm with 10 W power

Overview	
Input	Wafer(s) in wafer containers, photomask
Consumables	AZ4620 photoresist, aluminum foil, cleanroom wipe
Equipment	MA6 aligner, Laurell spinner, Soft-bake furnace (90 °C), Hard-bake furnace (120 °C)
Output	Photoresist coated wafers

Critical Parameters	
Adhesion	45 mins dehyration @ 120 °C followed by HMDS
Spin	AZ4620, 500 rpm 10 secs - 5000 rpm 40 secs (ACCL 5 for both)
Soft-bake	20 minutes @ 90 °C
Exposure	Soft-contact @ 25 µm, 35 secs exposure @ 10 W lamp power
Development	3.5:1 - AZ400K:DI water, 30 seconds to 1 minute
Hard-bake	Optional

A.1.0.1 Important Notes

Recipe is only valid for 10 W power on MA6, do not use if the lamp power is different.

A.1.0.2 Process

1. Make sure that you know which side of the wafer is up, this is particularly difficult to tell on glass wafers.

   After this point onward the top side of the wafer should never touch anything, i.e. it should not be placed upside down onto a cleanroom wipe or aluminum foil.

2. Place a large enough aluminum foil into soft-bake furnace, wafers will be placed on this aluminum foil.

3. Dehydrate the wafers at 120 °C in the clean dehydration furnace for 45 minutes (the one in the stepper room, do not use the furnace in the lithography room for this step).

4. Apply HMDS inside the HMDS furnace.

   Watch the LCD screen during your run to make sure the HMDS is actually doing its job. Make sure that the yellow light is blinking at the end of your run.

5. Spinning:

   (a) Make sure the spinner is clean, if previous user left resist residue clean with acetone and wipe with cleanroom wipes.

   (b) If it is an important wafer or you are doing 4 wafers or more at a time buy new resist. Resist couple months old causes problems.

   Each bottle lasts for about 8 wafers if you are generous with your resist.

   (c) Set Laurell spinner to:

      i. 1st step: 500 rpm, accel. 5, 10 seconds

      ii. 2nd step: 5000 rpm, accel. 5, 40 seconds

   (d) Place the wafer on the spinner, check for vacuum.

   (e) If the vacuum is working center the wafer.

(f) Do a dry run to make sure the program works.

(g) Hit F1 twice to reset the recipe.

If you don't do this it continues from the previous run and messes up your spin.

(h) Take off the glass pipette inside the photoresist bottle and throw it away, we do not use the pippette.

(i) Pour photoresist to about 2/3 of the wafer, do not use the pippette. At this step pouring more than necessary is always better than pouring not enough.

(j) Spin the resist, put the wafer into the soft-bake furnace for 20 minutes onto the aluminum foil.

Never place wafers into furnaces without an extra layer of aluminum foil. We have double-sided processes that are very sensitive to contamination on the back-side of your wafer.

(k) When done, wipe the photoresist bottle with a dry cleanroom wipe, this minimizes dried resist particulates next time you do lithorgraphy.

(l) Cleanup the spinner, dump the acetone container of the spinner.

6. Exposure:

(a) When soft-bake is done, get your wafers and mask ready near MA-6.

(b) Inspect the photomask visually, if there is any visible photoresist residue do a solvent clean on the photomask. If it does not remove the residue, a proper mask clean is required.

Never place the mask onto cleanroom wipe, always hold from the edges and dry it while holding. Masks start getting dirty only after 12 or so wafers, so it is usually not an issue. However, if you have fine features (i.e. SOI process, or metal traces) dirt on the mask will mess up your lithography by pushing the mask away from the wafer.

(c) Place the mask, blow nitrogen on it, load it.

(d) Always do a lamp test on the MA-6 aligner before your first run, there is a button for it, just push the button, kneel down and look at the power supply. It should read 10 W. If it is not, stop and talk with Jake.

(e) Set the mask aligner to soft-contact with 25 µm gap. 35 seconds exposure time.

(f) Use the wafer alignments knobs that are around the stage that holds the wafer and set them both (x and y) to 10.00 mm exactly.

If you don' t do this the mask will not be centered on the wafer which can cause you to lose the dies at the edges.

(g) Place the wafer, make sure that the white mark on the stage aligns with the aluminum pin. So that your wafer is not rotated at all.

(h) Turn on vacuum, check the vacuum by trying to gently nudge the wafer with your tweezers.

(i) Blow nitrogen on the wafer.

(j) Align the wafer if you need alignment. If you started from 10.00 mm on x and y, the alignment marks should be very close.

Make sure both alignment marks are aligned perfectly. If you can't find the alignment marks or alignment marks are damaged, stop and do not expose.

(k) Expose, make sure that the tool is moving before you turn your eyes away.

(l) You will have to move the wafers to the second lithography room, try to keep them in a dark container while doing that.

7. Development:

   (a) Fill one container with 50 ml AZ400K and 175 ml water, 1:3.5 ratio. This is the minimum amount you should use, if you are doing more than 5 wafers use 100 ml AZ400K and 350 ml water.

If you don't use enough, development time starts drifting from wafer to wafer.

(b) Fill a second container fully with DI water.

(c) Develop for 30 seconds to 1 minute.

i. Shake the bowl once every 15 seconds.

ii. Grab the wafer with tweezers every 1 minute, raise it a little bit and inspect if the development is done. The motion will also help the development go smoother by mixing the developer.

(d) If the features are beginning to show up do the following to remove the wafer from the developer solution:

i. Turn on the DI water

ii. Remove the wafer, immediately dunk it into the DI water container, remove it, immediately rinse it with the running water.

iii. Place the wafer on a cleanroom wipe face-side up.

iv. Blow nitrogen.

v. Move the wafer to a different spot so that the backside dries.

vi. Blow nitrogen.

Under no condition do not turn the wafer upside down.

Repeat this procedure every time you remove the wafer from the developer.

8. Inspect the wafer with the microscope to see if the development is done, if not continue developing for another 15 seconds.

If it is complete you should see a completely clean, smooth, pink surface (on silicon substrate) in the exposed areas. On glass you will be able see behind the wafer.

9. Observe the wafer at multiple positions, make sure the lithography is right:

(a) Look for under-developed areas that shows as thin pink lines.

(b) Look for dried resist residue

(c) Look at the finest features on the wafer to see if they have fallen off or are deformed. This is usually the alignment mark on most of our wafers.

A.2 Poly-Si Removal for Plasma Bonding

Overview	
Input	Wafer(s) in separate plastic petri-dishes
Consumables	400 ml 45% pre-mixed KOH solution, clean-room wipes, aluminum foil, plastic petri-dishes or wafer pucks
Equipment	4 pieces of 5" Pyrex container, plastic mesh, closed loop hot-plate
Output	Stripped wafer(s), picture of the wafer after strip

A.2.0.3 Important Notes

Normally a single KOH bath is enough to strip Poly-Si from wafers, however if plasma bonding is going to be performed, this is not enough. Even nanometer amounts of Poly-Si residue can prevent bonding of the wafers. This recipe encompasses steps to prevent this problem.

A.2.0.4 Process

1. Before you start, make sure that you are working with fresh KOH. It is very common to recycle KOH baths. For this process, recycled KOH will not work due to contamination issues. Also makes sure the wafers are clean and does not have organic residue on the surface. Any residue will mask the poly-Si thin film preventing complete strip.

2. Put two 5" containers onto the same hot-plate. Fill 200 ml KOH into each Pyrex container and mark the containers #1 and #2. Put plastic meshes into each glass container, these will lift the wafer up so that the back-side can be etched. Set the hotplate to 80 °C and wait for hot-plate to reach equilibrium.

   KOH etch rate is a non-linear function of temperature and goes up exponentially with temperature. Make sure the temperature is not overshooting. If you overheat and start

boiling the solution, you will end up with KOH crystals in your glass-ware. Make sure the process is performed under a hotplate with adequate ventilation.

3. While KOH is heating up, prepare a DI water bath close to the sink into another Pyrex container.

4. Prepare new containers for the wafers. PolySi leaves particulates in wafer pucks after HF etching. It is almost impossible to remove this residue from the pucks, so we will dump the containers when we start the process.

5. Take the wafer out, do solvent clean (acetone ==¿ IPA). Rinse under DI water and throw into the #1 KOH bath. Solvents and KOH do not mix. Make sure that the wafer is thoroughly rinsed with DI-water after the solvent clean. It is better if you keep the solvents away from the hot-plate and the KOH baths.

6. For 2 µm thick LPCVD it takes approximately 6 minutes to visibly remove the poly-Si (making the wafer transparent). However this number is not exact, the correct time needs to be found by observation in the following manner: Observe the wafer in KOH bath, the poly-Si will gradually fade away, leaving the wafer transparent (for glass wafers). Wait till there are no dark spots on the wafer (certain spots on the wafer etch slower). Once the last dark spot is gone, wait for an extra 60 seconds and take the wafer out (Usually it is around: 5 minutes to etch + 1 minute extra = 6 minutes).

   KOH attacks SiO2 (glass) at a known rate, prolonged exposure will damage the surface which can cause issues further down the road (bonding). It is very important that 5+1=6 minute rule is followed to prevent excess etch.

7. Once the wafer is out of the first bath, quickly do the following: Dump it into the DI water bath, rinse under running water, do solvent clean, rinse under running water and finally place into #2 KOH bath. While the wafer is in the second container replace the

DI water bath with fresh DI water. Each rinse should be performed in fresh DI water bath.

Do not flip the wafers at any point during the process, the top should always be top. Solvents and KOH do not mix. Make sure that the wafer is thoroughly rinsed with DI-water after the solvent clean. It is better if you keep the solvents away from the hot-plate and the KOH baths.

8. Second KOH bath is timed, wait for 5 minutes and take out the wafer.

   It might sound like an overkill, but if you do not do double KOH bath and rigorous rinsing in between baths, it is absolutely guaranteed that the wafers do not plasma bond.

9. Follow the rinse/solvent clean instructions on number 7 after the #2 KOH bath. Put the wafer onto a cleanroom wipe and dry the wafer without ever flipping it over (top should always be top).

10. Place the wafer into a fresh container.

    Do not ever use the old container (puck) of the wafer, it is contaminated at this point.

11. If there are more than one wafers, replace the DI water bath. You can keep the KOH baths running and reuse it within the same run. Continue from step 4 for the next wafer. Just make sure that you have enough KOH and not crystallizing. Also the etch rate gradually gets lower due to KOH depletion, it might take a little bit longer for the next wafer.

12. Once the run is complete, take the KOH baths off the hot-plate. Cover and mark the KOH bath, let it cool overnight before dumping.

13. Both the KOH bath and the initial wafer containers (pucks) should be dumper after each run.

KOH attacks Pyrex glass-ware overtime. Although the attack is very slow and not noticeable at all, do not leave KOH for weeks inside the Pyrex container.

A.3 Plasma-assisted Fusion Bonding of Glass and Silicon

Overview	
Input	Wafer(s) in separate plastic petri-dishes
Consumables	Chemicals for one RCA-1 bath, acetone, IPA, clean-room wipes, aluminum foil
Equipment	Complete RCA-1 bath equipment with teflon wafer holder for multiple wafers (Hotplate, glassware, aluminum foil) separate glassware to rinse wafers after RCA-1
Output	Bonded wafer pair

A.3.0.5 Important Notes

Bonding is abnormally sensitive to contamination, because of this wafer handling is different than most other processes:

- *Bonding surface of the wafer should absolutely touch not other object during the whole process. Even accidentally dropping a cleanroom wipe or cleanroom wipe blowing from underneath and folding itself to the top surface messes it up.*
- *During nitrogen dry only one wafer should be expose at a time. The nitrogen gun pushes all of the dust on the wet bench onto the rest of the wafers, that is why while drying one wafer, the rest should be kept in a container or DI water.*

A.3.0.6 Process

1. Each wafer should have individual plastic petri-dishes, which should be thrown out after the run. Cleanroom wipes can be placed on the backside of the petri-dishes to

prevent stiction, however the wipes need to be cut to size to prevent the wipe from touching the front side.

2. The spot where you grab the wafer usually does not bond. For this reason it is very important to use a clean pair and further clean it with solvents before the run. It is also important to always grab from the same side to minimize bond defects (flat of the wafer for example).

   Wafer pucks are definitely a no go for this process as they touch the wafer everywhere.

3. Process starts with solvent cleaning of the wafers: Acetone rinse, followed by IPA rinse, followed by DI water rinse.

4. Right before doing the RCA-1 clean, start a 20 minute high power O2 plasma run in the empty plasma chamber to clean organic residues from the previous user. For PlasmaTherm this step is 20 mins of "O2ASH" recipe, which gives 200 W power and 24 sccm of O2 flow.

   This is a dry run, no wafers are placed into the tool. We do the run at this step so that the tool is ready at the same time the RCA-1 is complete.

5. Then all wafers are placed into RCA-1 solution and cleaned for 20 minutes. It is important that all wafer pairs are cleaned in the same run as the plasma activation will follow right after.

   Cleaning the wafers and bonding a few days later is known to cause issues. Never clean any other wafers in a plasma bonding run. If you are trying to clean photoresist residue etc on the same run, you will have bonding issues. All wafers that enter the bath should be "clean" with no residue.

6. When RCA-1 is complete, transfer the teflon wafer holder into DI water container. Hold the glassware under continuous running DI water. This ensures that any organics on the water surface flow away.

7. Once this is done, makes sure the wafers are still submerged in the container. Take one wafer out rinse the bond surface under running DI water for 60 seconds.

8. Place the wafer onto the top left portion of the cleanroom wipe. Nitrogen dry for 30 seconds. Move the wafer to the bottom right portion of the same cleanroom wipe nitrogen dry until no water is remaining anywhere on the wafer. Dispose of the wipe.

   Never flip the wafer, front side never touches the wipe.

   Make sure you have weights on the corners of the wipe or it is sitting on the suction holes of the wet bench, otherwise nitrogen gun causes the wipe to fold on top of the wafer, which prevents bonding.

   Notice that we are not blowing nitrogen to the back side, it is not worth it. Instead we are moving the wafer on the wipe to different position to absorb bulk of the water. That is why one wipe = one wafer.

9. Place the wafer into previously prepared petri-dish. Close the petri dish, put it away.

10. Repeat steps 7-9 for each wafer that is still submerged in the DI water.

    Notice that only one wafer is exposed at a time.

11. Next step is plasma activation, ideally the wafer pair that is going to be bonded is loaded at the same time, to activate both surfaces simultaneously. If this is not possible they can be activated one after another in rapid succession.

12. Load the wafers into the plasma chamber still holding from the same point, make sure you do not keep the wafers exposed for too long. Standard recipe for PlasmaTherm is "O2", which is 50 W power for 2 minutes, 105 V bias and 20 sccm O2 flow.

    Note that plasma power is significantly lower than the "ashing" recipe we used to clean the chamber, the duration is shorter. Too strong plasma or too long exposure causes plasma damage to the wafer surface, which creates bonding issues. In short there is an

optimal amount of plasma the wafer needs to go through: Too short and not enough activation, too long and too much surface damage.

13. Carefully put the wafers back to the plastic petri-dishes, bring them back to the wet bench.

14. Take one of the wafers out, rinse the bond surface under DI water for 1 minute. Dry the wafer following instructions on step 8.

    This step is black magic, some people claim it helps because it removes particles that land on the wafer surface inside the plasma chamber. Other people claim it helps by humidifying the surface and promoting hydroxyl bonds. Bottom line is we do not know why, but it seems to help.

15. Place the first wafer back into its container, take out the second wafer and follow step 8 to rinse it for 1 minute as well. Move this wafer to the center of a new (dry) cleanroom wipe.

16. Make sure you have clean/dry gloves, change them if you need to. Bulky gloves don't work for this step, if you have large chemical gloves you have to take them off. Take the first wafer from its container using the tweezers. Grab the first wafer from the outer perimeter of the wafer in your dominant hand. Hold it such that your palm is facing to the back-side of the wafer. Turn the wafer upside-down so that the bond surface is facing down. Align the wafer on top of the second wafer (the one that is on the wet bench right now) as well as you can. Once you are at close enough gab use one finger of your other hand to push the wafer down onto the other wafer, so that they are contacting on one side. Let go of the hand that is holding the wafer, so that wafers are contacting fully. if the wafers are glass, you should visibly see the bond surface propogating and encompassing the whole wafer. Due to contamination it will not be perfect. Move the wafer pair onto a very flat surface and push from top using your fingers, this usually helps bond more surface area.

This step is a little bit tricky the first time, just because if the wafers slide and the top wafer touches the cleanroom wipe, it will not bond there.

17. With any luck the wafer pair should be holding together using van-der waals forces now (the bond is temporary at this step). Put the wafer pair in a petri dish and keep it for 100 hours (4 days) at laboratory conditions, this promotes hydroxyl bonds to form. The wafer pair can be handled like a normal wafer now without being as picky about cleanliness.

    It is not always necessary to cure for 4 days, but if there are cavities on the wafer surface, this helps keep the wafers together.

18. Next step is annealing on hotplate. For fused silica or ULE TSG we go up to 400 °C because the material can handle it, if there is a coefficient of thermal expansion mismatch between the wafers this won't be possible due to cracking. (For example ULE TSG to silicon pair cracks above 120 °C). It is important to ramp slowly if there are cavities, otherwise expanding air inside the cavity pushes the wafer pair apart. 6 hours ramp up to 400 °C and 2 hour hold at 400 °C is the default recipe. When the 8 hours is complete, you can simply turn off the hot-plate.

19. Once the anneal is done and wafers have cooled off, gently probe the bond interface using a razor (crack opening method). It is possible to measure bond strength using this method. For glassblowing runs a successful bonding run means that: it is not possible to push the razor into the crack and trying to force it would break the wafers instead of separating the bond.

20. Below is an example of a bonded fused silica pair (4" OD - 500 µm thickness on each wafer). Picture is taken using a regular digital camera, colors are enhanced to display the bond defects. Note that wafers are slightly misaligned due to user error on step 16, after the first contact occurs the wafers stick together and there is no opportunity to slide/align them. The colorful spots are bond defects, the waviness in unbonded areas

is caused by interference fringes, these are also known as "Newton rings" and can be used to measure the gap at the bond defect. You will also notice that there is a large bonded are at the very bottom of the wafer and at the west edge, these are the spots where the tweezer was holding the wafer pair. The bond strength of this wafer pair was above the fracture strength of the fused silica (i.e. it is not possible to separate the bond without breaking the wafers).

A.4 Blue-tape Application for Wet Etching of Glass

Overview	
Input	Wafer(s) inside wafer carrier, one-sided blue-tape
Consumables	
Equipment	
Output	

A.4.0.7 Process

1. Make sure wafer is placed top-side down inside the wafer carrier.

2. Open the wafer carrier, do not remove the wafer.

   Top surface usually has sensitive features or is a bond surface, for that reason we will use the wafer carrier to hold the wafer while applying the blue-tape.

   Never place the wafer top-side down onto a cleanroom wipe or any other surface, it damages the top-side. Use wafer carriers to do work on the back-side of the wafer.

3. At this point wafer will be sitting inside the wafer carrier, top-side facing down onto the bottom piece of the wafer carrier.

4. Peel of the blue-tape and touch it at one edge of the wafer.

5. Slowly work your way to the other edge, till the whole wafer is covered with blue tape.

   If bubbles form, you can peel back the blue-tape a little bit and stick it again to remove the bubbles.

6. Once the blue-tape is sticking to the wafer nicely, take a razor blade and run it around the edges.

7. Remove and throw away excess blue-tape.

8. Remove the wafer, hold it around the edges with your gloves.

9. Run the razor edge to trim the excess blue-tape.

   Small pieces of blue-tape sometimes stick to the wafer or carrier, make sure all of the pieces are removed and none of them are sticking to the front-side.

10. Throw away excess blue-tape, place the wafer back into the wafer carrier.

A.5 Fused Silica Wet Etch

Overview	
Input	Wafer(s) to be etched inside wafer carrier(s) with PolySi on top
Consumables	49% HF, blue-tape and plastic mesh (optional), clean-room wipes
Equipment	4 Teflon containers, HF resistant tweezer, dehydration oven
Output	Etched wafer

A.5.0.8 Process

1. Pour 300 ml 49% HF into a Teflon container.

   The container should be about half-full, otherwise the etch rate varies across the wafer and over time, due to HF consumption and the absence of buffer. HF should also be fresh/unused.

2. Fill two Teflon containers with plenty of DI water.

3. Fill a Teflon container with IPA.

4. (Optional) If need to protect back-side, mask one side of the wafer using one-sided blue-tape. Refer to "Blue-tape Application" document.

   Blue-tape is not impervious to HF as it starts etching from the edges, but works fine for short durations or if it is only a test run.

5. (Optional) Place a plastic mesh underneath if etching both sides of the wafer.

6. Place the wafer into HF bath.

7. Etch for required duration.

1.07 µm/min is the typical etch rate we get on fused silica with this recipe. The etch rate measurement is fairly accurate ($R^2 = 0.996$). The etch depth variation across the wafer is usually 0.1 µm.

8. Remove the wafer and place it into first DI water bath.

9. Take it out and rinse under DI water, thoroughly.

10. (Optional) Very carefully remove the blue-tape if there is one.

11. Place into second DI water bath for 5 minutes, rinse under DI water.

12. Place into IPA bath for 5 minutes.

13. Rinse in DI water for 1 minute, to get rid of IPA residue.

14. Take out and place the wafer onto a cleanroom wipe.

    Do not blow dry the wafer, it will break the PolySi film. Use the dehydration oven to dry the wafers (10 mins should be sufficient).

    Never turn the wafer upside-down during the process, the PolySi thin film is very fragile.

    Never blow dry the wafers, it breaks the PolySi thin film.

15. Take a snap-shot of the whole wafer. Take microscope images of the mask edge at center east and north of the wafer and at the alignment (if present) mark if they are intact.

16. Measure the etch depth in the middle and at the edge using DEKTAK. The variation is usually as low as 0.1 µm for this process. If you are seeing significantly higher variation, that means that the amount of HF used is not enough. *DEKTAK usually damages the PolySi thin film where you make the measurement, if you are taking multiple measurements at different etch depths make sure you take the measurement from the same point to minimize the damage.*

17. There are usually broken pieces of PolySi thin film inside the containers after this process. Try to remove them using cleanroom wipes, as they can contaminate the next wafer you do in these containers.

Appendix B

Effect of Thickness Variation on Wineglass Frequency Split

To understand why only the 4th harmonic of the thickness variation has an effect on fundamental frequency splitting (Δf), we look at the vibrational kinetic energy of the resonator, which is used in Rayleigh-Ritz solution of the resonance frequencies of wineglass geometries [113, 139]:

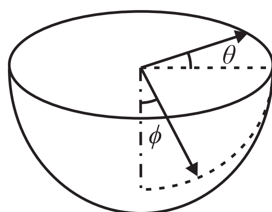

Figure B.1: Sketch of an ideal wineglass (perfectly spherical), showing θ as the angle along the central axis of symmetry and, ϕ as the secondary angle.

$$K_0 = \frac{1}{2} r\rho h \int_0^{\pi/2} \int_0^{2\pi} (\dot{u}^2 + \dot{v}^2 + \dot{w}^2) \sin\phi d\theta d\phi \,, \tag{B.1}$$

where $\dot{u}, \dot{v}$ and $\dot{w}$ are the velocity terms, which are represented as:

$$u = U(\phi, t)\ \sin(n\theta)\ , \tag{B.2}$$

$$v = V(\phi, t)\ \sin(n\theta)\ , \tag{B.3}$$

$$w = W(\phi, t)\ \sin(n\theta)\ , \tag{B.4}$$

and r is the radius of an ideal wineglass ρ is the density of the material, θ is the angle along the central axis of symmetry and, ϕ is the secondary angle, Fig. B.1.

However, above equations for vibrational kinetic energy assume a perfectly symmetric geometry with no thickness variation. If we derive the same equation for an imperfect wineglass resonator with a thickness variation as in equation 4.1, then the kinetic energy equation will become:

$$K = \frac{1}{2} r\rho \int_0^{\pi/2} \int_0^{2\pi} (\dot{u}^2 + \dot{v}^2 + \dot{w}^2)\ h(\varphi)\ \sin\phi d\theta d\phi\ . \tag{B.5}$$

The difference between kinetic energies of the ideal wineglass resonator in equation B.1 and

the one with thickness variations in equation B.5 can be summarized as:

$$K = K_0 + K_{unbalance} \, . \tag{B.6}$$

The $K_{unbalance}$ term, which is the difference in kinetic energy due to thickness variations becomes:

$$K_{unbalance} = \frac{1}{2} r\rho \int_0^{\pi/2} \int_0^{2\pi} A \, B \, \sin\phi d\theta d\phi \, , \tag{B.7}$$

where A is a collection of velocity terms and:

$$B = h_i \, \sin(2n\theta) \, \sin(i\theta) \, . \tag{B.8}$$

Index i is the thickness harmonics under consideration. The B term is the focus of the analysis, as it will make the whole integral (and consequently $K_{unbalance}$) equal to zero if $2n \neq i$. In other words, only thickness variations with harmonics at $2n = i$ can cause changes in the kinetic energy (and frequency) of the wineglass.

Appendix C

Gyro Front-end PCB

Front-end PCB electronics used in this dissertation is presented in this section. The PCB is compatible with all 3 devices presented in this thesis: micro-wineglasses, Toroidal Ring Gyroscope (TRG) and Dual Foucault Pendulum (DFP) Gyroscope. In Figure C.1 schematic of the socket housing gyroscope's LCC package is shown. In Figure C.2 schematic for the vacuum chamber feed-through is shown. Pick-off and forcer electronics are shown in Figures C.3 and C.4, respectively. Finally, the schematics for the on-board LDO power regulators are shown in Figure C.5 along with an optional connectors for heater and temperature sensors, Figure C.6.

Layout of top and bottom layers are shown in Figures C.7 and C.8, respectively. Component placement is shown in Figure C.9 and finally a combined view of all layers is shown in Figure C.10. It is worth noting that the x-y pick-off and forcer electronics are placed in a symmetric manner, such that x and y forcer electronics are located at east and north sections of the PCB, respectively. Whereas x and y pick-off electronics are located at west and south sections of the PCB, respectively.

On the gyroscope socket, Figure C.1, FX and FY, denote connections to forcer electrodes,

whereas PX and PY denote connections to pick-off electrodes. For all differential channels (-) and (+) denote the polarity of the respective channel. FM is a constant DC bias or an AC signal applied to the body of the resonator. PARAM is an optional connection to parametric drive electrodes, Q is the connection to optional DC quadrature null electrodes on the device. On the vacuum chamber interface, Figure C.2, PXOUT and PYOUT are x-y pick-off channels from the gyroscope, FORCER-X and FORCER-Y are AC signals for x-y forcer channels. DC-X and DC-Y are DC bias voltages applies to x-y forcer channels and are used for frequency tuning. V+SUPPLY and V-SUPPLY are power supply rails. Finally, HEATER and T are optional connections for heater and temperature sensor.

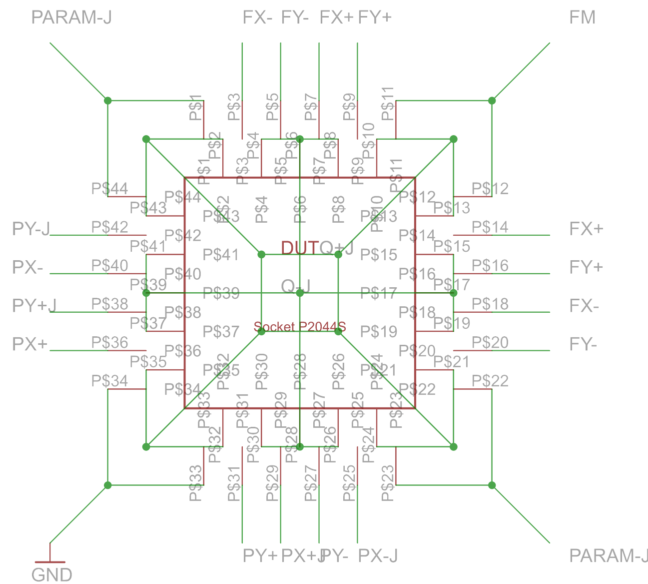

Figure C.1: Schematic for pin-out to 44 pin LCC gyroscope package.

PYOUT	P$1
PXOUT	P$2
T-	P$3
T+	P$4
Q+	P$5
Q-	P$6
PARAM	P$7
FORCER-Y	P$8
DC-Y	P$9
FM	P$10
DC-X	P$11
FORCER-X	P$12
V+SUPPLY	P$13
V-SUPPLY	P$14
HEATER+	P$15
HEATER-	P$16
GND	P$17
GND	P$18
GND	P$19

Figure C.2: Schematic of PCB interface to the vacuum chamber feed-through.

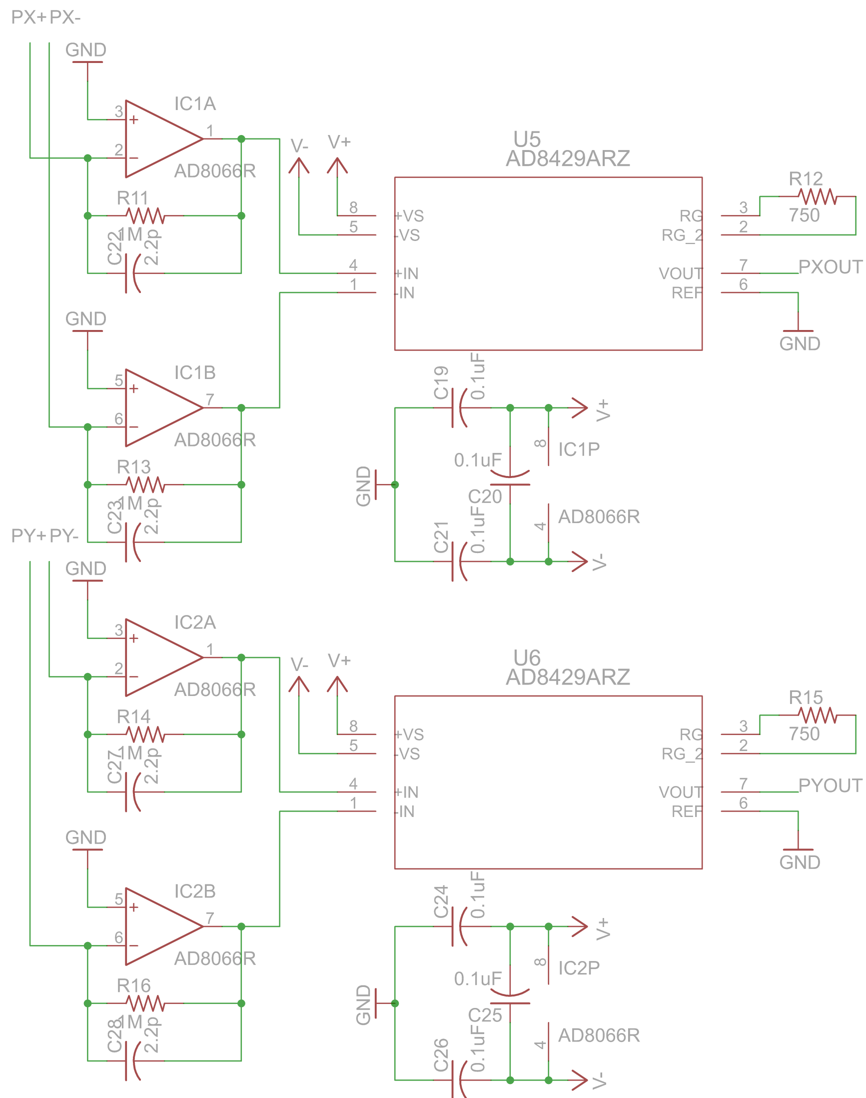

Figure C.3: Schematic of pick-off electronics, showing first and second stage amplification.

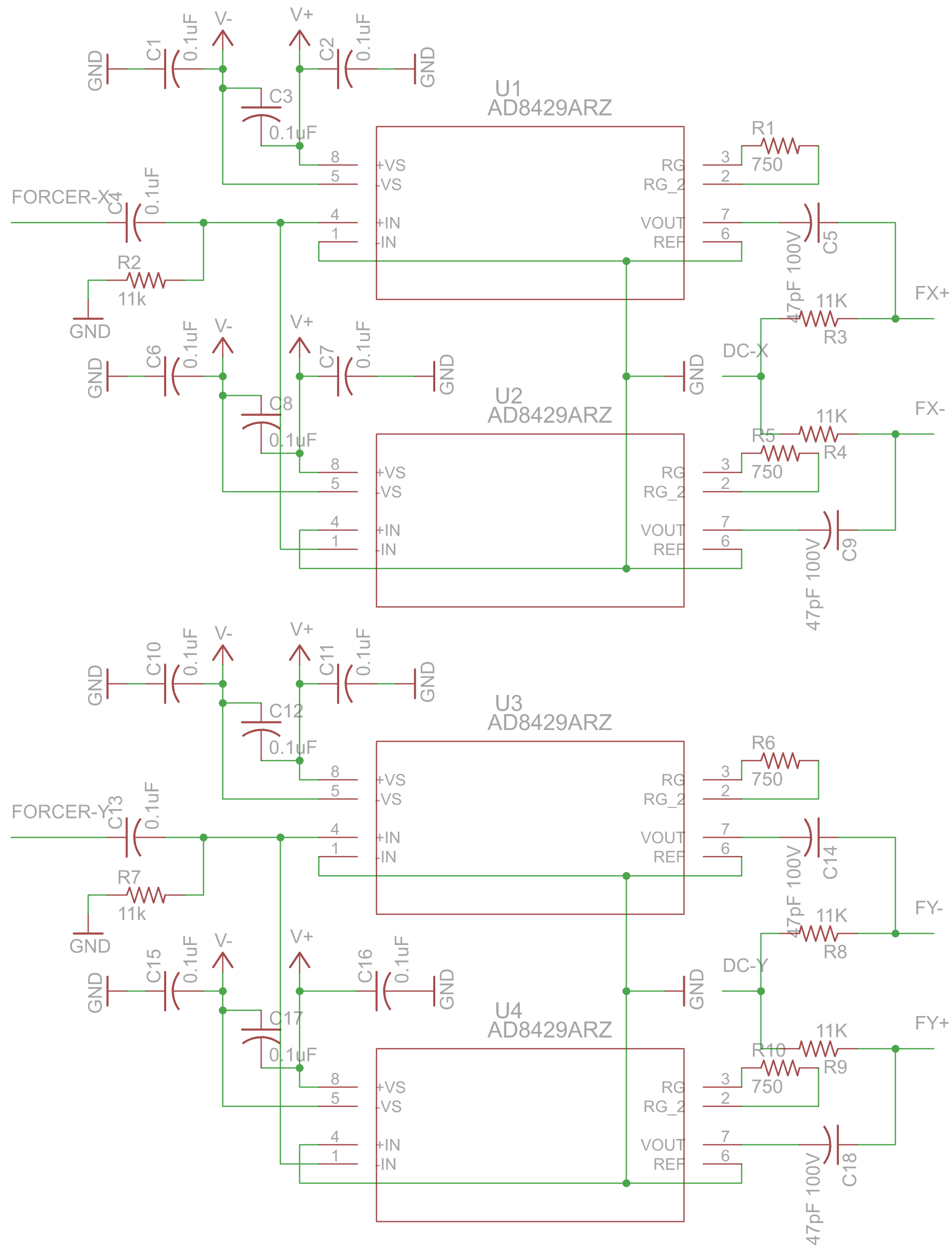

Figure C.4: Schematic of forcer electronics, showing instrumentation amplifiers for differential drive and DC biasing scheme.

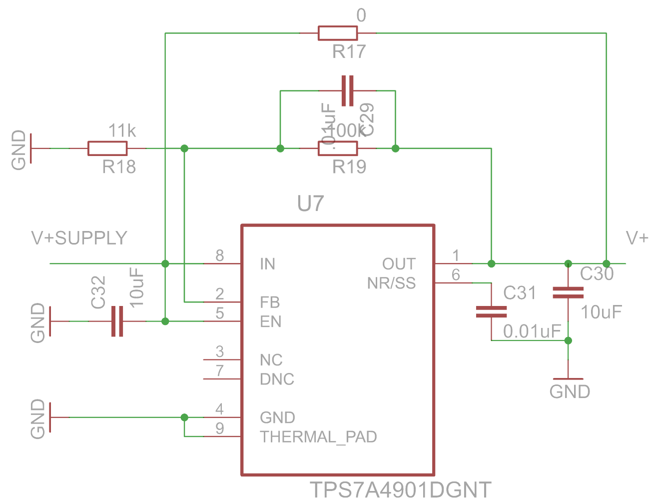

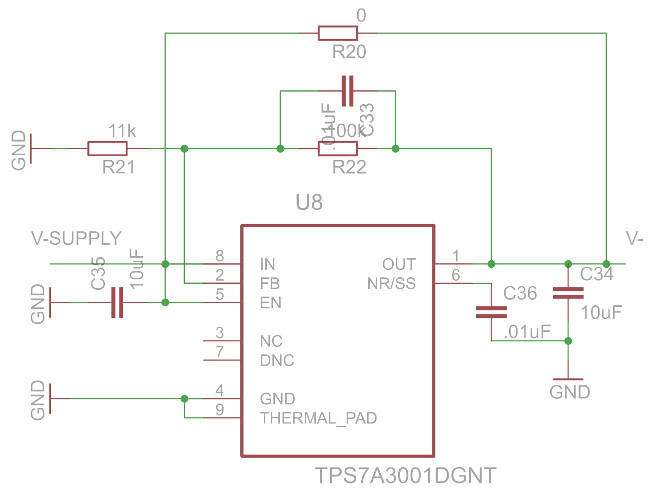

Figure C.5: Schematic of low-noise low-dropout (LDO) voltage regulators used for powering the active components.

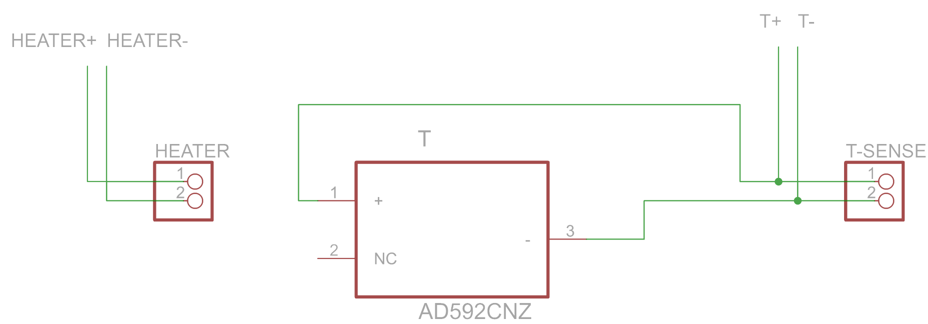

Figure C.6: Schematic for heater and temperature sensor connectors.

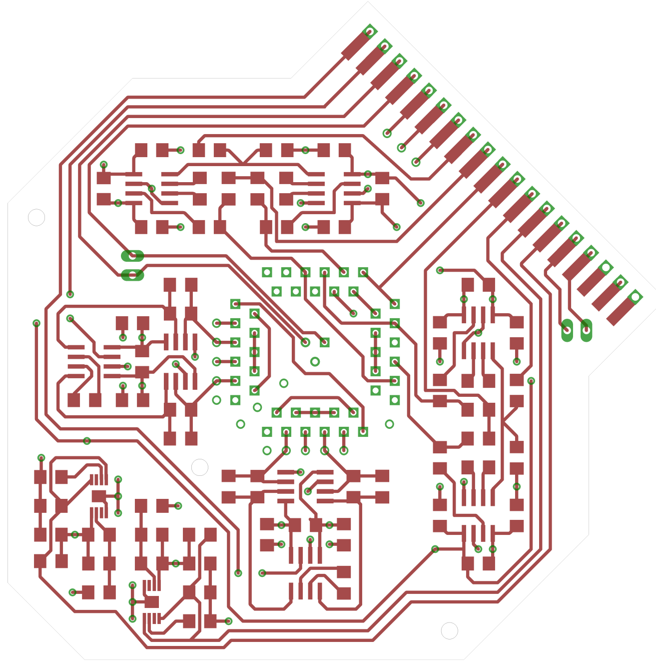

Figure C.7: Layout of top layer, vias and pads, scale is 1:1.

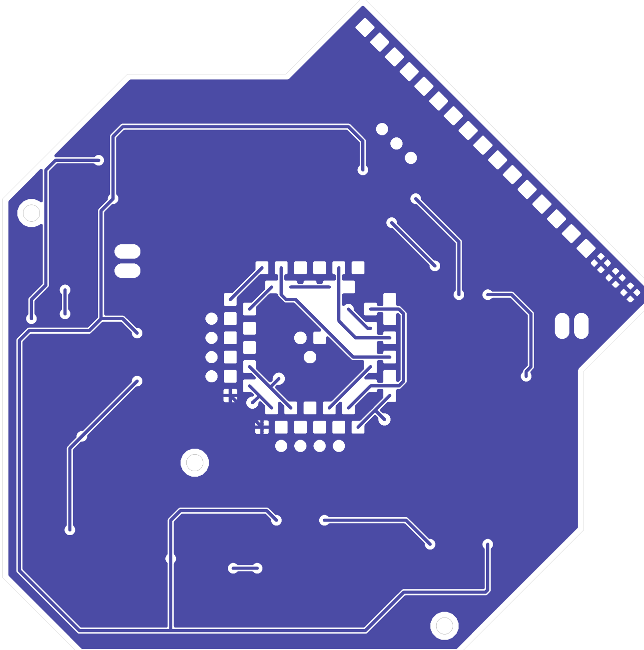

Figure C.8: Layout of bottom layer, scale is 1:1.

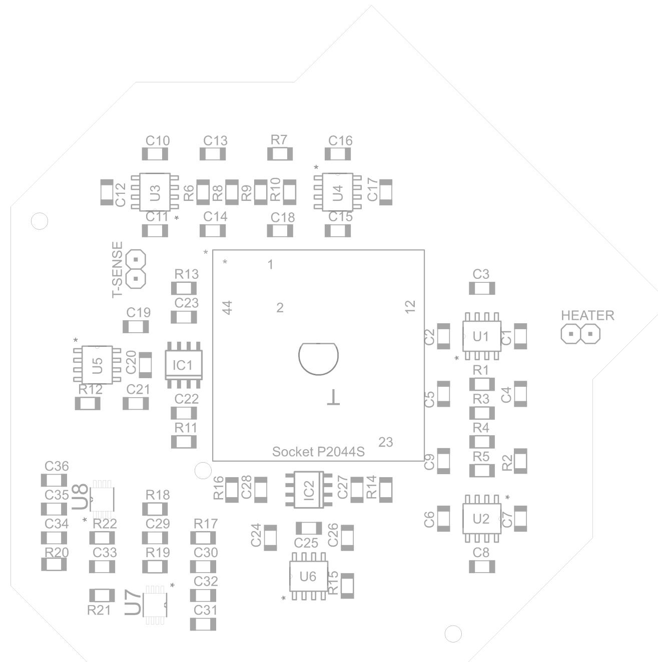

Figure C.9: Component placement, scale is 1:1.

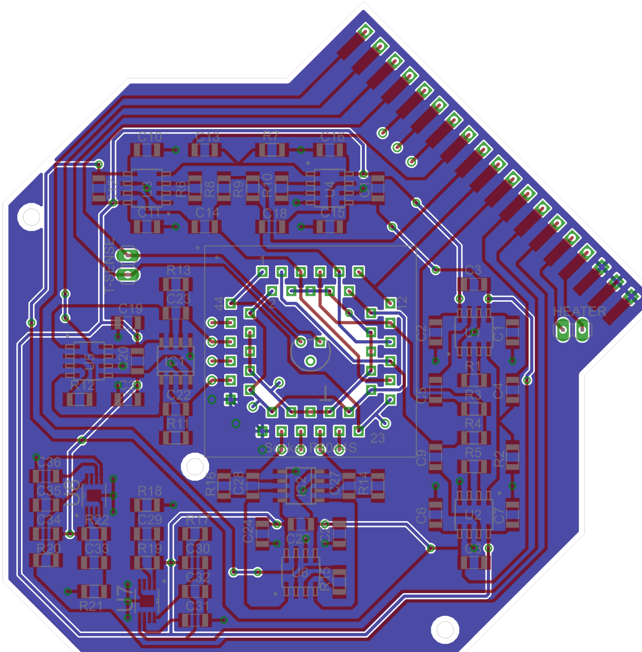

Figure C.10: Layout showing all layers on the PCB, scale is 1:1.

Appendix D

Gyro Controller Users Manual

D.1 Setup

Core of the gyro controller is a Artix 7 Field Programmable Gate Array (FPGA) board connected to an Arduino Due Micro-controller board, Table D.1. FPGA board houses the ADC and DACs and connects to the micro-controller board through RS232 communication, Table D.2. The micro-controller in turn connects to the PC through RS232 communication, which is used data acquisition and changing the controller parameters, Table D.3

Table D.1: Digital hardware used for the gyro controller.

Part	Supplier	Description
Nexsys 4 FPGA Board	Digilent	Artix 7 FPGA board
Arduino Due Board	Arduino	ARM Cortex-M3 micro-controller board
PulSAR Pmod ADC	Digilent	18 bit - 1 MHz ADC board (AD7982 ADC)
PmoDA3 DAC	Analog Devices	16 bit - 1 MHz DAC board (AD5541 DAC)

Once the controller boards are connected according to Table D.4 the boards will be ready for programming. Both boards can be powered from an external power supply or through the

Table D.2: Key parameters of the Nexsys 4 FPGA board.

FPGA chip	Xilinx Artix 7 (Part number XC7A100T-1CSG324C)
	15850 logic slices
	4860 Kbits of block RAM
	240 DSP slices
Clock speed	100 MHz
External RAM	16 MB
Programming	Digilent USB-JTAG or USB memory stick
IO	4 full size PMOD connectors

Table D.3: Key parameters of the Arduino Due Micro-controller board.

CPU	Atmel ARM Cortex-M3 (Part number AT91SAM3X8E)
Clock speed	84 MHz
Flash memory	512 KB
Programming	USB port or flash memory

on-board USB connectors. The PMOD DA3 DAC boards can use the FPGA board power, however the PulSAR Pmod ADC boards require external power of $-2.5\,\mathrm{V} - 0\,\mathrm{V} - 7.5\,\mathrm{V}$, please refer to PulSAR Pmod ADC schematic from ADI for details.

For fastest startup time and convenience, the code for the Nexsys 4 FPGA board can be downloaded to a USB memory stick and connected to the USB port of the board, after which the board needs to be set to boot from USB for startup (please see Nexsys 4 users manual from Digilent for instructions). The Arduino Due Micro-controller board is programmed through USB programming port, which is also used for data acquisition and command line interface (CLI).

For the RS232 communication between the PC and the micro-controller to work, the PC needs to be set to 115200 baud rate, no parity (8n1), no flow control and set to use carriage return (CR) at the end of line.

Table D.4: FPGA and micro-controller board connection guide.

FPGA PMOD JD (pins 1-12)	PulSAR Pmod ADC (x pick-off channel)
FPGA PMOD JC (pins 1-12)	PulSAR Pmod ADC (y pick-off channel)
FPGA PMOD JB (pins 1-6)	PmoDA3 DAC (x drive channel)
FPGA PMOD JB (pins 7-12)	PmoDA3 DAC (y drive channel)
FPGA PMOD JA (pins 1-6)	PmoDA3 DAC x 1 ADC (param. drive channel)
FPGA PMOD JA (pins 8, 10 and 11)	Arduino Due (GND, RX1 (19) and TX1 (18))
FPGA board USB port	USB memory with downloaded FPGA code
FPGA board micro-USB connector	PC USB (Power)
Micro-controller programming port	PC USB (Power and data)

D.2 Data Stream

Once the connection is established the controller will output gyro state at a prescribed rate (10 Hz default). Each line contains 12 comma separated values and is terminated by <CR>. Starting from left, these values are: times stamp, PLL frequency, AGC input, AGC output, parametric AGC output, quadrature error input, quadrature null output, force to rebalance error, force to rebalance output, pattern angle set point and unwrapped/wrapped pattern angle position. Any printed text other than the datastream (such as commands, virtual carouseling results) is printed with a % symbol in front of the line to facilitate easy import into Matlab.

Listing D.1: datastream.txt

```
% Starting...
% Time, Frequency, Ein, Eout, E2out, Qin, Qout, Fin, Fout, TS,
   Theta, ThetaMod
% s, Hz, Ein, V^2, V, V^2, V, rad, V, deg, deg, deg
0.11, 2658.59779469, 0.21141573, 0.00000000, 0.00000000,
   -0.07652859, 0.00000000, -1.49718765, 0.00000000, 0.00000000,
   85.78253334, 1.51488526
0.21, 2678.91317933, 0.20670928, 0.00000000, 0.00000000,
   -0.04388248, 0.00000000, -1.54141599, 0.00000000, 0.00000000,
   88.31663086, 1.54551911
0.31, 2679.06131213, 0.19984150, 0.00000000, 0.00000000,
   -0.00918373, 0.00000000, -1.55490056, 0.00000000, 0.00000000,
   89.08923946, 1.55576538
0.41, 2679.02803142, 0.19311090, 0.00000000, 0.00000000,
   0.02394279, 0.00000000, -1.54808182, 0.00000000, 0.00000000,
   88.69855468, 1.54547259
0.51, 2678.99322711, 0.18699664, 0.00000000, 0.00000000,
   0.05284728, 0.00000000, -1.51790299, 0.00000000, 0.00000000,
   86.96943512, 1.51115509
```

It should be noted that the micro-controller clock is used to create the time stamps, whereas the master FPGA clock is used to generate the 10 Hz data stream. Slight variation in time stamps can be observed over the course of a day.

D.3 Command Line Interface

The controller uses a command line interface (CLI) for changing the controller parameters. All commands follow the same basic format:

ABX.Y <CR>

For every command A is the subset of the controller being addressed (AGC, force-to-rebalance etc), B is the specific parameter being adjusted and X.Y is a floating point number to be assigned. The commands are case insensitive, such that the commands

ABX.Y <CR>

abX.Y <CR>

AbX.Y <CR>

would all have the same effect.

At any time while the controller is running

AB? <CR>

will print the existing value for the parameter AB. It is important to note that new values assigned through the CLI are only retained during runtime and the controller will revert to default values after a reset. Default values of each parameter can be adjusted by changed through the micro-controller code.

Table D.5: Amplitude gain control (AGC) commands.

Command	Value	Description
EE	0	Disable AGC and set output of to zero
	1	Enable AGC
	2	Reset and enable AGC
	3	Disable AGC and enable parametric drive AGC (EE0 and 2E1)
	9	Set AGC to open loop, only the feed-forward term will be used
EF	X.Y	Change feed-forward term
ES	X.Y	Target set-point
EP	X.Y	Change proportional (P) gain
EI	X.Y	Change integrator (I) gain
EV	X.Y	Enable pattern angle dependent feed-forward term

D.3.0.8.1 Startup

Once the gyroscope front-end electronics is connected to the controller, the following startup routine listed below can be used to initialize the gyro:

1. Establish RS232 communication with the micro-controller. This will create a data stream (default 10 Hz) with all the relevant gyro parameters.
2. Reset the controller using the reset button on Arduino Due board, which will initialize the FPGA and the micro-controller to default values.
3. Set the gyro center frequency using PFX.Y<CR>.
4. Set the desired AGC set-point using ESX.Y<CR>.
5. Enable PLL and AGC using PE1<CR> and EE1<CR> respectively.
6. (Optional) at this point parametric drive can be enabled using the command 2E1, which will turn off the main AGC and enable the parametric drive AGC.

Table D.6: Parametric drive amplitude gain control (AGC) commands.

Command	Value	Description
2E	0	Disable parametric drive AGC and set output to zero
	1	Enable parametric drive AGC
	2	Reset and enable parametric drive AGC
	9	Set AGC to open loop, only the feed-forward term will be used
2F	X.Y	Change feed-forward term
2S	X.Y	Target set-point
2P	X.Y	Change proportional (P) gain
2I	X.Y	Change integrator (I) gain
2V	X.Y	Enable pattern angle dependent feed-forward term
2D	X.Y	Change phase shift of parametric drive

7. (Optional) Default AGC and PLL parameters are sufficient to start most gyros. However, if the controller is unstable or the gyro does not start, these parameters can be changed using the commands listed in Tables D.9 and D.5.

8. Reset pattern angle counter using TR1.

9. Enable quadrature null using QE1.

10. Enable pattern angle control using TE1, which puts the gyro in whole-angle mode.

11. (Optional) Enable force-to-rebalance using FE1, which will lock the pattern angle to zero degrees.

12. (Optional) Similar to AGC and PLL, force-to-rebalance and quadrature null loops can be tuned using the commands listed in Tables D.8 and D.7.

13. (Optional) Once the force to rebalance has locked and the pattern angle control is enabled (FE1 and TE1), the gyro can be driven at an arbitrary orientation using TSX.Y<CR>. i.e. TS90<CR> would change the drive orientation to y mode.

Table D.7: Quadrature null commands.

Command	Value	Description
QE	0	Disable quadrature null and set output to zero
	1	Enable quadrature null
	2	Reset and enable quadrature null
	9	Set quad. null to open loop, only the feed-forward term will be used
QF	X.Y	Change feed-forward term
QS	X.Y	Target set-point
QP	X.Y	Change proportional (P) gain
QI	X.Y	Change integrator (I) gain
QV	X.Y	Enable pattern angle dependent feed-forward term

14. (Optional) At any time disabling the force-to-rebalance loop using FE0<CR> would put the gyro back into the whole angle mode.

15. To turn off the gyro, the following series of commands can be used: FE0<CR>, QE0<CR> and EE0<CR>, which will disable FRB, quadrature null and AGC.

D.3.0.8.2 Virtual Carouseling

Typical virtual carouseling cycle can be initiated with the routine described below. This routine assumes that the startup procedure described in the previous section has been followed and the force-to-rebalance is enabled.

1. Make sure the pattern angle is at zero degrees, if the gyro was moved from this position it can be brought back using TS0<CR>.

2. Set the number of virtual carouseling cycles using VNX. For example VN10<CR> would cause the gyro to complete 10 full 360° cycles.

3. Set the increment using VDX.Y<CR> and time interval using VIX.Y<CR>. For

Table D.8: Force-to-rebalance commands.

Command	Value	Description
FE	0	Disable force-to-rebalance and set output to zero
	1	Enable force-to-rebalance
	2	Reset and enable force-to-rebalance
	9	Set force-to-rebalance to open loop
FF	X.Y	Change feed-forward term
FS	X.Y	Target set-point
FP	X.Y	Change proportional (P) gain
FI	X.Y	Change integrator (I) gain
FV	X.Y	Enable pattern angle dependent feed-forward term

example VD1<CR> and VI10<CR>, would cause the precession pattern to rotate at 1° increments every 10 seconds, causing the gyro to complete a full cycle over 1 hour.

4. Once desired virtual carouseling cycles is reached (set through VN) the gyro will dwell at TS0, until a new command is issued.

Table D.9: Phase lock loop (PLL) commands.

Command	Value	Description
PE	0	Disable PLL and set output to zero
	1	Enable PLL
	2	Reset and enable PLL
	9	Set PLL to open loop, only the feed-forward term will be used
PF	X.Y	Change feed-forward term (center frequency)
PS	X.Y	Target set-point (not used)
PP	X.Y	Change proportional (P) gain
PI	X.Y	Change integrator (I) gain
PV	X.Y	Enable pattern angle dependent feed-forward term
PD	X.Y	Change phase shift of vector drive
PC	X.Y	Change cut-off frequency (Hz) of PLL low pass filter

Table D.10: Drive and pick-off (ADC and DAC) gains.

Command	Value	Description
GX	X.Y	Change x drive gain
GY	X.Y	Change y drive gain
GA	X.Y	Change x pick-off gain
GB	X.Y	Change y pick-off gain

Table D.11: Direct drive and debugging parameters.

Command	Value	Description
DD	0	Disable direct drive (default)
	1	Enable direct drive
DB	0	Disable debug mode (default)
	1	Enable debug mode (will report ADC - DAC values)
SX	X.Y	Amplitude of sine term on x drive channel
SY	X.Y	Amplitude of sine term on y drive channel
CX	X.Y	Amplitude of cosine term on x drive channel
CY	X.Y	Amplitude of cosine term on y drive channel
D2	X.Y	Amplitude of parametric drive

Table D.12: Theta control parameters (whole angle mode).

Command	Value	Description
TE	0	Disable whole angle operation
	1	Enable whole angle operation (pattern angle estimation)
TR	0	Reset and wrap the pattern angle estimation
TS	X.Y	Orientation of drive vector in degrees (only valid if TE0)
TC	X.Y	Change cut-off frequency (Hz) of theta estimation
TF	X.Y	Rotate the drive vector by a set amount (deg.)
TP	X.Y	Rotate the pick-off vector by a set amount (deg.)

Table D.13: Virtual carouseling parameters.

Command	Value	Description
VE	0	Stop virtual carouseling and hold pattern angle
	1	Start virtual carouseling
VD	0	Step rate for virtual carouseling (deg.)
VI	X.Y	Time interval between steps (seconds)
VN	X.Y	Number of virtual carouseling cycles
VC	X.Y	Report/change the number of current virtual carouseling cycle

Appendix E

Gyro Controller FPGA and Micro-controller Code

Main body of the FPGA code (Artix 7 - VHDL) and the micro-controller code (Arduino Due - C++) are listed in this section. First the FPGA code will be listed, which will be followed by the micro-controller code.

Listing E.1: main.vhd

```
1  library IEEE;
2  use IEEE.STD_LOGIC_1164.ALL;
3  use IEEE.NUMERIC_STD.ALL;
4  -- Uncomment the following library declaration if instantiating
5  -- any Xilinx leaf cells in this code.
6  --library UNISIM;
7  --use UNISIM.VComponents.all;
8  entity main is
9  GENERIC(
10         ADCbit : INTEGER := 18; -- Change this if you change the ADC bit count
11         ADCdiv : INTEGER := 200; -- Clock division to get the controller speed (100 MHz / 00 = 1
               MHz)
12         counterSize : INTEGER := 8; -- Counter for clock division
13         NCOcounterSize : INTEGER := 32; -- This is a 64 bit counter used for NCO
```

```vhdl
14          UARTcounterSize : INTEGER := 20; -- This is a 20 bit counter used for UART
15          angleWIDTH : INTEGER := 12; -- MSB 12 bits of NCOcounter is mapped to be used in sin LUT
16          NdataIn : INTEGER := 25; -- UART input buffer in bytes
17          NdataOut : INTEGER := 18 -- UART output buffer in bytes
18          );
19      Port ( SW       : in  STD_LOGIC_VECTOR (15 downto 0);
20             --BTN      : in  STD_LOGIC_VECTOR (4 downto 0);
21             CLK      : in  STD_LOGIC;
22             LED      : out  STD_LOGIC_VECTOR (15 downto 0);
23             --SSEG_CA    : out  STD_LOGIC_VECTOR (7 downto 0);
24             --SSEG_AN    : out  STD_LOGIC_VECTOR (7 downto 0);
25             UART_TXD   : out  STD_LOGIC;
26             UART_RXD   : in  STD_LOGIC;
27             JA           : inout STD_LOGIC_VECTOR (6 downto 0);
28             JB           : out STD_LOGIC_VECTOR (7 downto 0);
29             JC           : inout STD_LOGIC_VECTOR (3 downto 0);
30             JD           : inout STD_LOGIC_VECTOR (3 downto 0)
31             );
32  -- Dummies
33      Signal dummy_outX, dummy_outY, dummy_out2x, dummy_inX, dummy_inY, dummy_2ndADC_1,
            dummy_2ndADC_2, dummY_GPIO_UART: STD_LOGIC := '0';
34      Signal dummy_vector_X : STD_LOGIC_VECTOR(15 DOWNTO 0):= (OTHERS => '0');
35      Signal dummy_vector_Y : STD_LOGIC_VECTOR(15 DOWNTO 0):= (OTHERS => '0');
36      Signal JX            :  STD_LOGIC_VECTOR (7 downto 0):= (OTHERS => '0');
37  --  ADC and DAC
38      Signal data_inX, data_inY: STD_LOGIC_VECTOR (ADCbit-1 downto 0) := (OTHERS => '0');
39      Signal data_outX, data_outY, data_out2x: STD_LOGIC_VECTOR (15 downto 0) := (OTHERS => '0');
40      Signal data_outXbuf, data_outYbuf, data_out2xbuf: STD_LOGIC_VECTOR (15 downto 0) := (OTHERS
            => '0');
41  --  Input and output, signed variables
42      Signal inX, inY: SIGNED(17 downto 0);
43      Signal inX_filtered, inY_filtered: SIGNED(31 downto 0);
44      Signal outX, outY, out2x: SIGNED(31 downto 0):= (OTHERS => '0');
45  --  Internal signals
46      Signal sx, sy, cx, cy: SIGNED(47 downto 0);
47      Signal sxf, syf, cxf, cyf: SIGNED(31 downto 0);
48  --  Force vectors, 16 bit signed
49      Signal Fsx, Fcx, Fsy, Fcy, F2x: SIGNED(15 downto 0);
50  --  NCO related signals
51      Signal carrAngle, angle: unsigned (11 downto 0):= (OTHERS => '0');
52      Signal phase: unsigned (11 downto 0):= "001000000000";
```

```
53      Signal phase2x: unsigned (11 downto 0):= (OTHERS => '0');
54      Signal carrFreq : unsigned (NCOcounterSize-1 downto 0):= (OTHERS => '0');
55      Signal NCOFreq : unsigned (NCOcounterSize-1 downto 0):= (OTHERS => '0');
56      Signal sin, cos, sinPha, cosPha, sin2x, sinCarr: SIGNED(15 downto 0):= (OTHERS => '0'); --
            Various NCO outputs
57  --  Control signals
58      Signal tick, tick2, FilterCLK : STD_LOGIC := '0';
59      Signal UARTtick : STD_LOGIC := '0';
60      Signal reset : STD_LOGIC := '0';
61      Signal inCtrlReg, outCtrlReg : STD_LOGIC_VECTOR(15 DOWNTO 0):= (OTHERS => '0');
62      Signal reset_SPI : STD_LOGIC := '1'; -- SPI is always on
63      Signal reset_SPI_out : STD_LOGIC := '1'; -- SPI is always on
64  --  UART signals
65      Signal UART2DSPin : STD_LOGIC_VECTOR(NdataIn*8-1 DOWNTO 0):= (OTHERS => '0');
66      Signal UART2DSPout : STD_LOGIC_VECTOR(NdataOut*8-1 DOWNTO 0):= (OTHERS => '0');
67      Signal UARTdiv : INTEGER := 1000000; -- Clock division to get the controller speed (1 MHz /
            10000 = 100 Hz)
68  --  Registers
69      Signal counter, counter_next : unsigned(counterSize-1 downto 0) := (others=>'0');
70      Signal Genericcounter, Genericcounter_next : unsigned(counterSize-1 downto 0) := (others
            =>'0');
71      Signal NCOcounter, NCOcounter_next : unsigned(NCOcounterSize-1 downto 0) := (others=>'0');
72      Signal Carrcounter, Carrcounter_next : unsigned(NCOcounterSize-1 downto 0) := (others=>'0');
73      Signal UARTcounter, UARTcounter_next : unsigned(UARTcounterSize-1 downto 0) := (others=>'0');
74  -- Filter signals
75      Signal LPDEMODcoeff : signed(15 downto 0) := to_signed(16384, 16);
76  end main;
77  architecture arch of main is
78  --component GPIO is
79  --    Port(  SW       : in  STD_LOGIC_VECTOR (15 downto 0);
80  --           BTN      : in  STD_LOGIC_VECTOR (4 downto 0);
81  --           CLK      : in  STD_LOGIC;
82  --           LED      : out  STD_LOGIC_VECTOR (15 downto 0);
83  --           SSEG_CA    : out  STD_LOGIC_VECTOR (7 downto 0);
84  --           SSEG_AN    : out  STD_LOGIC_VECTOR (7 downto 0);
85  --           UART_TXD   : out  STD_LOGIC
86  --         );
87  --end component;
88  component spi_master is
89  GENERIC(
90    slaves  : INTEGER := 1;  --number of spi slaves
```

```
91    d_width : INTEGER := 16); --data bus width
92  PORT(
93    clock   : IN     STD_LOGIC;                             --system clock
94    reset_n : IN     STD_LOGIC;                             --asynchronous reset
95    enable  : IN     STD_LOGIC;                             --initiate transaction
96    cpol    : IN     STD_LOGIC;                             --spi clock polarity
97    cpha    : IN     STD_LOGIC;                             --spi clock phase
98    cont    : IN     STD_LOGIC;                             --continuous mode command
99    clk_div : IN     INTEGER;                               --system clock cycles per 1/2 period of
          sclk
100   addr    : IN     INTEGER;                               --address of slave
101   tx_data : IN     STD_LOGIC_VECTOR(d_width-1 DOWNTO 0);  --data to transmit
102   miso    : IN     STD_LOGIC;                             --master in, slave out
103   sclk    : OUT STD_LOGIC;                             --spi clock
104   ss_n    : OUT STD_LOGIC_VECTOR(slaves-1 DOWNTO 0);   --slave select
105   mosi    : OUT    STD_LOGIC;                             --master out, slave in
106   busy    : OUT    STD_LOGIC;                             --busy / data ready signal
107   rx_data : OUT    STD_LOGIC_VECTOR(d_width-1 DOWNTO 0) --data received
108   );
109 end component;
110 component UART2DSP is
111     GENERIC(NdataIn : INTEGER := 1;
112             NdataOut : INTEGER :=1);
113     Port ( dataIncoming : out STD_LOGIC_VECTOR(NdataIn*8-1 downto 0);
114            dataOut : in STD_LOGIC_VECTOR(NdataOut*8-1 downto 0);
115            clk : in STD_LOGIC;
116            reset : in STD_LOGIC;
117            UARTtick : in STD_LOGIC;
118            rx : in STD_LOGIC;
119            tx : out STD_LOGIC);
120 end component;
121 component LUTsin is
122     Port ( carrAngle, angle, phase, phase2x : in unsigned (11 downto 0):= (OTHERS => '0');
123            sin, cos, sinPha, cosPha, sin2x, sinCarr : out signed (15 downto 0):= (OTHERS => '0')
124          );
125 end component;
126 -- Filters
127 component ADCfilter IS
128 PORT( clk                            :   IN     std_logic;
129       clk_enable                     :   IN     std_logic;
130       reset                          :   IN     std_logic;
```

```
131        filter_in                          :   IN    signed(17 DOWNTO 0); -- sfix16
132        filter_out                         :   OUT   signed(31 DOWNTO 0)  -- sfix16_E4
133        );
134  END component;
135  component DEMODfilter IS
136  PORT( clk                                :   IN    std_logic;
137        clk_enable                         :   IN    std_logic;
138        reset                              :   IN    std_logic;
139        filter_in                          :   IN    signed(47 DOWNTO 0); -- sfix16
140        filter_out                         :   OUT   signed(31 DOWNTO 0)  -- sfix32
141        );
142  END component;
143  component LPfilter IS
144      GENERIC(
145        Ninput : INTEGER := 16; -- input and output width
146        Ncoeff : INTEGER := 16); -- coefficient width
147      Port ( tick : in STD_LOGIC;
148             reset : in STD_LOGIC;
149             input : in SIGNED (Ninput - 1 downto 0);
150             coeff : in SIGNED (Ncoeff - 1 downto 0);
151             output : out SIGNED (Ninput - 1 downto 0));
152  end component;
153  begin
154  process(CLK, reset)
155  begin
156  if (reset='1') then
157      counter <= (others=>'0');
158      Genericcounter <= (others=>'0');
159      NCOcounter <= (others=>'0');
160      Carrcounter <= (others=>'0');
161      UARTcounter <= (others=>'0');
162  elsif (CLK'event and CLK='1') then
163      counter <= counter_next;
164      Genericcounter <= Genericcounter_next;
165      if (counter=(ADCdiv-1)) then
166          NCOcounter <= NCOcounter_next;
167          Carrcounter <= Carrcounter_next;
168          UARTcounter <= UARTcounter_next;
169      else
170          NCOcounter <= NCOcounter;
171          Carrcounter <= Carrcounter;
```

```
172          UARTcounter <= UARTcounter;
173      end if;
174  end if;
175  end process;
176  process(clk, reset)
177  begin
178  if (reset='1') then
179      FilterCLK<='0';
180  elsif (clk'event and clk='1') then
181      FilterCLK <= not FilterCLK;
182  end if;
183  end process;
184  counter_next <= (others=>'0') when counter=(ADCdiv-1) else counter + 1;
185  Genericcounter_next <= Genericcounter + 1;
186  UARTcounter_next <= (others=>'0') when UARTcounter>=(UARTdiv-1) else UARTcounter + 1;
187  NCOcounter_next <= NCOcounter + NCOFreq;
188  Carrcounter_next <= Carrcounter + carrFreq;
189  tick <= '1' when  counter=(ADCdiv-1) else '0';
190  UARTtick <= '1' when UARTcounter=(UARTdiv-1)else '0';
191  -- Input from ADC (Map 12 bit unsigned to LSB of 16 bit signed)
192  --inX(15) <= not data_inX(ADCbit-1);
193  --inY(15) <= not data_inY(ADCbit-1);
194  --inX(14 downto 0) <= signed(data_inX(14 downto 0));
195  --inY(14 downto 0) <= signed(data_inY(14 downto 0));
196  inX<=signed(data_inX);
197  inY<=signed(data_inY);
198  -- NCO assignments
199  angle <= NCOcounter(NCOcounterSize-1 downto NCOcounterSize-angleWIDTH);
200  carrAngle <= Carrcounter(NCOcounterSize-1 downto NCOcounterSize-angleWIDTH);
201  -- Internal signals
202  sx <= inX_filtered * sin;
203  sy <= inY_filtered * sin;
204  cx <= inX_filtered * cos;
205  cy <= inY_filtered * cos;
206  -- UART assignments
207  UART2DSPout <= outCtrlReg & std_logic_vector(sxf) & std_logic_vector(cxf) & std_logic_vector(syf)
          & std_logic_vector(cyf); --(2 + 4 x 4 = 18)
208  inCtrlReg <= UART2DSPin(15 downto 0);
209  Fsx <= signed(UART2DSPin(31 downto 16));
210  Fcx <= signed(UART2DSPin(47 downto 32));
211  Fsy <= signed(UART2DSPin(63 downto 48));
```

```
212 Fcy <= signed(UART2DSPin(79 downto 64));
213 NCOfreq <= unsigned(UART2DSPin(111 downto 80));
214 Carrfreq <= unsigned(UART2DSPin(143 downto 112));
215 phase <= unsigned(UART2DSPin(155 downto 144));
216 phase2x <= unsigned(UART2DSPin(171 downto 160));
217 F2x <= signed(UART2DSPin(191 downto 176));
218 -- GPIO
219 --LED <= inCtrlReg;
220 --outCtrlReg <= SW;
221 LED <= SW;
222 reset_SPI_out <= not SW(0);
223 reset_SPI <= not SW(1);
224 reset <= SW(2);
225 UARTdiv <= 500000 when SW(15) = '1' else
226            500 when SW(14) = '1' else
227            5000;
228 -- Test code
229 --LED <= std_logic_vector(data_inX(17 downto 2));
230 --Fsx <= inX;
231 --Fcx <= signed(SW);
232 --Fsy <= signed(SW);
233 --Fcy <= signed'(x"7FFF");
234 --F2x <= signed'(x"7FFF");
235 --UART2DSPout<=x"444f";
236 --data_outX(15)<=not inX_filtered(15);
237 --data_outX(14 downto 0) <= std_logic_vector(inX_filtered(14 downto 0));
238 --data_outY(15)<=not inY_filtered(15);
239 --data_outY(14 downto 0) <= std_logic_vector(inY_filtered(14 downto 0));
240 --data_out2x <=data_inX;
241 -- Force vectors
242 outX <= sinPha * Fsx + cosPha * Fcx;
243 outY <= sinPha * Fsy + cosPha * Fcy;
244 out2x <= sin2x * F2x;
245 -- Output to DAC (Map MSB of 32 bit signed to 16 bit unsigned)
246 -- Has saturation blocks to prevent DAC rollover
247 data_outX<= std_logic_vector(not outX(31) & outX(29 downto 15));
248 data_outY<= std_logic_vector(not outY(31) & outY(29 downto 15));
249 data_out2x<= std_logic_vector(not out2x(31) & out2x(29 downto 15));
250 --data_outXbuf<= x"FFFF" when outX(31 downto 15) > signed'("00111111111111111") else
251 --              x"0000" when outX(31 downto 15) < signed'("11000000000000000") else
252 --              std_logic_vector(not outX(31) & outX(29 downto 15));
```

```
253 --data_outYbuf<= x"FFFF" when outY(31 downto 15) > signed'("00111111111111111") else
254 --             x"0000" when outY(31 downto 15) < signed'("11000000000000000") else
255 --             std_logic_vector(not outY(31) & outY(29 downto 15));
256 --data_out2xbuf<=x"FFFF" when out2x(31 downto 15) > signed'("00111111111111111") else
257 --             x"0000" when out2x(31 downto 15) < signed'("11000000000000000") else
258 --             std_logic_vector(not out2x(31) & out2x(29 downto 15));
259 --data_outX<= data_outXbuf when SW(3) = '0' else
260 --             data_inX(ADCbit-1 downto ADCbit-16);
261 --data_outY<= data_outYbuf when SW(3) = '0' else
262 --             data_inY(ADCbit-1 downto ADCbit-16);
263 --data_out2x<=data_out2xbuf;
264 ADC_X:spi_master
265 generic map(slaves=>1, d_width=>ADCbit)
266 port map(clock => CLK, reset_n=> reset_SPI, enable=>tick, cpol=>'0', cpha=>'1', cont=>'0',
        clk_div=>1, addr=>0, tx_data=>(others=>'0'), miso=>JC(2), sclk=>JC(3), ss_n(0)=>JC(0),
        rx_data(ADCbit-1 downto 0)=>data_inX);
267 ADC_Y:spi_master
268 generic map(slaves=>1, d_width=>ADCbit)
269 port map(clock => CLK, reset_n=> reset_SPI, enable=>tick, cpol=>'0', cpha=>'1', cont=>'0',
        clk_div=>1, addr=>0, tx_data=>(others=>'0'), miso=>JD(2), sclk=>JD(3), ss_n(0)=>JD(0),
        rx_data(ADCbit-1 downto 0)=>data_inY);
270 Filter_X:ADCfilter
271 port map(clk=>clk, clk_enable=>tick, reset=>reset, filter_in=>inX, filter_out=>inX_filtered);
272 Filter_Y:ADCfilter
273 port map(clk=>clk, clk_enable=>tick, reset=>reset, filter_in=>inY, filter_out=>inY_filtered);
274 Filter_sx:DEMODfilter
275 port map(clk=>clk, clk_enable=>tick, reset=>reset, filter_in=>sx, filter_out=>sxf);
276 Filter_sy:DEMODfilter
277 port map(clk=>clk, clk_enable=>tick, reset=>reset, filter_in=>sy, filter_out=>syf);
278 Filter_cx:DEMODfilter
279 port map(clk=>clk, clk_enable=>tick, reset=>reset, filter_in=>cx, filter_out=>cxf);
280 Filter_cy:DEMODfilter
281 port map(clk=>clk, clk_enable=>tick, reset=>reset, filter_in=>cy, filter_out=>cyf);
282 DAC_X:spi_master
283 generic map(slaves=>1, d_width=>16)
284 port map(clock => CLK, reset_n=> reset_SPI_out, enable=>tick, cpol=>'0', cpha=>'0', cont=>'0',
        clk_div=>1, addr=>0, tx_data=>data_outX, sclk=>JB(3), ss_n(0)=>JB(0), mosi=>JB(1), miso=>
        dummy_outX);
285 JB(2)<='0';-- Write enable
286 DAC_Y:spi_master
287 generic map(slaves=>1, d_width=>16)
```

```
288 port map(clock => CLK, reset_n=> reset_SPI_out, enable=>tick, cpol=>'0', cpha=>'0', cont=>'0',
        clk_div=>1, addr=>0, tx_data=>data_outY, sclk=>JB(7), ss_n(0)=>JB(4), mosi=>JB(5), miso=>
        dummy_outY);
289 JB(6)<='0'; -- Write enable
290 DAC_2x:spi_master
291 generic map(slaves=>1, d_width=>16)
292 port map(clock => CLK, reset_n=> reset_SPI_out, enable=>tick, cpol=>'0', cpha=>'0', cont=>'0',
        clk_div=>1, addr=>0, tx_data=>data_out2x, sclk=>JA(3), ss_n(0)=>JA(0), mosi=>JA(1), miso=>
        dummy_out2x);
293 JA(2)<='0'; -- Write enable
294 --GPIO1: GPIO
295 --port map(SW => SW, BTN=>BTN, CLK=>CLK, SSEG_CA=>SSEG_CA, SSEG_AN=>SSEG_AN, UART_TXD=>
        dummY_GPIO_UART);
296 NCO: LUTsin
297 port map(carrAngle=>carrAngle, angle=>angle, phase=>phase, phase2x=>phase2x, sin=>sin, cos=>cos,
        sinPha=>sinPha, cosPha=>cosPha, sin2x=>sin2x, sinCarr=>sinCarr);
298 UART1 : UART2DSP
299 generic map(Ndatain=>Ndatain, Ndataout=>Ndataout)
300 port map(dataIncoming=>UART2DSPin, dataOut=> UART2DSPout, clk=>clk, reset=>reset, UARTtick=>
        UARTtick, tx=>JA(6), rx=>JA(5));
301 end arch;
```

Listing E.2: microcontroller.ino

```
1  // Timing variables
2  unsigned long currentMicros = 0, prevMicros = 0, sampleCount = 0, scriptSampleCount; // timing
       variables
3  const unsigned long rs232rate = 100, sampleDIV = 10; // sampling rate in microseconds, RS232
       reporting frequency
4  double virtualCInterval = 1; // Virtual carousel interval in seconds
5  // Time constant
6  const double sampleRate = 100; // Hz
7  const double tau = 0.01; //secs
8  const double FPGAclock = 500000; // Hz
9  // ADC / DAC scale factors
10 const double dblADCscale = 1073741823 / 25;
11 const double DACscale = (32768 - 1) / 2.5;
12 const double DACsaturate = 0.2;
13 const double DACsaturate2x = 1;
14 double DACscaleX = 16.71;//3.75;
15 double DACscaleY = 1;
16 double ADCscaleX = 1;
17 double ADCscaleY = 1;
18 // FPGA UART variables
19 // Raw data
20 unsigned long FPGASerialLength = 0;
21 const unsigned long FPGASerialMaxLength = 18;
22 char FPGASerialCharArray[FPGASerialMaxLength], FPGASerialNumber[FPGASerialMaxLength - 2],
       FPGALastChar;
23 // Incoming from FPGA
24 unsigned int inCtrlReg = 0;
25 long longsx = 0, longcx = 0, longsy = 0, longcy = 0;
26 // Outgoing to FPGA
27 unsigned int outCtrlReg = 0, intphase = 0, intphase2x = 0;
28 int intFsx = 0, intFcx = 0, intFsy = 0, intFcy = 0, intF2x = 0;
29 unsigned long longNCOfreq = 0, longCarrFreq = 0;
30 // PC UART variables
31 unsigned long commSerialLength = 0;
32 const unsigned long commSerialMaxLength = 20, commSerialMinLength = 4;
33 char commSerialCharArray[commSerialMaxLength], commSerialNumber[commSerialMaxLength - 2],
       commLastChar;
34 double dblPoutOld = 0, dblEinOld = 0, dblEoutOld = 0, dblQoutOld = 0, dbl2outOld = 0, dblQinOld =
        0, dblFerrorOld = 0, dblFoutOld = 0, dblTSOld = 0, dblThetaExpOld2 = 0, dblThetaExpModOld2 =
```

```
    0; // LP filter buffer for RS232 reporting
35 double dblPoutFiltered = 0, dblEinFiltered = 0, dblEoutFiltered = 0, dblQoutFiltered = 0,
     dbl2outFiltered = 0, dblQinFiltered = 0, dblFerrorFiltered = 0, dblFoutFiltered = 0,
     dblTSFiltered = 0, dblThetaExpFiltered = 0, dblThetaExpModFiltered = 0; // LP filter buffer
     for RS232 reporting
36 // Command Line Interface (CLI) variables
37 boolean isSerialNumber = true;
38 double dblTemp = 0; // Received data
39 // PLL variables
40 double dbl2D = 250, dblPD = 238; // Phases for parametric and regular drive
41 double dblPC = 10; // PLL cut-off frequency (Hz)
42 double dblPCrad = 2 * dblPC * M_PI;
43 double dblCF = 0;  // Carrier frequency
44 double dblRC = 10; // RS232 LP filter cut-off (Hz)
45 // Direct drive variables (for debugging the DACs)
46 double dblDD = 0, dblDFsx = 0, dblDFcx = 0, dblDFsy = 0, dblDFcy = 0, dblDF2x = 0;
47 double dblDB = 0; // Debug mode on/off
48 double dblVE = 0, dblVD = 1, dblVS = 1, dblVN = 4, dblVC = 0; // Virtual carouseling
49 // Slow moving variables
50 // Demodulated quantities
51 double dblsx = 0, dblcx = 0, dblsy = 0, dblcy = 0;
52 double dblsxp = 0, dblcxp = 0, dblsyp = 0, dblcyp = 0;
53 double dblsxOld = 0, dblcxOld = 0, dblsyOld = 0, dblcyOld = 0;
54 // Square of demodulated quantities
55 double dblsx2 = 0, dblcx2 = 0, dblsy2 = 0, dblcy2 = 0;
56 // Pendulum variables
57 double dblE = 0, dblQ = 0, dblL = 0, dblR = 0, dblS = 0;
58 double dblEOld = 0, dblQOld = 0, dblLOld = 0, dblROld = 0, dblSOld = 0;
59 // Pattern angle variables
60 double dbl2ThetaRaw = 0, dbl2ThetaRawPrev = 0, dbl2ThetaExp = 0, dblThetaExp = 0, dblThetaExpMod
     = 0, dblThetaOut = 0;
61 long revCounter = 0;
62 double dblTE = 0, dblTS = 0, dblTSdeg = 0, dblTG = 0, dblTGdeg = 0, dblThetaExpOld = 0, dblTF =
     0, dblTP = 0, dblTPdeg = 0;
63 double dblTC = 100;
64 double dblTR = 0;
65 double dblTCrad = 2 * 10 * M_PI;
66 const int nHarmonics = 4;
67 // Drive vector
68 double dblFsx = 0, dblFcx = 0, dblFsy = 0, dblFcy = 0, dblF2x;
69 // Dummy variables
```

```
70  double dummy = 0;
71  // Feedback loops
72  namespace Pendulum {
73  // PID variables
74  struct vars {
75    double dblE, dblF, dblS, dblP, dblI, dblR, dblin, dblError, dblout, dblV, dblinOld, dbloutOld,
        dblsaturate;
76    double n0G;
77    double sG[nHarmonics];
78    double cG[nHarmonics];
79    double n0;
80    double s[nHarmonics];
81    double c[nHarmonics];
82  } E, E2, Q, F, P, B;
83  void ExtractHarmonics(struct vars *z, double thetaDeg, double incrementDeg, char nameHarmonic) {
84    double noOfPoints, thetaRad = 0;
85    noOfPoints = 360 / incrementDeg;
86    thetaRad = thetaDeg * M_PI / 180;
87    if (fmod(thetaDeg, 360) == 0) {
88      Serial.print("%␣");
89      Serial.print((double)millis() / 1000);
90      Serial.print("␣H");
91      Serial.print(nameHarmonic);
92      Serial.print(":␣");
93      for (int i = 0; i < nHarmonics; i++) {
94        Serial.print(z->c[i], 8);
95        Serial.print(",␣");
96        Serial.print(z->s[i], 8);
97        Serial.print(",␣");
98        z->c[i] = 2 * (z->dblout * cos((i + 1) * thetaRad)) / noOfPoints;
99        z->s[i] = 2 * (z->dblout * sin((i + 1) * thetaRad)) / noOfPoints;
100     }
101     Serial.println(z->n0, 8);
102     z->n0 = (z->dblout) / noOfPoints;
103     dblVC = dblVC + 1;
104   }
105   else {
106     z->n0 = (z->dblout) / noOfPoints + z->n0;
107     for (int i = 0; i < nHarmonics; i++) {
108       z->c[i] = 2 * (z->dblout * cos((i + 1) * thetaRad)) / noOfPoints + z->c[i];
109       z->s[i] = 2 * (z->dblout * sin((i + 1) * thetaRad)) / noOfPoints + z->s[i];
```

```
110       }
111     }
112   }
113   void PID(struct vars *z, double theta, double tau) {
114     double dblFF = 0;
115     if (z->dblV == 1) {
116       for (int i = 0; i < nHarmonics; i++) {
117         dblFF +=  z->cG[i] * cos((i + 1) * theta) + z->sG[i] * sin((i + 1) * theta);
118       }
119     }
120     else {
121       double dblFF = 0;
122     }
123     z->dblError = 0;
124     z->dblout = 0;
125     z->dblError = z->dblS - z->dblin;
126     if (z->dblE == 1) {
127       z->dblR = Saturate((z->dblR + z->dblError * z->dblI * tau), z->dblsaturate);
128       z->dblout = Saturate((z->dblP * z->dblError + z->dblR + z->dblF + dblFF), z->dblsaturate);
129     }
130     else if (z->dblE == 2) {
131       z->dblE = 1;
132       z->dblout = (z->dblP * z->dblError + z->dblR + z->dblF + dblFF);
133       z->dblR = 0;
134     }
135     else if (z->dblE == 4) {
136       z->dblout = z->dblF + dblFF;
137       z->dblR = 0;
138     }
139     else if (z->dblE == 9) {
140       z->dblout = z->dblF + dblFF;
141       z->dblR = 0;
142     }
143     else {
144       z->dblR = 0;
145       z->dblout = 0;
146     }
147   }
148   double LP(double input, double cutOffFreqRad, double *yregister, double tau) {
149     double a = 0, output = 0;
150     a = tau / ( 1 / (cutOffFreqRad) + tau);
```

```
151      output = (1 - a) **yregister + a * input;
152      *yregister = output;
153      return output;
154    }
155    void SerialCLI(char command[2], double *dblFromCLI) {
156      if (commSerialLength >= commSerialMinLength) {
157        for (int i = 0; i < commSerialLength; i++) {
158          // Serial.print(serialCharArray[i]); // Echo, echo, echo...
159          if (i >= 2) {
160            commSerialNumber[i - 2] = commSerialCharArray[i];
161            // Number portion must contain CR.-0123456789, if anything else is in there, stop
                   assignment
162            if (commSerialCharArray[i] != '-' && commSerialCharArray[i] != '.' && commSerialCharArray
                   [i] != 13 && isDigit(commSerialCharArray[i]) == false)
163            {
164              isSerialNumber = false;
165            }
166          }
167        }
168        // Start interpreter
169        if (isSerialNumber == true || commSerialCharArray[2] == '?') { // If it is a number or and
               inquiry
170          if (commSerialCharArray[0] == command[0] || commSerialCharArray[0] == (command[0] + 32)) {
                 // Check first letter
171            if (commSerialCharArray[1] == command[1] || commSerialCharArray[1] == (command[1] + 32))
                   { // Check second letter
172              // Extract number
173              if (isSerialNumber == true) { // Assign only if it is a number
174                dblTemp = atof(commSerialNumber);
175                *dblFromCLI = dblTemp;
176              }
177              Serial.print("%␣");
178              Serial.print(command[0]); // Echo the variable
179              Serial.print(command[1]);
180              Serial.print("␣=␣");
181              Serial.println(*dblFromCLI, 6);
182            }
183          }
184        }
185      }
186      isSerialNumber = true; // Rinse and repeat
```

```
187 }
188 }
189 void setup() {
190   // Order is: dblE, dblF, dblS, dblP, dblI, dblR, dblin, dblError, dblout, dblinOld, dbloutOld,
        dblsaturate
191   Pendulum::E = {0, 0.01, 0.5, 0.5, 2, 0, 0, 0, 0, 0, 0, 0, 0.05};
192   Pendulum::E2 = {0, 0.15, 0.4, 1, 1, 0, 0, 0, 0, 0, 0, 0, 0.05};
193   Pendulum::Q = {0, 0, 0, 0.5, 0.5, 0, 0, 0, 0, 0, 0, 0, 0.4};
194   Pendulum::F = {0, 0, 0, 0.5, 0.5, 0, 0, 0, 0, 0, 0, 0, 0.2};
195   Pendulum::P = {1, 2679, 0, 0.1, 2, 0, 0, 0, 0, 0, 0, 0, FPGAclock};
196   Pendulum::B = {0, 0, 0, 0.1, 2, 0, 0, 0, 0, 0, 0, 0, 2};
197   Pendulum::P.c = {0, 0, 0, 0};
198   Pendulum::P.s = {0, 0, 0, 0};
199   Pendulum::P.cG = {0, 0, 0, -0.2};
200   Pendulum::P.sG = {0, 0.15, 0, 0};
201   Pendulum::Q.cG = {0, 0.05, 0, 0};
202   Pendulum::Q.sG = {0, 0.09, 0, 0.08};
203   Pendulum::F.cG = {0, 0.014, 0, 0};
204   Pendulum::F.sG = {0, 0.018, 0, 0.015};
205   // Set up communication
206   // UART to PC
207   Serial.begin(115200);
208   Serial.println("%␣Starting...␣");
209   Serial.println("%␣Time,␣Frequency,␣Ein,␣Eout,␣E2out,␣Qin,␣Qout,␣Fin,␣Fout,␣TS,␣Theta,␣ThetaMod"
        );
210   Serial.println("%␣s,␣Hz,␣Ein,␣V^2,␣V,␣V^2,␣V,␣rad,␣V,␣deg,␣deg,␣deg");
211   // UART to FPGA
212   Serial1.begin(115200);
213 }
214 void loop() {
215   // Gyro control
216   FPGAListen();
217   // PC interface
218   commListen();
219 }
220 void FPGAListen() {
221   // RS232 commandline interpreter
222   while (Serial1.available() > 0) {
223     FPGALastChar = Serial1.read();  // Read next char in serial buffer
224     FPGASerialCharArray[FPGASerialLength] = FPGALastChar;
225     FPGASerialLength++;
```

```
226 }
227 //  for(int i = 0; i < FPGASerialLength; i++){
228 //    Serial.print(FPGASerialCharArray[i]); // Echo, echo, echo...
229 //  }
230 if (FPGASerialLength > FPGASerialMaxLength) {
231   if (FPGASerialCharArray[FPGASerialMaxLength] == 13) {
232     //      toc();
233     //      tic();
234     // Read incoming data
235     inCtrlReg = (int(FPGASerialCharArray[0] << 8)) + (int(FPGASerialCharArray[1]));
236     longsx = (long(FPGASerialCharArray[2] << 24)) + (int(FPGASerialCharArray[3] << 16)) + (int(
          FPGASerialCharArray[4] << 8)) + (int(FPGASerialCharArray[5]));
237     longcx = (long(FPGASerialCharArray[6] << 24)) + (int(FPGASerialCharArray[7] << 16)) + (int(
          FPGASerialCharArray[8] << 8)) + (int(FPGASerialCharArray[9]));
238     longsy = (long(FPGASerialCharArray[10] << 24)) + (int(FPGASerialCharArray[11] << 16)) + (
          int(FPGASerialCharArray[12] << 8)) + (int(FPGASerialCharArray[13]));
239     longcy = (long(FPGASerialCharArray[14] << 24)) + (int(FPGASerialCharArray[15] << 16)) + (
          int(FPGASerialCharArray[16] << 8)) + (int(FPGASerialCharArray[17]));
240     // Pick-off demodulatated quantities
241     //      dblsx = LP((double)longsx / dblADCscale, dblPCrad, &dblsxOld, tau);
242     //      dblcx = LP((double)longcx / dblADCscale, dblPCrad, &dblcxOld, tau);
243     //      dblsy = LP((double)longsy / dblADCscale, dblPCrad, &dblsyOld, tau);
244     //      dblcy = LP((double)longcy / dblADCscale, dblPCrad, &dblcyOld, tau);
245     // Unfiltered Pick-off demodulatated quantities
246     dblsxp = (double)longsx / dblADCscale * ADCscaleX;
247     dblcxp = (double)longcx / dblADCscale * ADCscaleX;
248     dblsyp = (double)longsy / dblADCscale * ADCscaleY;
249     dblcyp = (double)longcy / dblADCscale * ADCscaleY;
250     // Coordinate transformation on pick-off
251     dblTP = dblTPdeg * M_PI / 180;
252     dblsx = dblsxp * cos(dblTP) + dblsyp * sin(dblTP);
253     dblcx = dblcxp * cos(dblTP) + dblcyp * sin(dblTP);
254     dblsy = dblsyp * cos(dblTP) - dblsxp * sin(dblTP);
255     dblcy = dblcyp * cos(dblTP) - dblcxp * sin(dblTP);
256     // Pendulum variables
257     dblsx2 = dblsx * dblsx;
258     dblcx2 = dblcx * dblcx;
259     dblsy2 = dblsy * dblsy;
260     dblcy2 = dblcy * dblcy;
261     dblE = dblsx2 + dblcx2 + dblsy2 + dblcy2;
262     dblQ = 2 * (dblcx * dblsy - dblcy * dblsx);
```

```
263         dblL = 2 * (dblcx * dblsx + dblcy * dblsy);
264         dblR = (dblsx2 + dblcx2) - (dblsy2 + dblcy2);
265         dblS = 2 * (dblcx * dblcy + dblsx * dblsy);
266         Pendulum::E.dblin = dblE;
267         Pendulum::E2.dblin = dblE;
268         Pendulum::Q.dblin = dblQ;
269         Pendulum::P.dblin = -1 * Pendulum::LP(dblL, dblPCrad, &dblLOld, tau);
270         // Theta estimate
271         dbl2ThetaRaw = atan2(dblS, dblR);
272         dbl2ThetaExp = ExpRadian(dbl2ThetaRaw, &dbl2ThetaRawPrev, &revCounter);
273         dblThetaExp = dbl2ThetaExp / 2;
274         dblThetaExpMod = fmod(dblThetaExp, 2 * M_PI);
275         if (dblThetaExpMod < 0) {
276           dblThetaExpMod += 2 * M_PI;
277         }
278         // Pattern angle FRB input
279         Pendulum::F.dblin = dblThetaExp;
280         Pendulum::F.dblS = dblTS;
281         // Drive at an arbitrary angle or follow the measured pattern angle (WA mode)
282         if (dblTE == 0) {
283           dblThetaOut = dblTS;
284         }
285         else if (dblTE == 1) {
286           dblThetaOut = Pendulum::LP(dblThetaExp, dblTCrad, &dblThetaExpOld, tau) + dblTF * M_PI /
                180;
287         }
288         //PIDs
289         Pendulum::PID(&Pendulum::E, dblThetaOut, tau);
290         Pendulum::PID(&Pendulum::E2, dblThetaOut, tau);
291         Pendulum::PID(&Pendulum::Q, dblThetaOut, tau);
292         Pendulum::PID(&Pendulum::F, dblThetaOut, tau);
293         Pendulum::PID(&Pendulum::P, dblThetaOut, tau);
294         Pendulum::PID(&Pendulum::B, dblThetaOut, tau);
295         // Construct force vectors
296         // E and F (same phase)
297         dblFcx = Pendulum::E.dblout * cos(dblThetaOut) - Pendulum::F.dblout * sin(dblThetaOut);
298         dblFcy = Pendulum::E.dblout * sin(dblThetaOut) + Pendulum::F.dblout * cos(dblThetaOut);
299         // Q (in quadrature to E and F)
300         dblFsx = - Pendulum::Q.dblout * sin(dblThetaOut);
301         dblFsy = Pendulum::Q.dblout * cos(dblThetaOut);
302         dblF2x = Pendulum::E2.dblout;
```

```
303        //Forcer
304        if (dblDD == 1) {
305          intFsx = (int)(Saturate(dblDFsx, DACsaturate) * DACscale);
306          intFcx = (int)(Saturate(dblDFcx, DACsaturate) * DACscale);
307          intFsy = (int)(Saturate(dblDFsy, DACsaturate) * DACscale);
308          intFcy = (int)(Saturate(dblDFcy, DACsaturate) * DACscale);
309          intF2x = (int)(Saturate(dblDF2x, DACsaturate2x) * DACscale);
310        }
311        else {
312          intFsx = (int)(Saturate(dblFsx, DACsaturate) * DACscale * DACscaleX);
313          intFcx = (int)(Saturate(dblFcx, DACsaturate) * DACscale * DACscaleX);
314          intFsy = (int)(Saturate(dblFsy, DACsaturate) * DACscale * DACscaleY);
315          intFcy = (int)(Saturate(dblFcy, DACsaturate) * DACscale * DACscaleY);
316          intF2x = (int)(Saturate(dblF2x, DACsaturate2x) * DACscale);
317        }
318        // Pass the PLL freq and NCO phase
319        longNCOfreq = (long)(Pendulum::P.dblout * (4294967296 - 1) / FPGAclock);
320        longCarrFreq = (long)(dblCF * (4294967296 - 1) / FPGAclock);
321        intphase = (int)(dblPD / 360 * 4096);
322        intphase2x = (int)(dbl2D / 360 * 4096);
323        // End calculations
324        // Write to FPGA
325        Serial1.write((byte*)&inCtrlReg, 2);
326        Serial1.write((byte*)&intFsx, 2);
327        Serial1.write((byte*)&intFcx, 2);
328        Serial1.write((byte*)&intFsy, 2);
329        Serial1.write((byte*)&intFcy, 2);
330        Serial1.write((byte*)&longNCOfreq, 4);
331        Serial1.write((byte*)&longCarrFreq, 4);
332        Serial1.write((byte*)&intphase, 2);
333        Serial1.write((byte*)&intphase2x, 2);
334        Serial1.write((byte*)&intF2x, 2);
335        Serial1.write(13);  // CR
336        // Filter variables to be printed to RS232
337        dblPoutFiltered = Pendulum::LP(Pendulum::P.dblout, 2 * dblRC * M_PI, &Pendulum::P.dbloutOld
               , tau);
338        dblEinFiltered = Pendulum::LP(Pendulum::E.dblin, 2 * dblRC * M_PI, &Pendulum::E.dblinOld,
               tau);
339        dblEoutFiltered = Pendulum::LP(Pendulum::E.dblout, 2 * dblRC * M_PI, &Pendulum::E.dbloutOld
               , tau);
```

```
340       dbl2outFiltered = Pendulum::LP(Pendulum::E2.dblout, 2 * dblRC * M_PI, &Pendulum::E2.
              dbloutOld, tau);
341       dblQinFiltered = Pendulum::LP(Pendulum::Q.dblin, 2 * dblRC * M_PI, &Pendulum::Q.dblinOld,
              tau);
342       dblQoutFiltered = Pendulum::LP(Pendulum::Q.dblout, 2 * dblRC * M_PI, &Pendulum::Q.dbloutOld
              , tau);
343       dblFerrorFiltered = Pendulum::LP(Pendulum::F.dblError, 2 * dblRC * M_PI, &Pendulum::F.
              dblinOld, tau);
344       dblFoutFiltered = Pendulum::LP(Pendulum::F.dblout, 2 * dblRC * M_PI, &dblFoutOld, tau);
345       dblTSFiltered = dblTSdeg;
346       dblThetaExpFiltered = Pendulum::LP(dblThetaExp * 180 / M_PI, 2 * dblRC * M_PI, &
              dblThetaExpOld2, tau);
347       dblThetaExpModFiltered = Pendulum::LP(dblThetaExpMod * 180 / M_PI, 2 * dblRC * M_PI, &
              dblThetaExpModOld2, tau);
348       Serial2PC();
349       VirtualC();
350     }
351     // Rinse and repeat
352     FPGASerialLength = 0;
353     FPGALastChar = 0;
354   }
355 }
356 void tic() {
357   prevMicros = micros();
358 }
359 void toc() {
360   currentMicros = micros();
361   Serial.println(currentMicros - prevMicros);
362 }
363 void commListen() {
364   // RS232 commandline interpreter
365   while (Serial.available() > 0 && commLastChar != 13) {
366     commLastChar = Serial.read();  // Read next char in serial buffer
367     commSerialCharArray[commSerialLength] = commLastChar;
368     commSerialLength++;
369     if (commSerialLength >= commSerialMaxLength) {
370       Serial.println("% Error: Command too long or carriage return is missing.");
371       commSerialLength = 0;
372       commLastChar = 0;
373       break;
374     }
```

```
375 }
376 if (commLastChar == 13 && commSerialLength > 0) {
377   // Serial.print(">> Command received, string length: ");
378   // Serial.println(serialLength - 1, DEC);
379   Serial.print("%␣");
380   for (int i = 0; i < commSerialLength; i++) {
381     Serial.print(commSerialCharArray[i]); // Echo, echo, echo...
382   }
383   // Run interpreter
384   // E variables from interpreter
385   Pendulum::SerialCLI("EE", &Pendulum::E.dblE);
386   Pendulum::SerialCLI("EF", &Pendulum::E.dblF);
387   Pendulum::SerialCLI("ES", &Pendulum::E.dblS);
388   Pendulum::SerialCLI("EP", &Pendulum::E.dblP);
389   Pendulum::SerialCLI("EI", &Pendulum::E.dblI);
390   Pendulum::SerialCLI("EV", &Pendulum::E.dblV);
391   // Parametric E variables from interpreter
392   Pendulum::SerialCLI("2E", &Pendulum::E2.dblE);
393   Pendulum::SerialCLI("2F", &Pendulum::E2.dblF);
394   Pendulum::SerialCLI("2S", &Pendulum::E2.dblS);
395   Pendulum::SerialCLI("2P", &Pendulum::E2.dblP);
396   Pendulum::SerialCLI("2I", &Pendulum::E2.dblI);
397   Pendulum::SerialCLI("2V", &Pendulum::E2.dblV);
398   // Q variables from interpreter
399   Pendulum::SerialCLI("QE", &Pendulum::Q.dblE);
400   Pendulum::SerialCLI("QF", &Pendulum::Q.dblF);
401   Pendulum::SerialCLI("QS", &Pendulum::Q.dblS);
402   Pendulum::SerialCLI("QP", &Pendulum::Q.dblP);
403   Pendulum::SerialCLI("QI", &Pendulum::Q.dblI);
404   Pendulum::SerialCLI("QV", &Pendulum::Q.dblV);
405   // F variables from interpreter
406   Pendulum::SerialCLI("FE", &Pendulum::F.dblE);
407   Pendulum::SerialCLI("FF", &Pendulum::F.dblF);
408   Pendulum::SerialCLI("FS", &Pendulum::F.dblS);
409   Pendulum::SerialCLI("FP", &Pendulum::F.dblP);
410   Pendulum::SerialCLI("FI", &Pendulum::F.dblI);
411   Pendulum::SerialCLI("FV", &Pendulum::F.dblV);
412   // PLL variables from interpreter
413   Pendulum::SerialCLI("PE", &Pendulum::P.dblE);
414   Pendulum::SerialCLI("PF", &Pendulum::P.dblF);
415   Pendulum::SerialCLI("PS", &Pendulum::P.dblS);
```

```
416     Pendulum::SerialCLI("PP", &Pendulum::P.dblP);
417     Pendulum::SerialCLI("PI", &Pendulum::P.dblI);
418     Pendulum::SerialCLI("PV", &Pendulum::P.dblV);
419     // Voltage control variables from interpreter
420     Pendulum::SerialCLI("BE", &Pendulum::B.dblE);
421     Pendulum::SerialCLI("BF", &Pendulum::B.dblF);
422     Pendulum::SerialCLI("BS", &Pendulum::B.dblS);
423     Pendulum::SerialCLI("BP", &Pendulum::B.dblP);
424     Pendulum::SerialCLI("BI", &Pendulum::B.dblI);
425     Pendulum::SerialCLI("BV", &Pendulum::B.dblV);
426     // PLL variables from interpreter
427     Pendulum::SerialCLI("PC", &dblPC);
428     Pendulum::SerialCLI("PD", &dblPD);
429     Pendulum::SerialCLI("2D", &dbl2D);
430     dblPCrad = dblPC * 2 * M_PI;
431     // ADC and DAC gains for x and y channels
432     Pendulum::SerialCLI("GX", &DACscaleX);
433     Pendulum::SerialCLI("GY", &DACscaleY);
434     Pendulum::SerialCLI("GA", &ADCscaleX);
435     Pendulum::SerialCLI("GB", &ADCscaleY);
436     // Direct drive variables from interpreter
437     Pendulum::SerialCLI("DD", &dblDD);
438     Pendulum::SerialCLI("sx", &dblDFsx);
439     Pendulum::SerialCLI("cx", &dblDFcx);
440     Pendulum::SerialCLI("sy", &dblDFsy);
441     Pendulum::SerialCLI("cy", &dblDFcy);
442     Pendulum::SerialCLI("D2", &dblDF2x);
443     // Theta variables
444     Pendulum::SerialCLI("TE", &dblTE);
445     Pendulum::SerialCLI("TS", &dblTSdeg);
446     Pendulum::SerialCLI("TG", &dblTGdeg);
447     Pendulum::SerialCLI("TC", &dblTC);
448     Pendulum::SerialCLI("TR", &dblTR);
449     Pendulum::SerialCLI("TF", &dblTF);
450     Pendulum::SerialCLI("TP", &dblTPdeg);
451     dblTCrad = dblTC * 2 * M_PI;
452     dblTS = dblTSdeg * M_PI / 180;
453     dblTG = dblTGdeg * M_PI / 180;
454     // RS232 variables
455     Pendulum::SerialCLI("RC", &dblRC);
456     Pendulum::SerialCLI("DB", &dblDB);
```

```
457     Pendulum::SerialCLI("VE", &dblVE);
458     Pendulum::SerialCLI("VD", &dblVD);
459     Pendulum::SerialCLI("VN", &dblVN);
460     Pendulum::SerialCLI("VC", &dblVC);
461     Pendulum::SerialCLI("VI", &virtualCInterval);
462     // Control scripts
463     if (Pendulum::E.dblE == 3) {
464       Pendulum::E.dblE = 0;
465       Pendulum::E2.dblE = 1;
466     }
467     if (dblTR == 1) {
468       dblTR = 0;
469       revCounter = 0;
470       dblTG = dblTS;
471     }
472     // Rinse and repeat.
473     commSerialLength = 0;
474     commLastChar = 0;
475   }
476 }
477 // UART to PC
478 void Serial2PC() {
479   if (sampleCount >= sampleDIV - 1) {
480     Serial.print((double)millis() / 1000);
481     Serial.print(",␣");
482     Serial.print(dblPoutFiltered, 8);
483     Serial.print(",␣");
484     //Debug mode on
485     if (dblDB == 1) {
486       Serial.print(longsx, DEC);
487       Serial.print(",␣");
488       Serial.print(longcx, DEC);
489       Serial.print(",␣");
490       Serial.print(longsy, DEC);
491       Serial.print(",␣");
492       Serial.print(longcy, DEC);
493       Serial.print(",␣");
494       Serial.print(dblsx, 6);
495       Serial.print(",␣");
496       Serial.print(dblcx, 6);
497       Serial.print(",␣");
```

```
498	      Serial.print(dblsy, 6);
499	      Serial.print(",␣");
500	      Serial.println(dblcy, 6);
501	    }
502	    // Debug mode off
503	    else {
504	      Serial.print(dblEinFiltered, 8);
505	      Serial.print(",␣");
506	      Serial.print(dblEoutFiltered, 8);
507	      Serial.print(",␣");
508	      Serial.print(dbl2outFiltered, 8);
509	      Serial.print(",␣");
510	      Serial.print(dblQinFiltered, 8);
511	      Serial.print(",␣");
512	      Serial.print(dblQoutFiltered, 8);
513	      Serial.print(",␣");
514	      Serial.print(dblFerrorFiltered, 8);
515	      Serial.print(",␣");
516	      Serial.print(dblFoutFiltered, 8);
517	      Serial.print(",␣");
518	      Serial.print(dblTSFiltered, 8);
519	      Serial.print(",␣");
520	      Serial.print(dblThetaExpFiltered, 8);
521	      Serial.print(",␣");
522	      Serial.println(dblThetaExpMod, 8);
523	    }
524	    sampleCount = 0;
525	  }
526	  else {
527	    sampleCount++;
528	  }
529	}
530	// Virtual carouseling
531	void VirtualC() {
532	  if (dblVE == 1) {
533	    if (dblVS == 1) {
534	      ExtractHarmonics(&Pendulum::E, dblTSdeg, dblVD, 'E');
535	      //ExtractHarmonics(&Pendulum::E2, dblTSdeg, dblVD, 'E2');
536	      ExtractHarmonics(&Pendulum::Q, dblTSdeg, dblVD, 'Q');
537	      ExtractHarmonics(&Pendulum::F, dblTSdeg, dblVD, 'F');
538	      ExtractHarmonics(&Pendulum::P, dblTSdeg, dblVD, 'P');
```

```
539        dblVS = 0;
540      }
541      if (dblVC >= (dblVN + 1)*4) {
542        dblVE = 0;
543        scriptSampleCount = 0;
544        dblVS = 1;
545        dblVC = 0;
546      }
547      else {
548        if (scriptSampleCount >= virtualCInterval * rs232rate - 1) {
549          dblTSdeg += dblVD;
550          dblTS = dblTSdeg * M_PI / 180;
551          scriptSampleCount = 0;
552          ExtractHarmonics(&Pendulum::E, dblTSdeg, dblVD, 'E');
553          //ExtractHarmonics(&Pendulum::E2, dblTSdeg, dblVD, 'E2');
554          ExtractHarmonics(&Pendulum::Q, dblTSdeg, dblVD, 'Q');
555          ExtractHarmonics(&Pendulum::F, dblTSdeg, dblVD, 'F');
556          ExtractHarmonics(&Pendulum::P, dblTSdeg, dblVD, 'P');
557        }
558        else {
559          scriptSampleCount++;
560        }
561      }
562    }
563    else if (dblVE == 2) {
564      dblVE = 0;
565      scriptSampleCount = 0;
566      dblVC = 0;
567    }
568    else if (dblVE == 0) {
569      dblVS = 1;
570      dblVC = 0;
571    }
572  }
573  // Dummy function
574  void DummyTest(double *dummy, double enable, double tau) {
575    *dummy = (*dummy + 1 * tau) * enable;
576    Serial.println(*dummy);
577  }
578  // Unwind the theta angle
579  double ExpRadian(double inputRad, double *inputRadPrev, long *revCounter) {
```

```
580    double output = 0;
581    double increment = 0;
582    increment = inputRad - *inputRadPrev;
583    if (increment > M_PI) {
584      *revCounter = *revCounter - 1;
585    }
586    else if (increment < -M_PI) {
587      *revCounter = *revCounter + 1;
588    }
589    output = inputRad + 2 * M_PI **revCounter;
590    *inputRadPrev = inputRad;
591    return output;
592  }
593  // Saturation function
594  double Saturate(double input, double saturationPoint) {
595    if (input > saturationPoint) {
596      return saturationPoint;
597    }
598    else if (input < -1 * saturationPoint) {
599      return (-1 * saturationPoint);
600    }
601    else {
602      return input;
603    }
604  }
```

Appendix F

List of Vendors

Allied High Tech Products, Inc.

Location: Rancho Dominguez, CA, USA

Phone: +1 (800) 675-1118

E-mail: orderalliedhightech.com

Multiprep Polishing System from Allied High Tech Products, Inc. was used through this dissertation for back lapping of fused silica wineglass resonators. The 12" Multiprep is capable of rough and fine lapping up wafers up to 4".

Disco Hi-Tech America, Inc.

Location: Santa Clara, CA, USA

Phone: +1 (408) 987-3776

E-mail: richard_b@discousa.com

Stealth dicing technology from Disco Hi-Tec America was used to dice in-house fabricated silicon-on-insulator gyroscopes developed as part of this dissertation. The process eliminates process dust and need for the associated cleaning that typically happens after dicing.

dSPACE, Inc.

Location: Wixon, MI, USA

Phone: +1 (248) 295-4700

E-mail: cpasque@dspaceinc.com

dSPACE 1103 PPC controller board was used for early controller development. The system provides rapid control system development by integrating Simulink environment with a powerful DSP based controller.

Gamma Vacuum

Location: Shakopee, MN, USA

Phone: +1 (952) 445-4841

E-mail: orders@gammavacuum.com

A macro-scale Non-evaporable Getter (NEG) pump from Gamma Vacuum was integrated into a macro-scale getter assembly for gyroscope characterization on a rate table with continuous 360° rotation.

Kurt J. Lesker

Location: Livermore, CA, USA

Phone: +1 (925) 449-0104

E-mail: salesus@lesker.com

Vacuum chamber components and the vacuum gauges were purchased from Kurt J. Lesker.

Mark Optics, Inc.

Location: Santa Ana, CA, USA

Phone: +1 (714) 545-6684

E-mail: quote@markoptics.com

Mark Optics, Inc. is a custom optics provider that specializes in glass wafers. Fused silica, Borosilicate Glass (BSG) and Ultra Low Expansion Titania Silicate Glass (ULE TSG) wafers used throughout this thesis were machined by Mark Optics.

MTI Corporation

Location: Richmond, CA, USA

Phone: +1 (510) 525-3070

E-mail: info@mtixtl.com

A high temperature Rapid Thermal Processing (RTP) furnace from MTI Corporation was used for micro-glassblowing of fused silica shells.

National Aperture, Inc.

Location: Salem, NH, USA

Phone: +1 (800) 360-4598

E-mail: wgrenier@nationalaperture.com

Micro positioning stages from National Aperture, Inc. was used for various precision positioning applications in this dissertation. A motorized rotary stage and two linear stages were combined to create a precision positioning setup for laser ablation of micro-wineglass resonators. Another linear stage was used for the construction of piezo pinger described in Chapter 3.

Photosciences, Inc.

Location: Torrance, CA, USA

Phone: +1 (310) 634-1500

E-mail: fasttrack@photo-sciences.com

Photomasks used throughout this dissertation were fabricated by Photosciences, Inc.

Physik Instrumente LP

Location: Auburn, MA, USA

Phone: +1 (508) 832-3456

E-mail: info@pi-usa.us

Piezo actuators used throughout this dissertation were fabricated by Physik Instrumente LP. The piezo actuators were both used as a shaker and a piezo pinger in combination with a Laser Doppler Vibrometer (LDV) to test micro-wineglass resonators.

ProtoCAM

Location: Allentown, PA, USA

Phone: +1 (610) 261-9010

E-mail: sales@protocam.com

Various rapid prototyped parts and fixtures used in this dissertation were fabricated by ProtoCAM. The fixtures were used to build the piezo pinger setup described in Chapter 3.

Rigol Technologies, Inc.

Location: Oakwood Village, OH, USA

Phone: +1 (440) 232-4488 x110

E-mail: chris_armstrong@rigol.com

Oscilloscopes and function generators from Rigol Technologies, Inc. were used for characterization of devices and testing of front-end PCBs.

Sierra Circuits, Inc.

Location: Sunnyvale, CA, USA

Phone: +1 408-735-7137 x9838

E-mail: webpcb@protoexpress.com

Majority of the front-end PCBs used in this dissertation were fabricated by Sierra Circuits, Inc. Part of the PCBs were also assembled by Sierra Circuits, whereas the rest was assembled in house.

South Bay Technology, Inc.

Location: San Clemente, CA, USA

Phone: +1 949 492-2600

E-mail: mhonore@southbaytech.com

Sputtering targets and part of the diamond lapping films were purchased from South Bay Technologies, Inc.

Spectrum Micromechanical, Inc.

Location: San Diego, CA, USA

Phone: +1 (858) 453-3941

E-mail: jeff@spmmi.com

Fused silica and Borosilicate Glass (BSG) devices presented in this dissertation were diced by Spectrum Micromechanical, Inc.

Stanford Research Systems

Location: Sunnyvale, CA, USA

Phone: +1 (408) 744-9040

E-mail: info@thinksrs.com

Analog filters, scaling amplifiers and precision voltage sources from Stanford Research Systems were used for characterization of MEMS gyroscopes presented in this dissertation.

Technical Glass Products, Inc.

Location: Painesville Twp, OH

Phone: +1 (440) 639-6399

E-mail: tgp@tgpohio.com

Fused silica rods and various glass parts were purchased from Technical Glass Products, Inc.

Transene Company, Inc.

Location: Danvers, MA, USA

Phone: +1 (978) 777-7860

E-mail: Lynn@transene.com

Chrome and gold etchants were purchased from Transene Company, Inc. These engineered enchants have very high selectivities and work extremely well for etch back processes.

Ultrasil Corporation

Location: Hayward, CA, USA

Phone: +1 (510) 266-3700

E-mail: rduque@ultrasil.com

Silicon wafers used thought this dissertation were purchased from Ultrasil Corporation.

Westbond, Inc.

Location: Anaheim, CA, USA

Phone: +1 (714) 978-1551 x206

E-mail: sales@westbond.com

Westbond Epoxy and Wire Bonders were used for die attachment and wire bonding of devices developed as part of this dissertation.